High Resolution Infrared Spectroscopy of Slit-Jet Cooled Radicals and Ions

by

Melanie A. Roberts

B.A., Macalester College, 2005

A thesis submitted to the

Faculty of the Graduate School of the

University of Colorado in partial fulfillment

of the requirements for the degree of

Doctor of Philosophy

Department of Chemistry and Biochemistry

2012

This thesis entitled:
High Resolution Infrared Spectroscopy of Slit-Jet Cooled Radicals and Ions
written by Melanie A. Roberts
has been approved for the Department of Chemistry and Biochemistry

David J. Nesbitt

G. Barney Ellison

Date

The final copy of this thesis has been examined by the signatories, and we find that both the content and the form meet acceptable presentation standards of scholarly work in the above mentioned discipline.

Roberts, Melanie A. (Ph.D., Chemical Physics)

High Resolution Infrared Spectroscopy of Slit-Jet Cooled Radicals and Ions

Thesis directed by Prof. David J. Nesbitt

This thesis presents high-resolution spectra of supersonically-cooled organic radicals in the mid-infrared, the details and design of the instruments necessary to obtain the spectra, and the theory to understand the spectra and the larger context of the results. Specifically, four organic radicals are studied: singly-deuterated methyl radical (CH_2D), phenyl radical (C_6H_5), hydroxymethyl radical (CH_2OH), and ethynyl radical (C_2H). All of the spectroscopic studies presented use an existing mid-infrared high-resolution spectrometer with a frequency precision of better than 10 MHz. The radicals are generated using a discharge to dissociate a neutral precursor and form the radicals. The discharge is localized at the orifice of a slit supersonic expansion, which cools the radicals to around 20 K and allows for sub-Doppler spectral resolution. In addition to the description of the existing spectrometer, the design, construction, and successful testing of a new, automated mid-infrared spectrometer is presented. The new spectrometer is based upon difference frequency generation of a scanning Ti:Sapphire laser and a single-frequency Nd:YAG laser to create high-resolution mid-infrared radiation. The new system speeds up data-taking by fully automating the scanning process.

The four radicals studied in this thesis are all intermediates in combustion processes of hydrocarbon fuels. First, the out-of-phase symmetric stretch of phenyl radical is presented. As the first high-resolution infrared study of phenyl, it paves the way for future studies of this and other aromatic radicals. Second, the two fundamental CH stretches in CH_2D are studied with full rotational resolution. The narrow linewidth of the transitions reveals resolved fine structure and partially resolved hyperfine structure. This resolution yields additional information regarding the distribution of electrons in the radical. With this study of CH_2D, a nearly complete set of vibrational frequencies is present in the literature. This inspired us

to develop a comprehensive model that is capable of simultaneously fitting the CH and CD stretches of all the hydrogenic isotopomers of methyl radical. Third, while ethynyl absorbs in the mid-infrared, the transition studied are low-lying electronic states. The combination of a cold source of C_2H and high frequency precision allows us to clarify line assignments and find new transitions. Additionally, localized shifting of transition frequencies allows for identification and partial characterization of the dark perturber states. Fourth, the symmetric CH stretch of hydroxymethyl radical is studied at high-resolution. The high-resolution spectra improve upon band origin and structural information in the radical as well as set the stage for further experimental studies into potential large amplitude dynamics in the radical.

Dedication

To My Grandparents

Acknowledgements

First and foremost I would like to acknowledge my advisor, David Nesbitt. I truly appreciate all the effort he has put into helping me become a scientist and continually pushing me to grow as a student. He spent many long days in the lab teaching me how the high-resolution spectrometer works and guiding me through learning everything from reading a circuit diagram to solving quantum mechanical problems. I am constantly inspired by his dedication to science and endless energy to think deeply and clearly about even the seemingly simplest of problems.

I would like to thank the Nesbitt group, past and present members, for creating a supportive and inspiring atmosphere to work in. While I was working in B212 by myself, Tom Baker, Brad Perkins, and Alex Zolot were always willing to answer my questions at any time and I learned a lot from them. I worked with several post-docs in B212 and I thank them for helping me along the way; Feng Dong, Chandra Savage, Richard Walters, Chih-Hsuan Chang, and Erin Sharp-Williams. I want to thank Erin for her friendship and constant support for all problems scientific and personal, and for always being willing to laugh about it. I have also enjoyed working with the younger B212-ers Grant Buckingham and Nathan Hinkley who made sure life in lab was never dull. To the other members of the Nesbitt group, I have enjoyed working with you: Mike Ziemkiewicz, Mike Deskevitch, Danny Bell, Rob Roscioli, Julie Fiore, Andrej Grubisic, Andy Gisler, Lora Nugent-Glandorf, Vasiliy Fomenko, Mia Zutz, Dan Nelson, Larry Fiegland, Monika Gruetter-Kasumaj, Kevin Early, Nick Dupuis, Eric Holmstrom.

It has been a great honor to have worked in JILA and there are many people helped me from informal talks of quantum mechanics at cookie time to building a much-needed piece of equipment. I am grateful to the members of my annual review committee, Roberts Parson and Carl Lineburger, for their guidance. I also would like to thank the JILA staff members. I would like to thank the electronics shop, especially Terry Brown, James Fung-A-Fat, and Paul Beck. The computing group has helped me through many problems, especially Pete Ruprect, Jim McKown, Mike Paige, Alan Dunwell, and J.R. Raith. J.R. deserves special thanks for having rebuilt and saved every one of the six computers that run my two instruments. Hans Green, Blaine Horner, Ariel Paul, and rest of the instrument shop for building integral parts of my instruments and teaching me about machining along the way.

I feel very grateful to have had the opportunity to attend Macalester College since it was the chemistry faculty (Tom Varberg, Keith Kuwata, Rebecca Hoye, and Ronald Brisbois) whose classes were so enjoyable that I decided to major in the subject. I would especially like to thank my undergraduate research advisor, Tom Varberg, for somehow convincing me that a summer spent in a dark spectroscopy lab would be more fun and rewarding than a summer in the Boundary Waters of Minnesota, a truly life-changing decision.

Finally, I would like to thank my friends and family for supporting me on this long and, at times, arduous endeavor. I don't think I would have finished this process without my brother, Mike, who trained me to be tough; my sister, Meg, for always being there; and my parents for their support and love. Last, but not least, I thank my best friend and the love of my life Ted Reber.

Contents

Chapter

Tables

Table

Figures

Figure

Chapter 1

Introduction

The existence of infrared radiation was first recognized by Hershel by using a thermometer to measure the temperature of different regions of the visible spectrum and eventually mapped out measured temperatures of what we now know to be different frequencies of light. He wasn't the first person to explore different spectral regions, a few people had done so in the 1770's and again the 1790's, but he was the first to realize the significance of his measurements and identify a new region of radiation lower in frequency than the visible spectrum. He even used mirrors to reflect the IR radiation to determine that the new region of radiation had similar properties to visible radiation. The characterization of this region of light was furthered with the help of a few technological breakthroughs, specifically of the thermocouple by Nobili and Melloni around 1830. The thermocouple allowed faster temperature readings and avoided the problem of the radiation having to pass through glass, which has variable attenuation as a function of wavelength. With the discovery by Melloni that rock salt transmitted IR radiation without attenuation, researchers began to make rock salt prisms and optics and subsequently were able to begin to characterize IR radiation.[10] In 1859, Tyndall did the first study of molecular gas absorption by passing IR radiation through four foot-long gas-filled cells.[11] In the late 1800's several other researchers explored the IR absorption of molecular gases and ascertained that the wavelength-dependant absorptions could be attributed to molecular structure. In the first third of the twentieth century, physicists around the world continued to explore and characterize IR absorption of molecules. Many notable

contributions to the fields of infrared technology and spectroscopy during this period came from Coblentz. One example, in a collaboration with Mabery, who had the largest collection of purified hydrocarbon samples, Coblentz took IR spectra of the molecules that could be used to unambiguously identify each molecule.[12] This was the beginning of the link between the petroleum industry and IR spectroscopy. With World War II came a huge influx of government and industrial money and interest in the development of IR technology and its use as an indispensable tool for chemical identification, often with the added complication of classified research and technologies. The British initially invested in the technology to be able to identify the source of German fuel by examining the specific chemical composition. The Americans also heavily invested in the technology. The subsequent influx in funds for IR spectroscopy led to widely used commercial instruments that non-specialists could use to take IR spectra of samples. Original spectrometers of both Perkin-Elmer and Beckman were a result of this period and became a tool in chemistry research laboratories around the world.[13]

The work presented in this thesis uses direct absorption spectroscopy in the mid-infrared (mid-IR) region using a straight-forward application of Beers law,

$$\mathrm{A} = -\ln \frac{\mathrm{I}}{\mathrm{I}_\circ} = \mathrm{Nl}\sigma \tag{1.1}$$

where A is the absorbance, $I_\circ$ is the initial intensity of light sent to the sample, I is the intensity of light after passing through the sample, N is the number of absorbing molecules in the sample, l is the pathlength, and σ is the absorption cross section. In words, we compare the amount of light before passing through a sample with the amount of light after passing through a sample as a function of the frequency of the light, yielding the absorption spectrum of the sample. The energy of the photons in the IR region generally corresponds to fundamental vibrational excitation of molecules, with microwave frequencies corresponding to rotational excitation and the visible corresponding to electronic excitation. In this thesis, we study the CH-stretching vibrations of phenyl radical (C_6H_5), singly-deuterated methyl

radical (CH_2D) and hydroxymethyl radical (CH_2OH). Ethynyl radical (C_2H) is also studied in this thesis, but the presence of a low-lying electronic state makes the transitions studied in this region electronic transitions.

With our high resolution system, we gain more information than only the location of the vibrational (or electronic) transitions since we fully resolve the rotational structure. We can then obtain valuable information concerning the structure of the molecule and how it changes with vibrational excitation. In CH_2D, the coupling between rotational and electron spin angular momentum is large enough to be resolved in the spectra (fine structure). Additionally, we obtain partial resolution, in the form of broadened lineshapes, of the coupling of electron spin and nuclear spin angular momentum (hyperfine structure). In C_2H, we see transitions out-of and into different spin orbit states. Information obtained from high-resolution spectra can lead to many insights; for example, about the specific nature of bonding in the molecule, as is the case in CH_2D, or the nature of nearby dark states that do not have an IR absorption spectra, as happens in C_2H. We therefore work hard to obtain high-resolution spectra of these molecules, including a method for creating cold (10-30 K) molecules with sub-Doppler linewidths and a tunable laser system with a frequency precision of 10 MHz (30 parts-per-trillion) or better.

There are two high-resolution spectrometers presented in this thesis, both based upon difference frequency generation to obtain mid-IR light. The spectrometer described in chapter 2 has been evolving since initial development by the first students in the Nesbitt group; this spectrometer is used for all the projects in this thesis except for those in chapters 3 and 8. It is a testament to everyone who has worked on this spectrometer that it remains with so many original elements and design ideas even as improvements and changes were added with each new generation. For example, the over 100 optics and mounts on the table walks you through a bit of the history of optical mounts. The dye laser locking setup still employs optics mounts hand machined by graduate students epoxied to the table; many of the wavemeter optics use magnetic bases attached to JILA mounts from before set-screw optics mounting

became standard; the other frequency locking and diagnostic elements use early generation commercial mounts with very large optical mounting plates; the IR beampath has some of the newest mounts with sleek set-screw mounts for the optics and very high turns-per-inch adjustments. The heart of the instrument is a tunable ring dye laser and a single frequency argon ion laser that are combined in a periodically poled lithium niobate crystal where difference frequency generation takes place producing mid-IR radiation. The tunability of the dye laser is therefore transferred to the IR light as well as the narrow linewidths of both the argon ion and dye lasers. The IR light then passes through a 16 pass Herriot cell where a 4 cm long supersonically expanding slit nozzle flows the gas of interest. The details of this spectrometer are presented in chapter 2. The molecules studied in this thesis fall under the category of transient intermediates, short-lived molecules that play important roles in many chemicals systems such as combustion, atmospheric chemistry, and interstellar space. Each chapter introduces the historical background, chemical application, and spectroscopic interest in studying each molecule so the remainder of this chapter is a brief introduction to the molecule and summary of some of the highlights of each project.

Chapter 3 describes in detail the new high-resolution infrared spectrometer and uses the OH stretch of doubly deuterated hydronium ion, HD_2O^+, to demonstrate the quality of the spectrometer. The HD_2O^+ detection is made possible by utilizing the high ion densities formed in supersonically cooled pulsed discharge methods, the sensitive detection from concentration modulation techniques, and long absorption path lengths. The spectrometer utilizes difference frequency mixing in a periodically poled lithium niobate crystal of a scanning single mode Ti:Sapphire laser and a fixed frequency single mode Nd:YAG laser to create narrow-linewidth radiation from 1700 - 3900 cm^{-1} (5.9 - 2.6 μm). The relative frequency of infrared light is determined by locking the Nd:YAG laser to a stabilized cavity and tracking the scanning of the Ti:Sapphire laser on two stabilized cavities. The absolute frequency is determined by D_2O absorption in the mid-infrared region. There are two major improvements of this instrument over its predecessor: an increased frequency range and nearly fully

automated scanning. The increased frequency range means that we are now able to take data in the OD stretching region specifically of HD_2O^+; however, to test the spectrometer we record OH stretching lines and compare them to the OH stretch lines taken previously on the instrument in chapter 2. Frequency comparisons of many lines over multiple scans on different days resulted in a frequency precision of 10 MHz. With the addition of automated scanning, data are much faster and easier to obtain with this instrument than with the old instrument and will hopefully prove to be a great instrument for taking the massive amounts of data required for these high-resolution spectroscopy experiments.

Chapter 4 discusses the rigid nearly symmetric top radical, phenyl radical (C_6H_5). Phenyl is one of the largest molecules we have studied at high resolution and yet has a relatively simple spectra. The cyclic structure with largely sp^2 hybridized bonds creates a relatively rigid and planar molecule well described by rigid rotor calculations. Phenyl radical is formed by homolytic cleavage of a CH bond in the stable benzene molecule and, as such, is highly reactive. Phenyl is of interest in combustion chemistry as an aromatic species since typical fossil fuels are rich in aromatic species. Furthermore, an unwanted byproduct of combustion is the formation of soot, which signals incomplete and inefficient combustion. The formation of soot involves making large ring compounds, as soot is generally a mix of large ring and aromatic compounds. Similarly, phenyl radical is of astronomical intereste as an intermediate in the formation of polycyclic aromatic hydrocarbons. In chapter 4, the ν_{19} out-of-phase CH symmetric stretch mode is presented and analyzed. Using ground state rotational constants from a microwave study by Thaddeus and coworkers,[14] we are able to determine the excited state rotational constants for the first time. We also obtain the first gas phase value of the vibrational band origin and, upon comparison with the matrix values, find that there is a remarkably small shift between the matrix value and the gas phase values. The ability to resolve the rotational structure of this relatively large prototypical ring molecule is a promising start towards *in situ* measurement of observation of complex aromatic species during combustion.

In chapter 5, the CH symmetric and asymmetric stretches of mono-deuterated methyl radical (CH_2D) are presented with full rotational and fine structure resolution and partially resolved hyperfine structure. CH_2D is smaller and more asymmetric than phenyl radical and, as a result of the decreased symmetry, the rovibrational spectra doesn't have the easily recognizable P-, Q-, and R-branch structure of a symmetric top. Using *ab initio* predictions for the structure and a rigid rotor Hamiltonian as an initial guide, we begin to assign the spectrum. The assignment is confirmed by four line combination differences. Additionally, the slit expansion collisionally quenches the transverse velocity distribution along the laser probe direction, yielding sub-Doppler resolution of spin-rotation structure and even partial resolution of nuclear hyperfine structure for each rovibrational line. The fine and hyperfine structure manifest as a complex lineshape of each rotational line. Global least-squares fits to the lineshapes provide additional information on spin-rotation and nuclear hyperfine constants, which complement and clarify previous FTIR studies of CH_2D in the out-of-plane bending region. Finally, analysis of the spectral data from the full isotopomeric CH_mD_{3-m} series based on harmonically coupled Morse oscillators (HCMO) establishes a predictive framework for describing the manifold of planar stretching vibrations in this fundamental combustion radical.

In contrast to phenyl and CH_2D where we were exciting CH stretching vibrations, the molecule presented in chapter 6, C_2H, has low lying electronic states that absorb in the mid-IR region. C_2H, ethynyl radical, is known to be a key intermediate in acetylene (C_2H_2) combustion[15] and has been detected in outer space.[16] Acetylenic combustion is of interest in chemical and industrial applications and in the study of combustion since C_2H_4 is a known intermediate in the combustion of fuel-rich systems of large molecules.[17] High resolution infrared spectra for five $^2\Pi$-$^2\Sigma^+$ bands of jet-cooled C_2H in the gas phase are reported. The combination of slit-jet cooling ($T_{rot} \approx 12$ K) and sub-Doppler resolution (≈ 60 MHz) permits satellite branches in each $^2\Pi$-$^2\Sigma^+$ band to be observed and resolved for the first time as well as help clarify a systematic parity misassignment from previous studies.[18, 19] The observed

lines in each band are least squares fit to a Hamiltonian model containing rotational, spin-rotational, spin-orbit, and lambda-doubling contributions for the $^2\Pi$ state, from which we report revised excited state constants and band origins for the observed bands. Three of the four bands fit extremely well within a conventional $^2\Pi$ model (i.e. $\sigma < 20$ MHz), while one band exhibits a local perturbation due to an avoided crossing with a near resonant dark state. Vibronic assignments are given for the observed bands, with the dark state clearly identified as a highly excited stretch and bending overtone level $\tilde{X}$ (1,2^2,0) by comparison with high level *ab initio* efforts.

Additionally, the $\tilde{A}^2\Pi$- $\tilde{X}^2\Sigma^+$ origin band exhibits a strong, parity-specific local perturbation in the upper $^2\Pi_{1/2}$ state. Based on revised parity assignments of the levels, the perturbing state is unambiguously determined to be $^2\Sigma^+$ symmetry, and thus coupled to the $\tilde{A}^2\Pi_{1/2}$ state by Δ K $= \pm 1$ Coriolis interactions. By incorporating $\Sigma - \Pi$ Coriolis coupling into the unperturbed Hamiltonian (containing only rotational, spin-rotational, spin-orbit, and lambda-doubling contributions), we are now able to fit the observed $^2\Pi$-$^2\Sigma^+$ origin band to a sub Doppler experimental uncertainty of 15 MHz (0.0005 cm^{-1}). In addition, the observation of pairs of transitions to mixed states permits determination of the band origin and rotational constant (B_{pert}) for the dark $^2\Sigma^+$ state, which prove to be in remarkably quantitative agreement with full vibronic predictions of Tarroni and Carter[8] as well as UV dispersed fluorescence studies of Hsu et al.[20] A dark state perturbation is identified from shifts in the frequency and intensity of transitions as well as the appearance of an additional transition. This represents an important benchmark in mapping out non-BornOppenheimer vibronic interactions and energy level structure in a polyatomic combustion radical system, an understanding of which will be key to modeling chemical reactions in both terrestrial and astronomical environments.

Chapter 7 presents the first high resolution direct absorption study of hydroxymethyl radical, CH_2OH, in the infrared CH stretching region. As a result of the low rotational temperature and sub-Doppler linewidths obtained in the slit supersonic expansion, the K_a

$= 0 \leftarrow 0$ band of the symmetric CH stretch for CH_2OH is unambiguously identified and analyzed. By way of additional chemical confirmation, hydroxymethyl radical is generated via two different chemical synthesis: a pure methanol discharge and a methanol plus molecular chlorine discharge. The identified transitions are fit to a Watson A-reduced symmetric top Hamiltonian to yield the first precision experimental values for the ground state rotational constants as well as improved values for the symmetric stretch rotational constants and vibrational band origin. The results both complement and substantially improve upon spectral efforts via previous double resonance ionization detected IR methods by Feng et al., which obtained partially rotationally resolved spectra in the CH and OH stretching regions.[21]

Chapter 8 presents a novel method for improving the frequency precision and accuracy of the Coherent 899-29 Ti:Sapphire laser and Autoscan system while augmenting the automated scanning capability. This laser system is widely used for high resolution spectroscopy because of the narrow linewidth, wide tuning range, and automated scanning. To improve the resolution of the system, we present a solution incorporating two locked cavities, one with 250 MHz free spectral range (FSR) and one with a 1.5 GHz FSR, to provide a more accurate and precise frequency reference for the existing wavemeter. To illustrate the versatility of this system, a method for integrating the Ti:Sapphire and Autoscan system into a sophisticated mid-IR high-resolution automated spectrometer for studying transient species is presented. The spectrometer is based upon difference frequency generation between the tunable Ti:Sapphire laser and a stabilized, single frequency YAG laser in a Periodically Poled Lithium Niobate crystal. The precision of the absorption lines of molecular ions generated by the instrument is 9.3 MHz.

Chapter 2

Experimental Apparatus

2.1 Introduction

Elements of this instrument have been used since the eighties to do spectroscopy and has been improved upon, added to, and changed with every new post-doc and graduate student in the lab. While several thesis talk in depth about most of the pieces of the instrument as they were added, there is no thesis that includes it in its current form. Specifically, the locking circuits are described in depth in Chris Lovejoy's thesis[22] and John Farrell's thesis[23], the wavemeter and several other aspects of the optical layout are in Scott Davis's thesis[24], and the computer programs to process and analyze data are described in Erin Whitney's thesis[25]. The components of the instrument that have been discussed in detail before will only be discussed briefly and emphasis will be places on elements that are not described in detail in other thesis. The most significant change that has happened is the switch from a lithium niobate crystal to a periodically poled lithium niobate crystal. More minor changes have been made to certain electronics, parts of the optical layout, and computer programs.

2.2 Generation of Tunable High-Resolution Infrared Light

The tunable infrared light is generated by difference frequency generation of a single frequency argon ion laser (Ar^+) and a tunable narrow-linewidth dye laser based on an original design by Pine.[26] An overview of the optical layout of the experiment is shown in Figure

2.1. Briefly, the light from the tunable dye laser is sent through a waveplate to rotate the polarization 90° so that it is vertical to match the vertical polarization of the Ar^+ laser and as is required by the nonlinear crystal. The dye light then passes through two telescoping lenses before being overlapped with the Ar^+ light and focused into the non-linear crystal. The telescoping lens system is necessary to make the dye laser beam, which is expanding upon exiting the laser, have a beam profile that will match the Ar^+ laser beam after they both are focused into the crystal. The lenses and lens position are chosen by first profiling both laser beams and then using the ABCD law to solve for the two lenses and positions that will best overlap the dye laser with the Ar^+ laser.[27]

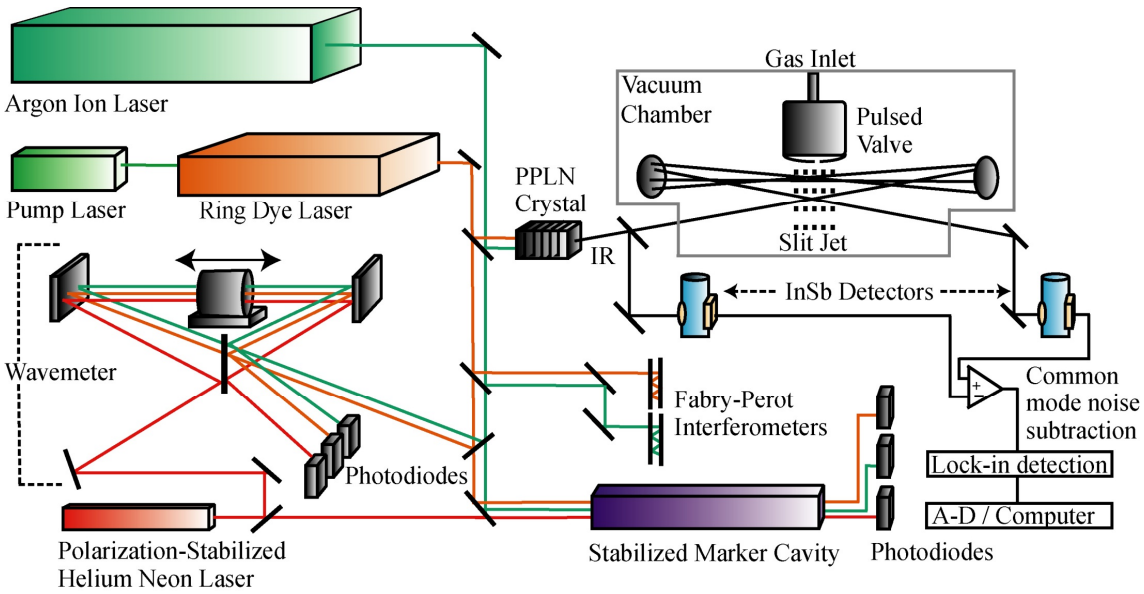

Figure 2.1: Schematic of the instrument.

The nonlinear crystal used here for different frequency generation is a periodically-poled lithium niobate crystal (PPLN). There are two crystals for use with this experiment,

one with 8 poling periods and one with 12 poling periods. The PPLN crystal uses quasi phase matching for difference frequency generation of the Ar^+ and dye laser frequencies. A more complete description of difference frequency generation, quasi phase matching, and periodic poling are in chapter 3. The single frequency laser can lase at any of the visible Ar^+ lines, with 514 nm and 488 nm as the two strongest lines and the ones used in this thesis. One crystal is for use with the 514 nm line and one is for use with the 488 nm line. Each poling period covers about 150 cm^{-1} with the ability to temperature tune for the proper phase matching conditions within that 150 cm^{-1}. Temperature tuning from 100-200 degrees Celsius is achieved with a commercial brass oven and temperature controller.

As three frequencies of light exit the crystal, a filter blocks the visible dye and Ar^+ light while the infrared radiation gets focused and split into two roughly equal beams. One beam is directly focused into the reference, liquid nitrogen cooled, InSb detector and the other beam goes into the Herriot cell. The Herriot cell consists of two mirrors, both with a 30 cm radius of curvature, spaced approximately 60 cm apart. This cell is easily configured for up to 18 passes. The Herriot cell configuration increases the pathlength while continually focusing the beam as it passes through the sample. Each pass is also sent very nearly overlapping the previous pass in space. More details of the Herriot cell are found in Chapter 3. Upon exiting the Herriot cell, the beam is focused onto the signal InSb detector.

2.2.1 Dye Laser

The tunability of the system comes from the dye laser. The layout of the Spectra-Physics model 380A ring dye laser can be found in Figure 2.2, not drawn to scale.. With the exception of locking elements, all of the necessary elements to create a small linewidth, tunable laser are found in the laser cavity. A few notes on the cavity in general are in order before going into each element in more detail. The distance from M1 to M2 is about 8.4 cm and the distance from M3 to M4 is about 53.1 cm. The second general consideration is that all relevant surfaces are at Brewster's angle with respect to the horizontal component. This

means that the laser will lase purely with horizontal polarization. This is exploited in some of the elements described below.

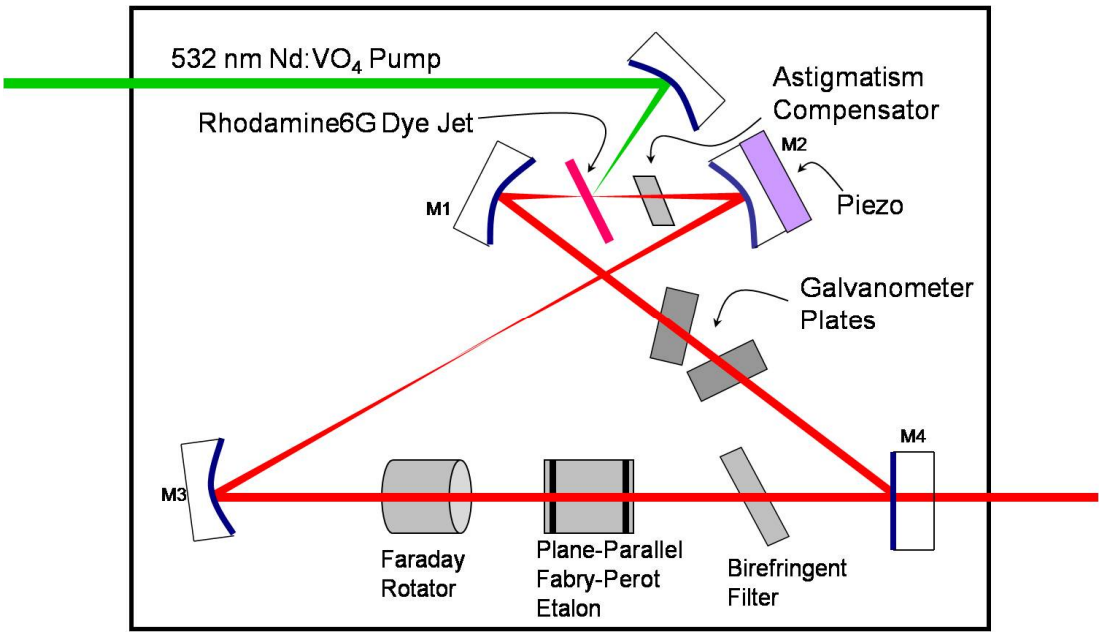

Figure 2.2: Schematic of the ring dye laser.

The next major design aspect of the cavity is that it is a ring cavity. In a linear cavity, there is the presence of standing waves due to the superposition of waves traveling in both directions. In a ring cavity, with the help of a unidirectional device, the waves propagate in only one direction and are thus traveling waves. The unidirectional device used in this case is a Faraday rotator. The Faraday rotator consists of magnetized Faraday plate and a quartz plate and takes advantage of the Faraday effect to create a unidirectional device.[28] Briefly, both the Faraday plate and the quartz plate rotate the polarization of an incoming beam by 45°. When a beam travels in the forward direction, the two rotations cancel and

the polarization of the outgoing beam is the same as the incoming beam. Conversely, when a beam propagates in the opposite direction, the 45° rotations add and the outgoing beam has a perpendicular polarization to the incoming beam. The perpendicularly polarized beam is lost through either parallel polarizers on the input and output of the Faraday rotator assembly or on the Brewster surfaces of the optics in the laser. A schematic of what this effect looks like is in figure 2.3 with thin arrows representing the polarization direction. The Faraday rotator has the effect of suppressing the cavity modes in the opposite direction, making the cavity unidirectional.

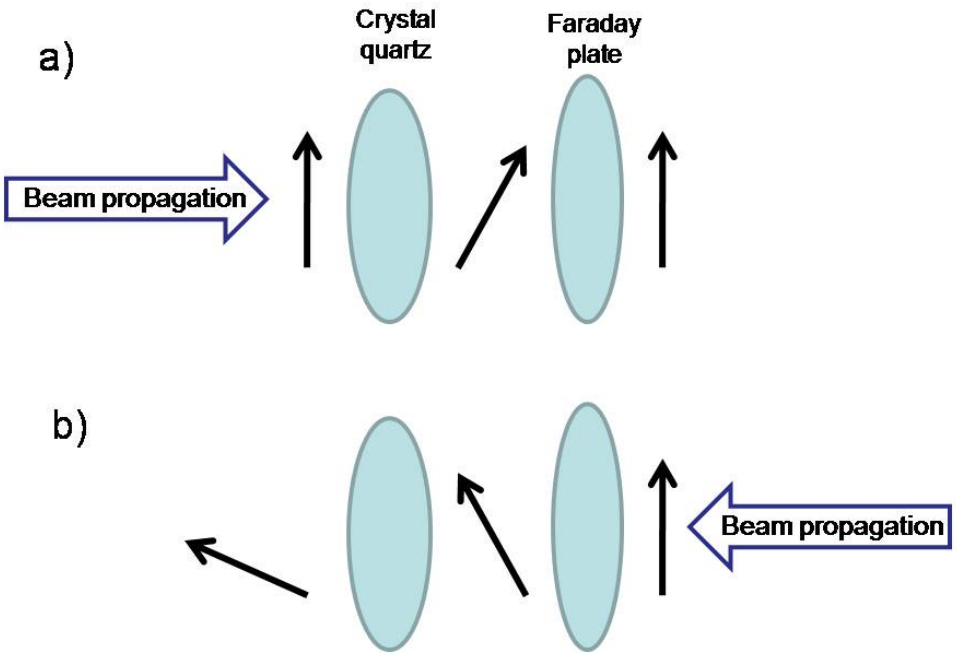

Figure 2.3: Faraday rotator operation, the black arrows represent the state of linear polarization. a) shows the beam propagating in the desired direction. Note that the input and output polarizations are the same. b) shows the beam propagating in the backwards direction. Note that the two polarization rotations add.

The cavity longitudinal modes are approximately 200 MHz apart, so it is necessary to

have a way to reliably suppress these modes in order to get single frequency operation. This is done with two elements, a birefringent filter and a Fabry-Perot etalon. The birefringent filter takes advantage of a birefringent material, whereby the index of refraction of the material, n, is dependant upon the direction of travel through the crystal. The index through the material can be described by two different values of n, one for the ordinary axis (n_o) and one for the extraordinary axis (n_e) of the crystal. Upon hitting the crystal, the incoming radiation divides into two components that travel with different velocities as a result of the different n values. There becomes a phase difference between the component traveling along the ordinary axis and the component traveling along the extraordinary axis. This phase retardation, ϕ, can be expressed as[27, 29, 30]

$$\phi = 2\pi \frac{(\mathrm{n_o} - \mathrm{n_e})\mathrm{T}}{\lambda \sin[\beta]} (\sin^2[\alpha]) \tag{2.1}$$

where n_o and n_e are the ordinary and extraordinary indices of refraction, β is the Brewster angle, α is the angle between the fast axis of the plate and the high loss polarization of the Brewster surfaces, T is the plate thickness, and λ is the wavelength. The β is the incident angle, Brewsters angle in this case, and α is the angle between the optic axis and the light ray in the plate. The birefringent filter will be a high loss element in the cavity for wavelengths that do not have a phase retardation that is an integer multiple of the wavelength. Tuning is achieved by rotation of the filter. The phase shift from the birefringent filter is a relatively broad function of wavelength, illustrated in figure 2.4.

For spectroscopic applications, an element with better mode selectivity is needed. In this case, a Fabry-Perot etalon with plane parallel mirrors is used to select out a single cavity mode. The free spectral range of this etalon is about 75 GHz and the mirrors used have a reflectivity on the order of 30%. The transmission of a Fabry-Perot is

$$\mathrm{T} = (1 + \frac{4\mathrm{R}}{(1-\mathrm{R})^2} \sin^2[\frac{2\pi \mathrm{nd}}{\lambda}])^{-1} \tag{2.2}$$

where R is the reflectivity of the mirrors, n is the integer mode number, and d is the cavity length. Equation 2.2 gives the familiar Fabry-Perot transmission fringes seen in figure 2.4.

This form assumes the reflectivity, R, of the mirrors to be the same, as they are in this laser. The elements for longitudinal mode selectivity are now in place. The birefringent filter selects only a few Fabry-Perot cavity modes and the Fabry-Perot lock loop keeps the cavity on just one mode, see figure 2.4. To decrease the potential for mode hops in the Fabry-Perot cavity, a smaller etalon with a 900 GHz free spectral range originally came with the laser but is not currently used.

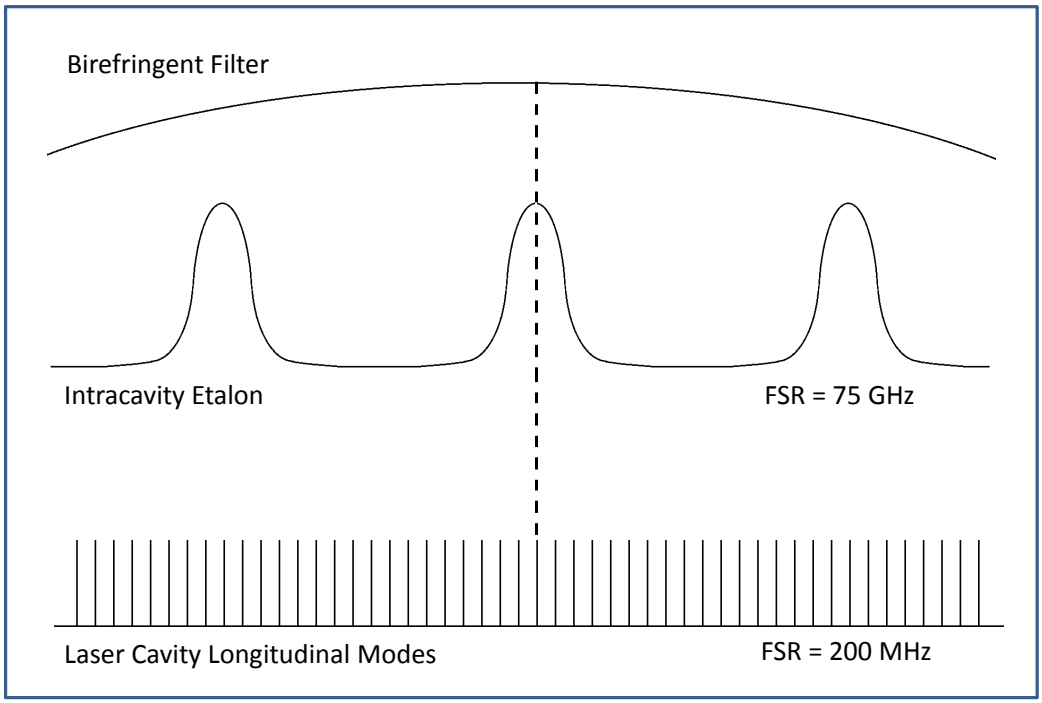

Figure 2.4: Schematic illustrating how the birefringent filter and Fabry-Perot etalon select out a single cavity mode.

As mentioned above, in order to insure that the etalon remains on the same mode, it is actively stabilized by a "top-of-line" lock loop. A "top-of-line" lock loop does exactly as the name implies, the lock maintains the laser frequency at the top (instead of the side) of the transmission fringe of the etalon. To accomplish this locking technique, there is a

cylindrical piezo-electric element between the two mirrors that controls the length of the cavity (figure 2.5). A small voltage 2 KHz sine wave dither is applied to the piezo, which causes the intensity of the output to vary by a negligibly small amount. A small percentage of the output of the laser is picked off by a beamsplitter just after the output coupler of the laser. The intensity of this pickoff is monitored by the laser control box electronics. The laser electronics box sends proportional and integral error signals to the laser in the form of correction voltages applied to the piezo. The feedback from this locking circuit keeps the Fabry-Perot cavity at a distance that corresponds to the peak of a transmission fringe. This locking circuit is the commercial one that is built into the laser.

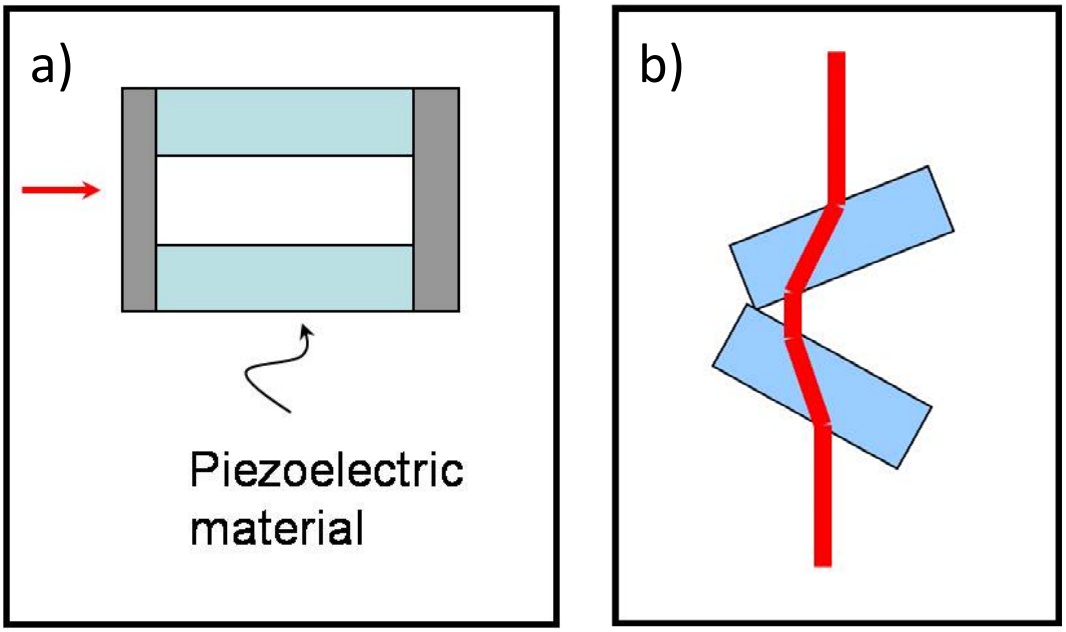

Figure 2.5: a) The inter-laser Fabry-Perot cavity geometry. b) Scanning galvanometer plates. Notice that the distance the beam propagates through the plates is dependent upon their angle.

To further stabilize the frequency output of the laser, in addition to the etalon lock loop, the output of the laser is locked to an external cavity and a correction voltage applied to the piezo element on M2. This loop is a "side-of-line" lock, thus there is no dither voltage applied to the laser or external cavity. The external cavity is a Fabry-Perot cavity with a galvanometer plate in the center. The principle that this lock loop operates on is as follows. Part of the dye laser beam is sent to a power detector and another part sent through the external cavity and onto a signal detector. The output of the two detectors is divided so that power fluctuations in the laser output do not effect the frequency lock loop. The locking circuit employs a standard feedback loop in which the piezo on the laser M2 is adjusted to keep the output of the external cavity locked on a side of the Fabry-Perot transmission fringe.

The last unexplained element in the laser cavity are the two galvo plates, also known as Brewster plates. These are essentially pieces of glass on rotation motors set at approximately Brewster's angle. Figure 2.5 shows how the light will travel through the plates. As the plates rotate, the distance the beam travels through the galvo plates changes. This changes the length of the cavity slightly and results in a change of wavelength of the laser. The galvo plates can scan using just the electronics on the laser control box. However for this experiment, the galvos are controlled as part of a master-slave scanning system, where the laser is the slave and an external cavity is the master.

The external master cavity is also used to further stabilize the dye laser. This external cavity is made from Zerodur material, which has a very low thermal expansion coefficient as a method of stabilization, and aligned in a bowtie configuration. A quartz plate mounted to a galvo is inside the cavity to change the cavity length, making the cavity frequency tunable. The dye laser is locked to this cavity using a "side-lock" technique. A small amount of the dye light is sent to the "reference" detector while some light is sent through the cavity and onto the "power" detector. The signals are then divided, to account for any power fluctuations, and an offset added so that the signal level crosses zero half way up a transmission fringe.

The lock then has a zero-crossing to lock on and a directionality in the signal to know how to correct for the error. Feedback is sent to laser control box to maintain the lock.

As mentioned earlier, the laser control box has the capability to scan the laser over a small frequency range. It moves the Brewster plates while the internal laser etalon tracks to maintain lock on the peak of a transmission fringe. However for implementation in this instrument, we use a step-scan method whereby the laser frequency is stepped by some amount and held at that frequency while recording data. In this case, the scanning is controlled via a LabWindows program on a computer. The computer outputs a step voltage, which is sent to the galvo plates in the master cavity. A feed forward is sent to the laser galvo plates, via the laser control box, and the laser is able to follow the scanning of the master cavity.

With the use of an internal etalon stabilization and overall laser stabilization to an external cavity, the output of the dye laser can have linewidths on the order of 1 MHz. Internal galvo plates, which follow the scanning of an external master cavity, provide stable computer-controlled scanning of the dye laser. The range of this scanning is limited to the ability of the galvo plates to change the cavity length without hoping a mode of the internal etalon or birefringent filter. Longer frequency scans are obtained by changing internal Fabry-Perot modes manually by tuning the birefringent filter. Many of the smaller scans are stitched together to get continuous data for hundreds of wavenumbers.

2.3 Frequency Stabilization and Determination

The frequency reproducibility of the experiment is arguably the most important piece of the experiment, without which the data we take would be useless. The error in the frequency of the infrared laser is just the quadratic sum of the error of each of the Ar^+ and dye lasers, $\Delta\nu_{IR}^2 = \Delta\nu_{dye}^2 + \Delta\nu_{Ar^+}^2$ where $\Delta\nu$ is the error in the frequency. We exploit this by locking the Ar^+ laser to a single frequency and monitoring the dye laser frequency as it scans so that the precision of the visible lasers is transferred to the infrared radiation. A known molecular

absorption line serves to calibrate the frequency axis to make the frequencies absolute. These components are described in great detail in other thesis and papers, but for completeness, I will summarize each piece here.

The frequency stabilization starts with a polarization stabilized HeNe laser. The laser is semi-homebuilt with a purchased laser tube and power supply but assembled here. The laser lases in two modes with perpendicular polarizations. Since both ends of the laser tube emit light, one end is sent for use in the experiment and the other output is used for the HeNe stabilization circuit. The HeNe light is sent through a polarization beam splitter so that each polarization, hence each mode, is sent to a detector. The subsequent signals from the two detectors are sent to the locking circuit where the signals are divided. This creates an error signal which the circuit uses to lock on and the error is zero when the two polarizations of the laser have equal magnitude. The laser tube is wrapped in heater tape, which will change the tube length when heated enough to change the relative intensities of the two HeNe modes. The HeNe is set to lock at equal magnitudes of both polarizations.

The output of the stabilized HeNe is split with one part sent to a Fabry-Perot cavity (a.k.a. marker cavity or optical transfer cavity)[31] and the other sent to a wavemeter. The marker cavity consists of two mirrors with a 30 cm focal length that are mounted to a 30 cm long cylinder consisting of two sections of pyrex glass, a section of stainless steal wrapped in heater tape, and a piezo section. The light is aligned in a bowtie configuration, preventing feedback into the laser. The free spectral range of this cavity is $\approx$ 250 MHz. The cavity is locked to a peak of a HeNe transmission fringe using a "top-of-lock" method with the necessary small 4.4 KHz dither applied to the piezo. The feedback has a fast, proportional response delivered to the piezo, on top of the dither, and a slow, integrated response sent to the heater tape. The cavity length changes to maintain a constant optical path length and compensate for changes in temperature and pressure that may occur. The locked cavity is stable to better than a few MHz over the course of days. This stable cavity provides the necessary optical tool for being able to stabilize the Ar^+ laser and track the dye laser

scanning frequency.

A pellicle beam splitter sends $\approx 5\%$ of the Ar^+ and dye laser beams to all of the necessary diagnostics and locks; specifically the wavemeter, marker cavity, commercial Fabry-Perot interferometers, and the dye laser lock (dye laser only). Starting with the Ar^+ laser lock, the Ar^+ beam is overlapped with the HeNe directly before entering the marker cavity and a photodiode records the transmission of the Ar^+ through the cavity. The locking circuit here is also a "top-of-line" lock with the same dither signal modulating the cavity for the cavity lock is used to create the error signal for the Ar^+ laser. The circuit works to keep the Ar^+ laser lasing with a frequency that corresponds to the peak of a transmission fringe through the marker cavity. The feedback is in the form of a voltage sent to the piezo mounted on the back of the Ar^+ high reflector mirror.

In addition to locking the dye laser and monitoring the scanning, it is necessary to detect when the dye laser mode hops. To detect mode hops, we employ a time-to-amplitude conversion technique (TAC). We map the change in frequency to make sure it is a linear function in time so that mode hops become easily recognized as a change from the linear plot. To accomplish this, we send the dye laser light into the commercial Fabry-Perot cavity that is changing length in a sawtooth pattern. There is a photodiode at the output of the commercial cavity that monitors the signal of the laser through the cavity. The TAC signal measures the time from the start of the FPI ramp until the signal reaches a certain voltage threshold, corresponding to the presence of a fringe. As the laser scans, the fringe position relative to the start of the ramp changes, creating the linear function mentioned earlier. While the FPI is commercial, the ramping and TAC electronics are homebuilt.

The final optical piece of the instrument is a homebuilt wavemeter. The wavemeter, a traveling Michelson interferometer that uses the locked HeNe as a reference, is described in detail in Scott Davis's thesis[24]. The wavemeter is used to take the starting frequency of the scan, which is always set to be to top of a marker cavity fringe. While not used for absolute frequency measurements, the wavemeter reading is used to be able to compare marker cavity

fringes, described fully in Erin Whitney's thesis[25] and summarized in section 3.6.

2.4 Radical Generation

The specifics of creating each of the radicals presented in this thesis are found in the chapter pertaining to that radical. However, the same pulsed nozzle, discharge, and vacuum chamber setup are used and will be described here for completeness. The neutral precursor is prepared in a holding tank with a buffer gas, usually Ne70 (i.e., 70% Ne, 30% He) with a final concentration of about 5% precursor. The buffer gas choice is important to balance efficient cooling while minimizing the formation of clusters in the jet[32] and Ne70 is the gas used in most of the experiments presented here. The buffer gas and precursor mixture is further diluted to typically $\sim$ 1.0% in Ne70 using mass flow controllers to regulate the gas flow into the slit stagnation region.

The slit valve is a JILA-made solenoid-driven pulsed injector with a 4 cm by usually a 300 μm slit orifice operating at a 19 Hz repetition rate and about a 1000 μs duration.[33] The pressure in the stagnation region is maintained at usually anywhere from 200 - 1000 Torr, with the vacuum chamber kept at $<$ 50 mTorr during operation of the pulsed valve, by a Roots blower (560 liters/sec). During the pulse, a 50 KHz, 50% duty cycle, high negative voltage (up to -1 KV relative to the nozzle body), high current pulse is applied to the jaws of the nozzle. The jaws are attached to an Ultem insulator, which is attached to the main body of the nozzle. When the pulsed current is applied, a discharge strikes between the jaws and the main nozzle body. Since the jaws form the limiting orifice of the expansion and the distance between the jaws can be changed, the slit width is easily adjustable. Lock-in detection with double balanced mixers is used to phase sensitively detect concentration modulation of the radicals produced in the pulsed discharge, thereby greatly minimizing spectral congestion due to absorption by precursor molecules. Typical rms noise levels are 0.003% in a 10 KHz bandwidth.

2.5 Data Acquisition and Processing

The computer program that collects the data is the same program that controls the dye laser scanning. It is written in LabWindows and employs two analogue-digital (A/D) cards, NI6110 and NI6025E. The triggers that control the pulse valve and discharge are also generated by the LabWindows program and sent to the respective electronic controls via the NI6110 A/D card. The signal from the lock-in detector is recorded via the NI6025E card. All of the frequency diagnostics are sent to the computer via the NI6110 card and include the IR power from the signal detector, the TAC, the dye laser marker cavity fringes, and the wavemeter readings. The data is recorded coincident with the valve pulse and can be averaged for any number of pulses the user wishes to specify. The signal is treated slightly differently in that it goes through a gated integration process before being averaged over the specified number of valve pulses. Briefly, the gated integration process involves a time average of the signal while the valve is open and an average of a baseline before and after the gas pulse. The baseline averages are then subtracted from the signal average. This will correct for the possibility of a rolling baseline and decrease the noise as a result of the averaging. To approximate the reduction in noise from the gated integration process, just combine the idea that averaging reduces the noise by $\frac{1}{\sqrt{N}}$, where N is the number of points averaged, and then propagate the error through the subtraction of the gated regions. The result of this calculation is that the specific noise reduction is

$$\sigma' = \sigma\sqrt{(\frac{1}{\sqrt{\mathrm{N_s}}})^2 + (\frac{1}{\sqrt{2\mathrm{N_b}}})^2} \tag{2.3}$$

where σ' is the new standard deviation of the noise, σ is the noise before averaging, N_s is the number of points averaged for the signal, and N_b is the number of points in each baseline gate. The time bin for each of the data points is 1 μs. After the gated integration process, the value of the signal at that point is recorded along with the diagnostics.

The LabWindows data acquisition program stores all of the recorded data as one long string of numbers for each individual scan. The numbers must be converted from bits to

% absorbance (or voltage for the etalon and TAC signals) as a function of frequency. This process was described in Erin Whitney's thesis, but since then the code has been moved to Origin's LabTalk language (a C-based language) and C, however the concept of how the axis is obtained is the same. First, the long string of numbers is broken up into columns of the signal, etalon, TAC, and IR power as a function of data point number. The scan parameters are recorded on a separate spreadsheet, called scanlist, and include the wavemeter reading for the start frequency of the dye and Ar^+ lasers. The dye laser marker cavity fringes are counted and peak positions as a function of data point number are found using the Snyder peak finder algorithm[34]. The signal is turned into a % absorbance measurement by dividing out all sources of gain (A/D gain, gain on the lock-in amplifier, etc) and dividing by the IR power.

One scan is used as the reference scan, specifically the reference scan provides the fringe number that will be labeled as 10000 so that all other fringes taken that day can be assigned a fringe number relative to 10000. The start frequency of each scan, which corresponds to the top of an etalon fringe and is the average of ten wavemeter measurements, is subtracted from the reference scan start frequency and divided by the free spectral range. The result of this should be an exact integer number of fringes. Since we are using experimental measurements, it will not be exact but should be within about 5% of an integer (ie $\pm$ 0.05). Each starting fringe now has a relative fringe number assigned to it. A new frequency axis is then created by using the etalon peaks numbers and linearly interpolating between fringes to assign a fractional fringe number to each data point. The free spectral range is then used to convert the fractional fringe number axis into a relative frequency axis, in GHz. At this point, all of the scans now have a relative frequency axis such that frequency differences between absorbance peaks in difference scans are precise to < 10 MHz or so. The Snyder peak finder is used to find the frequency of a known absorption line, which is used to convert the relative frequency axis to an absolute wavenumber axis. Specific absorption lines used for each project are found in the chapter about that project. On the scanlist sheet, the frequency

of the start and end point for each scan to be added to the concatenated data is entered. The scans are then combined into one long spreadsheet, or concatenated, and converted to absolute wavenumbers. The frequency reproducibility usually has a root-mean-squared value of about 5 MHz.

Chapter 3

A new high-resolution spectrometer for the study of radicals and ions

3.1 Introduction

Transient species, such as radicals and ions, play an essential role in a range of chemical systems including atmospheric chemistry, combustion, interstellar chemistry, molecular biology, pollution processes, and chemical vapor deposition[35]. For example, the chemistry of the interstellar medium involves a variety of ions that, while often short-lived on earth, are long lived in the conditions found in space[36]. These ions are formed by a variety of processes including particle collisions, UV radiation, or even cosmic rays. Once formed, ions take part in many reactions, in spite of low concentrations, in part because ion-neutral reactions have no reaction barrier and there are attractive forces between the particles. By way of an example, H_3O^+ is predicted to be one of the more abundant polyatomic species in interstellar dust clouds and is a key ion for oxygen chemistry. The dissociative recombination reaction, $H_3O^+ + e^- \rightarrow OH + H_2O$, produces OH, which can react with O to form O_2. In addition to CO, models predict O_2 and H_2O to be the dominant oxygen-containing molecules in interstellar clouds. Unfortunately, it is often difficult to directly observe O_2 and H_2O in much of the interstellar medium because of interference from the Earth's atmosphere, making H_3O^+ ion a useful probe of interstellar H_2O and O_2 dynamics and concentrations. The mid-infrared is an especially useful region for probing interstellar chemistry because it is not limited to studying molecules with permanent electric dipole moments, like the microwave region, and has less atmospheric interference than the ultraviolet region. Another recent

motivation for developing high resolution systems has stemmed from a desire to accurately measure the Boltzmann constant using molecular transition line profiles, which also requires high accuracy and precision[37, 38]. Additional uses of the mid-IR include remote sensing applications[39, 40], molecular spectroscopy, and various industrial applications.

The tools used to study the mid-IR region evolved as new and better technology was introduced. One of the older technologies for creating tunable infrared (IR) light is the color center laser. While useful, these lasers have a limited tuning range and are experimentally challenging and delicate. By way of example, the crystals are very hygroscopic and light sensitive and therefore must be keep under high vacuum, cooled by liquid nitrogen, and away from light[41]. Another relatively old technology is the use of a continuous-wave (cw) tunable dye lasers. To access the IR region, dye lasers are generally combined with difference frequency generation to reach in the mid-IR. Dye lasers are very reliable, but since the gain medium is liquid, there are some inherent instabilities. Solid state gain mediums are reliable way to gain stability; lead salt Diode lasers are are possible alternative, but are limited by a relatively small tuning range. Quantum cascade lasers (QCL) are another type of solid state laser, however currently most QCL's have a limited continuous tuning range, usually on the order of several tens of wavenumbers. The external cavity quantum cascade lasers can have up to 250 cm^{-1} tuning range, but compared to a 1500 cm^{-1} tuning range of a dye laser, it is still quite small[42, 43, 44].

For a versatile high-resolution system with a large continuous tuning range, dye or Ti:Sapphire lasers, which lase in the visible (the most stable dyes) and near-IR, respectively, are still the only way to get the large continuous tunability. The best dyes, both for stability and conversion efficiency, lase in the visible and the Ti:Sapphire lases in the near-IR region. This necessitates the use of a conversion medium to generate light in the mid-IR region. Miller and coworkers have used Raman stimulation of a gas cell to create mid-infrared light, but the resolution of that is limited to 200 MHz[45]. The most common way to generate cw mid-IR light is through difference frequency generation, first implemented for high resolution

spectroscopy was first reported by Pine et al. in 1974. They mixed a single frequency argon ion laser with a tunable dye laser in a lithium niobate crystal to create mid-infrared light[26]. Since then, many variations of this have been implemented by groups around the world and including the other high resolution spectrometer in the group. The choice of nonlinear crystal depends upon the desired wavelength region with lithium niobate and $AgGaS_2$ crystals being the most common until periodic poling of lithium niobate, the advantages of which will be discussed in section 3.2.1, became a readily available alternative[46].

As a goal of building a new instrument for doing high-resolution spectroscopy in the mid-IR on many difference molecular systems we look for i) a large, continuously tunable frequency range in the mid-IR, ii) frequency precision and accuracy of 10 MHz or better, iii) an improvement in speed and ease of data acquisition, iv) high detection sensitivity, and v) ability to create relatively large concentrations of radicals and ions. By way of comparison, the experiment occupying the other half of the lab satisfies most of these requirements, however it cannot reach the lower frequency region including the OD stretching region and data taking is still a very slow and manual process. Additionally, the Ar^+ and dye lasers are notoriously unstable and difficult to work with. To our knowledge, there are two other Ti:Sapphire and YAG DFG systems, but published about the same time, in 2008, for sensing applications[47, 48] and measuring the Boltzmann constant[49]. They utilized much more complicated methods to stabilize their YAG laser and were limited by the stability of the Ti:Sapphire laser, but still achieved similar resolution to what is reported here. However, their system lacks the scanning infrastructure to scan continuously for long distances and they are setup to only look at Doppler-limited neutrals. The system presented here is unique in combining the laser system, with the sub-Doppler radical and ion generation system, with the machinery for extended and automated continuous scanning.

The instrument presented here does direct absorption spectroscopy using a straight

forward application of Beer's law

$$\mathrm{A} = -\ln \frac{\mathrm{I}}{\mathrm{I}_\circ} = \mathrm{Nl}\sigma \tag{3.1}$$

where A is the absorbance, $I_\circ$ is the initial amount of light sent to the sample, I is the intensity of light after it goes through the sample, N is the number of absorbing molecules in the sample, l is the pathlength, and σ is the absorption cross section. From this equation, we see there are two ways to increase in the absorbance signal. Since σ is a property of the molecule, we cannot change that, however we can increase the number of molecules and the pathlength. The slit discharge setup generates radicals and ions in high concentrations and the Herriot cell and 4 cm long slit increases the pathlength considerably. These concepts have been used before, including in the other high resolution spectrometer in the group, and are well established as a reliable way to look at radicals and ions.

What separates this spectrometer from its predecessors is most notably the fast and automated scanning; there are also other improvements including an extended frequency range, different method of obtaining the frequency axis, and the use of solid state lasers providing a more stable setup. The infrared light is generated by difference frequency generation in a periodically poled lithium niobate crystal between a Nd:YAG laser and a tunable Ti:Sapphire laser. A schematic of the experiment is shown in figure 8.5. The laser system is described in section 3.2 with the infrared generation described first in section 3.2.1 and the the description of the scanning system in section 3.2.2. The method of accurately and precisely determining the frequency axis is described in section 3.3 and the molecular source and y-axis determination in section 3.4. The data acquisition process and the data processing are described in sections 3.5 and 3.6, respectively. Results from the HD_2O^+ test system are in section 3.7.

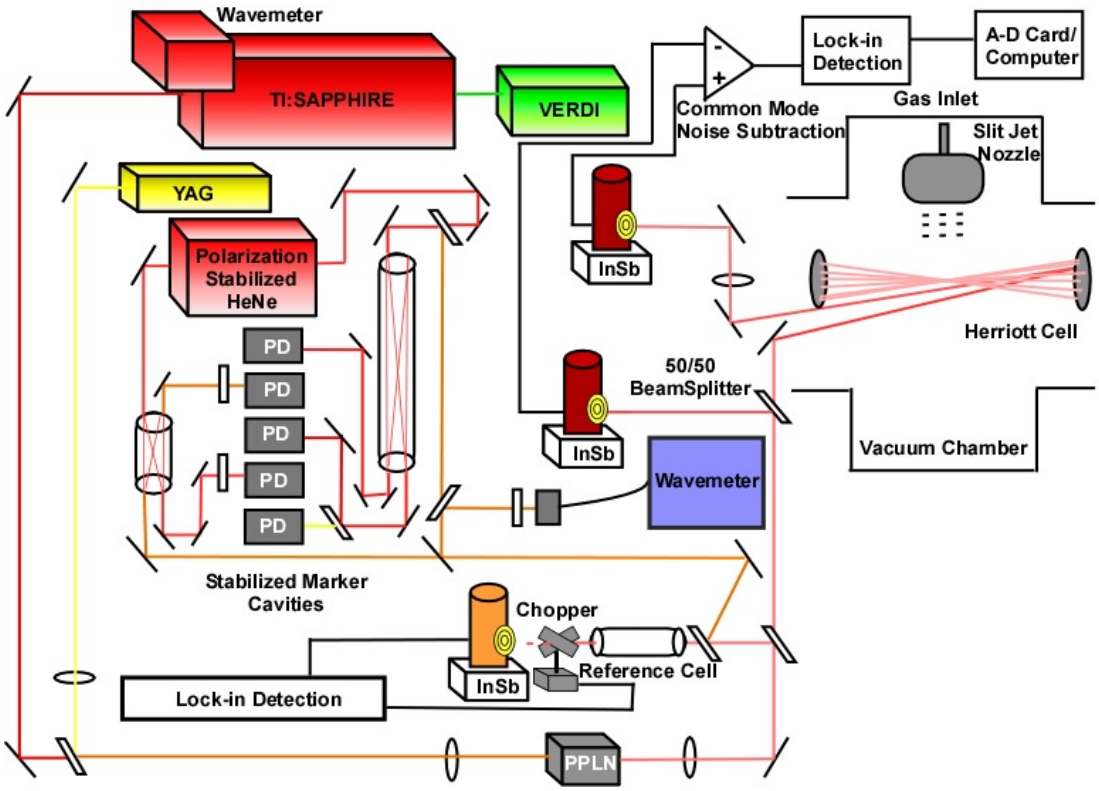

Figure 3.1: Optical layout of the high-resolution spectrometer. The radiation from a tunable Ti:Sapphire laser is overlapped with the single-frequency light of a Nd:YAG laser in a periodically poled lithium niobate crystal (PPLN) and via difference frequency generation to produce the mid-infrared light. The frequency axis is precise to 10 MHz.

3.2 Laser System

3.2.1 Infrared Generation

The tunable mid-IR light is created through difference frequency generation using the tunable Ti:Sapphire laser and a single frequency Nd:YAG laser. The Ti:Sapphire laser is a vertical ring cavity with most optics mounted directly to an Invar bar for length stability. The gain medium is an on-axis pumped Titanium-doped sapphire crystal and the pump

laser is a 6-Watt Coherent Verdi (Nd:YVO_4) laser. The Ti:Sapphire crystal has a very broad tuning range ($\approx$ 720-1000 nm) and with this laser requires three sets of optics to cover the entire tuning range; however it is worth noting that there are now optics available that cover the entire tuning range, which would be a nice upgrade at some point. With a ring laser design, it is necessary to have an element in place to promote lasing in only one direction, in this case there is an optical diode in the beam path, which uses optical activity and the Faraday effect, to achieve unidirectional lasing. Single frequency operation achieved with the combination of a birefringent filter and two intracavity etalons, similar to the dye laser described in chapter 2.

The single-frequency laser is a commercial diode pumped Neodymium-doped Yttrium Aluminum Garnet (Nd:YAG) laser. The basic operation and design is documented in the manual and will be briefly summarized here. It is a non-planar ring oscillator design, in which the laser cavity is confined to the Nd:YAG crystal with the cavity mirrors being the polished surface of the crystal exploiting either total internal reflection or a reflective coating. The ring configuration is made unidirectional by applying a magnetic field to the crystal to create an effective optical diode thereby increasing the gain in one direction such that the laser doesn't lase in the other direction. The laser has a small amount of tunability by changing the crystal temperature and straining the crystal by way of an attached piezoelectric element. We use the laser at a single frequency and exploit the tunability features to keep the laser frequency locked and stabilized, described in detail in section 3.3.

The single frequency Nd:YAG laser overlaps the Ti:Sapphire laser and is sent into the nonlinear crystal for difference frequency generation. The amount of mid-infrared radiation that we get out is directly related to amount of light pumping the crystal as well as the quality of overlap of the beams. To insure good spatial overlap, two iris have been placed in the beampath, on right after the lasers are combined and after the crystal as far down the table as possible, and both the YAG and Ti:Sapphire lasers are aligned through the irises. The IR power is also increased by focusing the pump beams in the crystal, to increase the

power density, and have the beams tightly focused for the entire length of the crystal. The Rayleigh range is the propagation distance, z, necessary for the beam width to increase from ω_0 to $\sqrt{2}\omega_0$. The optimum beam profile as the lasers travel through the crystal is going to be a compromise between a tight focus and long Rayleigh range. Additionally, the beams from the two laser are diverging at different rates so to get a good spatial overlap it is necessary to add in a lens or set of lenses. Using the ABCD law, we calculate a solution to not only make the beams have the same mode, but make it a good compromise between having a tight focus and long Rayleigh length. In this case, it is only necessary to add one lens to the YAG beam path to sufficiently match to profile of the Ti:Sapphire laser.

The nonlinear crystal used here is a periodically poled lithium niobate crystal, which takes advantage of quasi phase matching to generate the mid-IR radiation. To start with a physical picture of difference frequency generation, the radiation incident on the crystal causes the charges to accelerate and those accelerating charges generate electromagnetic radiation. Mathematically it is common to use polarization to describe nonlinear optical processes, which is simply that a polarization changing with time can drive an electromagnetic field[50]. More specifically for difference frequency generation, incident radiation causes an oscillating dipole moment with components at each incident frequency with a nonlinear response. This time-varying polarization can act as a source of new components of the electromagnetic field, in this case the difference frequency. From a mathematical perspective, the polarization as a function of time is expressed as

$$\overrightarrow{P}(\mathrm{t}) = \epsilon_{\circ}[\chi^{(1)}\overrightarrow{E}(\mathrm{t}) + \chi^{(2)}\overrightarrow{E}^{2}(\mathrm{t}) + \chi^{(3)}\overrightarrow{E}^{3}(\mathrm{t}) + ...] \tag{3.2}$$

where $\overrightarrow{P}(\mathrm{t})$ is the time-varying polarization, $\overrightarrow{E}(\mathrm{t})$ is the electromagnetic field and χ is the nonlinear optical susceptibility. In a material with only a linear response, the expansion is truncated after the first term and we see that polarization is directly proportional to the applied electric field. The second order term is the nonlinear response that describes difference frequency generation. The $\chi^{(2)}$ is tensor for materials, but can be simplified to a

3 x 6 matrix for most materials because of the inherent symmetries present in the crystal lattice such that $d_{il} = (\frac{1}{2}\chi^{(2)}_{ijk})$ where i, j, k are indices and $l = j + k$. Any given material will have many dipoles oscillating with the phase of the incident field. With correct relative phase, the radiation produced by each dipole will constructively add and the system will act like a phased array of dipoles and output radiation, which is described mathematically as the phase matching condition, $\overrightarrow{k}_3 = \overrightarrow{k}_1 + \overrightarrow{k}_2$ and is also conservation of momentum. The other condition necessary for a nonlinear process is one that conserves energy, $\omega_3 = \omega_1 + \omega_2$.

By satisfying both the conservation of energy and conservation of momentum conditions, we can describe difference frequency generation. By writing the magnitude of the wavevector as $n\omega/c$ and substituting it into the phase matching condition, an apparent contradiction appears: $\frac{n_3\omega_3}{c} = \frac{n_1\omega_1}{c} + \frac{n_2\omega_2}{c}$ and it seems that phase matching can only occur if the index of refraction is the same for all wavelengths of light, which is not the case. The reason this is not a problem is that phase matching occurs in birefringent materials, materials where the index of refraction varies with direction in the crystal. This allows light with different polarizations and/or directions through the crystal to experience different indices and satisfy the phase matching condition. Lithium niobate has a temperature dependant index of refraction so as the frequency of radiation changes the phase matching condition can continue to be met by changing the temperature of the crystal. Birefringent phase matching is doable and still commonly used, but it is much easier to use a process called quasi-phase matching whereby the strict condition of phase matching doesn't need to be met. In a material like periodically-poled lithium niobate, the properties of the crystal have been periodically reversed so that while the phase is mismatched it is periodically reversed to mismatch the phase in the other direction, thus allowing the light to propagate without perfect phase matching. The poling period is made specifically for a certain set of wavelengths and corresponds to the length of crystal at one orientation before it is switched.

Because of the wide tuning range of the Ti:Sapphire laser, we have 3 PPLN's of 7 poling periods each in order to cover most of the frequency range reachable by the laser.

Experimental tuning curves for one of the PPLN crystals is shown in figure 3.2. The $LiNbO_3$ crystals used here are actually doped with MgO to make them less absorbent at the lower infrared frequencies. The necessary poling period to generate IR light from any given input beams is calculated using the Sellmeier equation, which calculates the index of refraction for a given temperature and involves parameters that are fit experimentally[51, 52]. The standard expression finds the index of refraction, n_e at a given temperature, T, and a given wavelength, λ,

$$\mathrm{n_e^2}(\lambda, \mathrm{T}) = \mathrm{a_1} + \mathrm{b_1 f(T)} + \frac{\mathrm{a_2} + \mathrm{b_2 f(T)}}{\lambda^2 - (\mathrm{a_3} + \mathrm{b_3 f(T)})} + \frac{\mathrm{a_4} + \mathrm{b_4 f(T)}}{\lambda^2 - \mathrm{a_5^2}} \tag{3.3}$$

where the temperature dependence, in Celsius, enters through

$$\mathrm{f(T)} = (\mathrm{T} - \mathrm{T_\circ})(\mathrm{T} + \mathrm{T_\circ} + 2 \times 273.16) \tag{3.4}$$

where $T_\circ$ is the reference temperature, 24.5° here. The other parameters are numerically fit from experimental data and can be found in Jundt et al.[51] Once the index of refraction for each wavelength is calculated at a given temperature, the poling period is easily calculated using the phase matching condition or quasi-phase matching:

$$\Delta \mathrm{k} = 2\pi\left(\frac{\mathrm{n_p}}{\lambda_\mathrm{p}} - \frac{\mathrm{n_s}}{\lambda_\mathrm{s}} - \frac{\mathrm{n_i}}{\lambda_\mathrm{i}} - \frac{1}{\Lambda}\right) = 0 \tag{3.5}$$

where n_p is the extraordinary index of refraction for the pump wavelength as calculated above and n_s and n_i are the corresponding values for the signal and idler, respectively. The poling period needed to satisfy this condition is Λ. The experimental tuning curves for one of the PPLN crystals at three different temperatures is in figure 3.2. This calculation doesn't indicate the efficiency of the conversion process. The commonly used expression[53] for the conversion efficiency for a difference frequency generation process is

$$\mathrm{P_i} = \frac{4\omega_\mathrm{i}^2 \mathrm{d_{eff}^2 l^2 P_s P_p}}{\mathrm{n_p n_s n_i c^3 \pi \epsilon_\circ}(\omega_\mathrm{s}^2 + \omega_\mathrm{p}^2)} \tag{3.6}$$

where ω_i is the frequency of the idler beam frequency; P_s and P_p are the signal and pump beam powers, respectively; n_s, n_p, n_i are the appropriate refractive indices for each of the

signal, pump, and idler beams; l is the length of the crystal, 4 cm here; and d_{eff} is the $2\pi/d_{33}$.

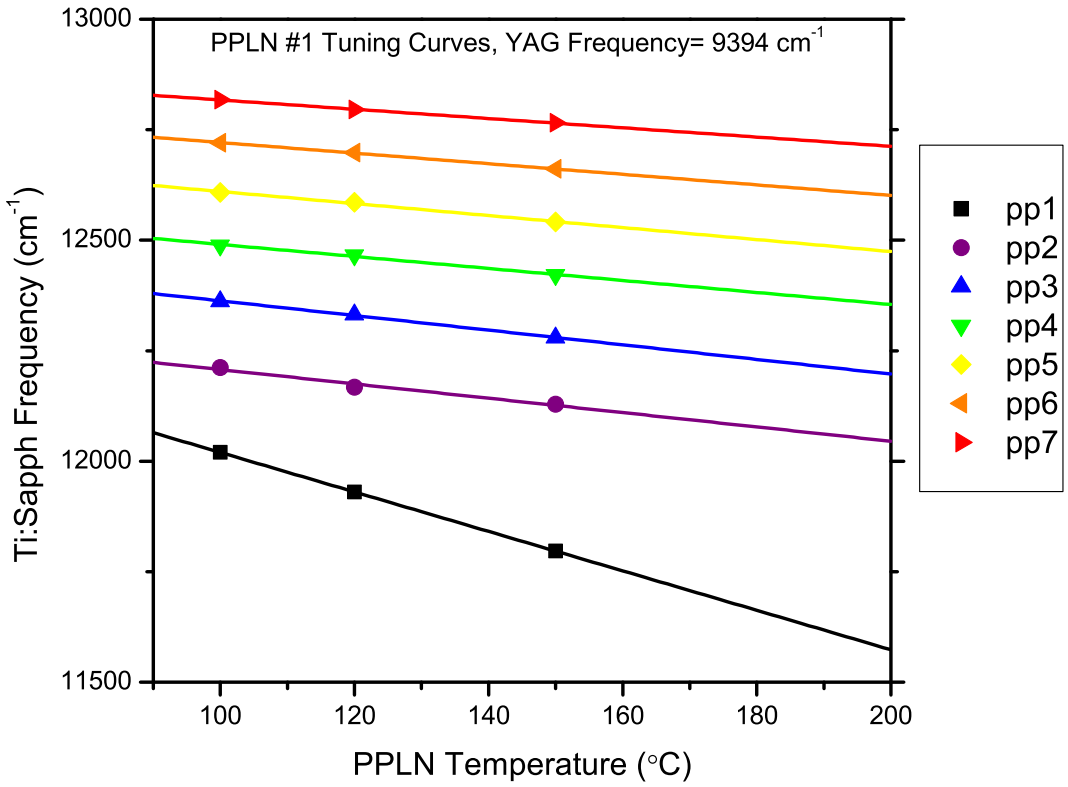

Figure 3.2: Experimental tuning curves for one PPLN. There are three PPLN's, each with 7 separate poling periods, necessary to cover the full tuning capability of the Ti:Sapphire laser.

Upon exiting the crystal, the infrared radiation is split into two approximately equal parts, with one portion directed into the liquid-nitrogen cooled InSb reference detector. The other portion is sent into the vacuum chamber, through a 16-pass Herriot cell before exiting the chamber and subsequently focused onto the liquid-nitrogen cooled InSb signal detector. A Herriot cell increases the pathlength of the absorption while probing the center of the slit-jet and maintaining a focused laser beam. The Herriot cell consists of two 2" gold mirrors spaced twice the radius of curvature apart. In this case, the radius of curvature of the

mirrors and subsequent size of the Herriot cell is limited by the available vacuum chamber to be 20 cm, making a 40 cm long cell. The beam enters the cell just below one of the mirrors through a CaF_2 window, the bottom right of the cell. The beam should be focused at this point in order for it not to clip the underside of the mirror as it passes through on the way to the diagonally opposite corner of the other mirror. Upon hitting the top left of the mirror, the beam heads to the bottom right of the first mirror, just above where the beam passed through the first time. The beam is passed back and forth in this way so as to make an upside-down U pattern on the mirror by the CaF_2 window and a right-side up U on the other mirror. Figure 3.3 panel a) shows a schematic of the laser beam pattern on each of the mirrors. At the center of the cell, the beams pass each other in a narrow region where the 4 cm-long jet of molecules is. The 16 passes through the 4 cm of gas makes for 64 cm for an absorption pathlength. In an ideal design, the laser beams would pass straight through the slit of gas, at a constant distance from the slit orifice. However, because of the geometry of laser beams passing through the Herriot cell, the laser beams actually come in at slight angles from the jet. The larger the Herriot cell, the better the approximation that the beams pass straight through the gas jet. In a 40 cm cell such as this one, the deviation from this linear approximation is significant and is the major cause of line broadening in the experiment. Based upon the geometry, the total vertical span of the jet probed at the ends is about 7.5 mm and the horizontal span is 2.5 mm. A place for future improvement could be to extend the arms of the Herriot cell to be 60 or more cm apart.

The second aspect of the Herriot cell involves the focus of the beam due to the curvature of the mirror. The radius of curvature of the mirror is set to be half the distance between the two mirrors. Using the ABCD law of Gaussian optics, we simulate what the beam size for each pass at one of the mirrors and the center of the cell. Figure 3.3 panel b) shows the results for a simulation based upon placing the mirrors exactly twice their radius of curvature apart. While the beam size at the center of the cell, where the slit jet is, remains small the beam size at the mirror blows up. This is undesirable because after a few passes the light

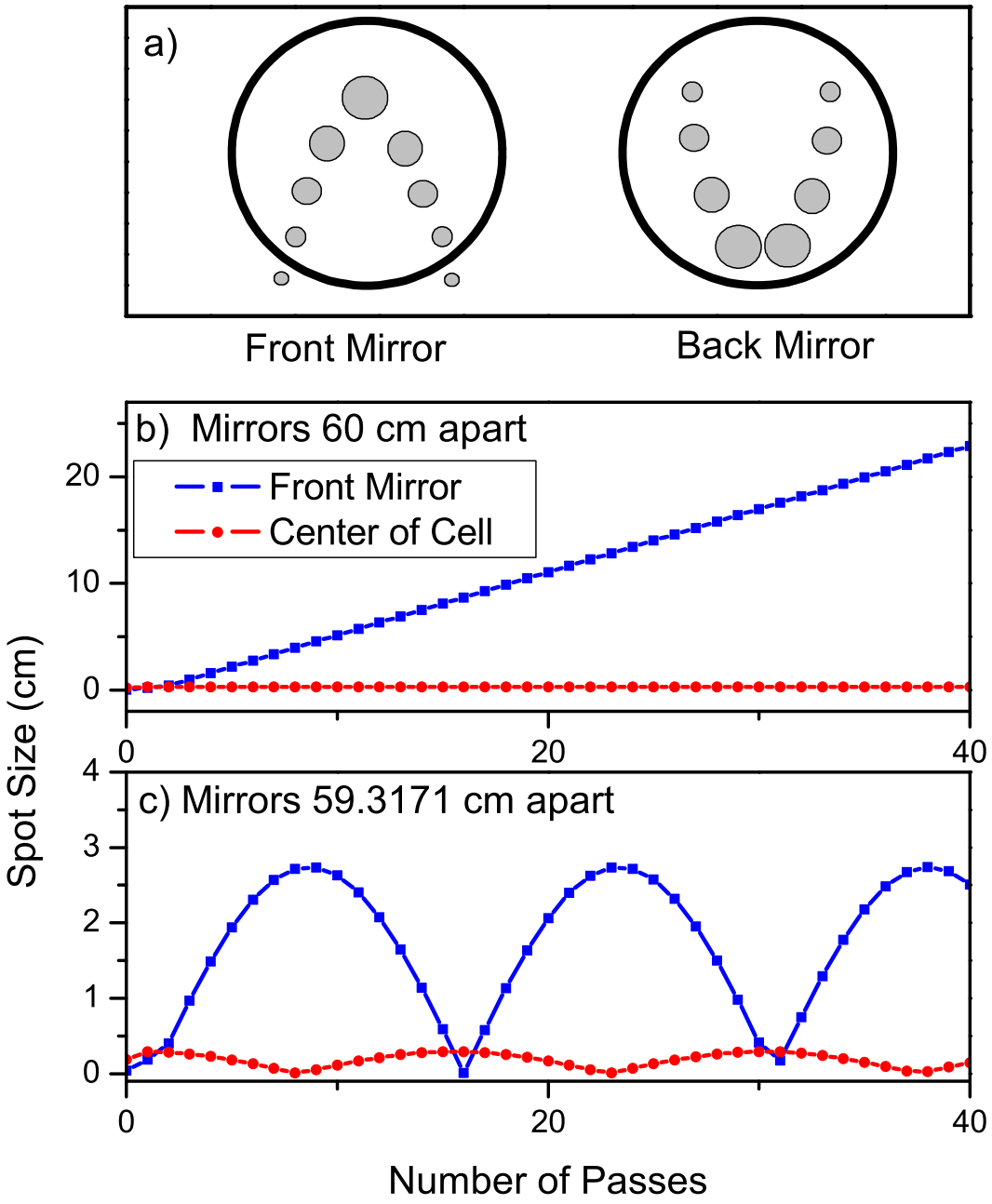

Figure 3.3: Properties of a Herriot cell. Panel a) is a schematic of the U-shaped pattern of the laser beams on both the front and back mirror of the Herriot cell. Panel b) plots the beam spot size as a function of pass number both at the center of the cell and on the front mirror of the cell for a mirror spacing exactly equal to twice the radius of curvature (60cm). Since the spot size at the front mirror is continually expanding and will likely not cleanly exit the cell. Panel c) illustrates the optimal mirror spacing so that the exit beam is small enough to easily exit the cell without clipping the mirror.

wouldn't fit on the mirror and it would be hard to direct the beam out of the cavity without it clipping on the mirror. Panel c) of figure 3.3 shows the calculations for the scenario where the mirrors are moved 0.687 cm closer together. Now the beam stays relatively focused at the center of the cell as well as on the mirror. It is advantageous to have the mirrors at such a distance apart that the beam is most tightly focused as it is exiting the cell because it maximizes your ability to get the beam cleanly out of the cell. Once the light exits the Herriot cell, it is focused onto a liquid nitrogen cooled InSb detector.

An important feature of this spectrometer is how sensitive it is, for which the shot noise on the detectors provides the ultimate lower limit of the detection sensitivity. The amount of IR light generated depends upon the powers of the Ti:Sapphire and YAG lasers on a given day at a given frequency, in addition to things like quality of the alignment, therefore the amount of light generated has some variation. On a typical day, we might have 2 volts of IR light on the signal detector. The IR detector has a 100 kΩ transimpedence amplifier followed by an amplifier with a gain of 1, which translates to 20 μA of current. The shot noise on this amount of current is given by $\sqrt{2ie}$, where i is the current and e is the charge of an electron. A typical shot-noise absorbance sensitivity is 2×10^{-5} in a 10 kHz bandwidth.

3.2.2 Scanning

At the heart of the infrared generation system is a cw Ti:Sapphire ring laser, a commercially available system that includes computer controlled scanning and wavemeter. The Ti:Sapphire laser operation is discussed in detail in the manual, however it is briefly summarized below before discussion of how the labwindows program controls the scanning. The Ti:Sapphire cavity is a vertical ring cavity with the pump beam, a Coherent Verdi Nd:YVO_4, hitting the crystal on axis. The Ti:Sapphire crystal has a broad tuning curve and there are three sets of optics in order to cover the whole range. A birefringent filter serves to narrow the tuning range. Then there are two etalons placed inside the cavity in order to obtain single-frequency operation. The free spectral range of the cavity is about 280 MHz. The

thin etalon has a free spectra range of 225 GHz and the thick etalon has an FSR of 10 GHz. A small pick-off of the laser output split into two parts, one goes directly to a detector and the other goes through the reference cavity and then into a detector. The reference cavity serves as the master cavity and the laser as the slave cavity while scanning. The reference cavity has a quartz plate attached to a galvo. The Autoscan computer sends a voltage to the reference cavity galvo to step the size of the reference cavity. The laser cavity is locked to the reference cavity, so it adjusts the laser cavity galvos and etalons accordingly. A reflection off the thin etalon is sent to a detector and used to keep the etalon tracking with the laser frequency. The thick etalon also tracks with the scanning. The locking controls are located in the 899 control box and the scanning controls are part of the Autoscan computer.

The Ti:Sapphire laser also has a wavemeter that is attached to the box and is integral to the automatic scanning system, called Autoscan. The stated accuracy of the wavemeter is ± 200 MHz and the stated precision is ± 50 MHz; we have a good measure of the accuracy and are usually better than the stated accuracy and precision, depending upon the quality of the alignment. The Autoscan wavemeter combines the precise measurement from thermally stabilized etalons with an absolute frequency device to obtain the frequency. The absolute measurement comes from an optical activity device (OAM) consisting of a crystalline quartz piece and a spinning polarizer wheel. The light is sent through the optical axis of two different lengths of the quartz crystal; which causes the polarization to rotate by an amount dependant upon the length traveled through the crystal and the frequency of the light. The two rotated beams then go through the spinning polarizer wheel to determine the degree of polarization. The polarizer wheel is able to determine the polarization angle to about 0.1 degree or about a part in 10^3 so by comparing the two beams, with different rotations, the accuracy reaches the ± 2.5 cm^{-1} level necessary for interpreting the etalon data. The light is also sent to two Zerodur 10 GHz etalons, stabilized to ± 0.03°C. The transmission through the two cavities is compared and a precise, but inaccurate, frequency is obtained. By using the OAM to get an absolute measurement and the VET measurement to add precision to

that number, the wavemeter obtains a precise and accurate frequency reading. The frequency reading from this wavemeter is used for the automatic scanning function, which makes this laser so nice for scanning large amounts of data quickly.

In order to understand how we obtain a high quality x-axis it is necessary to understand a little about how the Autoscan scans. Figure 3.4 illustrates the logic of Autoscan and how the rest of the experiments fit in. Autoscans starts by moving the laser to the desired start frequency and reading the frequency to verify that it is at the correct start frequency. You can specify how large or small a tolerance you would like on this frequency reading, but since the accuracy and precision of the wavemeter is 100-200 MHz, it is not meaningful to specify a tolerance less than that; 100 MHz is usually sufficient. After the laser is at the desired frequency it step-scans 10.2 GHz, the step-size is flexible and specified by the user. The laser takes steps by changing the voltage on the galvo; it does not read the frequency during the 10.2 GHz scans but rather relies on a linearization calibration. This calibration is imperfect and has systematic deviations from linear by several MHz and is something we will have to correct for. After the laser has scanned the 10.2 GHz segment, it adds 10.2 GHz to the desired starting frequency and attempts to move the laser to that frequency. It adjusts the laser until the frequency the wavemeter reads is within the specified tolerance of the specified frequency. This has a few important consequences. The first consequence is that if one segment is off for some reason, that error is not carried over into the rest of the scan. The second consequence is that the laser is resetting itself many times during a scan, so the wavemeter correction needs to be quick and reliable enough to do it numerous times during each scan. A scan will continue for how ever many segments the user specified. More details on how we correct for this are found in the following section.

3.3 Frequency Determination

The heart of the precision of the frequency axis is a home-built polarization-stabilized helium neon laser (HeNe) based upon the design of Niebauer et al[54]. The HeNe laser

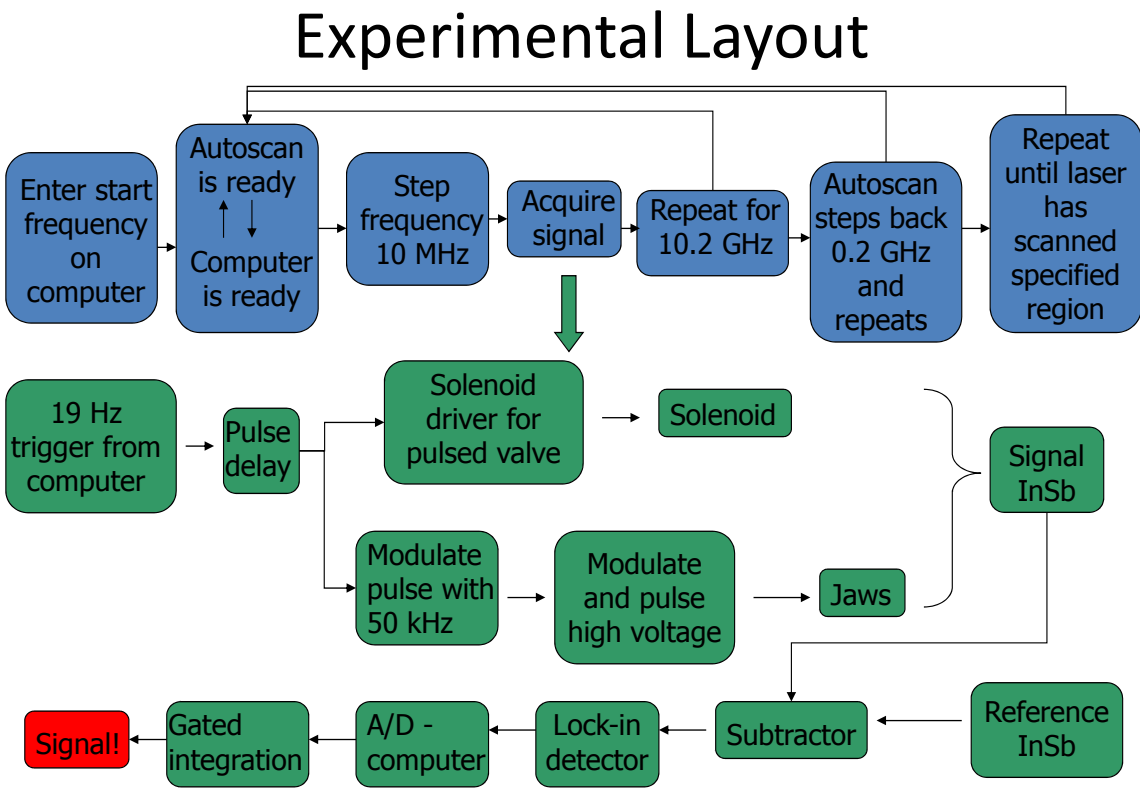

Figure 3.4: Illustration of the timing of the Autoscan (in blue) and the data acquisition sequence (green).

starts with a commercial tube powered by a partially home-built power supply. This HeNe laser has enough gain to support two simultaneously lasing modes, but only enough gain to support those two modes in perpendicular polarizations. Because of the HeNe gain curve and the mode spacing of the laser, only one mode of each polarization is present. The way we achieve a stabilized frequency is by matching the relative intensities of the two modes. This works because as the frequency of the modes change, they move along the gain curve, and the relative intensities change. We exploit this by making the relative intensities of the two polarizations equal. To do this, at one output of the HeNe is a polarizing beamsplitter

with the two subsequent beams sent to photodiodes. The signals from the two photodiodes are subtracted and locked such that the subtracted signal is zero. A piece of heater tape wrapped around the HeNe tube provides the feedback for the locking system in order to maintain a zero subtracted signal. Once the HeNe is stabilized, it is used to provide a stable source to lock the cavities needed in the rest of the instrument[31].

To correct for both the nonlinearity in scanning and the inaccurate and imprecise frequency readings of the Autoscan, we adopted a two cavity solution. At the start of each segment the Autoscan wavemeter sets itself to within ± 100 MHz of the desired starting frequency for that segment and starts to step-scan. As the laser scans, we record the inference fringes of the Ti:Sapphire laser output through two locked bow-tie confocal cavities, one with an approximate free spectral range of 1.5 GHz and the other with about a 250 MHz free spectral range. Since we don't have control over where each segment begins, we are not able to always start on the peak of the fringe, which is not an issue with the two cavity method. The frequency determination can be quantified with propagation of error calculations. Each Autoscan wavemeter reading has an error, based upon the specification, of 200 MHz; this error is usually less than the specified error and can depend upon how well the wavemeter is aligned and calibrated. This means that every time Autoscan reads the frequency there is an error of 100 MHz, which is too large for high-resolution spectroscopy. Additionally, if we wanted to stich together scans the way the old spectrometer does, with a 250 MHz cavity, we would likely make fringe assignment errors every few segments; since we scan tens of segments a day, this is an unacceptable number of errors.

To get around the limitations of the Ti:Sapphire wavemeter while making full use of the automated scanning, a two cavity solution is used. Complete details about the design and implementation are in chapter 8. In short, a locked 1.5 GHz FSR cavity and a locked 250 MHz FSR cavity are used. The wavemeter is accurate enough to assign a fringe number to the transmission fringes of the 1.5 GHz cavity. The fringe number of the 1.5 GHz cavity is used to assign a fringe number to the 250 MHz FSR cavity transmission fringes. The 250

MHz cavity fringes are then used to stitch together scans. With this method, the frequency precision is better than 10 MHz. Since the two locked cavities record only the Ti:Sapphire transmission fringes, and not the mid-IR fringes, it is important that the YAG laser is locked at a stable frequency.

The 250 MHz cavity is used to stabilize the YAG laser; it is important that the YAG laser be stable over a day of scanning since the frequency axis is stitched together using signals from the Ti:Sapphire laser. The YAG laser has a good internal stabilization for fast frequency noise, however in the long term (minutes and hours) the laser frequency drifts. To correct for this drift, the laser is locked to the 250 MHz cavity. Because the error that needs correcting is just the slow error, the servo-loop has only a integrated error signal; this is in contrast to the cavity locks, which have proportional and integrated errors. The lock takes advantage of the dither already being applied to the cavity by using the dither signal as the local oscillator input on a double balanced mixer, with the signal from the silicon photodiode as the input. The error signal is then integrated to provide the feedback to the laser. The laser response is 12 GHz/Volt, so only mV's are needed to correct for the errors. A signal on the order of a few volts is sent to a voltage divider, which is attached directly to the laser control box, to attenuate the signal to give a reasonable change in frequency. This eliminates the problem of sending very small voltages along a long wire, which could easily pick up noise of that magnitude along the way. More details of this lock are in chapter 8. This lock is stable over a single day of scanning.

As an added check of the absolute frequency, there is a room temperature reference cell to record a spectra of any reference molecule in the mid-IR in real time. Figure 3.5 shows a small section of a scan with the 1.5 GHz cavity, 250 MHz cavity and the reference cell. The mid-IR used for the reference cell is just the small amount reflected off of the visible light filter just before the reference/signal beamsplitter. Depending upon the gas used, the cell has three different pathlength options. The cell has sapphire windows and is followed by a commercial chopper just before the liquid-nitrogen cooled InSb detector. The signal

from the detector is passed through a lock-in detector with the reference frequency of the lock-in is the chopper frequency. This signal is recorded along with all of the other scan diagnostics of the NI-6025E card. With proper choice of reference gas and pressure in the cell, this provides a Doppler-limited room-temperature spectra of a well known reference gas while scanning to have a valuable check of the frequencies.

The instrument also has a commercial Bristol wavemeter used to check and calibrate the Ti:Sapphire wavemeter and provide the YAG laser frequency. A small amount of YAG and Ti:Sapphire light is sent to the wavemeter. Because this model of wavemeter can only read one frequency at a time, there are filters to either block just the YAG or block just the Ti:Sapphire. The light is then coupled into a broadband fiber and coupler and sent to the wavemeter. This allows either frequency to be read at any time during the scan without any disruption of the scan. The Autoscan wavemeter needs periodic (monthly) calibration to remain accurate, so having a quick way to complete the calibration process as well as a daily check of the accuracy is necessary. At present, the wavemeter interfaces with a secondary computer and is separate from the data recording process; this is necessary because the main computer is too old to interface with the new wavemeter. This might be something to change in the future as it would be advantageous to record the start frequency of the scan with the Bristol wavemeter since it is much more accurate and precise than the Autoscan wavemeter.

3.4 Molecular Source

The source of radicals and ions is based upon the designs on the west table with the additions of some modernization and adaptations. The molecular source is based upon the JILA-built slit nozzle as in use on the adjacent instrument[55, 33], but there are many supporting pieces of the instrument that have been modified, added, and improved before being implemented in this setup. Large mixing tanks are filled to usually between 1 and 10 % precursor in a buffer gas, usually molecular hydrogen or a 70% neon, 30% helium mixture. The larger of the two welded manifolds is used easily create these tanks and even have

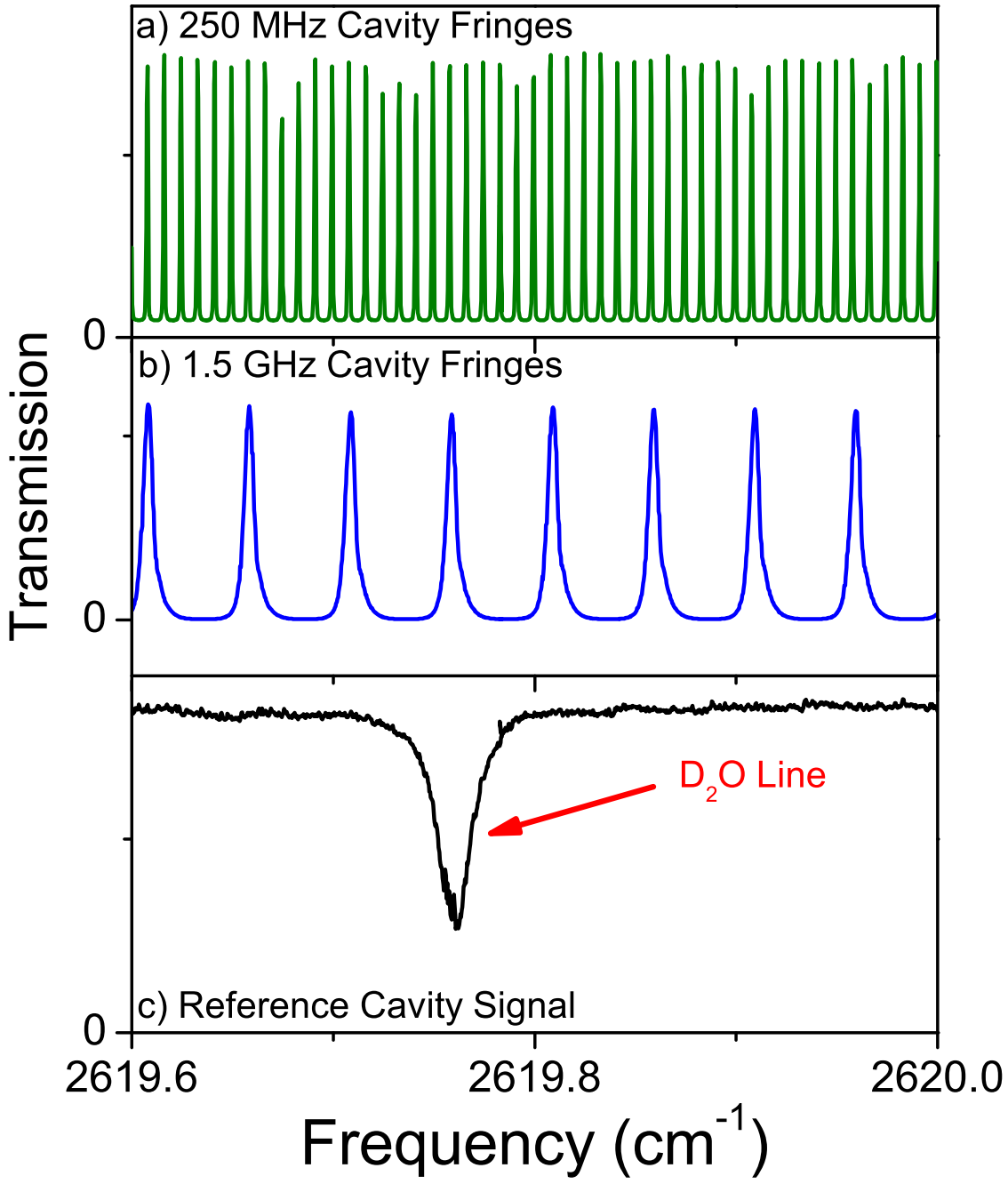

Figure 3.5: Sample scan showing the frequency diagnostic tools. Panel a) shows the Ti:Sapphire laser fringes from the 250 MHz cavity, panel b) shows the Ti:Sapphire fringes from the 1.5 GHz cavity, and panel c) is the transmission of the IR through the room temperature reference cell with < 5 Torr D_2O.

several tanks available at one time. The premixed tanks are combined with more buffer gas directly before going into the nozzle stagnation region, thus providing the 0.1% precursor in buffer gas that often provides the best radical or ion signal. To easily change the percentage of precursor without having to make a new tank, as well as reproduce the same precursor concentration every time an experiment is run, we use mass flow controllers to regulate the amount of gas from each tank that enters the stagnation region.

The nozzle is completely enclosed in the vacuum chamber, so a single continuous gas line brings the gas into the vacuum chamber via an ultratorr feedthrough and attaches to the nozzle using Swagelok. The nozzle is a mirror image of the nozzle in the other chamber and detailed drawings are in several thesis[24, 22, 23] and papers[56, 55, 33]. The nozzle end has a plate with a 4 cm long slit, most are 500 μm wide, against which the plunger makes the seal. An Ultem insulator is secured against the plate and has a similar, often slightly larger, slit cut through it. The two jaws are what actually form the limiting orifice of the slit expansion; they are secured to the insulator and can be adjusted to the desired slit width. It is the distance between the two jaws, measured and set using metal shims, that forms the limiting orifice for the expansion. The advantage of using a slit, instead of a pinhole, for the expansion geometry is the expansion is effectively only in one dimension rather than two dimensions. The laser beam is sent down the axis of the slit, and to a good approximation for a long slit, the molecules cannot move along the slit axis decreasing the Doppler broadening of the absorption lines.

While neutral, closed-shell molecules can be studied with the slit jet, we employ a discharge to generate the radicals and ions. The discharge is generated by applying a 50 KHz square-wave voltage to the jaws and since the nozzle is at ground a localized discharge is created at the slit orifice. The discharge is powered by a 1 kV high voltage power supply, which sends the voltage to the "offset pulser" where the 2 ms of a 50 KHz square-wave is imprinted on the voltage. The voltage is then sent to a set of ballast resisters before heading to the jaws. The ballast resisters can easily be switched, but 100 Ω, 200 Ω, and 500 Ω

resisters are currently installed. Following Ohms Law, changing the ballast resisters changes the amount of current sent to the jaws for a given voltage, which even though the current is the most important indicator of how many radicals or ions will be made, the voltage setting and ballast choice can effect the stability of the discharge as well as the amount of the target molecule.

A slit nozzle, even when pulsed, flows much more gas than a pinhole nozzle and consequently is best pumped by a pump that can handle a large throughput of gas. There are some adjustments to the amount of flow going through the nozzle, they are often made at the expense of signal, such as shortening the slit length or flowing less gas. The average flow used for optimum discharge conditions in the generation of radicals and ions is often about one standard liter per minute (slm). Another way to look at the pumping requirements is to calculate the average pressure in the chamber during an experiment. The pressure in the chamber is just the gas flow divided by the effective pumping speed. By way of example, for 1 slm of flow (12.7 Torr l/s) and the WS2000 roots blower, which has a pumping speed of 654 l/s, the average pressure in the chamber would be 20 mTorr. This is a good running pressure for several reasons, for example the pressure is low enough for a supersonic expansion with the 300 Torr backing pressure in the nozzle and the discharge is nicely localized and stable. It also allows for an increase in flow without any problem. If we compare that to the option of pumping with a large turbo pump, which has a pumping speed of 1700 l/s for H_2, a common buffer gas, the pressure in the chamber would be 8 mTorr, which is unfortunately too high for most turbo pumps. So even though the turbo has a much higher pumping speed, it is not necessarily the best pump to use for a high gas flow experiment like the slit nozzle. The gas flow of the nozzle is adjustable, but yield of radicals and ions decreases with decreasing flow, thus lowering the total signal level.

3.5 Data Acquisition

Automation of the instrument is one of the major improvements over the west table instrument. Even though the nozzles on both tables are pulsed at 19 Hz, dictating how fast we can take actual data points, the rate of data-taking is also limited by how fast the user can reset each scan and turn all the knobs that need to be turned. By automating the scanning and other equipment, it becomes computer controlled and is no longer a rate-limiting step. Automating the system is largely made possible by the addition of a stepper motor on the birefringent filter in the laser, electrically controlled tilting of the thin etalon, and the piezo-controlled thick etalon. These three elements allow electronic control over the frequency supported by the cavity. The Autoscan setup contains all the code and electronics to set the laser scanning over an arbitrary frequency distance with the push of a button. What we have done to automate the entire system is create a LabWindows program that remotely controls Autoscan as well as most of the other equipment, specifically the pulse valve and gas flow manifold, and records all of the relevant data.

The LabWindows program on the main computer communicates with the Autoscan computer via an RS232 connection. Once the connection is initiated all control over Autoscan is done through the main LabWindows program. The frequency of the laser is changed by typing in the desired frequency into the main program. This main program controls the scan parameters, specifically the scan length and step size, in the form of predefined scan types; this is necessary because Autoscan needs a file with all the parameters already on its computer, so having a set of predefined types avoids the problem of needing to create a file with the scan parameters. While the Autoscan computer executes the scan, the hard work of the scanning is all done by the Autoscan electronics box, which in turn sends info to the laser control box, which sends the information to the tuning elements in the laser. The Autoscan electronics box has two trigger and two monitors to control the scanning. When a scan is started, the LabWindows computer reads the trigger to say Autoscan is ready to

start a segment and then sends an output to signify that LabWindows is ready to scan a segment. This communication occurs each time a new segment is started. Autoscan then sends a signal to say it is ready to take a data point and LabWindows responds by indicating it is ready to take a data point. All of this communication occurs through BNC cables from the NI-6025 breakout box directly into the Autoscan electronics box. The system is then ready to record data.

Once ready to record a data point, after the specified delay from the trigger, the LabWindows program performes gated integration. It records the average over a specified length of both the baseline gates and the signal gate and divides that number by the gate length. It then takes the signal and subtracts the average of the baseline measurements. After the signal is recorded, the signal detector voltage is recorded along with the Ti:Sapphire transmission signal through the 1.5 GHz cavity, the 150 MHz cavity, and the IR reference cell. If signal averaging is being used, it now loops back through acquiring the data and gated integration and averages the values collected. Once all the data acquisition is done for a given data point, the data point signaling between LabWindows and Autoscan repeats, Autoscan steps the frequency, and the next data point is taken. This repeats for the 10.2 GHz segment length. The communication about the segments is repeated to ready the laser for the start of the next segment. At the end of a segment, Autoscan changes the laser frequency to the frequency for the start of the next segment by tilting the birefringent filter and the both etalons. The internal wavemeter is used to set the frequency to 10 GHz from the start of the previous segment, providing a 0.2 GHz overlap between segments. The scan ends once the segment loop has gone through the specified number of segments.

While the main computer and Autoscan coordinate the scanning, there is a whole string of signals that must be collected and processed to provide the signals eventually recorded at each data point. The trigger for the pulse valve goes through a homebuilt pulse delay generater to supply triggers to the pulse valve and the discharge with independent delays. The pulse valve signal is sent to the solenoid driver box, which sends a large amount of

current to the solenoid mounted on the valve and opens the valve, allowing gas to flow. Simultaneously, the pulse delay generater sends a signal to a modulator box which puts a 50 kHz square-wave on the first 2 ms after the trigger. This waveform is then imprinted on the voltage from a 1 kV high voltage power supply, applied to a set of ballast resisters to generate the current, which is sent into the vacuum chamber and the jaws of the nozzle. The amount of current sent to the jaws in controllable by either changing the set voltage on the high voltage power supply or by changing the ballast resistors (the current box has 100 Ω 200 Ω and 500 Ω resisters).

In addition to the outgoing triggers, the computer records the absorbance signal, which goes through a bit of processing before being recorded on the computer. Both the signal and reference InSb detectors have attached transimpedence amplifiers to turn the signal from a current into a voltage. The voltages from both detectors are then sent to a subtractor box, which uses common mode noise subtraction to subtract the signals between the signal and reference detectors. The subtracted signal then goes into a home-built lock-in detector. The local oscillator for the lock-in detector is the 2 ms of 50 kHz square-wave that was turned into high voltage and sent to the jaws. Since the signals we are interested in are encoded with that same waveform, the lock-in amplifier provides a way to look at only the signals we are interested in. The signal from the lock-in amplifier is then sent to the NI-6110 card and recorded on the computer as described above. The timing and signal flow of the experiment is displayed graphically in Figure 3.4.

3.6 Data Processing

The data as it is recorded by the LabWindows program are in the form of voltages as a function of data point, so there is a bit of processing that needs to happen in order to get the data to be in terms of percent absorbance as a function of a precise and accurate frequency axis. After loading the data into the Origin file, the first step is to recreate the axis according to what Autoscan thinks is correct. To do this, the start frequency is used

as the frequency of the first data point in the first segment. The starting frequencies of each subsequent segment is just 10 GHz higher in frequency from the start of the previous segment. A frequency is assigned to each data point after that using the specified step size. This is the same algorithm that the Autoscan computer uses to create the frequency axis if you were to import the frequency axis from Autoscan. Panel a) of figure 3.6 shows the signal of the Ti:Sapphire through both the 1.5 GHz cavity and the 250 MHz cavity with the Autoscan axis, illustrating the lack of precision of the Autoscan frequency.

To correct the Autoscan axis, we find the peak frequency in terms of the Autoscan axis of 1.5 GHz peaks using the Snyder peak-finder algorithm. The 1.5 GHz frequency axis is then created in the following steps by the program in Origin LabTalk and Origin C. One segment of one scan is designated as the reference scan. The frequency of the second fringe of the reference scan is used to compare the relative frequencies between that scan and the rest of the scans taken that day. The Autoscan frequency of the second fringe in each segment is then subtracted from the reference scan fringe frequency and divided by the free spectral range of the cavity. This calculation gives a relative fringe number for the second fringe in each scan, an offset is added so that there are no negative fringe numbers for ease of the calculation. If the Autoscan frequency were perfect, each of the relative fringe numbers would be a perfect integer, which is not the case. The fringe number should, however, be with 5% or less of a perfect integer to insure a very low uncertainty in the value of the relative fringe number. The relative fringe number is then rounded to the nearest integer. To begin to correct for the uncertainly in the step size taken by the laser, linear interpolation is used to find the fractional fringe number for each of the data points between each etalon peak. At this point, the frequency axis is in terms of a large etalon relative fringe axis. The numbers are then turned into a frequency using the free spectral range of the cavity. This step has now made the frequency axis accurate enough for us to find the relative fringe number of the small etalon peaks. The process used to create a relative frequency axis for the 1.5 GHz etalon, the large etalon, is repeated for the 250 MHz etalon, the small etalon except the large

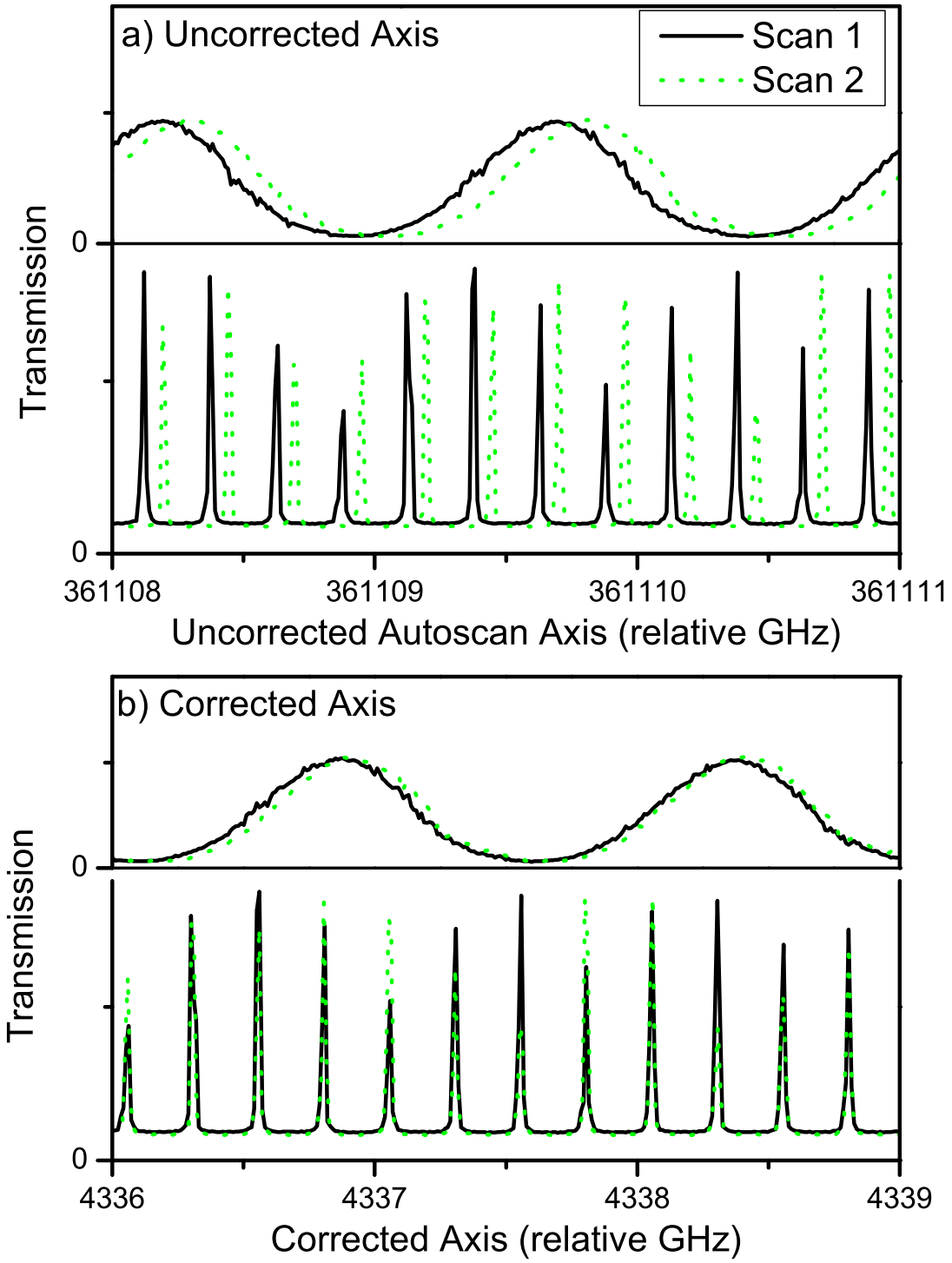

Figure 3.6: Comparison of the precision of the raw Autoscan axis [panel a)] and the corrected x-axis [panel b)]. The 1.5 GHz and 250 MHz are locked to a frequency-stabilized HeNe laser and the emission of the Ti:Sapphire through these two cavities is plotted against the uncorrected and corrected x-axis.

etalon axis is used as the frequency axis instead of the Autoscan axis. Panel b) of figure 3.6 shows the precision of the corrected frequency axis. After those steps are completed, the frequency axis is in terms of a very precise relative frequency; to turn the axis into a absolute frequency, a reference line, such as a methane transition, is used to find the offset needed to shift the axis to the correct absolute frequency.

3.7 Test Systems

3.7.1 Stability and Reproducibility

For high resolution spectroscopy, the most important piece of information is the accuracy and precision of the frequency axis. The test the frequency axis, we repeatedly recorded molecular absorption lines and compared the peak frequency positions obtained on different days. Specifically, a $\sim$100 cm^{-1} region is scanned with D_2O in H_2 discharge. The region is fully scanned at least three times and all lines appearing in each scan are used to compare how well the spectrometer reproduced the frequencies. Figure 3.7 is a plot of the frequency of each line on the frequency axis with the standard deviation of the repeated measurements on the absorbance axis. The average standard deviation of all the lines taken is 9.3 MHz, which is right in the target range. The lines looked at include known D_2O lines and H_3^+ lines, as well as many unidentified lines, many of which belong to HD_2O^+. This level of frequency reproducibility is good enough for doing high-resolution studies of radicals and ions.

3.7.2 HD_2O^+ Comparison

The initial project for this new spectrometer was to look at the the OD stretches of HD_2O^+ to complement the study of the OH stretch done on the older instrument in the lab[57]. This is also a useful test for the instrument as it was already studied in the lab so we have a comparison to assess how the new instrument compares to the existing instrument. As determined by previous spectroscopic studies[57, 58] HD_2O^+ is a near-prolate top with

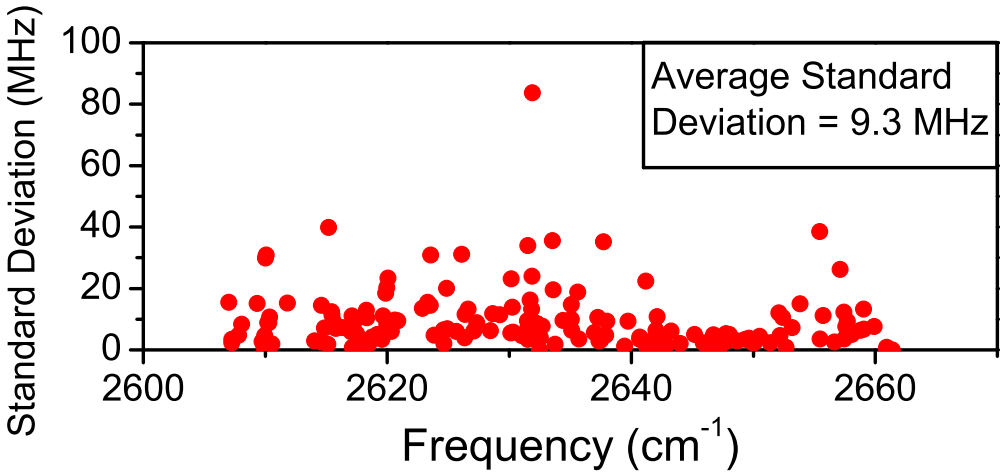

Figure 3.7: Illustration of the precision of the new instrument. This region is scanned a minimum of three time and the standard deviation of the measurements for each line in the region is plotted as a function of the frequency position of the line. The average standard deviation of the measurements is 9.3 MHz.

a low barrier to inversion along the umbrella coordinate. Even with the low temperature of the slit jet expansion, the first excited tunneling level of the ground vibrational state is populated, however transitions from the lower tunneling level of the ground state to the lower tunneling level are the most intense. To test the creation and detection of ions in the new system, lines from the OH stretch are recorded and checked against the published lineshapes and intensities. The OH stretch is an b-type transition and the $2_{20} \leftarrow 1_{11}$ and $1_{11} \leftarrow 0_{00}$ transitions are shown in figure 3.8. The integrated intensity for the $2_{20} \leftarrow 1_{11}$ transition as published in Figure 5 of Dong et al.[57] is reproduced.

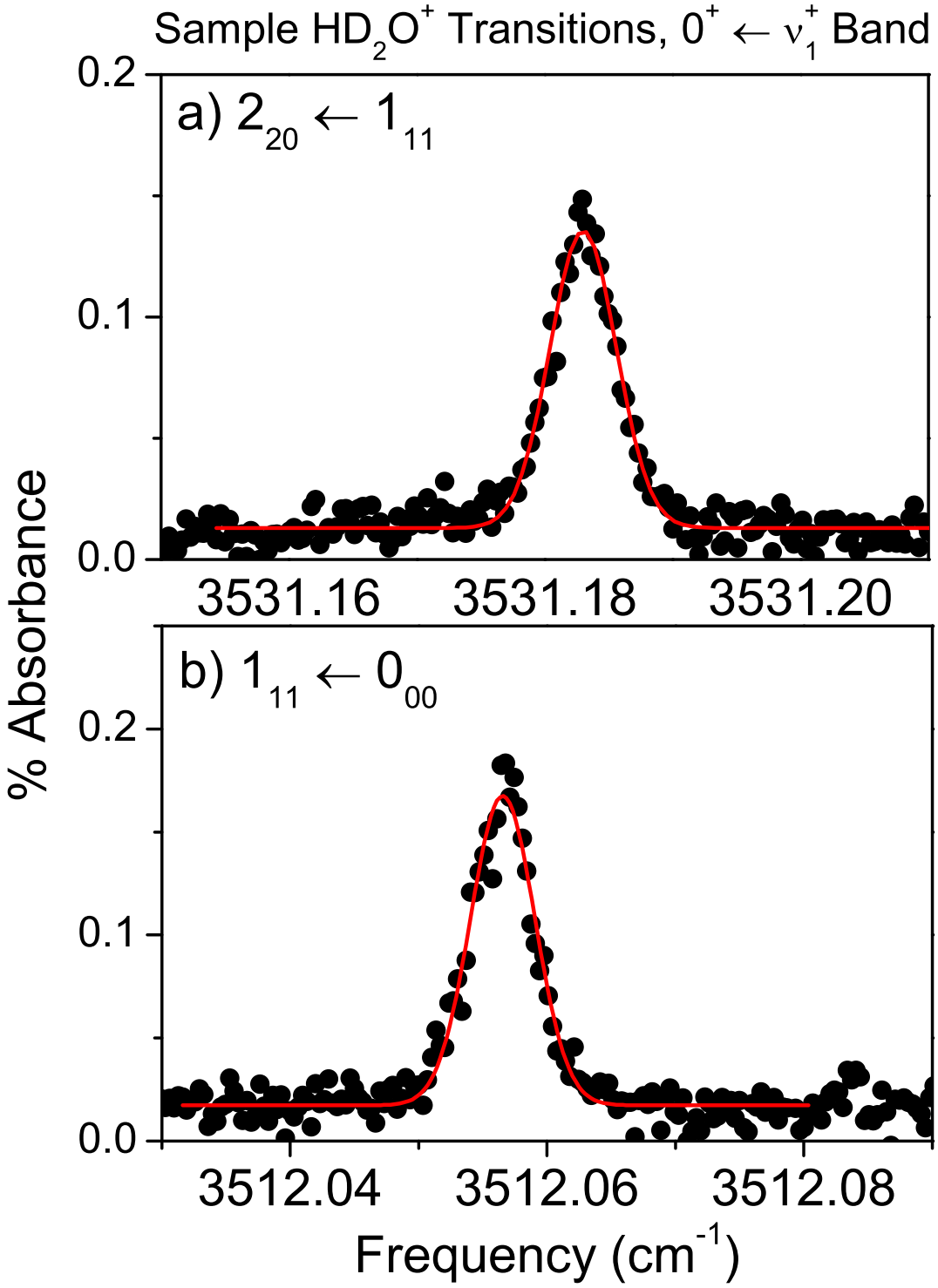

Figure 3.8: Sample HD_2O^+ data in the OH stretching region illustrating the ability of the new instrument to produce molecular ions in appreciable quantities.

Chapter 4

Rotationally resolved spectroscopy of phenyl radical in the out-of-phase symmetric CH stretching mode

4.1 Introduction

The phenyl radical (C_6H_5) is a highly reactive 6-membered organic hydrocarbon ring intermediate formed from homolytic cleavage of a CH bond in benzene[59, 14, 60]. By virtue of its overall reactivity, this radical plays a central role in combustion, specifically for fossil fuels which are typically rich in aromatics[61, 62]. Indeed, it is one of the simplest prototypes of an open-shell aromatic species, achieving partial stabilization of the radical due to resonance structures arising from electron delocalization around the ring. This radical stabilization also makes it a prime target intermediate for ring formation in complex combustion processes, which makes phenyl a crucial species in mediating the early stages of soot formation[63, 64, 65, 66]. From an astronomical perspective, phenyl is a key transient intermediate formed by 2- and 3-carbon-containing ion-molecule reactions in the interstellar medium, which therefore represents a rate limiting step toward low temperature synthesis of much larger polycyclic aromatic hydrocarbons[67, 68].

There has been considerable effort extended toward detailed spectroscopic characterization of this ubiquitous radical. Early electron spin resonance studies of phenyl by Bennett

The majority of this chapter has been previously published as Sharp, E. N.; Roberts, M. A.; Nesbitt, D. J. *Phys. Chem. Chem. Phys.* **2008**, 10, 6592-6596

et al.[69, 70] revealed electron-proton spin multiplet structures indicative of a C_{2v} radical with a $^2A_1$ ground electronic state, with later studies by Kasai et al.[71] confirming that the unpaired electron resides primarily in a non-bonding s-type orbital centered on the radical carbon (see Fig. 4.1). Low resolution infrared spectral assignment of phenyl formed by photolysis of acetyl benzoyl peroxide in Ar matrices was first obtained in the out-of-plane CH bending region by Pacansky et al. in the mid 1970s.[72] A higher resolution FTIR matrix isolation study of phenyl was reported by Ellison and coworkers[60] in 1996, followed by a more systematic study in 2001 addressing all IR active vibrations and multiple partially deuterated isotopomers.[59] During this same time period, multiple electronic bands[73, 74, 75] for phenyl radical were identified in the visible ($\tilde{A}(^2B_1) \leftarrow \tilde{X}(^2A_1)$, $\lambda \approx 510$ nm) and near UV (($\tilde{B}(^2A_1) \leftarrow \tilde{X}(^2A_1)$), $\lambda \approx 235$ nm, and ($\tilde{C}(^2B_2) \leftarrow \tilde{X}(^2A_1)$, $\lambda \approx 211$ nm). The weak $\tilde{A}(^2B_1) \leftarrow \tilde{X}(^2A_1)$ band in the visible has been exploited by Lin and coworkers with cavity ringdown spectroscopy for extensive study of phenyl radical H atom abstraction kinetics.[76, 77, 78, 79] Vibrational frequencies for two totally symmetric (a_1) low frequency modes of phenyl radical were deduced from electron photodetachment studies of phenide anion by Gunion et al.,[80] which both yielded good agreement and permitted a more definitive assignment to in-plane breathing modes (ν_9 and ν_{10}) by comparison with the matrix FTIR work of Ellison and coworkers.[59] Pure rotational spectroscopy of phenyl was made recently possible with the combination of discharge-excited molecular beams and FT microwave methods by Thaddeus and coworkers, which provided the first precise information on gas-phase rotational constants and molecular structure.[14]

This paper presents first reports on infrared CH stretch spectroscopy of a jet-cooled phenyl radical via high resolution direct laser absorption methods in the gas phase. This work represents the only IR spectroscopy of phenyl in the gas phase with rovibrational resolution, which has been used to monitor fundamental excitation of the out-of-phase symmetric CH stretching mode (see Fig. 4.1). Rigorous assignment of rotational structure in the gas-phase spectra can be obtained from precision 2-line ground-state combination differences from the

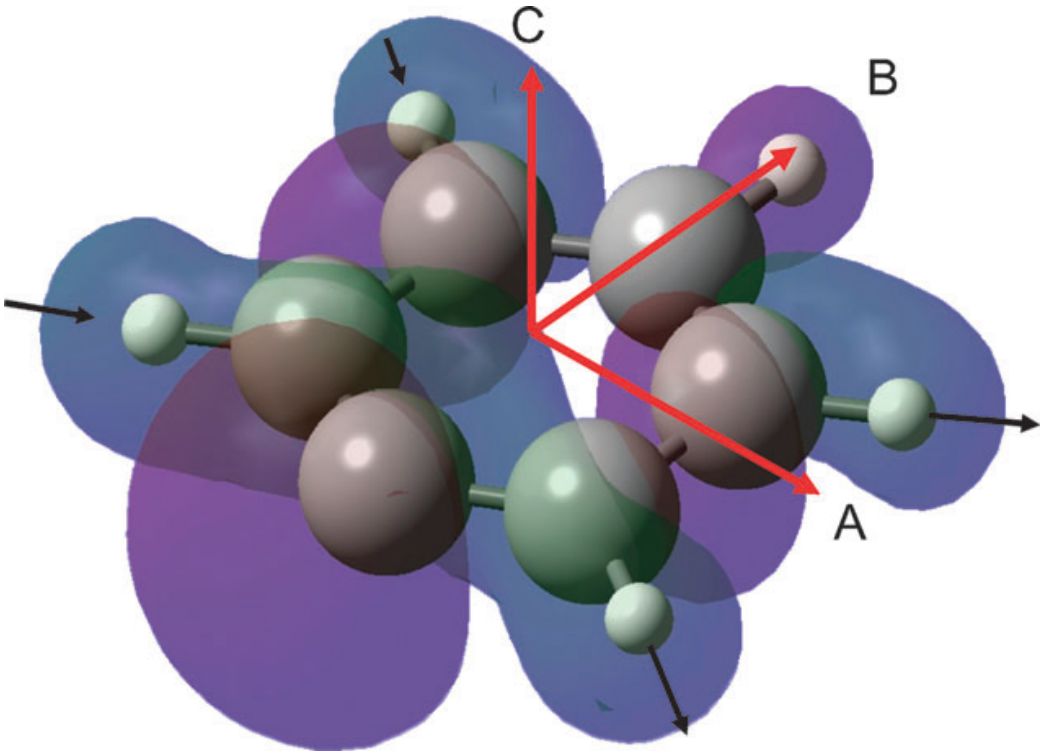

Figure 4.1: Geometric structure and highest occupied molecular orbital representation of phenyl radical, with principal inertial axes as indicated. The out-of-phase symmetric CH stretch excitation (b_2) observed in this work has a transition dipole moment along the A-axis. Note the nodeless, in-plane nature of the single filled HOMO at the radical C center, characteristic of a σ-radical.

radio frequency spectroscopy.[14] The analysis yields rotational constants and vibrational energy for the excited state, the latter of which proves to be in remarkable agreement with results from previous matrix isolation studies.[59] The ability to obtain rovibrationally resolved spectra for such a prototypical aromatic species represents an important milestone for spectroscopic study of highly reactive combustion intermediates, and bodes well for direct spectroscopic detection and analysis of many other complex aromatic radical species in the gas phase.

4.2 Experiment

Our approach for high sensitivity spectroscopic detection of jet-cooled hydrocarbon radicals via high-resolution infrared laser absorption in a slit-jet cooled supersonic discharge source is reported elsewhere and will be briefly summarized.[81, 82, 1] High resolution IR light (<2 MHz linewidth) is produced via difference-frequency generation (DFG) of a tunable single mode ring-dye laser (R6G) with a fixed-frequency single mode Ar^+ laser (514 nm) in a temperature-controlled, periodically poled $LiNbO_3$ (PPLN) crystal. Transient absorption in a 16-fold multipass Herriot cell through the long axis (4 cm) of the slit expansion is detected by differential change in signal minus reference beam power synchronous with the slit valve pulse. Absorption sensitivity is achieved via (i) fast electronic subtraction of common-mode amplitude noise on the split laser beam and (ii) 50 kHz concentration modulation of the DC discharge. Relative frequencies are obtained to $\approx$ 10 MHz precision ($\approx$ 0.0003 cm^{-1}) via fringe interpolation on the optical transfer cavity, with absolute frequencies obtained with respect to the set of CH_4 R(4) transitions[83] near 3067.30 cm^{-1}.

Jet-cooled phenyl radicals are produced by adiabatically expanding a mixture of 0.1% phenyl bromide (C_6H_5Br) in 70:30 neon-helium buffer gas through a pulsed-slit jet (19 Hz, 500 ms pulse duration), with radicals formed by electron associative detachment in a 50 KHz square wave modulated discharge (575 V, 0.2 A) localized upstream of the expansion orifice. The slit jet cooled discharge source yields peak absorbances of E 0.25% on typical phenyl

rotation-vibration transitions (see Fig. 4.2) which, based on *ab initio* estimates of integrated absorption strength (17 km mol^{-1}), correspond to radical densities in the probe region of 2×10^{10} cm^{-3}/quantum state. At noise levels of roughly 1×10^{-4} in a 10 kHz detection bandwidth, the peak absorption signals in Fig. 4.2 translate into signal-to-noise ratio (SNR) of approximately 10 - 20:1 for the strongest transition lines in the phenyl radical spectra.

4.3 Results and Analysis

By way of initial guidance, we performed quantum chemistry structure and harmonic frequency calculations for phenyl using density functional methods (B3LYP) over a systematic series of correlation consistent Dunning basis sets (AVnZ, n = 2,3,4,5).[3, 84, 85] The resulting frequencies, symmetries and intensities in the CH stretch region are summarized in Table 4.1. Also included are anharmonic predictions from similar series of B3LYP/6-311g++(3df,3pd) calculations, which are based on an empirical scaling factor of 0.9637(31) of Dong et al.[1] calibrated by benchmarking against previously observed high resolution gas-phase radical spectra in the CH stretch region. As anticipated, the results demonstrate good convergence with respect to basis set size and are in fundamental agreement with previous UB3LYP/cc-pVDZ calculations of Ellison and coworkers.[59] Of particular importance is the consensus frequency and intensity obtained for the strongest CH stretch transition, which is the out-of-phase symmetric CH stretch mode of b_2 symmetry. Based on the orientation of the principal axes shown in Fig. 4.1, this predicts the strongest band in the CH stretch region to be A-type and near 3067 $\pm$ 10 cm^{-1}. For an asymmetric rotor modeling of this band as a near oblate top spectrum with small changes in A, B, C rotational constants, one anticipates a progression of closely overlapped ${}^{p}P_{K}(N)$ and ${}^{r}R_{K}(N)$ branch lines (here K = K_c refers to the limiting values for an oblate top) with an approximate spacing of 2C $\approx$ 0.197 cm^{-1}, and a moderately prominent Q branch near the band origin.[86]

Scans in this region revealed extensive P and R branch progressions with an approximate spacing of 0.196 - 0.198 cm^{-1}, as well as a more complex Q branch feature near

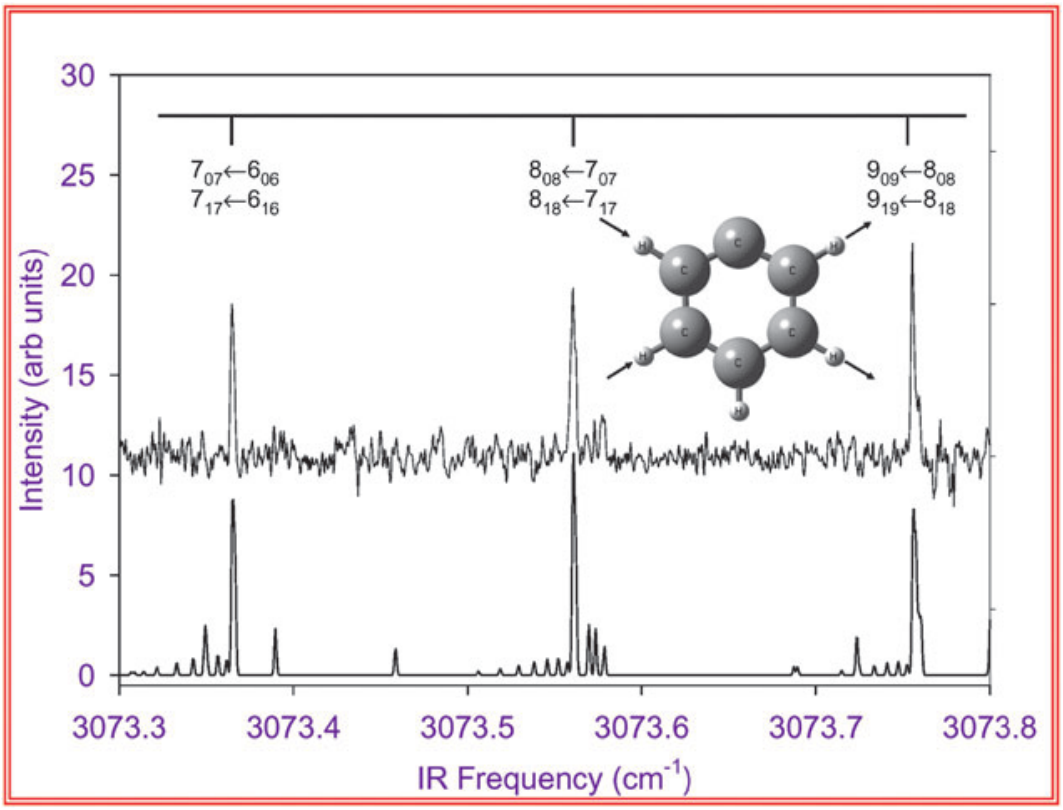

Figure 4.2: A sample 0.5 cm^{-1} high resolution data scan for phenyl radical in the out-of-phase CH symmetric stretch region (with 0.25% peak absorbances), along with spectral predictions based on T_{rot} = 15 K and the preliminary rotational constants reported in Table 4.2. Note the predominance of $N'_{K'_aK'_c} \leftarrow N''_{K''_aK''_c}$ progressions involving $N = K_c$ states, for which the asymmetry splittings in near oblate top phenyl radical are unresolved.

Table 4.1: Harmonic B3LYP/AVnZ (n = 2,3,4,5) *ab initio* predictions as a function of basis set size for fundamental CH stretch modes in phenyl radical. Numbers in parenthesis represent predicted intensities in km/mol. The rightmost column contains anharmonic estimates ($\Delta\nu \pm 10$ cm^{-1}) from density functional B3LYP/6-311g++(3df,3pd) calculations, based on a scale factor of 0.9637(31) benchmarked against CH stretch excitation frequencies for a series of high resolution studies of hydrocarbon radicals[1]

Symmetry	mode	AVDZ	6-311g++(3df,3pd)	AVTZ	AVQZ	AV5Z	Anharmonic Predictions
A_1	ν_1	3197.65(10.2)	3192.85(8.5)	3189.30(10.4)	3187.64(9.8)	3188.01(9.3)	3071
A_1	ν_2	3183.63(5.4)	3180.22(3.7)	3175.94(4.3)	3174.53(3.6)	3174.95(3.3)	3065
A_1	ν_3	3164.45(1.1)	3160.55(0.8)	3157.48(1.0)	3156.52(0.9)	3157.41(0.9)	3046
B_2	ν_{19}	3186.46(21.6)	3182.58(17.1)	3178.43(21.6)	3176.76(19.8)	3177.30(18.9)	3067
B_2	ν_{20}	3170.91(4.1)	3166.75(4.0)	3163.42(3.5)	3162.20(3.3)	3162.96(3.0)	3052

3071.80 cm^{-1}. Sample high resolution data over 0.5 cm^{-1} in the R-branch region are shown in Fig. 4.2, which indicates the level of signal to noise as well as the approximately 50 MHz sub-Doppler resolution. The complete spectrum exhibits more lines than currently assigned, which may indicate other transient species formed in the discharge or the presence of vibrationally excited hot bands. For the purposes of this work, therefore, we first restrict our attention to the prominent N = K_c, $\Delta N = \Delta K_c$ progression out of the ground vibrational state, for which the N-rotational assignment can be obtained unambiguously via 2-line combination differences from the mm-wave studies of Thaddeus and coworkers.[14] Specifically, pairs of P(N + 1) and R(N - 1) branch lines to the same upper N state yield spectral differences that match frequency predictions to better than 30 MHz. By way of further confirmation, this choice of N assignment is consistent with a predicted A-type band origin, as well as in excellent agreement with the position and structure of the experimentally observed Q branch feature.

Due to the highly oblate nature of phenyl radical, these strongest lines for an A-type band reflect a near perfect overlap between the two dominant progressions ($N'_{0N'} \leftarrow N_{0N}$ and $N'_{1N'} \leftarrow N_{1N}$) associated with K_c asymmetry doubling. As a result, these doublets remain unresolved even at sub-Doppler resolution and thus provide no information on the asymmetry of phenyl radical in the upper state. Furthermore, the additional condition of planarity for phenyl radical (B $\approx$ 2C) yields additional overlapping structure between $\Delta N = \Delta K_c = \pm 1$ transitions out of levels with K_c = N, N-2, N-4, etc. As a result, we first performed an oblate top fit to the main P/R branch progression, based on least squares adjusting (A′ + B′)/2 and C′ in the upper state, as well as the band origin, while maintaining the ground state at microwave values. The phenyl radical asymmetry (A′B′) could then be estimated from (A′ + B′)/2 and the assumption of a rigid planar molecule (*i.e.* $1/C' \approx 1/A' + 1/B'$). This first order analysis led to very good agreement between predicted and observed rotational structure in the Q branch, which permitted several additional P, Q, and R branch lines to be rigorously assigned with 2-line ground state combination differences.

As the Q branch transitions sample states with much larger asymmetry splittings, a rigid rotor least squares fit to the expanded data set permits independent extraction of A′, B′, C′ rotational constants and the band origin ν_0. Results from this preliminary analysis are summarized in Table 4.2, where, consistent with a rigid rotor model, all contributions due to centrifugal distortion as well as spin rotation fine structure have been neglected.

Table 4.2: Rovibrational spectroscopic constants for gas-phase phenyl radical from a rigid asymmetric rotor least-squares fit to the out-of-phase symmetric CH stretch band. Numbers in parentheses represent 1σ uncertainties in units of the least significant digit

Constant	Predictions[a] [b]	Ground state[c]	Excited state (ν_{19})
A(cm^{-1})	0.211218	0.209472(10)	0.20937(8)
B (cm^{-1})	0.188434	0.186793(7)	0.18655(12)
C (cm^{-1})	0.099588	0.098714988(20)	0.098616(20)
D (amu $\mathring{A}^2$)	-	0.046	0.061
ν_0 (cm^{-1})	3072	-	3071.8907(10)

[a] Rotational constant predictions from B3LYP/AV5Z calculations
[b] ν_{19} band origin from condensed phase Ar matrix isolation studies of Ellison and coworkers[59]
[c] Ground state constants from microwave studies of McMahon *et al.*[14]

A more complete analysis of the rovibrational spectra is underway and will be presented elsewhere; however several observations can be made at this time. First of all, the upperstate rotational constants are in very close agreement with the microwave values,[14] with small but systematic decreases in all values ($\Delta A/A = 0.05\%$, $\Delta B/B = 0.13\%$ and $\Delta C/C = 1.0\%$) qualitatively consistent with CH stretch in-plane excitation. Indeed, this provides a useful context for the quite close but systematically higher rotational constants predicted from density functional theory at the AV5Z level (see Table 4.2), which reflect an equilibrium geometry uncorrected for zero point motion in all 3N - 6 = 27 vibrational modes. Secondly, the independently fitted upper state rotational constants are consistent with a nearly planar radical, with an inertial defect ($\Delta = 0.061$ amu $\mathring{A}^2$) close to zero and similar to the ground state value ($\Delta = 0.046$ amu $\mathring{A}^2$). The vibrational band origin at 3071.8907(10) cm^{-1} is in very good agreement ($\Delta\nu = +4.8$ cm^{-1}) with the anharmonic prediction for ν_{19} shown

in Table 4.1, well within the $\approx \pm 10$ cm^{-1} statistical error. Though also relatively close in anharmonic predicted frequency, the ν_1 symmetric CH stretch can be conclusively ruled out as a possible carrier of the spectral intensity. This would yield a pure B-type rather than the pure A-type band observed experimentally, which from Fig. 4.1 is consistent with out-of-phase symmetric CH stretching excitation (ν_{19}).[86]

The present gas-phase spectral band origin for ν_{19} is in remarkably good agreement with the previous matrix isolation studies of phenyl radical by Ellison and coworkers,[59] who indeed obtained moderate resolution assignments for all IR allowed bands in phenyl radical. Also by detailed comparison with quantum mechanical calculations, these workers assigned their strongest band in the CH stretch region at 3072 cm^{-1} to ν_{19}, *i.e.* out-of-phase symmetric stretching of adjacent pairs of CH groups to either side of the phenyl radical center. The rotational resolution provided by gas phase spectroscopic techniques permits definitive confirmation of this vibrational mode symmetry; this predicts an in-plane transition dipole moment perpendicular to the C_{2v} radical axis, which is consistent with the observed A-type band rotational structure. The shift ($\Delta\nu \approx 0.1 \pm 1$ cm^{-1}) between condensed and gas phase results is essentially zero for the Ar matrix, which is noteworthy considering the more typical red shift to *lower* frequencies due to enhanced stabilization interactions in the excited vibrational state.[87] Comparison with the matrix results[59] suggests that we should also be able to detect other bands in the CH stretch region, for example, the B-type band corresponding to ν_1 symmetric CH stretching of all five H atoms.

As a final note, it is worth stressing that the ability to observe a relatively simple and assignable rovibrational line structure at high resolution in the 3.3 μm infrared CH stretch region is by no means obvious for such a large hydrocarbon radical. The reason for this is the presence of weak but finite anharmonic coupling between the optically allowed state, corresponding to the CH stretch in this case, and the dense bath of nearly resonant overtone and combination band states.[88, 89] For a coherently excited initial CH stretch state, such coupling leads to a time dependent energy flow into lower frequency modes in

the molecule, resulting in "intramolecular vibrational redistribution" or "IVR". From a completely equivalent frequency-domain perspective, such anharmonic coupling results in weak mixing of the zero order oscillator transition strength from the "bright state" into a bath of nearly isoenergetic background vibrational states. When this occurs, a transition out of a single lower state can become spectrally fragmented into a complex overlap of lines in the high resolution spectrum, with a spectral width that corresponds roughly to the inverse time scale for IVR out of a coherently prepared CH stretch state. Indeed, there have been elegant high resolution studies of jet cooled hydrocarbon molecules by several groups indicating the presence of such spectral fragmentation patterns, as well as direct verification of the relaxation dynamics in the time domain.[90, 91, 92, 93, 94]

For the case of a phenyl radical, we can predict the density of total vibrational states based on the quantum chemical harmonic predictions and direct state counting algorithms[95] to be 510 states per cm^{-1} at roughly 3000 cm^{-1} levels of internal excitation, *i.e.*, remarkably small for a non linear hydrocarbon molecule with 11 atoms. The size is primarily due to the presence of the ring, which raises the lowest frequency vibrational mode to > 400 cm^{-1}, and therefore greatly limits the density of states in the 3000 cm^{-1} region. The fact that we can see high resolution sub-Doppler rotational structure ($\Delta\nu \approx 50$ MHz) in jet cooled CH stretch excited phenyl radical, therefore, bodes quite favorably for the feasibility of high resolution IR studies in other radical hydrocarbon ring systems of key importance in both combustion and interstellar chemistry.

4.4 Conclusion and Summary

The first gas-phase high resolution infrared spectral data for phenyl radical have been obtained, corresponding to $\nu = 1 \leftarrow 0$ excitation of ν_{19}, the out-of-phase symmetric CH stretch mode. Rovibrational assignment has been unambiguously made based on (i) band type and (ii) 2-line ground state differences from previous microwave and mm-wave studies.[14] Density functional predictions of phenyl radical transition frequencies and inten-

sities are calculated for a series of Dunning basis sets (AVnZ, n = 2,3,4,5), which indicate very close agreement with the observed band origin.[84, 85] Rigid asymmetric top A, B, C rotational constants are obtained for the upper state, which are in good agreement with quantum chemical predictions as well as lower state microwave/mm-wave values by Thaddeus and coworkers.[14] The measured band origin is in remarkable agreement with the matrix studies of Ellison,[59] with essentially no shift ($\Delta\nu \approx 0.1 \pm 1$ cm^{-1}) due to the presence of the condensed phase environment. Further IR analysis of phenyl radical at higher resolution as well as detailed line shape modeling of the overlapped transitions is currently underway. The ability to obtain high resolution IR absorption spectra in the gas phase for such relatively large hydrocarbon radicals represents a significant step forward in the spectroscopy of transient species of particular relevance to complex combustion phenomena,[63] as well as to detailed modeling of chemistry in the interstellar medium.[68]

Chapter 5

A complete picture of stretching vibrations in methyl radical and its deuterated isotopomers: a high-resolution study of the CH stretches in CH_2D and a global harmonically coupled Morse oscillator model

Methane, CH_4, is one of the most abundant and strategically important fuel stocks, for which, along with other aliphatic hydrocarbon fuels, the critical first step in the combustion is the extraction of hydrogen atoms to form sp^3 hybridized radical centers on a carbon atom[96, 97]. This H abstraction reaction from CH_4 proceeds with combustion radicals such as H, O, and OH, to yield methyl radical, CH_3, which propagates the combustion process forward via a variety of mechanisms. Under low temperature flame conditions, CH_3 recombines with O_2 to form the relatively stable methyl peroxyl radical CH_3OO adduct. This can react by H atom abstraction from hydrocarbons to form CH_3OOH, which can fragment to form CH_3O + OH, and thereby regenerating chain radicals. As the temperature increases, the concentration of OH and O radicals increases relative to the concentration of O_2, so reactions such as CH_3 + O $\rightarrow$ CH_2O + H and other reactions with CH_3, OH, H, and O radicals dominate[98]. At even high temperatures (T > 1000 K), CH_3 is predicted also to recombine with O_2 to form CH_3OO, but now this peroxy radical dissociates to form two chain radicals CH_3O + O, followed by an additional H atom abstraction and propagation of the chain reactions.

The majority of this chapter has been previously published as Roberts, M. A.; Savage, C.; Dong, F.; Sharp-Williams, E. N.; McCoy, A. B.; and Nesbitt, D. J. *J. Chem. Phys.* **2012**, 136, 234308.

Methyl radical combustion chemistry also plays a critical role in shaping the end products of combustion reactions. For example, the final products of an efficient hydrocarbon combustion process would ideally be simply CO_2 and H_2O, where the product CO_2 is usually formed via the reaction CO + OH $\rightarrow$ CO_2 + H. However, this bimolecular reaction typically requires substantial concentrations of OH and CO, and thus CO_2 is not readily formed without both species relatively abundant. The presence of competing reactions, for example, CH_4 + OH $\rightarrow$ CH_3 + H_2O or CH_3O + OH $\rightarrow$ CH_2O + H_2O can deplete the OH and lead to unreacted CO in the final products. This results in both inefficient extraction of the combustion enthalpy as well as an undesired pathway to generating CO pollutant emissions, especially in fuel rich systems[98].

Though clearly ubiquitous in hydrocarbon combustion, methyl radical is also present in the troposphere, and serves as an intermediate in many important reactions throughout the lower and upper atmosphere[99, 100]. Methyl radical is formed by oxidative attack of atmospheric methane, which is present in significant quantities from natural gas leakage, incomplete combustion, fermentation, and other biological processes. The relevant chemistry is initiated by photochemical production of OH radical, followed by hydrogen abstraction reaction from CH_4 to form CH_3 radical, which then continues to react with nitrogen-containing compounds to make photochemical smog[98]. By virtue of an appreciably higher C-H bond strength (ΔH = 105 kcal/mol) with respect to any other non-methane hydrocarbons (ΔH = 96-101 kcal/mol)[101], methane is quite stable, with an approximately 11 year lifetime in the troposphere and therefore significant as a greenhouse gas. Indeed, the only appreciable source of chemical removal of methane in the lower atmosphere is via these relatively slow "scrubbing" reactions with OH radical. Because of the environmental implications, atmospheric reactions involving methane are currently an area of intense investigation, which currently includes using H/D isotopically substituted species to aid in modeling the chemistry[102].

Methyl radical is also thought to be an important radical intermediate in dense molecular clouds distributed throughout the interstellar medium[103, 104]. One of the most powerful

tools for probing reactive chemical species in the interstellar medium is that of microwave spectroscopy, which requires a permanent electric dipole moment to facilitate dipole allowed rotational transitions. At its planar equilibrium geometry, methyl radical exhibits D_{3h} point group symmetry and therefore has a dipole moment (μ) that vanishes identically. However, by asymmetrically deuterating the CH_3 radical to make CH_2D radical, the 3-fold symmetry is reduced to C_{2v}, which generates a weak permanent electric dipole moment and thus an allowed rotational spectrum. While no measurements of μ have been reported to date for CH_2D, the dipole moments of some related molecules have been calculated. For example, the CH_2D^+ ion should[105] have a large dipole moment of $\mu = 0.329$ D, while the more closely analogous CHD_2 species has been recently predicted[106] to have a much smaller moment of $\mu = 6.5 \times 10^{-3}$ D.

What makes this issue particularly interesting is that the relative abundance of partially deuterated molecular species can be substantially higher in the interstellar medium than observed on earth[103]. This is due to the presence of small, but non-negligible zero point energy differences between the isotopically shifted vibrational manifolds. These are largely negligible at typical terrestrial temperatures (300 K), but can become critically important thermodynamic driving forces at the much lower temperatures (20-50 K) of a dense molecular cloud. Thus the detection of methyl radical and, in particular, the isotopically substituted radical species, may provide an indispensable tool in both probing and modeling the complex chemistry of the interstellar medium.

Though CH_3 remains invisible to conventional microwave/mm wave spectroscopy, there has nevertheless been an exceptionally rich history of methyl radical spectroscopy. The first absorption spectrum of methyl radical was obtained by Herzberg and Shoosmith in 1956[107, 108] in the vacuum ultraviolet region, with the infrared spectrum reported by several groups in a matrix[109, 110, 111, 112] and later revisited using isotopic substitution to confirm the band assignments[113]. Observation of methyl radical in the gas phase proved to be much more challenging, with first spectra obtained in pioneering flash kinetic

IR spectroscopy studies by Pimentel and coworkers[114]. The development of high resolution diode lasers in the early 1980's offered an enormous increase in sensitivity over traditional IR glow bar sources. This permitted first reports of rotationally resolved spectra for gas phase CH_3 radical, with studies of the strongly IR-active out-of-plane umbrella mode (and hot bands thereof)[115] as well as the asymmetric C-H stretch mode[116]. Based on high resolution stimulated Raman methods of Nibler and coworkers, even the IR-inactive C-H stretching mode of gas phase CH_3 was successfully studied in 1991 with complete rotational resolution[117]. These ideas have been complemented using UV resonance Raman spectroscopy to yield considerable information on methyl radical, in particular with substantial vibrational excitation in totally symmetric modes. CH_2D has been used in a number of studies to probe complicated dynamics including in kinetic studies[118], studies of vibrationally mediated reactions[119], and a number of EPR studies looking at the dynamics of methyl radical in matrices[120, 121, 122].

In contrast to the variety of studies on CH_3 as well as fully deuterated CD_3 species, there has been some work on the partially H/D isotopically substituted radical species. Early spectroscopic studies of CH_2D included i) matrix isolation spectroscopy looking at the out-of-plane deformation fundamental[113], ii) resonance enhanced multiphoton ionization to obtain band origins of all the vibrational fundamental modes for each isotopomer[123], and iii) photoelectron spectroscopy[124]. Hyperfine structure, specifically the magnitude of the Fermi contact term, was studied using electron spin resonance (ESR) to look at methyl radical and all H/D isotopomers in a krypton matrix[125]. The most recent study involving CH_2D reflects combined threshold photoelectron spectroscopy and computational efforts[126].

The only previous high resolution spectroscopic data on CH_2D in the gas phase comes from the group of Kawaguchi in the out-of-place bending fundamental mode, ν_4, obtained by combined laser photolysis and Fourier transform infrared spectroscopy (FTIR)[2], which was able to fully resolve the asymmetric top rotational structure as well as partially resolve spin-

rotational splitting. Due to equipment limitations, only the Q- and R-branch transitions were observed, which nevertheless permitted an unambiguous fit of the rovibrational constants to Watson's A-reduced Hamiltonian. The partially resolved spin-rotation splittings were observed only in the R-branch but, if one assumes negligible hyperfine interactions, still permitted a first estimate of spin-rotation constants in the ground and vibrationally excited states. It is important to note that these estimates differ from isotopic scaling of the spin-rotation constants for CH_2D from CH_3, as will be discussed in Sec. 5.3.2.

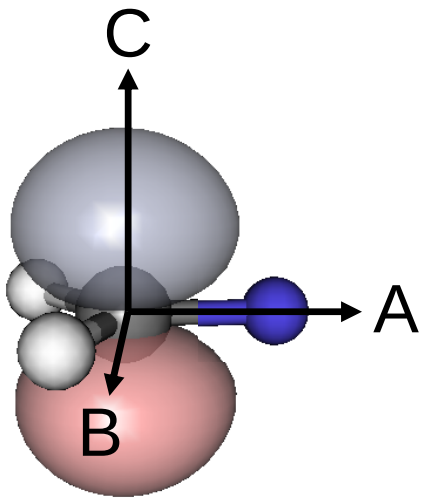

Figure 5.1: B3LYP/6-311++G(3df,3pd) calculated structure[3] of CH_2D with the HOMO and principal axes shown.

To date, there have been no high resolution studies of CH_2D in the C-H stretching region, and in particular no measurements whatsoever of gas phase CH_2D radical with sufficient resolution for detailed study of rovibrational, fine, and hyperfine structure. The focus of the present work is toward the C-H stretching modes on the partially deuterated methyl radical isotopomers using high-resolution IR spectroscopy. CH_2D is a planar π radical, with

the principal axes of the molecule as shown (see Fig. 5.1). CH_2D has six fundamental vibrations, two of which are CH stretching modes. This study looks at the CH antisymmetric and symmetric stretching vibrations using sub-Doppler techniques, which requires treating rotational as well as both fine and hyperfine structure in the analysis[127]. Since CH_2D has a non-vanishing dipole moment, this work should provide excellent guidance for the very challenging terrestrial detection of this radical in the microwave/mm wave region of the spectrum.

The organization of the paper is as follows: Sec. 5.1 provides a brief overview of the experimental apparatus used to obtain the CH_2D spectrum. This is followed by presentation of experimental results for symmetric and asymmetric C-H stretch data in Sec. 5.2. In Sec. 5.3.1, we focus initially on analysis of the high resolution transition frequencies to obtain rovibrational constants. We then take advantage, in Sec. 5.3.2 of sub-Doppler resolution in the slit-jet spectra to analyze the complex line shape structure on each transition and thereby extract novel information on fine and hyperfine interactions. In Sec. 5.4, we discuss these results in the context of previous efforts, as well as develop a simple model of in-plane vibrations for all CH_mD_{3-m} isotopomers in C_{2v} symmetry, with the results and prospects for future studies summarized in Sec.5.5.

5.1 Experiment

The radicals are produced and studied with slit supersonic discharge techniques and a high resolution infrared spectrometer that have been described in detail elsewhere[128, 129] and will only be summarized here. The halogenated precursor (CH_2DI, 99.9% Cambridge Isotope Laboratories) is purified using freeze-pump-thaw methods and then diluted with Ne70 (i.e., 70% Ne, 30% He) in a holding tank. This mixture is then further diluted down to 1.0% in Ne70 using mass flow controllers to regulate the gas flow into the slit stagnation region. The slit valve is a JILA-made solenoid-driven pulsed injector with a 4 cm by 300 μm slit orifice operating at a 19 Hz repetition rate and about a 1000 μs duration. The

pressure in the stagnation region is maintained at 300 Torr, with the vacuum chamber kept at $<$ 50 mTorr during operation of the pulsed valve, by a Roots blower (560 liters/sec). During the pulse, a 50 kHz, 0.5 A, 50% duty cycle, modulated discharge localized upstream of the slit orifice achieves efficient electron dissociative attachment at the C-I bond at near-Langevin rates to efficiently synthesize the desired CH_2D radicals. Lock-in detection with double balanced mixers is used to phase sensitively detect concentration modulation of the radicals produced in the pulsed discharge, thereby greatly minimizing spectral congestion due to absorption by precursor molecules.

The tunable infrared continuous-wave laser radiation for probing radicals is generated by difference-frequency mixing the 514 nm output of a single frequency continuous-wave argon ion (Ar^+) laser with the visible output of a tunable ring dye laser (Rhodamine 590, Exciton dyes) in a periodically poled $LiNbO_3$ crystal. The Ar^+ laser is stabilized ($<$ 2 MHz) by locking it to a Fabry-Perot cavity ($<$ 1 MHz), which is in turn locked to a polarization-stabilized helium neon (HeNe) laser. As this fabry-Perot optical transfer cavity is also used to monitor the dye laser scan, the fringes accurately report on the infrared difference frequency, i.e., $\omega_{Ar^+} - \omega_{dye} = \omega_{IR}$. This combination of a locked HeNe laser and a locked optical transfer cavity yields high reproducibility and precision in the IR frequency difference measurements, with excellent agreement between data collected over many months.

The IR radiation is split into a signal and reference beam of roughly equal intensity. The reference beam is directed onto a liquid nitrogen-cooled InSb detector, with the corresponding signal beam passing through a 16-pass Herriot cell (l = 4 cm $\times$ 16 = 64 cm) before being focused onto a matched InSb photodiode detector. We then subtract the outputs of the reference detector and the signal detectors and extract the demodulated lock-in signal on the computer via a fast (1 μs bin time) analogue-to-digital convertor. Absolute frequencies are obtained by comparison with known methane lines[130], yielding an overall precision and accuracy of the line center measurements of σ = 15 MHz and 20 MHz, respectively. Such procedures yield detection sensitivities of 5×10^{-7} $Hz^{-1/2}$, with a peak absorbance of 2%

and signal-to-noise ratios of roughly 500:1 on the more intense CH_2D lines.

5.2 Results

The combination of high resolution ($\Delta\nu \approx 0.0001$ cm^{-1}) and near shot noise limited sensitivity (5×10^{-7} Hz$^{-1/2}$) of the laser spectrometer comes at the expense of fast spectral scanning capabilities. Accurate initial estimates for the spectral search region are therefore quite important. The harmonic frequencies of both the symmetric and asymmetric CH stretch vibrations are calculated using density functional (DFT) methods available in the GAUSSIAN09 program [B3LYP/6-311++G(3df,3pd) basis set][131]. To account for anharmonicity in the vibration as well as residual method and basis set errors, we improve these harmonic DFT predictions with a scaling factor, 0.9637(31), which has been quantitatively benchmarked by comparing theoretical vs. experimental CH stretching frequecies for more than twenty hydrocarbon radicals[132]. From such calculations, the predicted frequency of the asymmetric C-H stretch in CH_2D is 3169 cm^{-1} with a 1-σ standard deviation of about 10 cm^{-1}. Furthermore, the asymmetric C-H stretch transition dipole moment lies along the B principal axis (see Fig. 5.1) and will have B-type rotational structure. Similarly, the symmetric C-H stretch vibration is predicted to be an A-type band centered at 3065(10) cm^{-1}. Recently, a computational study also reported anharmonically corrected *ab initio* frequencies of 3158 cm^{-1} and 3062 cm^{-1} for the asymmetric and symmetric stretch vibrations, respectively, i.e., in quite good agreement with our predictions[126].

To speed the process, an initial search procedure is performed with a relatively large step size of 12 MHz. After the CH_2D lines are identified, they are re-scanned at least two more times with a 3 MHz step size, which takes full advantage of the sub-Doppler slit jet spectrometer resolution and allows one to map out the fine and hyperfine spectral lineshapes. Based on ground state rotational constants from the FTIR study[2], two progressions of lines are readily identified as CH_2D by comparison with rigid rotor asymmetric top predictions, with details on the assignment confirmation discussed in Sec. 5.3. Figs. 5.2 and 5.3 summa-

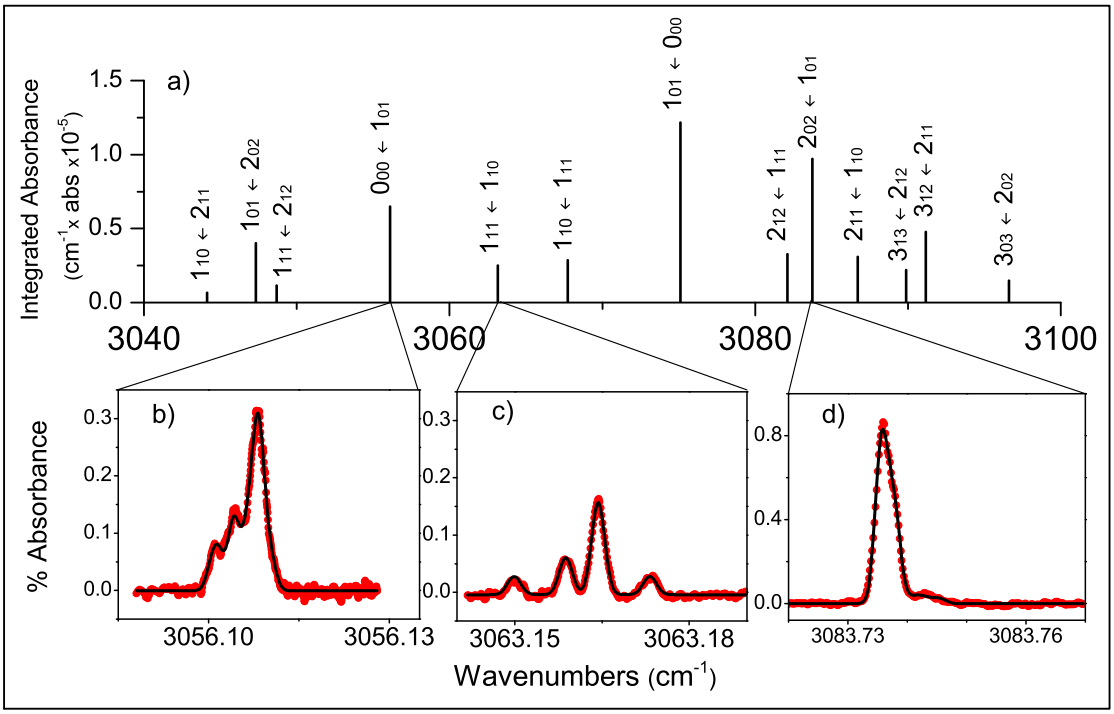

Figure 5.2: Sample CH symmetric stretch data for CH_2D. Panel a) plots the integrated absorbance of each of the observed $N'_{K'_aK'_c} \leftarrow N''_{K''_aK''_c}$ rotational lines versus frequency. Blowups of select transitions, panels b)-d), show additional structure at high resolution due to fine and hyperfine interactions. The black dots are the data and the red lines are simulations base upon constants obtained in lineshape fits of the fine and hyperfine structure.

rize data for the symmetric and asymmetric stretch, respectively, indicating the transitions observed and the high level of S/N. Due to the $> 10^5$-fold disparity between scan size($>$ 70 cm^{-1}) and the transition line widths ($<$ 0.003 cm^{-1}), the overview spectrum for each band is shown simply in Figs. 5.2 and 5.3 as a stick plot, with the height proportional to the integrated area of the transition. However, sample data transitions (lower panels) for each band are also shown at high resolution on a greatly expanded frequency scale. This more clearly reveals the rich presence of highly complex lineshapes, due to the combination of i) spin-rotation fine structure and ii) electron spin-nuclear spin hyperfine structure. In practice, our analysis procedure is to simultaneously fit the high resolution line contours to a fine/hyperfine Hamiltonian, obtain fine/hyperfine-free line centers, and then least-squares

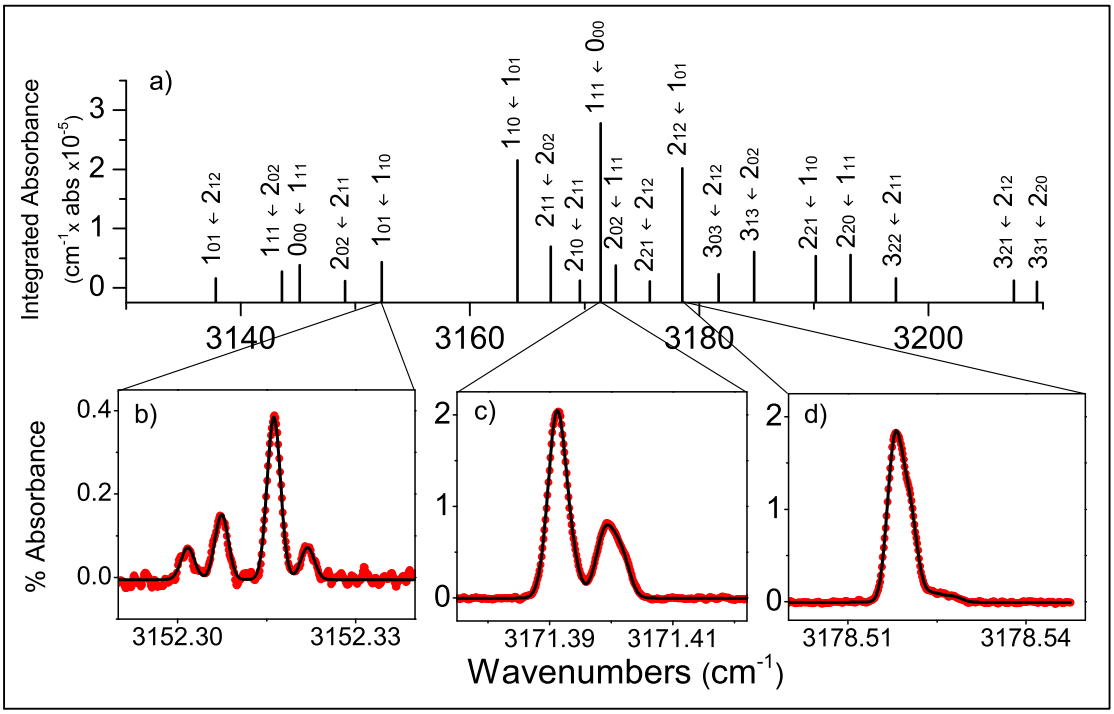

Figure 5.3: Sample CH asymmetric stretch data for CH_2D. Panel a) plots the integrated absorbance of each of the observed rotational lines, labeled as $N'_{K'_aK'_c} \leftarrow N''_{K''_aK''_c}$, versus measured frequency. Details of select transitions, in panels b)-d), show additional structure at high resolution attributed to fine and hyperfine interactions. The black dots are the data and the red lines are simulations base upon constants obtained in fits to the observed lineshapes.

fit these line centers to a Watson Hamiltonian. However, due to extreme differences in scale of rovibrational vs fine/hyperfine frequency information, we will first present the rovibrational analysis in Sec.5.3.1, followed by a more detailed inspection of the high resolution fine/hyperfine structure in Sec.5.3.2.

5.3 Analysis

5.3.1 Rovibrational Structure

The rotational structure of both the i) symmetric C-H stretch and ii) asymmetric C-H stretch bands are analyzed simultaneously, as they both originate from the ground

vibrational state. CH_2D is a moderately asymmetric top, κ = -0.2317, which implies the vibrational bands will have a complex structure. If we neglect fine/hyperfine coupling for the moment, the quantum number N for overall molecular rotation is conserved, with the quasi-quantum numbers K_a and K_c approximately representing the projection of N along the A and C axes, respectively. Additionally, the relatively large rotational constants for CH_2D implies that only a few rotational and/or nuclear spin levels will be populated at the rotational temperatures found in the slit jet. The symmetric stretch rotational structure is predicted to be a nearly pure A-type band, for which the selection rules are ΔK_a = even and ΔK_c = odd. Even at high sensitivity, only the most intense ΔK transitions are seen; thus the selection rules in effect reduce to $\Delta K_a = 0$ and $\Delta K_c = \pm 1$. In analogy to previous H/D isotopic studies of H_2DO^+[57, 1], there is in principle also a component of the symmetric C-H stretch dipole transition moment that carries C-type oscillator strength, arising from large amplitude motion over a significant barrier in the out of plane bending coordinate. However, due to absence of a barrier to planarity in CH_2D, these transitions correlate with weak combination band excitation of C-H stretch plus out of plane bending modes, which should occur much further to the blue. The asymmetric stretch is a pure B-type band so the selection rules for the allowed rotational transitions are ΔK_a = odd and ΔK_c = odd and, again, the transitions seen here are all ΔK_a and $\Delta K_c = \pm 1$.

The frequencies listed in tables 5.1 and 5.2 are the hyperfine and fine structure-free line centers of the symmetric and asymmetric stretch lines, respectively, obtained from a global fit to the high resolution lineshapes. Correct assignment of these lines has been unambiguously confirmed by several four-line combination differences that match to better than the 15 MHz experimental precision. The 32 line centers are fit simultaneously to a Watson asymmetric top Hamiltonian (A-reduction, Ir representation)[133], yielding A, B, C rotational and partial sextic centrifugal distortion constants for the ground state, symmetric stretch, and asymmetric stretch excited state. In a molecule with relatively large rotational constants and with the low rotational temperatures in the slit jet, only the lowest few N″

= 0-2 levels are populated. Therefore, two least squares fits have been pursued in parallel. The first uses only the high resolution rovibrational line centers from the current work, with results presented in the top portions of Table 5.3. The second fit takes additional advantage of previous mid IR study in the out-of-plane bending mode, for which lower resolution data are available on a significantly higher number of rotational states populated at room temperature. Specifically, the line positions from the previous study are added to the current data set, down-weighted by 100 (i.e., $1/\sigma^2$) to account for 10-fold lower precision and help better determine the ground state[2]. The results of this global fit and residuals are summarized in the bottom portions of Table 5.3. The resulting molecular constants are used to create a stick plot simulation of each band, as shown in Figs. 5.4 and 5.5.

Table 5.1: Experimental fine- and hyperfine-free line centers for the C-H_2 symmetric stretch band of CH_2D radical. Estimates of the frequency precision and accuracy are both 15 MHz. The calculated values used are from a global least squares fit to Watson's asymmetric top Hamiltonian of all the symmetric stretch, asymmetric stretch, and the out-of-plane bending mode[2] transitions.

N'	K'_a	K'_c	N''	K''_a	K''_c	Frequency (cm^{-1})	Obs - Calc ($\times 10^{-4}$ cm^{-1})
1	1	0	2	1	1	3044.12647	-1.5
1	0	1	2	0	2	3047.31847	4.8
1	1	1	2	1	2	3048.68316	-1.3
0	0	0	1	0	1	3056.10620	-4.9
1	1	1	1	1	0	3063.16258	2.2
1	1	0	1	1	1	3067.74521	0.5
1	0	1	0	0	0	3075.11432	4.3
2	1	2	1	1	1	3082.10866	1.4
2	0	2	1	0	1	3083.73676	-6.1
2	1	1	1	1	0	3086.71352	-0.3
3	1	3	2	1	2	3089.89100	-1.4
3	1	2	2	1	1	3096.61805	2.2
3	0	3	2	0	2	3091.16343	0.2

Table 5.2: Experimental fine- and hyperfine-free line centers for the C-H_2 asymmetric stretch band of CH_2D radical. Estimates of the frequency precision and accuracy are both 15 MHz. The calculated values used are from a global least squares fit to Watson's asymmetric top Hamiltonian of all the symmetric stretch, asymmetric stretch, and the out-of-plane bending mode[2] transitions.

N'	K'_a	K'_c	N''	K''_a	K''_c	Frequency (cm^{-1})	Exp - Calc ($\times 10^{-4}$ cm^{-1})
1	0	1	2	1	2	3137.83351	-0.3
1	1	1	2	0	2	3143.59854	-2.7
0	0	0	1	1	1	3145.13926	3.3
2	0	2	2	1	1	3149.11486	-8.8
1	0	1	1	1	0	3152.31315	5.9
1	1	0	1	0	1	3164.13198	-1.6
2	1	1	2	0	2	3167.04007	3.8
2	2	0	2	1	1	3169.60393	7.7
1	1	1	0	0	0	3171.39394	-7.7
2	0	2	1	1	1	3172.73286	-14.2
2	2	1	2	1	2	3175.67875	-4.8
2	2	2	1	0	1	3178.51875	22.9
3	0	3	2	1	2	3181.68072	13.3
3	1	3	2	0	2	3184.78745	-13.1
2	2	1	1	1	0	3190.15783	-4.7
2	2	0	1	1	1	3193.22184	1.4
3	2	2	2	1	1	3197.17710	1.2
3	2	1	2	1	2	3207.46030	-2.3
3	3	1	2	2	0	3209.46638	0.2

Table 5.3: Results from the least-squares fit to asymmetric top Watson's Hamiltonian (A-Reduction, Ir Representation). The parameters on the top part of the table are from a global fit including all lines from the symmetric stretch, asymmetric stretch, and the out-of-plane bending bands. The second part of the table includes the results of a fit involving the IR data only. The numbers in parenthesis indicate 1-σ uncertainties of the fit; the residual standard deviation for the global fit is 17 MHz and for the IR-only fit is 66 MHz.

Parameter	Ground State	Symmetric Stretch	Asymmetric Stretch	Out-of-Plane Vibration[2]
	Simultaneous Fit of all Three Vibrations			
A	9.57436(48)	9.398(11)	9.46583(26)	9.22156(75)
B	5.90743(17)	5.8739(62)	5.86369(34)	5.78659(29)
C	3.61984(23)	3.6049(50)	3.59607(32)	3.66570(24)
δ_J /10^{-4}	0.50(13)	0.31(42)	0.04(14)	0.38(14)
δ_K /10^{-4}	4.26(54)	-71(27)	8.5(10)	2.45(52)
Δ_J /10^{-4}	1.28(31)	-4.2(28)	1.67(18)	1.06(29)
Δ_{JK} /10^{-4}	4.1(11)	34(16)	3.97(62)	3.75(98)
Δ_K /10^{-4}	1.3(11)	-246(98)	1.69(69)	-0.99(84)
ν_o		3065.63346(55)	3158.33273(53)	560.5420(29)
	Simultaneous Fit to Present IR Data Only			
A	9.5734(21)	9.4190(25)	9.46639(85)	
B	5.90502(41)	5.88849(59)	5.85986(42)	
C	3.62098(37)	3.59270(39)	3.59689(24)	
Δ_{JK} /10^{-4}	8.5(4)	16.2(44)	8.8(10)	
ν_o		3065.6403(17)	3158.3336(17)	

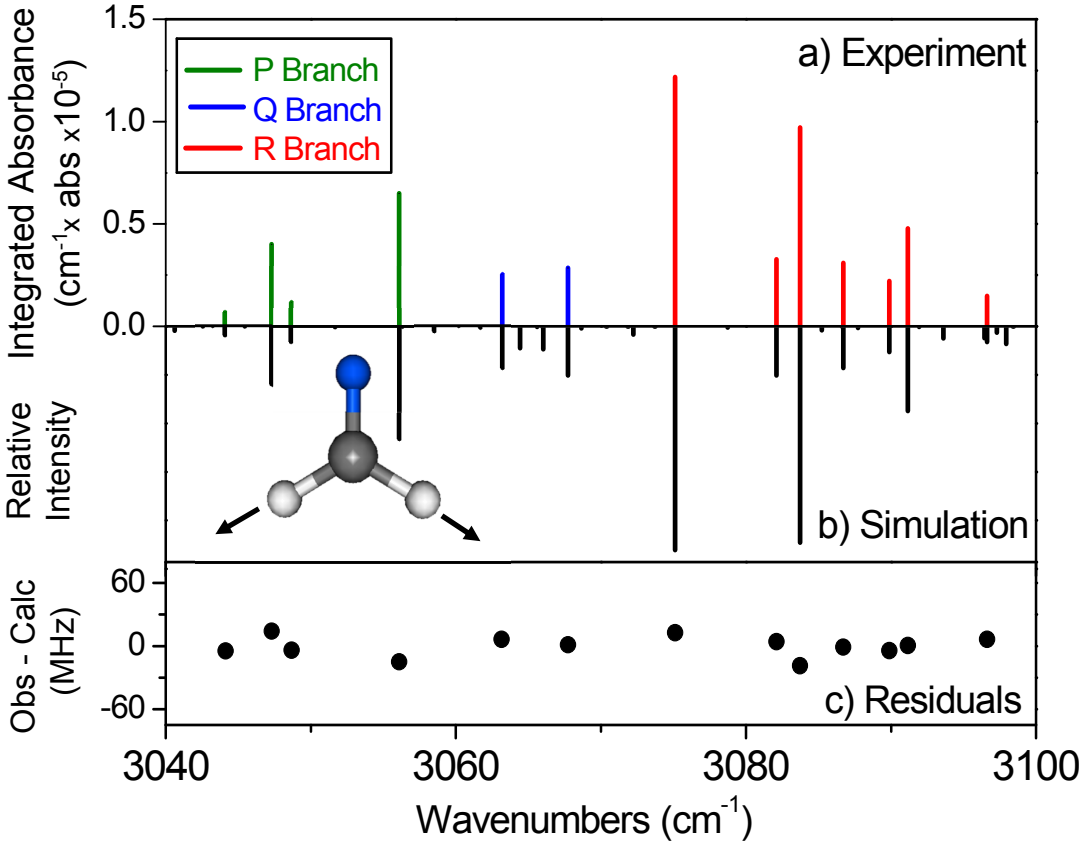

Figure 5.4: CH_2D symmetric stretch rotational structure and fit results. Panel a) is a plot of the experimental data shown as a stick plot with the integrated area under each rotational peak shown as the y-axis; P-branch transitions are in green, Q-branch in blue, and R-branch in red. Panel b) is a simulation based upon rotational and centrifugal distortion constants from the fit to Watson's asymmetric top Hamiltonian. Panel c) plots the observed minus calculated frequency, in MHz, for each of the observed lines.

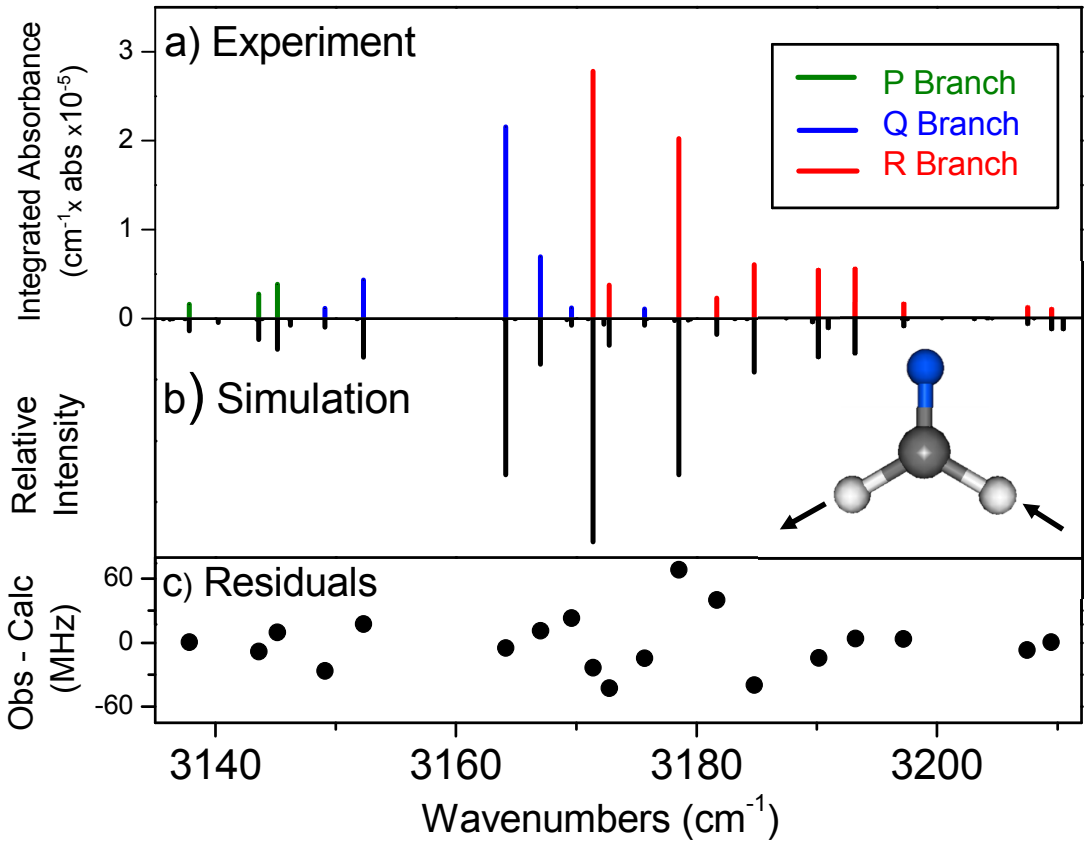

Figure 5.5: CH_2D asymmetric stretch rotational structure and fit results. Panel a) plots the experimental data as a stick plot with the integrated area under each rotational peak shown as the y-axis; P-branch transitions are in green, Q-branch in blue, and R-branch in red. Panel b) is a simulation based upon rotational and centrifugal distortion constants from the fit to Watson's asymmetric top Hamiltonian. Panel c) plots the observed minus calculated frequency, in MHz, for each of the observed lines.

5.3.2 Fine and Hyperfine Structure

As illustrated in Figs. 5.2 and 5.3, each rotational line has a complex lineshape as a consequence of partially resolved fine and hyperfine structure. The largest contribution to the lineshape is the spin-rotation interaction with the hyperfine structure manifesting itself as a general broadening of the peaks seen in Fig. 5.6. Spin-rotation interaction is the

coupling between molecular rotation, (**N**), and electron spin, (**S**) described by:

$$\mathrm{H_{sr}} = (1/2)\sum_{\alpha,\beta} \varepsilon_{\alpha,\beta}(\mathrm{N}_\alpha \mathrm{S}_\beta + \mathrm{S}_\beta \mathrm{N}_\alpha) \tag{5.1}$$

where $\varepsilon_{\alpha,\beta}$ is the spin-rotation tensor and α and β are the labels for the principal axis[134]. For molecules with orthorhombic symmetry, only the diagonal terms in the spin-rotation tensor are non-zero. The fine structure terms for methyl radical ground vibrational state are known to be ε_{bb} = -354(5) MHz and ε_{cc} = -3(63) MHz[135, 115]. As a first approximation, the spin-rotation tensor values for CH_2D can be estimated by scaling the corresponding diagonal values for CH_3 by the corresponding A, B, C rotational constant ratios. This is at least a reasonable first order anticipation, since spin-rotation interaction couples electron spin density (i.e., independent of isotopomer) with rotation around each of the three principal axes, whose semiclassical frequency scales inversely with the corresponding moment of inertia. The scaled values for the spin-rotation constants are ε_{aa} = -354 MHz, ε_{bb} = -218 MHz, and ε_{cc} = -2.3 MHz, which are used as initial estimates in the high resolution lineshape fits.

Similarly, it is also possible to use the known CH_3 hyperfine constants to make a prediction for the CH_2D hyperfine structure. The nuclear hyperfine Hamiltonian consists of the Fermi contact interaction, the dipole-dipole interaction and the electric quadrupole interaction, respectively:

$$\mathrm{H_{hf}} = \mathrm{H_F} + \mathrm{H_{DD}} + \mathrm{H_{eQ}} \tag{5.2}$$

where

$$\mathrm{H_F} = \mathrm{a_F}\mathbf{I}\cdot\mathbf{S} \tag{5.3}$$

$$\mathrm{H_{DD}} = \mathbf{S}\cdot\mathbf{T_{DD}}\cdot\mathbf{I} \tag{5.4}$$

$$\mathrm{H_{eQ}} = \mathbf{I}\cdot\mathbf{T_{eQ}}\cdot\mathbf{I} \tag{5.5}$$

where Fermi contact ($\mathrm{a}_{F(H)}$, $\mathrm{a}_{F(D)}$) represents the largest terms and T_{DD} and T_{eQ} are second-rank traceless tensors smaller in magnitude[134, 136, 137]. The Fermi contact parameter is

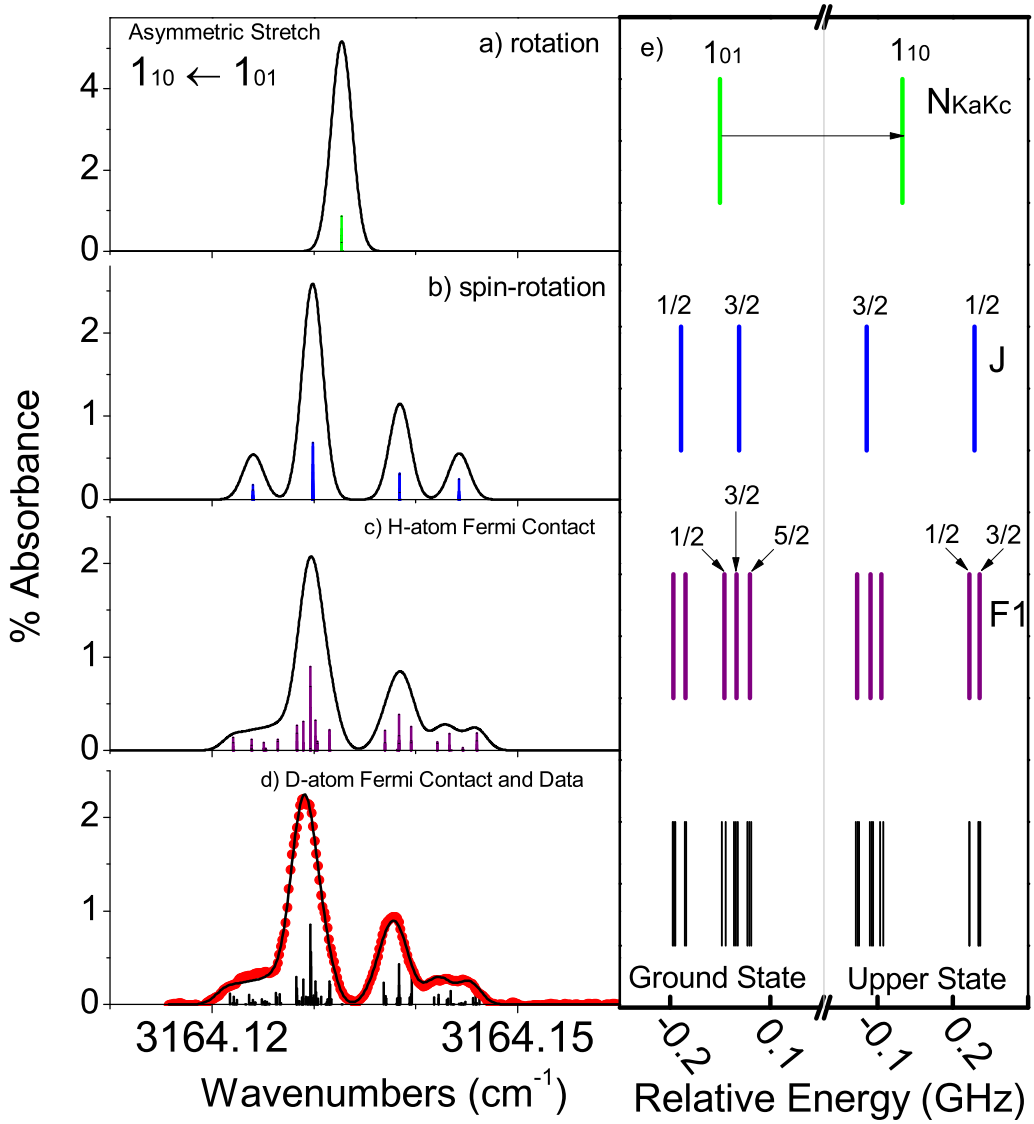

Figure 5.6: Segmented simulation of fine and hyperfine structure of the $1_{10} \leftarrow 1_{01}$ transition for CH_2D in the asymmetric stretch mode. Panel a) shows a simulation and stick spectrum of the transition based upon a 70 MHz Doppler with and no fine or hyperfine structure followed by successive inclusion in panel b) of spin-rotation (ε_{aa},ε_{bb},ε_{cc}, in panel c) H-atom Fermi contact term ($a_{f(H)}$), and panel d) D-atom Fermi contact ($a_{f(D)}$) terms. Panel e) illustrates how the energy level structure is split upon each successive addition of terms.

proportional to the nuclear g-factor, so $a_{F(D)}$ can be reliably estimated from $a_{F(H)}$ and the g-factor ratio of g(H)/g(D) = 6.514 for H vs D nuclei. Indeed, by way of validation, the Fermi contact parameter for CH_2D has been measured in a krypton matrix using ESR techniques and found to be $a_{F(H)}$ = -64.74 MHz and $a_{F(D)}$ = -9.896 MHz[125], i.e., in a ratio of $a_{F(H)}/a_{F(D)} = 6.541$. Since Fermi contact interactions are slightly sensitive ($\sim 5\%$) to the matrix environment[138, 135], rather than use matrix values, we float one common $a_{F(H)}$ value for the 3 vibrational states, subject to the constraint that $a_{F(H)}/a_{F(D)} = 6.541$. The other two terms in the nuclear hyperfine Hamiltonian, dipole-dipole and electric quadrupole, generate negligibly small splittings ($\sim$ 1 MHz) even at our sub-Doppler resolution in the slit jet. For example, previous study of CH_3 radical in our group attempted to obtain T_{DD} and found it to be $\leq$ 1 MHz[135]. Since this tensor also scales proportionally with the nuclear g-factor, it should decrease upon deuteration[136] and will be too small to resolve in CH_2D. Similarly, there will be a non-zero electric quadrupole interaction for CH_2D due to nuclear spin I(D) = 1, but the electric quadrupole coupling constant (eQq) is predicted to be a few hundred kHz and thus can be safely neglected in the analysis[139, 140, 141].

To extract the relevant information on spin rotation and Fermi contact interactions from the sub-Doppler IR lineshapes requires coupling diagonalization of the above Hamiltonian with a least squares fitting routine. To achieve this, all fine and hyperfine transitions and intensities are calculated for each $N'_{K'_aK'_c} \leftarrow N''_{K''_aK''_c}$ rovibrational line, convoluted over an instrumental profile, and compared with experiment, exploiting a lineshape fitting program developed and extensively tested for analysis of CH_2Cl and CH_2F data[142, 143, 127]. To minimize correlation issues, the full set of high resolution lineshapes is fit simultaneously, including a minimum of three scans over each rovibrational line for both the symmetric and asymmetric stretch manifold. All three non-zero elements of the spin-rotation tensor (ε_{aa}, ε_{bb}, ε_{cc}) as well as the Fermi contact term (a_F) are varied for each of the three vibrational states, with a common residual Doppler width for all transitions. The results are summarized in Table 5.4 and will be discussed below in Sec. 5.4. With these fitted lineshapes, it is

then straightforward to extract the pure rovibrational line center frequencies (i.e., fine- and hyperfine-free) used in the analysis described previously in Sec.5.3.1.

Table 5.4: Comparison of fine and hyperfine structure parameters from FTIR study[2], scaled estimates based on methyl radical, and least-squares fit results of the IR experimental line shapes. All values are in MHz. Note that $a_{F(H)}$ was floated in the fit, the $a_{F(D)}$ parameter was calculated using the experimentally determined ratio of 6.541. The numbers in parenthesis are 1-σ uncertainties from the least-squares fit.

Parameter	Ground State (from FTIR study[2])	Ground State (scaled from CH_3)	Ground State (fit results)	Symmetric Stretch	Asymmetric Stretch
ε_{aa}	-444(42)	-354	-353.4(3)	-352(2)	-350.4(2)
ε_{bb}	-135(13)	-218	-226.0(3)	-220(1)	-224.8(3)
ε_{cc}		-2.3	-6.7(3)	-3.4(8)	-2.5(2)
$a_{F(H)}$			-62.4(2)	-68.5(5)	-74.6(2)
$a_{F(D)}$			-9.54	-10.47	-11.40

5.4 Discussion

We first compare the experimental fine and hyperfine values for CH_2D with our predictions based upon the CH_3 radical. As shown in Table 5.4, the spin-rotation tensor values for each of the three vibrational states are in remarkably close agreement with the ε_{aa} = -354 MHz, ε_{bb} = -218 MHz, and ε_{cc} = -2.3 MHz estimates discussed above, with a rms deviation of < 4 MHz. By way of additional confirmation of the fit quality, even the considerably smaller magnitude Fermi contact parameters for the H/D nuclei are also in consistently good agreement with our expectations based on CH_3. Interestingly, our reported spin rotation values differ by 50-100 MHz from an earlier study of the out-of-plane umbrella mode (ε_{aa} = -444(42) MHz and ε_{bb} = -135(13) MHz[2]), which clearly deserves further discussion. By way of example, Fig. 5.7b displays i) experimental data for the $0_{00} \leftarrow 1_{11}$ asymmetric stretch transition in CH_2D along with ii) a lineshape simulation using the current spin-rotation constants, revealing deviations well outside of experimental S/N and resolution constraints. By way of contrast, Fig. 5.7a shows a similar plot based on predictions from the present

study, which fits the experimental data extremely well. The source of this discrepancy is unclear; however, one possibility is that the previous analysis did not include Fermi contact interaction terms in the Hamiltonian, which for incompletely resolved transitions could skew the spin-rotation parameters in a least squares fit. A second issue is that the previous studies were performed at room temperature and with Doppler limited resolution, which requires sampling spin rotation fine structure in a set of much higher rotational states than populated in a supersonic jet. Both the higher resolution of a sub-Doppler slit jet study and the excellent agreement with scaled predictions based on CH_3 generate strong confidence in the present fine/hyperfine analysis for CH_2D radical.

5.4.1 Intensity Analysis

The intensity of a given transition depends upon a nuclear spin weight, a Boltzmann factor, and a Hönl-London Factor. The two hydrogen atoms in CH_2D are fermions each with nuclear spin I = $\frac{1}{2}$; thus the overall wavefunction of the molecule, $\psi_{total} = \psi_{electronic}$ $\psi_{vibrational}$ $\psi_{rotational}$ $\psi_{nuclearspin}$, must be antisymmetric with respect to exchange of these hydrogen nuclei. As the electronic wave function can be thought of as a p-like orbital perpendicular to the plane of the molecule, $\psi_{electronic}$ must be antisymmetric with respect to 180° rotation about the C-D axis (for a C_{2v} planar reference geometry). The vibrational wave function, $\psi_{vibrational}$, is always symmetric with respect to H atom exchange for the molecule in the ground vibrational state. Since the A-axis is the same as the C_{2v} axis, the rotational wave function, $\psi_{rotational}$, is symmetric for even K_a values and antisymmetric for odd K_a values. Of the four possible nuclear spin wave functions, $\psi_{nuclearspin}$, three (ortho, I = 1) have even symmetry ($\alpha\alpha, \beta\beta, 1/\sqrt{2}\sqrt{(\alpha\beta + \beta\alpha)}$), and one (para, I=0) has odd symmetry ($1/\sqrt{2}\sqrt{(\alpha\beta - \beta\alpha)}$). This implies that states with even/odd K_a quantum numbers will correspond to 3:1 nuclear spin weights.

A second contribution to relative intensity comes from thermal population of the lower rotational state. The experimental integrated line intensity, S_{exp}, for a rovibrational transi-

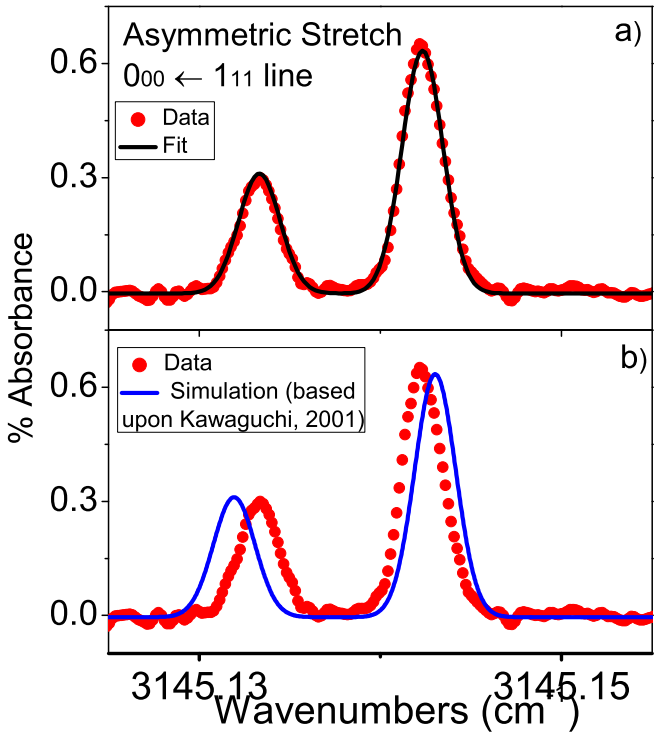

Figure 5.7: Comparison of fine structure splitting of the $0_{00} \leftarrow 1_{11}$ transition from the asymmetric stretch mode. Panel a) plots the data, in red dots, and the results of the fit results from the present study (black line). Panel b) plots the data from the current study, in red dots, and a lineshape simulation based upon spin-rotation constants from the FTIR study[2] (blue line). In the simulation, the upper and lower state spin-rotation constants are set equal and the hyperfine constants are those found in the present study. The high resolution of the data allows for a refinement of the spin-rotation constants from the FTIR study.

tion, from lower state, i, to upper state, j, is[132]

$$S_{exp} = N^{i} l (S_o)^{ij} \tag{5.6}$$

where

$$N^{i} = N_o^{vib} \frac{g_{NS} g_J}{Q_{rot}^{NS}} e^{-(E_i)/kT_{rot}} \tag{5.7}$$

where the absorption pathlength is l = 64 cm, $(S_o)^{ij}$ is the line strength per rotational state,

N_o^{vib} is the population in the ground vibrational state, g_{NS} and g_J are the nuclear spin and magnetic quantum number degeneracies, and Q_{rot}^{NS} is the rotational partition function for a given nuclear spin symmetry. Fig. 5.8 shows the experimental integrated line intensity, scaled by the line strength factors, plotted semi-logarithmically against the ground state rotational energy. The slope of the graph reveals that the molecules are well described by a rotational temperature of 23(1) K.

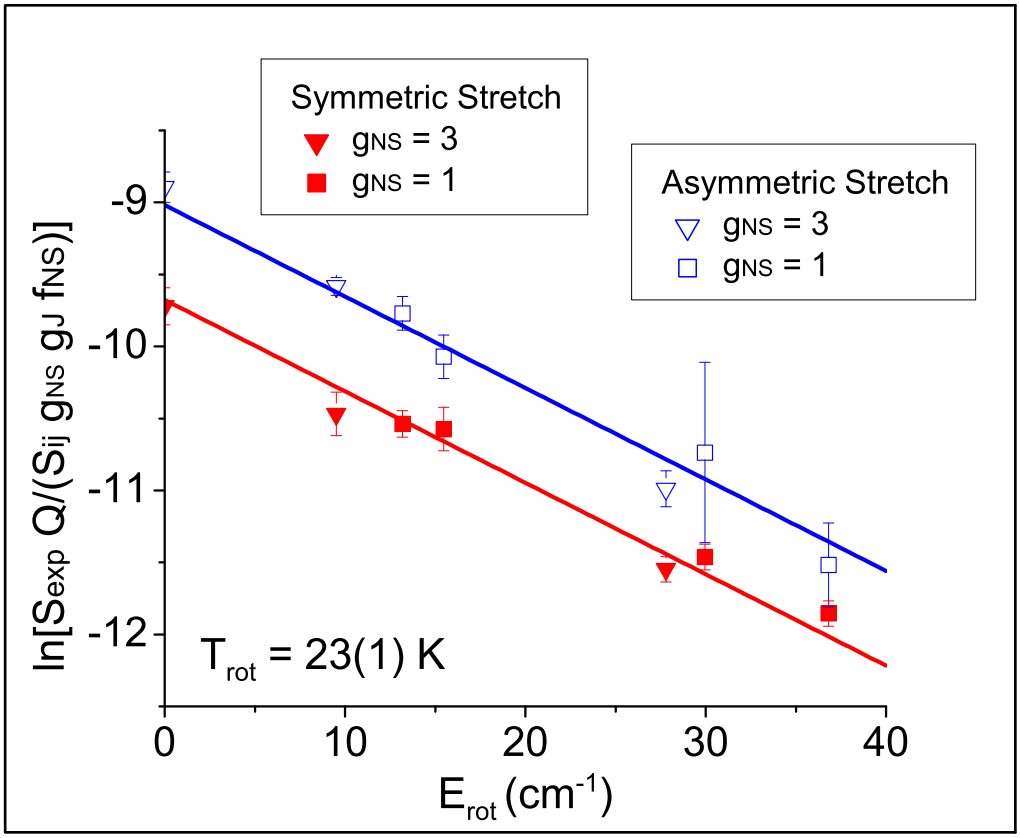

Figure 5.8: A semi-logarithmic plot of experimental integrated line intensities scaled by the calculated linestrength factors plotted against the rotational energy of the lower state. The symmetric and asymmetric stretch lines are denoted by filled and open symbols, respectively with the ortho lines are triangles and the para lines are squares. The solid lines represent least-squares fits of the data to a straight line.

Information about the relative intensities of the bands can also be extracted from this

Boltzmann plot. In particular, the y-intercept difference between asymmetric and symmetric CH stretches is the logarithm of the associated IR intensity ratio, which is found to be $I_{asym}/I_{sym} = 1.93(22)$. By way of comparison, the calculated ([B3LYP/6-311++G(3df,3pd) basis set][3]) relative intensity of the two bands is 2.38, i.e., slightly higher than the experimental ratio but smaller than the standard 3:1 bond-dipole prediction for a 120 degree HCH bond angle[143]. It is worth noting that this behavior is quite different from what was observed for both CH_2F and CH_2Cl radicals in our group[143, 142], where the symmetric stretch was found to be anomalously strong compared to the asymmetric stretch (i.e., $I_{asym}/I_{sym} < 1$) due to vibrationally induced charge "sloshing" of electron charge along the carbon-halide bond direction. The vibrational transition strength behavior in CH_2D is clearly unaffected by any strongly dipolar C-X bond, yielding results within 50% of the simple bond-dipole picture.

5.4.2 Vibrational Force Constants

There has been a rich history of spectroscopic analysis and modeling of CH_3 radical vibrations. In 1967, Pimentel and coworkers used force constants from analysis of CH_3 bending spectra to predict frequencies for CD_3 bending modes and to analyze out-of-plane and in-plane bending motion using a normal coordinate analysis[109, 114]. With inclusion of the CH_3 gas phase C-H stretching data, Hirota et al. exploited the known frequencies to calculate an approximate harmonic force field for the molecule[144]. Soon thereafter, Nibler and coworkers obtained the IR inactive symmetric C-H stretch in CH_3 by narrow band laser Raman methods, and with this inclusion used the high-low frequency separation method of Wilson[145] to predict the stretching frequencies for all four H/D methyl radical isotopomers[117]. Meanwhile, Spirko and coworkers developed nonrigid inverter Hamiltonian methods capable of describing the umbrella and C_{2v} vibrations of ammonia simultaneously[146, 147, 148, 149, 150, 151], which were subsequently applied to CH_3 and CD_3 [152, 153, 154]. Soon afterwards, Westre et al. obtained data on the Raman active

stretches and first overtones for all four isotopic species. This influx of new overtone data facilitated an analysis based on the harmonically coupled anharmonic oscillator (HCAO) model developed by Child[155] and Mills[156, 157] but it was still necessary to treat the CH and CD stretch manifolds separately for the four isotopomers[158]. With the additional high resolution for CH_2D from this work, we now have 9 of 10 in-plane CH and CD stretching frequencies, covering all 4 H/D isotopomers of methyl radical, with the symmetric CD stretch of CHD_2 as the only missing fundamental mode. With this more comprehensive body of high resolution data, our goal is to provide a predictive model for CH and CD in-plane stretching dynamics in all four H/D isotopomeric species.

Table 5.5: Results from least-squares fit of the vibrational frequencies to the harmonically coupled Morse oscillator model (HCMO) and then to an HCMO model that includes 2:1 Fermi coupling. The residual standard deviation of the HCMO plus Fermi coupling fit was 2.0 cm^{-1}.

Parameter	HCMO	HCMO and Fermi Interaction
De ($*10^{-10}$ ergs)	7.9(5)	7.1(4)
a ($\mathring{A}^{-1}$)	1.9(7)	2.02(6)
$f_{rr'}$ (cm^{-1})	2606.8065()	2211(280)
Scaling Factor		0.79 (7)

We approach this analysis with three increasing levels of complexity. As the simplest level, we model each of the three stretches as harmonic oscillators (i.e., f_{rr} and $f_{\theta\theta}$) and with harmonic coupling between each of the stretches (i.e., $f_{rr'}$). This is essentially a normal mode analysis for the high frequency in-plane vibrations, with results analytically expressible in terms of the G matrix elements from Wilson et al.[145]. Indeed, a similar high-low frequency separation analysis was performed by Nibler and coworkers[117], who used the force constant obtained from CH_3 stretching frequencies to predict frequencies for all stretching vibrations of the H/D isotopomeric species. The results of our fit are in Table 5.5 and the fit residuals are shown in Fig. 5.9. Note that the CH stretch data fit significantly better to the harmonic model than the CD stretches; this trend had been noted previously by several groups and attributed to anharmonicity in the CH and CD bonds[117, 158]. As we shall see below,

a more likely explanation is that CD stretch vibrations prove to be more susceptible to resonant interactions with the bending overtones.

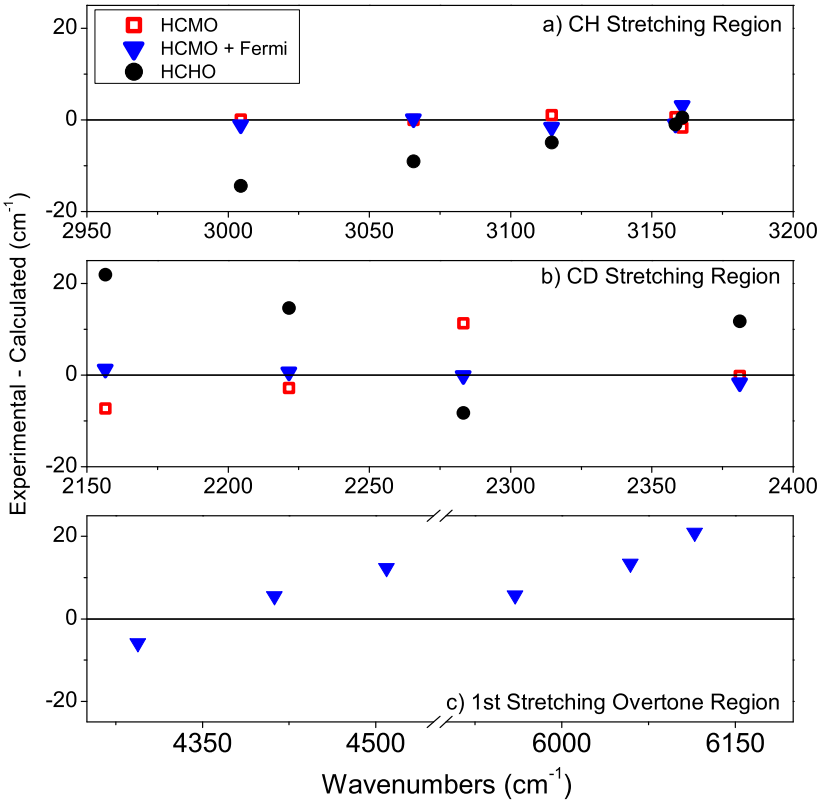

Figure 5.9: The experimental values minus the calculated values for all nine of the experimentally known stretches for each of the three models is shown. The black circles show residuals from a fit to a harmonically coupled harmonic oscillator model, the red squares are the residuals from the harmonically coupled Morse oscillator model (HCMO), and the blue triangles are residuals from the HCMO model but with 2:1 Fermi interactions added into the model. Panel c) shows difference between the experimental frequencies for the overtones and the predicted frequencies based upon the fit to the fundamental modes.

This modest level of agreement motivates our second level of attack, using harmonically coupled Morse oscillators (HCMO). In this model, each CH bond is represented by a simple Morse oscillator, with potential coupling between stretches described within the harmonic

approximation. The Morse oscillator model takes into account the difference in anharmonicity between the CH and CD bonds. This can easily be seen by looking at the Morse oscillator energy level expression: $E(n_\alpha) = \omega(n_\alpha + \frac{1}{2}) - \omega x(n_\alpha + \frac{1}{2})^2$ with $\omega = 2a\hbar\sqrt{(\frac{D}{2\mu})}$ and $\omega x = \frac{a^2\hbar^2}{2\mu}$ noting that ω and ωx scale differently with mass. The full model employed was first developed by Halonen and Child and used on a variety of tetra-atomic systems including methane and fully deuterated methane[159]. The Hamiltonian is

$$\mathrm{H_{tot}} = \sum_{\alpha=1}^{3}[\frac{1}{2}\mathrm{G_{\alpha\alpha}p_\alpha^2} + \mathrm{D}(1 - \mathrm{e}^{-\mathrm{ar}_\alpha})^2] + \sum_{\alpha=1}^{3}\sum_{\beta>\alpha}^{3}[-\mathrm{G_{\alpha\beta}p_\alpha p_\beta} + \mathrm{f_{rr'}r_\alpha r_\beta}] \tag{5.8}$$

where the sums over α and β run over the three local mode bonds, r_α are the bond displacement coordinates, D and a are the Morse oscillator dissociation energy and range parameter, respectively, and the $G_{\alpha\alpha}$ and $G_{\alpha\beta}$ are the corresponding Wilson G-matrix elements divided by hc to keep the expression in cm^{-1}. The first summation simply represents the Morse oscillator Hamiltonian, for which the analytic solutions are well known and therefore provide a convenient 3D product basis of Morse oscillator eigenfunctions. The second summation contains both kinetic and potential energy coupling terms in the harmonic approximation, the matrix elements of which we can obtain in a Morse basis from expressions provided by Halonen and Child[159]. However, it is possible to simplify these matrix elements further using recursion relations[160] and eliminate any need for calculating gamma functions altogether. The required matrix elements of the p and r operators can then be expressed as:

$$\begin{aligned} < \mathrm{n+j} \mid \mathrm{p} \mid \mathrm{n} > = \frac{\mathrm{a}}{2}(\imath\hbar(-1)^{\mathrm{j+1}})\sqrt{(\mathrm{k-2n-1})(\mathrm{k-2(n+j)-1})} \\ [\prod_{m=1}^{j}\frac{(n+m)}{(k-n-m)}]^{\frac{1}{2}}(1-\delta_{j0}); \qquad j \geq 0 \end{aligned} \tag{5.9}$$

$$\begin{aligned} < \mathrm{n+j} \mid \mathrm{r} \mid \mathrm{n} > = \frac{(-1)^{\mathrm{j+1}}}{\mathrm{a}}\frac{\sqrt{(\mathrm{k-2n-1})(\mathrm{k-2(n+j)-1})}}{\mathrm{j(k-2n-j-1)}} \\ [\prod_{m=1}^{j}\frac{(n+m)}{(k-n-m)}]^{\frac{1}{2}}; \qquad j \geq 1 \end{aligned} \tag{5.10}$$

$$< \mathrm{n} \mid \mathrm{r} \mid \mathrm{n} >= \mathrm{a}^{-1}[\ln(\mathrm{k}) - \Phi(\mathrm{k} - 1 - 2\mathrm{n}) + \sum_{\mathrm{m}=1}^{\mathrm{n}}(\frac{1}{\mathrm{k} - \mathrm{n} - \mathrm{m}}(1 - \delta_{\mathrm{n}0}))]. \quad (5.11)$$

where n labels the Morse oscillator eigenfunctions, k = $2\sqrt{(2\mu D)}/(a\hbar)$, μ is the reduced mass, a and D are the Morse oscillator range parameter and dissociation energy. Diagonal matrix elements in r (i.e., $< n \mid r \mid n >$) contain the digamma function, Φ , which can be calculated for one value of k - 1 - $2n$ numerically and then readily extended to all other arguments via recursion relations[160]. The results converge quickly with basis set size; specifically, it is only necessary to include up to n = 5 quanta in each of the three stretches to achieve convergence out to 5 digits (≈ 0.1 cm^{-1})

With eigenvalues from the harmonically coupled Morse oscillator model, we simultaneously fit the 9 planar stretching modes for which the gas phase experimental frequencies are known. The resulting Morse oscillator and harmonic coupling constants from the fit are listed in Table 5.5, with the residuals between experimental and calculated frequencies from the harmonically coupled Morse oscillator model are shown in red squares in Fig. 5.9. The Morse oscillator model does a qualitatively better job than a simple harmonic treatment, yielding an rms deviation of ≈ 5.2 cm^{-1} vs 14 cm^{-1}. However, it is still clear that the fit quality is much better for CH than CD stretches, which thus suggests the presence of additional terms still necessary to include in our Hamiltonian treatment.

To investigate this, we consider the effect of the inclusion of such cubic coupling terms in our third level of analysis. As a starting point, we need energies for the bend overtones, which we calculate using the harmonic frequencies reported by Cunha de Miranda et al.[126] The resulting energies of these states along with the CH and CD stretch fundamental frequencies are shown in Fig. 5.10. The labeling used for the CH_3 and CD_3 levels is $(\nu_1, \nu_2, \nu_3^l, \nu_4^l)$ and the notation used to label the states for CH_2D and CHD_2 is $(\nu_3, \nu_4, \nu_5, \nu_6)$ with ν_1 and ν_2 labeled separately. The planar bending overtone and combination frequencies are calculated in the harmonic approximation based on fundamental frequencies of Cunha de Miranda et al.[126]. Noticeably, the CD stretch manifolds for many of the isotopomers have nearby two

quanta states of the correct symmetry for a strong 2:1 Fermi interaction. This contrasts strikingly with the CH stretch manifolds, which do not have such candidate states within several hundred wavenumbers. This plot makes it clear that the energy differences between the CD stretch fundamental and the CD bend overtone is smaller than for the CH stretch fundamental, i.e., consistent with a greater impact of Fermi resonances in the CD stretch than for the CH stretch manifold.

Since the dataset we are fitting includes only the fundamentals in the CH and CD stretches, we are reluctant to introduce many more parameters into the model. Even though we lack exact frequencies for the perturbing states, it seems clear that there are consistently states that give rise to a Fermi interaction. Therefore we added a Fermi interaction to the Morse oscillator model using a simple two-state perturbation matrix as a qualitative way to test the idea. This is not such an unreasonable assumption, since the states that appear to be poorly described by the unperturbed coupled Morse oscillator model have nearby two-quanta bending states. To account for this perturbation, Herzbergs' classic model[86] is used,

$$\begin{vmatrix} E_n^0 - E & W \\ W & E_i^0 - E \end{vmatrix} = 0 \tag{5.12}$$

where W is the coupling matrix element and E_i^0 and E_n^0 are the unperturbed energy levels. Based on the above analysis and to minimize the number of additional parameters, we therefore start from theoretically predicted coefficients of the $(a_s^\dagger a_b a_b + a_s a_b^\dagger a_b^\dagger)$ and $(a_s^\dagger a_b a_{b'} + a_s a_b^\dagger a_{b'}^\dagger)$ terms in the cubic expansion of the normal mode Hamiltonians for CH_3, CH_2D, CHD_2, and CD_3, evaluated at the MP2/aug-ccpVTZ level with GAUSSIAN 09 for the equilibrium methyl radical structure.[131] Here a and $a^\dagger$ represent harmonic oscillator raising and lowering operators, respectively, with the s and b subscripts denoting stretching and bending modes.

We then fit the full set of observed CH and CD fundamental frequencies using a suitably augmented Hamiltonian and in a Morse oscillator basis, scaling the theoretical stretch/bend cubic terms obtained from the electronic structure calculation by a single adjustable param-

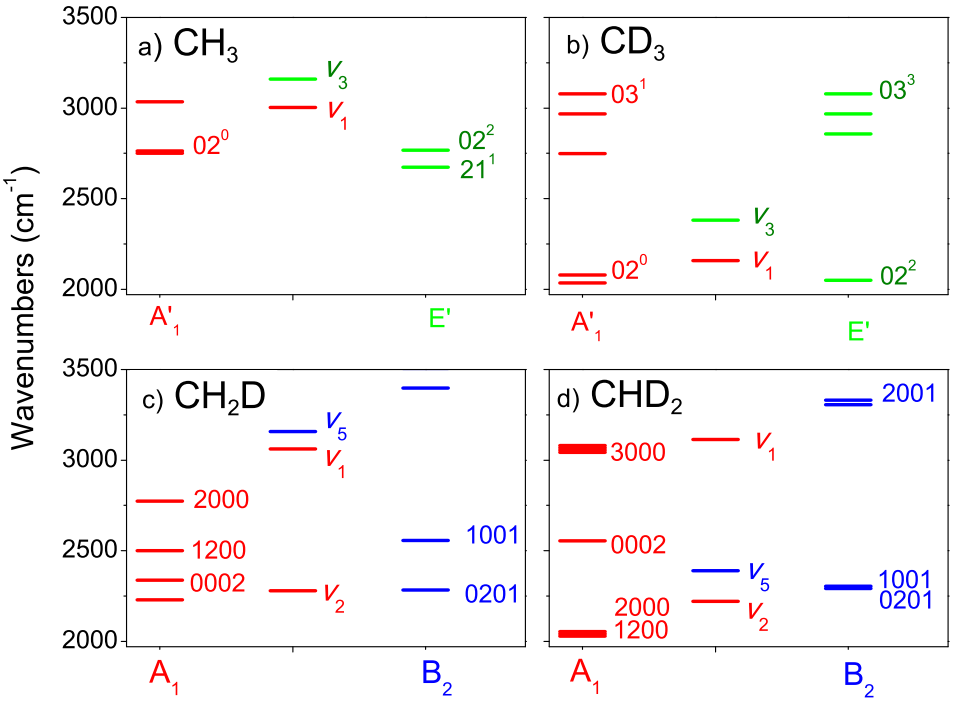

Figure 5.10: Graphs showing the fundamental stretching modes nearby overtone and combination bands that are of the correct symmetry to perturb each stretching mode. CH_3 and CD_3, shown in panels a and b, are of D_{3h} symmetry and the states are labeled with $(\nu_1, \nu_2, \nu_3^l, \nu_4^l)$; the symmetric stretch is of A_1' symmetry and the doubly-degenerate asymmetric stretch is of E′ symmetry. The asymmetrically substituted isotopomers, CH_2D and CHD_2, have three stretches: two of a1 symmetry, in red, and one of b2 symmetry, in blue. The labels for these species are $(\nu_3, \nu_4, \nu_5, \nu_6)$, with the stretches labeled explicitly. It is clear that the CD_3 symmetric stretch, the CH_2D CD stretch, and the CD stretches in CHD_2 all have nearby states that could have a Fermi interaction with a nearby bending overtone.

eter, γ. The results of the fit, as well as predicted frequencies for the first overtones and the as yet unobserved CHD_2 asymmetric stretch fundamental are listed in Table 5.6 with the fitting parameters in Table 5.5. This model now yields a 2.5-fold improvement in fitting the fundamental frequency data ($\sigma = 2.0$ cm^{-1} vs. 5.2 cm^{-1}). Of equal importance, it appears to predict the overtone transitions reasonably well (see Table 5.6), even though these data are

not included in the least-squares analysis. It is also noteworthy that the dissociation energy and other Morse parameters are consistent with experimental data for CH bond strengths, further indicating that the model provides a physically reasonable description of the stretches in methyl radical.[101] Finally, this improved treatment clearly suggests that the lower quality fit of the CH and CD stretch frequencies to the first two models is not dominated by isotopic anharmonicity effects, but rather due to a greater proximity of bending states in the CD manifold able to participate in resonant 2:1 Fermi interactions.

Table 5.6: Frequencies of the vibrational fundamentals and first overtones obtained from the harmonically coupled Morse oscillator model (HCMO) with the addition of three quanta Fermi coupling. Only the fundamental frequencies were included in the fit; the overtones were predicted by the model.

Isotopomer	Stretch	Experimental Frequency	Results From Fit	Predicted By Fit
CH_3	ν_1	3004.436	3005.53	
	$2\nu_1$	5959.7		5962.66
	ν_3	3160.82118	3157.67	
CH_2D	ν_1	3065.63346	3065.33	
	$2\nu_1$	6059.4		6058.63
	ν_2	2283.3	2283.37	
	$2\nu_2$	4509.3		4505.42
	ν_5	3158.33273	3159.17	
CHD_2	ν_1	3114.577	3116.18	
	$2\nu_1$	6114.9		6107.52
	ν_2	2221.5	2220.77	
	$2\nu_2$	4412.5		4413.31
	ν_5			2384.60
CD_3	ν_1	2156.5	2155.22	
	$2\nu_1$	4294.1		4294.69
	ν_3	2381.0886	2382.76	

5.5 Conclusion

First high-resolution IR spectra of supersonically cooled singly-deuterated methyl radical has been obtained, which has permitted investigations of both the A-type symmetric C-H stretch and B-type antisymmetric C-H stretch vibrations. Band origins, rotational constants

and centrifugal distortion constants have been fit to a Watson asymmetric top Hamiltonian, with fine structure and hyperfine parameters determined using a least-squares-fitting program previously developed in the group. The spin-rotation constants for the ground, symmetric, and asymmetric stretch states are obtained, with Fermi contact terms for each of the three states as well.

Since the spectroscopy of CH_3 radical has been extensively studied, this allows us to make simple predictions on the CH_2D constants, which in most cases proved to be in very good agreement with experiment. The predicted band origins of the symmetric and asymmetric CH stretches are each within one standard deviation of 10 cm^{-1} from the experimental value. This illustrates the utility of a scaling factor based upon analysis of previous C-H stretches in a family of radicals, combined with high level B3LYP calculations for predicting the band origin of new radical species. The spin-rotation constants have been demonstrated to scale with the A, B, C rotational constants upon deuteration. This again proved a useful approximation, with all predicted spin-rotation constants within 10 MHz of experimental values.

Chapter 6

Understanding the $^2\Pi$-$^2\Sigma^+$ bands in ethynyl radical: from the inclusion of satellite branches to vibronic coupling

6.1 Introduction

The ethynyl radical (C_2H) is known to be a key intermediate in the combustion of acetylene (C_2H_2),[15] which is of considerable interest both in chemical and industrial applications.[161] Additionally, acetylene is known to be produced as an intermediate in the combustion of fuel-rich mixtures of larger hydrocarbons.[17] Therefore, the formation of C_2H and its further reactions with other intermediates likely play an important role in modeling combustion mechanisms. Because of this, much experimental work has focused on elucidating the kinetic rate constants for the reaction of C_2H with a variety of species, with a recent review by Laufer and Fahr summarizing experimental findings.[162] Of particular interest is the formation of soot as a byproduct of the combustion of hydrocarbon fuels. While it is known that soot formation occurs through a nucleation process of larger and larger polycyclic aromatic hydrocarbons (PAHs) until solid particulates form, it is still not clear which mechanistic steps in combustion initiate PAH formation in the first place. One postulated mechanism[163] involves the reaction of free radical intermediates, such as phenyl

Portions of this chapter have been previously published as Sharp-Williams, E. N.; Roberts, M. A.; Nesbitt, D. J. *J. Chem. Phys.* **2011**, 134, 064314. and Sharp-Williams, E. N.; Roberts, M. A.; Nesbitt, D. J. *Phys. Chem. Chem. Phys.* **2011**, 13, 1747417483.

radical (C_6H_5), with small unsaturated hydrocarbons such as C_2H_2 and C_2H.

The ethynyl radical has also been detected in outer space[16] and is thought to participate in similar reaction chemistry there, even though the environment of the interstellar medium is quite different from that of a flame. Specifically, C_2H has been postulated to contribute to the formation of larger hydrocarbons and carbon clusters, particularly in dense interstellar clouds.[164] Additionally, Vuitton et al. proposed the following mechanism for the formation of haze particles in the atmosphere of Titan:[165]

$$C_{2n}H_2 + h\nu \rightarrow C_{2n}H + H \tag{6.1}$$

$$\underline{C_{2n}H + C_{2m}H_2 \rightarrow C_{2(n+m)}H_2 + H} \tag{6.2}$$

$$\text{net}: C_{2n}H_2 + C_{2m}H_2 \rightarrow C_{2(n+m)}H_2 + 2H \tag{6.3}$$

The above reaction sequence shows the potential involvement of C_2H (and other acetylene-like species) in the nucleation process in space, *i.e.*, the transformation of gas-phase molecules to particulate-sized species. Given the key role that ethynyl radical plays in both combustion and space chemistry, it is no surprise that there have been many theoretical and experimental studies conducted to fully understand its ground and excited states. Accurate kinetic modeling of reaction chemistry occurring both on earth and in space rests largely on the quality of the laboratory data available for the molecules present in that chemistry, including reactive intermediates such as C_2H.

Previous experimental work on C_2H has been quite extensive, with many studies measuring rate coefficients for reactions of C_2H with a variety of neutral molecules.[162, 166, 167, 168, 169, 170, 171] In addition, there has been a large amount of spectroscopic work, with studies aimed at understanding the vibrationless ground state,[16, 172, 7, 4] the excited vibronic levels of the $\tilde{X}$ state,[173, 174, 175, 176, 177, 178, 179, 20, 180] and the electronically excited $\tilde{A}$ state.[181, 182, 183] To summarize the most important results, these gas-phase experimental studies confirmed that (i) the ground state of C_2H is $^2\Sigma^+$ symmetry,[7] (ii) the lowest energy vibration, the CCH bending vibration, is located at 371.6034 cm^{-1} above

the vibrationless level of the ground state,[174] and (iii) the C-C stretching vibration is located at 1840.5711 cm^{-1} above the vibrationless level.[175] The location of the third and final vibrational frequency, that of the C-H stretch, is still under some debate, although currently the leading candidate[173] has been a band observed near 3299 cm^{-1}. What makes this interesting is that the electronically excited $\tilde{A}$ state of $^2\Pi$ symmetry is very low-lying with respect to the ground state, located only approximately 3600 cm^{-1} higher.[181] It is speculated that difficulties in assigning the C.H stretch mode may be due to anomalous $\tilde{A}$ state coupling with vibrational levels in the $\tilde{X}$ state.

Indeed, multiple challenges arise from vibronic coupling of the three lowest electronic states in C_2H, namely, $^2\Sigma^+$ (A′), $^2\Pi$ (A′), and $^2\Pi$ (A″). The $^2\Pi$ electronic state of linear C_2H splits into two potential energy curves of A′ and A″ symmetries as the molecule bends, due to the interaction of electronic and vibrational angular momenta, i.e., the Renner-Teller effect. The potential energy surfaces for these three electronic states are expected to lie close in energy, again with the $^2\Pi$ curves located approximately 3600 cm^{-1} above that of the $^2\Sigma^+$ ground state. The $^2\Pi$ (A″) and $^2\Pi$ (A′) components of the Renner-Teller pair become nondegenerate as the molecule bends, with the $^2\Pi$ (A″) state lower in energy. While the Wigner noncrossing rule permits the $\tilde{X}$ $^2\Sigma^+$ (A′) state to cross the $^2\Pi$ (A″) curve, there is an avoided crossing of the same symmetry $\tilde{X}$ $^2\Sigma^+$ + (A′) and $^2\Pi$ (A′) curves for bent, C-C stretch excited geometries, which yields a conical intersection (often termed a “pseudo” Jahn-Teller interaction) between these two states. Additionally, crossing of the $\tilde{X}$ and $\tilde{A}$ state potential energy curves is expected to occur near the equilibrium $\tilde{A}$ state geometry. This can promote strong vibronic mixing between the lowest energy vibrational levels of the excited state with excited vibrational levels of the ground state, which may account for a weak fundamental C-H stretching vibration.

As a direct consequence of the strong non-Born-Oppenheimer effects present in C_2H, there have been numerous theoretical studies focused on unraveling the spectral complexity and accurately calculating vibronic level positions for the ground and first excited states.[184,

185, 186, 187, 188, 189, 190, 8, 9] Specifically, recent work by Tarroni and Carter[8, 9] has predicted the frequencies, intensities, and identities of all the vibronic and electronic transitions in C_2H up to 6400 cm^{-1}. This variational method[191] requires diagonalizing the full Hamiltonian in a basis of electronic, vibrationally, and spin-rotational symmetry adapted functions, in conjunction with high level *ab initio* diabatic potential energy surfaces for all three electronic states: $^2\Sigma^+$ (A′), $^2\Pi$ (A′), and $^2\Pi$ (A″).[8] Of considerable interest with regard to the this work, their calculations found that the $\tilde{A}$ $^2\Pi$ electronic character is actually spread over as many as five Π levels in the 3300.4300 cm^{-1} range, with the largest fraction (0.301) contained in a state located at 3604.4 cm^{-1}. Indeed, their assignments for many levels in the 3300.4300 cm^{-1} region reflect $\tilde{A}$ $^2\Pi$ character in addition to highly vibrationally excited $\tilde{X}$ state contributions, indicating significant mixing between states probed at typical frequencies in the near IR.

Of particular relevance to this work, there have been several observations of $^2\Pi$-$^2\Sigma^+$ bands in C_2H, both in the matrix[192, 193, 194] and in the gas phase,[195, 18, 19, 196, 197, 198] as well as high resolution gas phase studies of C_2H hot bands[181] and $^{13}C_2H/C_2D$ isotopomers.[177, 182] Specifically, Curl and co-workers[18, 19] were first to observe and identify four $^2\Pi$-$^2\Sigma^+$ bands in C_2H between 3675 and 4125 cm^{-1}. Using color center laser absorption spectroscopy with magnetic rotation for sensitivity enhancement, they observed rotationally resolved IR bands with origins at 3692.606, 3786.096, 4012.259, and 4107.874 cm^{-1}. This magnetic rotation technique generates small shifts in observed peak positions,[19] which required detailed corrections in order to infer field free line frequencies in each of the $^2\Pi$-$^2\Sigma^+$ bands. Their production of C_2H by discharging pure argon over polyacetylene deposits created near room temperature radicals, which allowed them to observe rovibrational transitions originating from N″ levels up to as high as N″ = 19. Reported accuracy in determining line center positions was claimed to be 0.001 cm^{-1} (30 MHz),[18] with overall lineshapes broadened to approximately 0.01 cm^{-1} (300 MHz).

Later, Forney et al.[194] observed the same four $^2\Pi$-$^2\Sigma^+$ bands, previously reported

in the gas phase, in a matrix of solid neon at 3685.8, 3759.4, 3983.9, and 4085.4 cm^{-1}, respectively. These spectra were taken using a Fourier transform interferometer with 0.1 cm^{-1} (3 GHz) resolution and accuracy. Shepherd and Graham[193] verified these same $^2\Pi$-$^2\Sigma^+$ absorption bands in an argon matrix and confirmed their assignment to ethynyl radical via similar studies of its isotopomers, C_2D and $^{13}C_2H$. Vervloet and Herman[196] observed these four $^2\Pi$-$^2\Sigma^+$ bands via Fourier transform emission spectroscopy of C_2H in the gas phase. Later, Hsu *et al.*[197] observed three of the four aforementioned bands using laser induced fluorescence spectroscopy, exciting gas-phase C_2H radicals to their $\tilde{B}$ electronic state and recording emission down to many of the vibronic levels in the $\tilde{X}$ state. Zhou *et al.*[198] reported multiple vibronic bands of C_2H and C_2D, including the four previously reported $^2\Pi$-$^2\Sigma^+$ bands between 3675 and 4125 cm^{-1}, with slow electron velocity-map imaging. Of particular interest, this work provided Neumark and co-workers report updated assignments for their observed vibronic bands, based largely on the theoretical results of Tarroni and Carter,[8, 9] to which we will refer later.

The organization of this chapter is as follows. In Sec. 6.2, we present an overview of fundamental spectroscopic expectations for $^2\Pi$-$^2\Sigma^+$ bands, followed in Sec. 6.3 by a brief discussion of the slit jet discharge experimental apparatus for making jet cooled C_2H. In Sec. 6.4 we present high resolution infrared C_2H radical absorption spectra of five $^2\Pi$-$^2\Sigma^+$ bands reported by Curl and co-workers,[18, 19] and others,[193, 194, 197, 198] for which the current experimental combination of (i) low radical temperatures ($T_{rot} \approx 12$ K), (ii) sub-Doppler resolution ($\Delta\nu \leq 0.002$ cm^{-1} (60 MHz)), and (iii) high measurement precision ($\Delta\nu_{exp} \approx 0.00033$ cm^{-1} (10 MHz)) significantly augment and clarify the previous efforts. In Sec. 6.5.2, we report refined excited state constants as well as make vibronic assignments for each of the $^2\Pi$ states, guided by previous experimental and theoretical work mentioned above. Finally, in Sec. 6.6 we explore vibronic coupling interactions, introducing the idea of near resonant dark states affecting energy levels in the $^2\Pi$ upper states as well as discussing prospects of extending our Hamiltonian model to include this coupling. The chapter is summarized and

concluded in Sec. 6.7.

6.2 Expectations for $^2\Pi$ – $^2\Sigma^+$

Figure 6.1 demonstrates the allowed transitions expected for a $^2\Pi$-$^2\Sigma^+$ band, with the energy levels rigorously described by a total rotational quantum number (J) and parity (+ or -). The additional F_1/F_2 labels indicate whether the state corresponds to a lower/higher energy eigenvalue of the secular determinant for the same J, respectively. Here $\mathbf{K} = \mathbf{N}$ (end-over-end) + $\mathbf{L}$ (electronic orbital) represents angular momentum exclusive of electron spin, which couples with electron spin $\mathbf{S}$ to yield the total angular momentum $\mathbf{J} = \mathbf{K} + \mathbf{S}$. (To minimize confusion, we also note the use of other popular notational conventions,[199] whereby $\mathbf{K}$ and $\mathbf{N}$ are replaced by $\mathbf{N}$ and $\mathbf{R}$, respectively.)

For the lower $^2\Sigma^+$ state with L = 0 and S = 0.5, the ground state rotational level (i.e., N = K = 0) is nondegenerate with J = 0.5 and labeled F_1. By way of contrast, there are two possible values of J for K > 0, giving rise to nearly degenerate pairs of F_1 (J = K + 0.5) and F_2 (J = K - 0.5) levels, respectively, of the same parity. Whether the F_1 state is above or below the F_2 state for the same K value must be determined experimentally, as has been done for $^2\Sigma^+$ C_2H from high precision microwave measurements.[7, 4] The ordering in Figure 6.1 is consistent with the reported ground state constants from these microwave studies, with the difference between the F_1 and F_2 levels for each K state corresponding to spin-rotation splitting in the lower electronic state. Finally, the overall parity builds on the ground electronic $^2\Sigma^+$ symmetry; thus, the K = 0 (F_1, J = 0.5) level must be + parity, with parity alternating as $(-1)^K$. Note that this implies the presence of nearly degenerate spin rotation levels of the *same parity* for any K > 0.

For the $^2\Pi$ state, energy levels are again described by rotational quantum number (J) and parity (+ or -). The $^2\Pi$ state has two manifolds of energy levels, now more widely separated due to a stronger spin-orbit interaction term in the Hamiltonian. This generates F_1 (lower) and F_2 (upper) manifolds, split roughly by the magnitude of the spin-orbit coupling

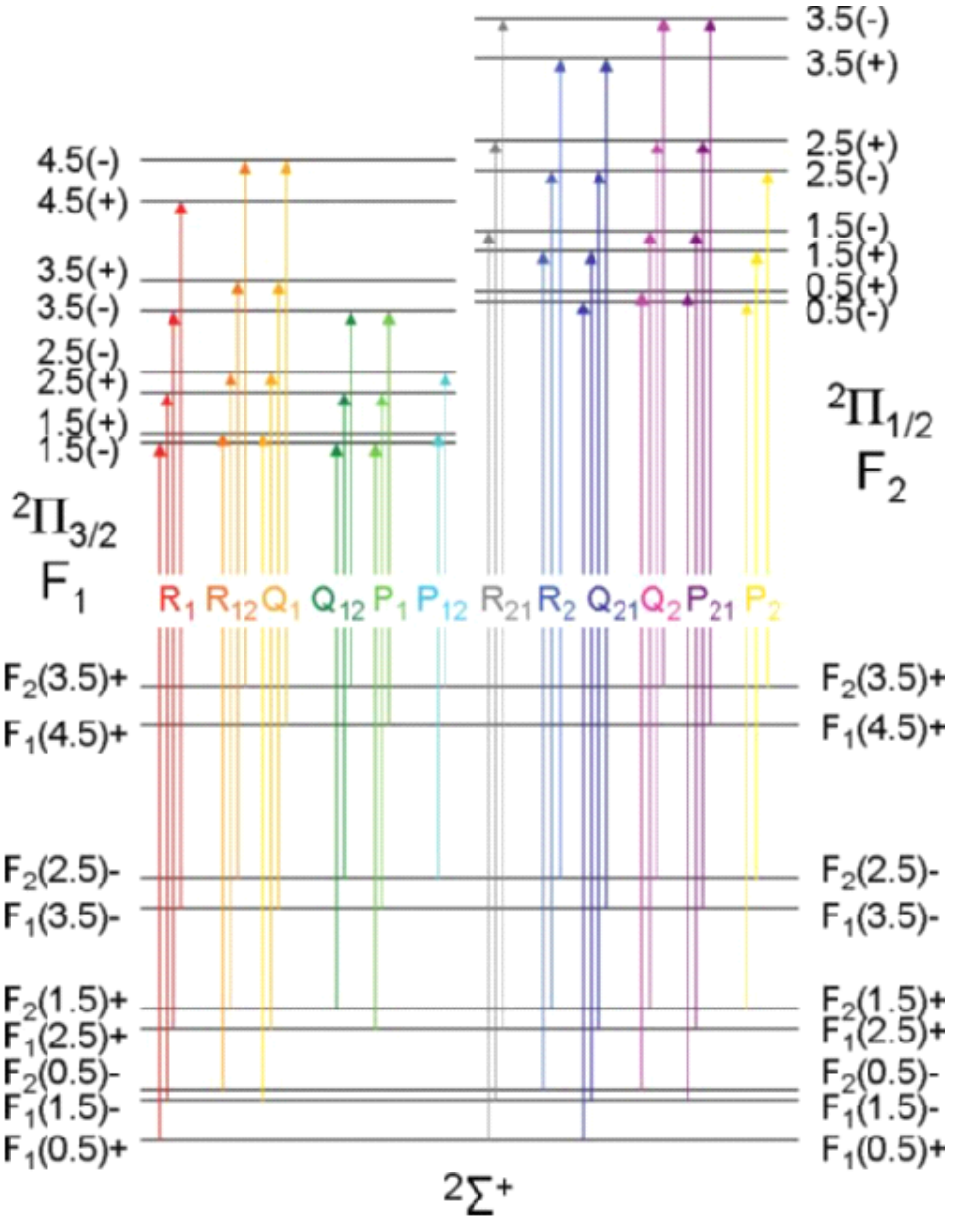

Figure 6.1: Energy level diagram for both $^2\Pi$ and $^2\Sigma^+$ states (with spacings exaggerated for the clearest view) and the possible transitions that can be observed between them. The energy levels are labeled as F_1 or F_2 levels and with the J and parity quantum numbers. The transitions are denoted with arrows and belong to one of four groups: (1) R_1 (also P_1 and Q_1), signifying transitions obeying the selection rule of $\Delta J = 1$ (for R_1 branch only) and originating from F_1 levels in the $^2\Sigma^+$ state and terminating in F_1 levels in the $^2\Pi$ state; (2) R_2 (also P_2 and Q_2), signifying transitions obeying $\Delta J = 1$ (for R_2 branch only) and originating from F_2 levels in the $^2\Sigma^+$ state and terminating in F_2 levels in the $^2\Pi$ state; (3) R_{12} (also P_{12} and Q_{12}) signifying transitions obeying the selection rule of $\Delta J = 1$ (for R_{12} branch only) and originating from F_2 levels in the $^2\Sigma^+$ state and terminating in F_1 levels in the $^2\Pi$ state; (4) R_{21} (also P_{21} and Q_{21}) signifying transitions obeying the selection rule of $\Delta J = 1$ (for R_{21} branch only) and originating from F_1 levels in the $^2\Sigma^+$ state and terminating in F_2 levels in the $^2\Pi$ state.

constant, |A|. This work confirms that the spin orbit constant A is negative for each of the four C_2H $^2\Pi$-$^2\Sigma^+$ bands; therefore, the $^2\Pi_{3/2}$ spin orbit state (F_1) lies below the $^2\Pi_{1/2}$ spin orbit state (F_2) in Figure 6.1. Every J value in a $^2\Pi$ state gives rise to two widely spaced pairs (F_1, F_2) of closely spaced energy levels of opposite parity, the difference between which corresponds to lambda-doubling in the $^2\Pi$ state. The sign of this lambda-doubling splitting and thus the ordering of parity labels in the $^2\Pi$ state can only be determined from experiment. It is important to note that the parity labeling in Figure 6.1 specifically corresponds to that which has been determined in this work for the $^2\Pi$-$^2\Sigma^+$ band observed at 3692 cm^{-1}, which differs from previous studies obtained at slightly lower resolution.

Along with the $^2\Sigma^+$ and $^2\Pi$ energy levels depicted in Figure 6.1, arrows are drawn in to illustrate all allowed transitions in a $^2\Pi$-$^2\Sigma^+$ band. While previous work of Curl et al.[19] reported observed lines from six main branches, e.g., R_i , Q_i , P_i (i = 1,2), corresponding to $\Delta J = 1, 0, -1$ transitions between F_i levels in $^2\Sigma^+$ and F_i levels in $^2\Pi$), there are also six additional branches indicated in Figure 6.1, often called satellite branches.[200] These satellite branches cross over from $F_1 \leftarrow F_2$ or $F_2 \leftarrow F_1$ and are labeled by both states accordingly. For example, R_{12} signifies transitions obeying $\Delta J = 1$ that go from F_2 levels in $^2\Sigma^+$ up to F_1 levels in $^2\Pi$. Figure 6.2 shows the predicted intensities for each of these branches, both main and satellite, as a function of J″, where predicted rotational line strengths[6] are functions of J″ and the ratio of spin-orbit coupling constant to the rotational constant, Y = A/B. The predicted intensities in Figure 6.2, therefore, reflect the A and B values determined in our analysis of the 3692 cm^{-1} $^2\Pi$-$^2\Sigma^+$ C_2H band reported herein.

It is easy from Figure 6.2 to appreciate why previous experimental studies at room temperature were relatively insensitive to these satellite transitions, with appreciable population mostly in high J″ (N″) levels.[19] The intensity drops off quickly with J for these satellite transitions, such that above J″ = 4.5, there is little observable intensity. However, there is considerable oscillator strength in the blowup region from J″ = 0.5 to J″ = 4.5 in Figure 6.2, which are preferentially populated at low rotational temperatures. Thus, it is the

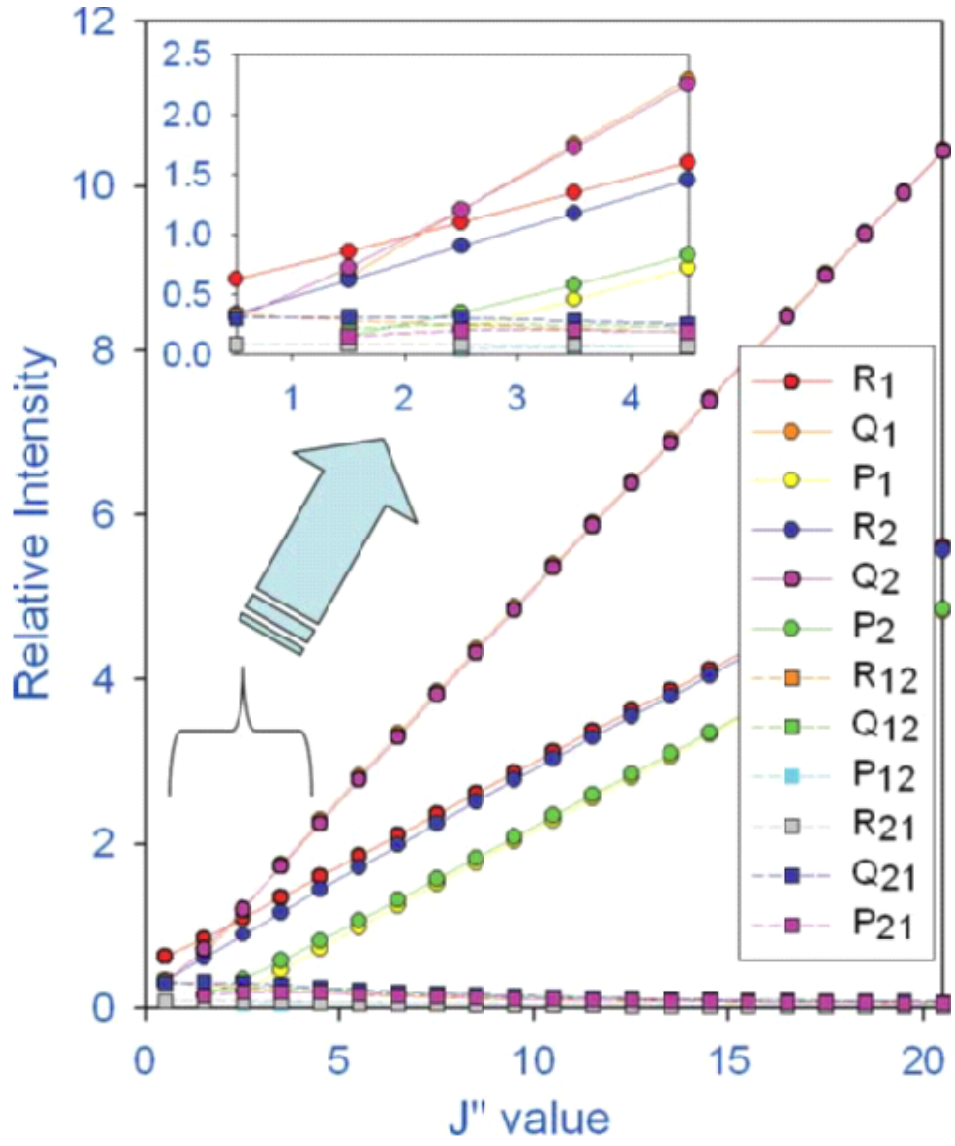

Figure 6.2: Predicted intensities for all possible transition types in $^2\Pi$-$^2\Sigma^+$ bands as a function of J″. The circle points with solid lines correspond to the main branches (R_1, P_1, Q_1, R_2, P_2, Q_2) and the square points with dashed lines correspond to the satellite branches (R_{12}, P_{12}, Q_{12}, R_{21}, P_{21}, Q_{21}).

combination of (i) jet-cooled C_2H radicals (12 K) and (ii) high resolution IR spectroscopic techniques that permits observation of both main branch and satellite branch transitions with high signal to noise (S/N). Most importantly, this permits much higher frequency pre-

cision and unambiguous assignment of the transitions, which in turn allows more detailed characterization of the upper state energy level structure.

6.3 Experiment

The approach for high sensitivity spectroscopic detection of jet-cooled hydrocarbon radicals via high resolution infrared laser absorption in a slit-jet cooled supersonic discharge source is reported elsewhere[82, 201, 1] and will be only briefly summarized here. High resolution IR light ($<$ 2 MHz linewidth) is produced by difference-frequency generation of a tunable single mode ring-dye laser (operated with R6G dye) with a fixed frequency single mode Ar^+ laser (operated at 488 nm) in a temperature-tuned, periodically poled $LiNbO_3$ (PPLN) crystal. This IR light is split onto a reference InSb detector (cooled to 77 K) and directed into the vacuum can, where it intersects the jet-cooled beam of radicals 16 times via a Herriot cell configuration, yielding an absorption path length of 64 cm (16 $\times$ 4 cm slit width). Light coming out of the vacuum can is directed onto a signal InSb detector (also cooled to 77 K), with transient absorption detected by the differential change in signal minus reference beam IR power, synchronous with the 50 kHz modulation of the slit valve pulsed discharge. Absorption sensitivity is achieved by fast electronic subtraction of common-mode amplitude noise on the laser beam as well as by phase sensitive lock-in detection at the 50 kHz dc discharge modulation frequency. Relative frequencies are obtained to 10 MHz precision via a λ-meter and fringe interpolation from the transmission of a marker cavity with a free spectral range of 250 MHz, whose free spectral range is stabilized absolutely by locking onto a polarization stabilized HeNe laser. Absolute frequencies are obtained with respect to known reference lines of stable molecules. Specifically, for the 3692 and 3786 cm^{-1} bands, the $1_{11} \leftarrow 0_{00}$ ($\nu_1 = 1 \leftarrow 0$) and $1_{01} \leftarrow 0_{00}$ ($\nu_3 = 1 \leftarrow 0$) reference transitions of H_2O at 3600.95753 and 3779.49376 cm^{-1} are used, whereas for the 4012 and 4108 cm^{-1} bands, the R(0) and R(1) transitions of HF($\nu = 1 \leftarrow 0$) at 4000.9894 and 4109.9363 cm^{-1} provide a suitable absolute frequency reference.[202, 203]

Jet-cooled C_2H radicals are produced by adiabatically expanding a mixture of $\approx 0.04\%$ acetylene in a 70%:30% neon. helium buffer gas through a pulsed slit-jet (operated at 19 Hz, $\approx$ 1 ms pulse duration), with a square wave modulated discharge (50 kHz) to form radicals by collisional electron induced dissociation. Optimum discharge conditions are 0.2 A and -450 V bias, utilizing lock-in detection in order to extract the absorption signal component synchronous with the modulation. For the C_2H lines reported herein, the slit-jet cooled discharge source yields absorbances from 0.01% to as high as 0.5% on the strongest C_2H lines. With typical rms noise levels of 0.0025% in a 10 kHz detection bandwidth, this translates into signal to noise ratios of 4:1 on the weakest and 200:1 on the strongest lines.

6.4 Results

6.4.1 3600 cm^{-1} Band

Figure 6.3 shows sample data for the C_2H $\tilde{A}^2\Pi \leftarrow \tilde{X}^2\Sigma^+$ origin band centered around 3600 cm^{-1} taken with the high resolution slit-jet infrared spectrometer. The black trace is the experimental data, while the red and pink traces are inverted simulations of the origin band, using different Hamiltonian models for the $^2\Pi$ state in each discussed in more detail later (see Section 6.5.1). The predicted intensities of the simulated lines correspond to the product of a rotational line strength factor[6] and a Boltzmann factor for a rotational temperature of 12 K. Lines from three different branches appear in the sample data, those of R_1 and Q_2 (main branches), as well as P_{21} (satellite branch). As evident in Figure 6.1, the P_{21} lines appear as blue-shifted shoulders to the corresponding Q_2 lines. Typical transitions correspond to sub-Doppler absorptions with essentially Gaussian profiles and an experimental linewidth of roughly 60 MHz. The transitions, which are comprised of two overlapping features (e.g., one main branch line and one satellite line in most cases), are least squares fit to a superposition of two Gaussian profiles, which also yields a comparable roughly 60 MHz sub-Doppler linewidth.

Table 6.1: Experimental lines observed in the 3600 cm^{-1} $^2\Pi$-$^2\Sigma^+$ band (all frequencies in cm^{-1}).

J″	N″	R_1	R_{12}	Q_1	Q_{12}	P_1	R_2	Q_{21}	Q_2	P_{21}	P_2
0.5	0	3598.9852	3596.0801				3607.2254	3605.3733	3602.4637		
1.5	1	3602.2549	3596.4603	3596.0822	3590.2412			3607.2286	3601.4132	3602.4657	3596.6281
2.5	2	3605.2336	3596.5677	3596.4654	3587.6815	3590.2461	3611.3015	3611.3091	3600.5101	3601.4187	3592.6550
3.5	3	3607.9834		3596.5751		3587.6888	3613.3711	3613.3801	3599.3240 3600.1404	3600.5160	
4.5	4	3610.5429		3596.4721					3599.0963	3599.3330 3600.1494	

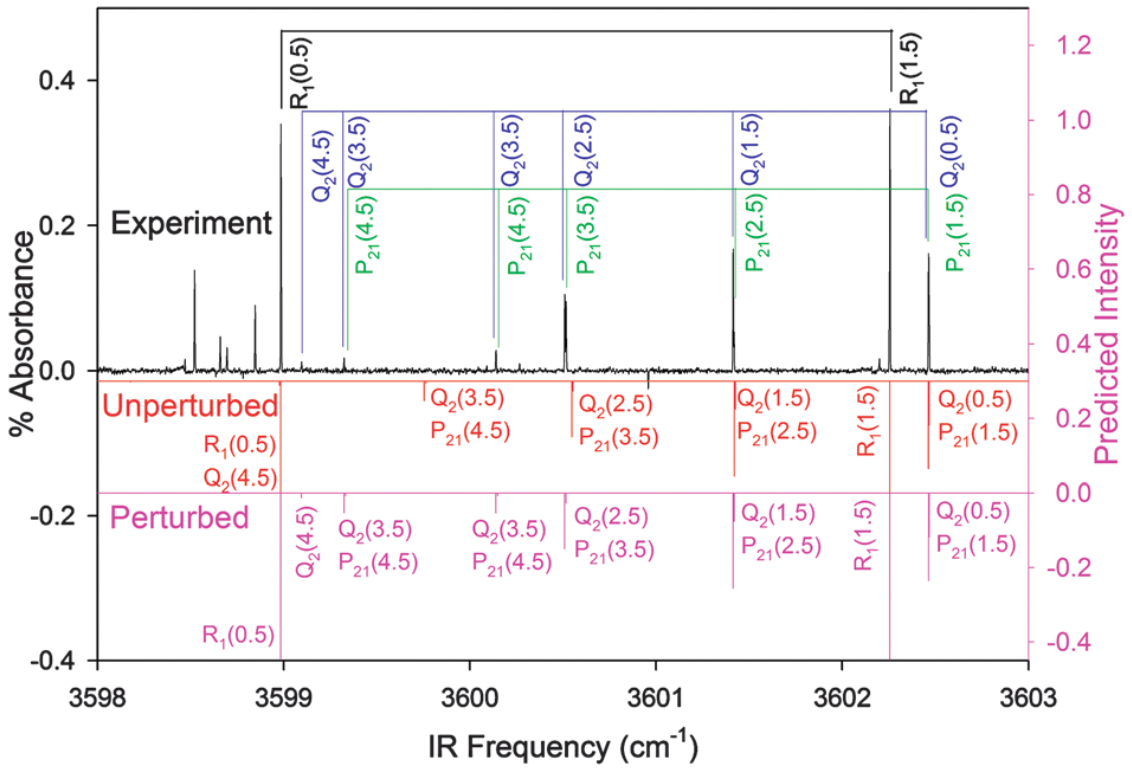

Figure 6.3: Sample experimental data for the 3600 cm^{-1} band. In this 5 cm^{-1} region, lines from the R_1 and Q_2 main branches were observed, as well as lines from the P_{21} satellite branch. The downward going red lines were simulated using our refined excited state constants from Table 6.11 (column 4, excluding the Coriolis coupling perturbation parameters), the ground state constants determined from previous microwave studies[4], and the energy level expressions for the unperturbed $^2\Sigma^+$ ground state and $^2\Pi$ excited state Hamiltonian models discussed in Section 6.5.1. The downward going pink lines were simulated similarly using our refined excited state constants from Table 6.11 (column 4), now including the perturbation parameters (β_0, ν_{pert} and B_{pert}) and the perturbative $\Sigma - \Pi$ Coriolis coupling as discussed in Section 6.5.3. The predicted intensities in both the red and pink traces were calculated using rotational line strength factors for $^2\Pi$-$^2\Sigma^+$ bands[5] and a Boltzmann factor for a rotational temperature of 12 K, to be the temperature achieved for our C_2H radicals produced in a slit-discharge of C_2H_2 coupled with supersonic expansion.

Table 6.1 lists the observed line positions for the $^2\Pi$-$^2\Sigma^+$ origin band. All frequencies reported in this paper represent an average of three measurements for each experimental line, with a standard deviation of approximately 10 MHz in the three measurements. In Table 6.1, individual rovibrational lines from each of the six main branches are reported, as well as from

four of the six possible satellite branches (all observed branches are pictured in Figure 6.1). Assignments of the observed lines are confirmed by using two-line ground state combination differences, based on the previous high accuracy microwave studies.[7, 4] Table 6.2 shows all possible 2-line combination differences of the observed lines in Table 6.1, and compares these to the corresponding ground state energy level differences (calculated using B, D, and γ constants determined from microwave studies). The experimental combination differences agree with the ground state energy level differences < 20 MHz in most cases. It should be noted that there are two lines reported in Tables 6.1 and 6.2 for both $Q_2(3.5)$ and $P_{21}(4.5)$. Curl and coworkers[182] similarly reported two $Q_2(3.5)$ lines, which they attributed to the presence of a local perturbation with a crossing at $N' = 4$. Assignments in the present case are further confirmed by ground-state combination differences, which agree with microwave predictions to better than 10 MHz for both pairs of lines. The implications of the multiple line shifts in this curve crossing at $J' = 3.5$ (or $N' = 4$) will be discussed in more detail in Section 6.5.3.

6.4.2 3692 cm^{-1} Band

Figure 6.4 shows sample data for the $^2\Pi$-$^2\Sigma^+$ band centered around 3692 cm^{-1} taken with the high resolution slit-jet discharge infrared spectrometer. The black trace is experimental data, while the inverted red trace is a simulation of the 3692 cm^{-1} band, based on (i) revised excited state constants from this work discussed in more detail later in Sec. 6.5 and (ii) ground state energy levels from previous microwave studies.[7, 4, 173] The intensities of the simulated lines are obtained from the product of (i) rotational line strengths[6] and (ii) jet cooled populations for a rotational temperature of 12 K determined from the Boltzmann analysis of the data (see Figure 6.5). Lines from four different branches appear in this sample data scan, that of R_1 and Q_2 (main branches) as well as Q_{21} and P_{21} (satellite branches). Most of the observed satellite branch transitions appear as weak shoulders to main branch transitions, which confirms why these were not resolved/observed in previous

Table 6.2: Experimental combination differences for the 3600 cm^{-1} $^2\Pi$-$^2\Sigma^+$ band compared with ground state energy level differences.

Lines	J″	ν (cm^{-1})	Comb. Diff. ($\Delta\nu$) (cm^{-1})	E″ (cm^{-1})	ΔE″ (cm^{-1})	$\Delta\nu$-ΔE″ (MHz)
$R_1(0.5)$	0.5	3598.9852	8.7391	0	8.738737	10
$P_1(2.5)$	2.5	3598.2461		8.738737		
$R_1(1.5)$	1.5	3602.2549	14.5661	2.912593	14.565668	12
$P_1(3.5)$	3.5	3587.6888		17.478260		
$R_1(0.5)$	0.5	3598.9852	8.7440	0	8.743957	3
$Q_{12}(1.5)$	1.5	3590.2412		8.743957		
$R_1(1.5)$	1.5	3602.2549	14.5733	2.912593	14.572977	10
$Q_{12}(2.5)$	2.5	3587.6815		17.485569		
$P_1(2.5)$	2.5	3590.2461	0.0050	8.738737	0.005221	-8
$Q_{12}(1.5)$	1.5	3590.2412		8.743957		
$P_1(3.5)$	3.5	3587.6888	0.0073	17.478260	0.007309	-1
$Q_{12}(2.5)$	2.5	3587.6815		17.485569		
$Q_1(1.5)$	1.5	3596.0822	0.0021	2.912593	0.003132	32
$R_{12}(0.5)$	0.5	3596.0801		2.915725		
$Q_1(2.5)$	2.5	3596.4654	0.0051	8.738737	0.005221	-3
$R_{12}(1.5)$	1.5	3596.4603		8.743957		
$Q_1(3.5)$	3.5	3596.5751	0.0074	17.478260	0.007309	3
$R_{12}(2.5)$	2.5	3596.5677		17.485569		
$R_2(0.5)$	0.5	3607.2254	14.5704	2.915725	14.569844	16
$P_2(2.5)$	2.5	3592.6550		17.485569		
$R_2(0.5)$	0.5	3607.2254	0.0032	2.915725	0.003132	1
$Q_{21}(1.5)$	1.5	3607.2286		2.912593		
$R_2(2.5)$	2.5	3611.3015	0.0076	17.485569	0.007309	9
$Q_{21}(3.5)$	3.5	3611.3091		17.478260		
$R_2(3.5)$	3.5	3613.3711	0.0091	29.140304	0.009397	-10
$Q_{21}(4.5)$	4.5	3613.3801		29.130907		
$P_2(1.5)$	1.5	3596.6281	8.7452	8.743957	8.743957	37
$Q_{21}(0.5)$	0.5	3605.3733		0		
$P_2(2.5)$	2.5	3592.6550	14.5735	17.485569	14.572977	17
$Q_{21}(1.5)$	1.5	3607.2286		2.912593		
$Q_2(0.5)$	0.5	3602.4637	0.0020	2.915725	0.003132	-34
$P_{21}(1.5)$	1.5	3602.4187		2.912593		
$Q_2(1.5)$	1.5	3601.4132	0.0052	8.743957	0.005221	9
$P_{21}(2.5)$	2.5	3601.4187		8.738737		
$Q_2(2.5)$	2.5	3600.5101	0.0059	17.485569	0.007309	-43
$P_{21}(3.5)$	3.5	3600.5160		17.478260		
$Q_2(3.5)$	3.5	3599.3240	0.0090	29.140304	0.009397	-11
$P_{21}(4.5)$	4.5	3599.3330		29.130907		
$Q_2(3.5)$	3.5	3600.1404	0.0090	29.140304	0.009397	-11
$P_{21}(4.5)$	4.5	3600.1494		29.130907		

[a] The ground state energy levels were calculated using the B, D and γ constants from previous microwave studies[7, 4].

gas-phase experimental studies.[18, 19] It is straightforward to predict from Figure 6.1 that the P_{21} progression should appear as blue-shifted shoulders on the Q_2 progression, with the

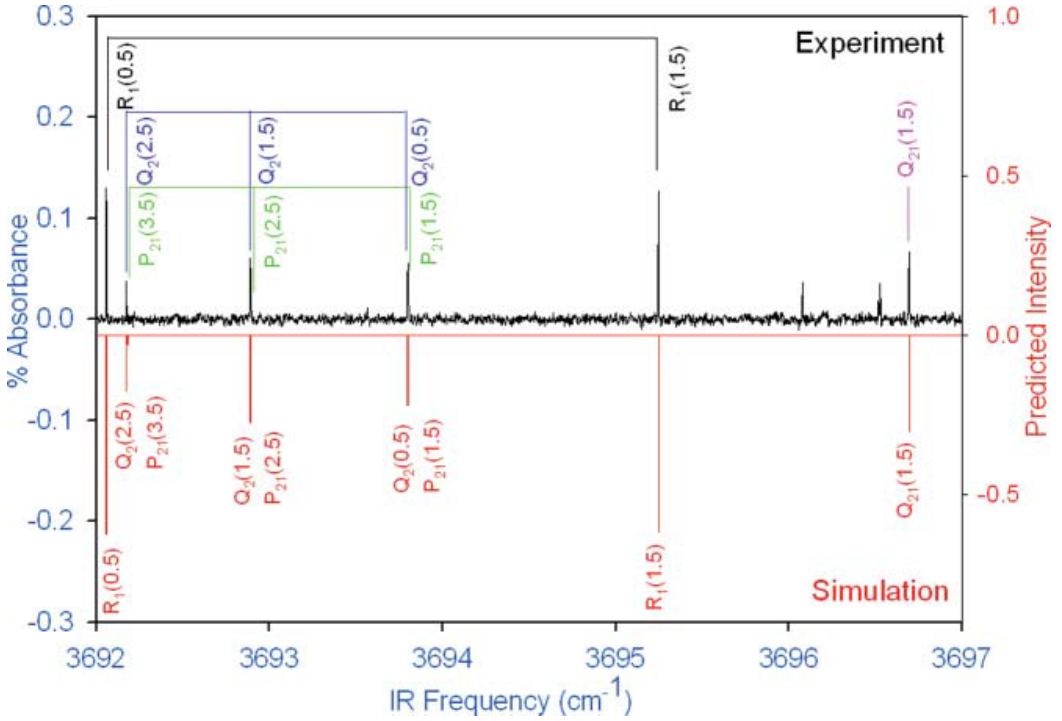

Figure 6.4: Sample experimental data for the 3692 cm^{-1} band. In this 5 cm^{-1} region, lines from the R_1 and Q_2 main branches were observed, as well as lines from the P_{21} and Q_{21} satellite branches. The downward going lines were simulated using our refined excited state constants from Table 6.8, the ground state constants determined from previous microwave studies[4], and the matrix elements for the Hamiltonian discussed in Section 6.5.1. The predicted intensities were calculated using rotational line strength factors for $^2\Pi$-$^2\Sigma^+$ bands[6] and a Boltzmann factor for a rotational temperature of 12 K.

difference between $Q_2(0.5)$ and $P_{21}(1.5)$ lines, for example, equaling spin-rotation splitting in the K = 1 $^2\Sigma^+$ ground state level. Blowup examples for each type of satellite line are shown in Figs. 6.6 and 6.8 for two other $^2\Pi$-$^2\Sigma^+$ bands centered around 3786 and 4107 cm^{-1}, respectively. Typical linewidths correspond to sub-Doppler absorption profiles, i.e., Gaussian fits determine an experimental linewidth of roughly 60 MHz and frequency precision of approximately 10 MHz in the Ne/He expansion. Those transitions comprised of an overlap of two lines (one main branch line and one satellite line in most cases) are well-represented by

a simple superposition of two Gaussian profiles with individual linewidths of approximately 60 MHz.

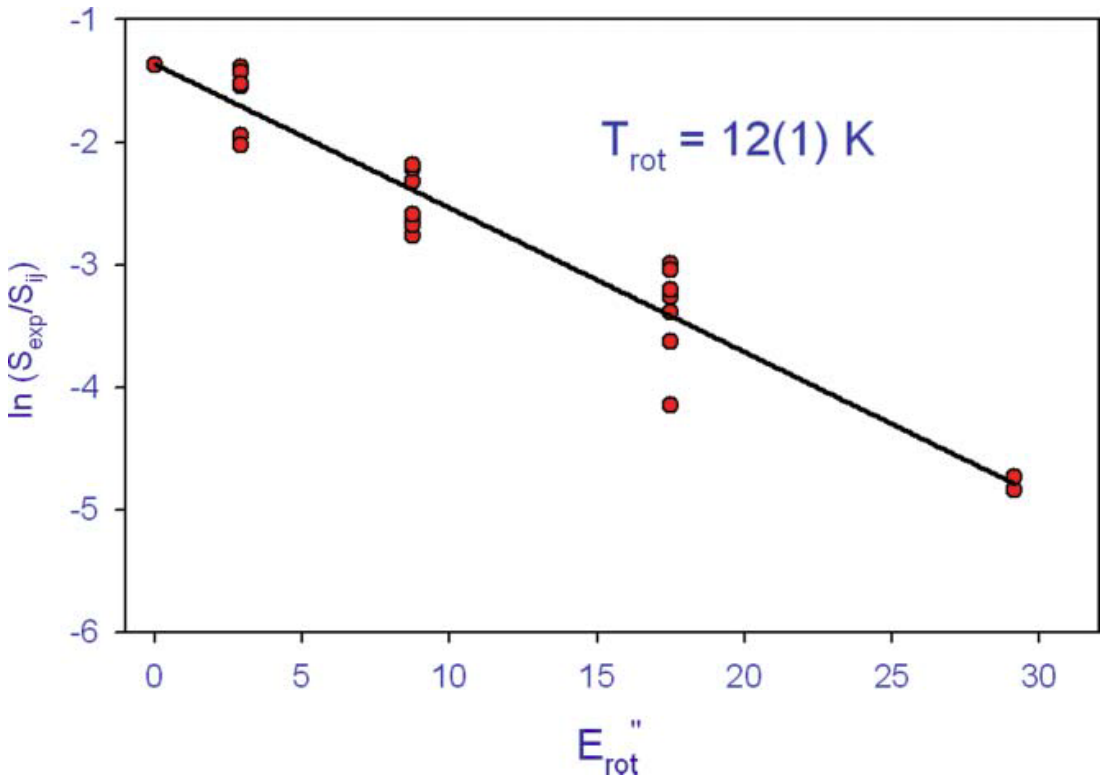

Figure 6.5: Boltzmann plot for the 3692 cm^{-1} band. S_{exp} are the experimental intensities (in % absorbance) and S_{ij} are the rotational line strength factors from Zare[6]. E''_{rot} was calculated using the ground state microwave constants[7, 4] and the appropriate energy level expressions for a $^2\Sigma^+$ state (see Section 6.5.1. The points were fit to a line, whose slope is equal to -1/kT.

Table 6.3 lists line positions for the $^2\Pi$-$^2\Sigma^+$ band centered around 3692 cm^{-1} observed in this work. Frequencies reported represent an average of three measurements for each experimental line, with a typical rms standard deviation of $\approx$ 10 MHz. From inspection of Table 6.3, individual rovibrational lines from each of the six main branches are observed as well as from four of the six possible satellite branches. Transitions from the P_{12} and R_{21} branches are not seen which were predicted to have the lowest transition intensities even at low J″ (see Figure 6.2). Since the ground state is known to high accuracy,[7, 4]

assignments of observed lines can be unambiguously confirmed by using two-line ground state combination differences. Table 6.4 displays all possible combination differences from the observed lines listed in Table 6.3, compared against corresponding ground state energy level differences from microwave studies.[7, 4] The experimental combination differences (CD) agree with precision ground state energy level differences to $\approx$ 10 MHz rms, with 19 out of 20 2-line CD's $<$ 20 MHz. Indeed, the only 2-line CD in excess of 20 MHz involves the weakest satellite line $R_{12}(2.5)$ at the S/N limit, which introduces an additional 20-30 MHz uncertainty in determining frequency differences.

Figure 6.5 shows a Boltzmann plot of the peak absorbance data used to determine the rotational temperature of the slit-jet generated C_2H radicals, which yields a rotational temperature of 12(1) K. A corresponding plot based on integrated versus peak intensities yields a rotational temperature of 11(1) K, i.e., the same within experimental uncertainty. This rapid drop off in population with energy at such low rotational temperatures explains why lines higher than $J'' = 4.5$ are not observed. However, the resulting lower spectral congestion and higher resolution provide valuable new information on C_2H, as described in more detail in Sec. 6.5.

It is also of interest to predict the radical densities at the slit jet orifice, based on a total absorbance of A = 0.0048(1) summed over all lines. The integrated cross-section per mole for this band, as calculated by Tarroni and Carter,[9] is 302 km/mol, which implies 5.0×10^{-17} cm/molecule or a peak cross section of 2.5×10^{-14} cm^2/molecule for a typical 60 MHz sub-Doppler linewidth. Based on a 64 cm Herriot cell absorption path length (4 cm $\times$ 16 passes), Beer's law predicts the concentration of C_2H radicals in the probe region to be $\approx 3.0 \times 10^9$ radicals/cm^3. If we correct for the 1/r drop off of radical density 5-10 mm downstream from a 300 μm slit width, this translates into roughly 10^{11} radicals/cm^3 at the slit orifice. This is notably lower than the 10^{14} radicals/cm^3 densities often observed from electron dissociative attachment of alkyl halides in the slit jet expansion, likely, due to C_2H being rapidly lost by reactive collisions with acetylene to make longer carbon chain

Table 6.3: Experimental lines observed in the 3692 cm^{-1} $^2\Pi$-$^2\Sigma^+$ band (all frequencies in cm^{-1}).

J″	N″	R_1	R_{12}	Q_1	Q_{12}	P_1	R_2	Q_{21}	Q_2	P_{21}	P_2
0.5	0	3692.0582	3689.1566				3698.6620	3696.6940	3693.8000		
1.5	1	3695.2475	3689.4632	3689.1587	3683.3140		3700.8051	3698.6650	3692.8900	3693.8020	3687.9497
2.5	2	3698.1755	3689.5308	3689.4685	3680.6747	3683.3196	3703.0102	3700.8098	3692.1739	3692.8956	3684.0917
3.5	3	3700.9092		3689.5367		3680.6822		3703.0175	3691.5404	3692.1807	
4.5	4	3703.4859		3689.4304							

Table 6.4: Experimental combination differences for the 3692 cm^{-1} $^2\Pi$-$^2\Sigma^+$ band compared with ground state energy level differences.

Lines	J″	ν (cm^{-1})	Comb. Diff. ($\Delta\nu$) (cm^{-1})	E″ (cm^{-1})	ΔE″ (cm^{-1})	$\Delta\nu$-ΔE″ (MHz)
$R_1(0.5)$	0.5	3692.0582	8.7386	0	8.738737	-4
$P_1(2.5)$	2.5	3683.3196		8.738737		
$R_1(1.5)$	1.5	3695.2475	14.5652	2.912593	14.565668	-1
$P_1(3.5)$	3.5	3680.6822		17.478260		
$R_1(0.5)$	0.5	3692.0582	8.7443	0	8.743957	9
$Q_{12}(1.5)$	1.5	3683.3140		8.743957		
$R_1(1.5)$	1.5	3695.2475	14.5728	2.912593	14.572977	-6
$Q_{12}(2.5)$	2.5	3680.5747		17.485569		
$P_1(2.5)$	2.5	3683.3196	0.0057	8.738737	0.005221	13
$Q_{12}(1.5)$	1.5	3683.3140		8.743957		
$P_1(3.5)$	3.5	3680.6822	0.0076	17.478260	0.007309	8
$Q_{12}(2.5)$	2.5	3680.6747		17.485569		
$Q_1(1.5)$	1.5	3689.1587	0.0021	2.912593	0.003132	30
$R_{12}(0.5)$	0.5	3689.1566		2.915725		
$Q_1(2.5)$	2.5	3689.4685	0.0053	8.738737	0.005221	2
$R_{12}(1.5)$	1.5	3689.4632		8.743957		
$Q_1(3.5)$	3.5	3689.5367	0.0060	17.478260	0.007309	-41
$R_{12}(2.5)$	2.5	3689.5308		17.485569		
$R_2(0.5)$	0.5	3698.6620	14.5703	2.915725	14.56984	14
$P_2(2.5)$	2.5	3684.0917		17.485569		
$R_2(0.5)$	0.5	3698.6620	0.0030	2.915725	0.003132	-5
$Q_{21}(1.5)$	1.5	3698.6650		2.912593		
$R_2(1.5)$	1.5	3700.8051	0.0047	8.743957	0.005221	-17
$Q_{21}(2.5)$	2.5	3700.8098		8.738737		
$R_2(2.5)$	2.5	3703.0102	0.0073	17.485569	0.007309	0
$Q_{21}(3.5)$	3.5	3702.0175		17.478260		
$P_2(1.5)$	1.5	3687.9497	8.7443	8.743957	8.743957	11
$Q_{21}(0.5)$	0.5	3696.6940		0		
$P_2(2.5)$	2.5	3684.0917	14.5733	17.485569	14.57298	10
$Q_{21}(1.5)$	1.5	3698.6650		2.912593		
$Q_2(0.5)$	0.5	3693.8000	0.0021	2.915725	0.003132	-32
$P_{21}(1.5)$	1.5	3693.8020		2.912593		
$Q_2(1.5)$	1.5	3692.8900	0.0056	8.743957	0.005221	11
$P_{21}(2.5)$	2.5	3692.8956		8.738737		
$Q_2(2.5)$	2.5	3692.1739	0.0068	17.485569	0.007309	-16
$P_{21}(3.5)$	3.5	3692.1807		17.478260		

[a] The ground state energy levels were calculated using the B, D and γ constants from microwave studies[7, 4].

species such as C_4H, C_6H, etc. In any event, the densities are clearly high enough to achieve excellent signal to noise on all $^2\Pi$-$^2\Sigma^+$ rovibrational bands reported in this work.

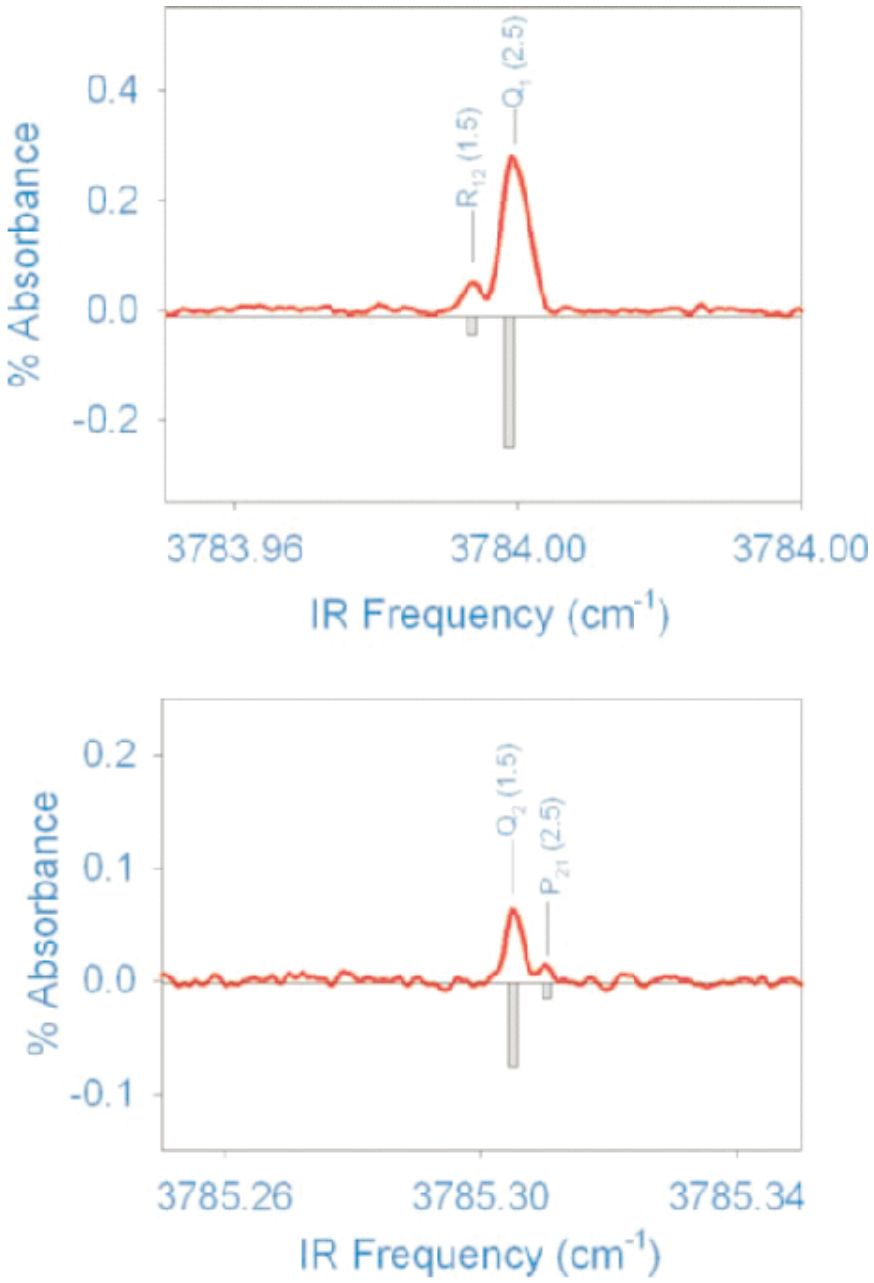

Figure 6.6: Sample data for the 3786 cm^{-1} band showing blow-ups of satellite transitions appearing as shoulders to main branch transitions. The downward going vertical bars represent simulations of each peak, with predicted frequency positions determined from excited state constants from Table 6.9, the ground state constants from previous microwave studies,[4] and the corresponding Hamiltonian expressions discussed in Sec. 6.5.1 for the $^2\Sigma^+$ and $^2\Pi$ states.

6.4.3 3786 cm^{-1} Band

Figure 6.6 shows sample data for the $^2\Pi$-$^2\Sigma^+$ vibronic band observed near 3786 cm^{-1} via high resolution IR absorption spectroscopy, with examples of stronger and weaker transitions. The two panels each show two lines corresponding to main and satellite branch transitions. For example, the top panel shows the main branch line, $Q_1(2.5)$, with the satellite branch line, $R_{12}(1.5)$, appearing as a red-shifted shoulder to the Q_1 line. From Figure 6.1, these two transitions terminate in the same $J' = 2.5$ level in the $^2\Pi_{3/2}$ upper state, and therefore they are spaced by the ground state spin-rotation splitting in $K'' = 2$. The downward going gray vertical bars represent simulations of each peak, where predicted frequency positions are determined from the excited state constants in Table 6.9 (column 2), the ground state constants from previous microwave studies,[4] and the appropriate matrix element expressions discussed in Sec. 6.5 for the $^2\Sigma^+$ and $^2\Pi$ states. The intensities of the simulated vertical bars are determined from the product of rotational line strength [6] and Boltzmann factors at T = 12 K, with Table 6.5 summarizing all observed lines in this band. As discussed in Sec. 6.4, the assignments of these lines are confirmed by 2-line combination differences, which agree with microwave predictions[7, 4] to approximately 10 MHz rms.

6.4.4 4012 cm^{-1} Band

Figure 6.7 shows sample high resolution IR data for the $^2\Pi$-$^2\Sigma^+$ vibronic band centered around 4012 cm^{-1}. The black and red traces reflect experimental data and simulation, the details of which will be discussed in Sec. 6.5. Briefly, the predicted frequency positions are determined from least squares fitted excited state constants reported in Table 6.9 (column 3) and ground state constants from previous microwave studies,[4] with predicted intensities based on line strengths and Boltzmann population analysis. The assignments of these lines (summarized in Table 6.6) are confirmed by 2-line combination differences, which agree to $\leq$ 20 MHz (10 MHz rms) with ground state energy level differences from microwave studies.[7, 4]

Table 6.5: Experimental lines observed in the 3786 cm^{-1} $^2\Pi$-$^2\Sigma^+$ band (all frequencies in cm^{-1}).

J″	N″	R_1	R_{12}	Q_1	Q_{12}	P_1	R_2	Q_{21}	Q_2	P_{21}	P_2
0.5	0	3786.7216	3783.8552				3790.9716	3788.7031	3785.8444		
1.5	1	3789.6689	3783.9937	3783.8582	3777.9776		3793.3720	3790.9739	3785.3050	3785.8468	3779.9588
2.5	2	3792.4220		3783.9995		3777.9840	3795.7700	3793.3773	3784.9551	3785.3101	
3.5	3	3795.0307						3795.7767	3784.6580	3784.9627	
4.5	4			3783.9134						3784.6626	

Interestingly, the higher signal to noise in Figure 6.7 reveals several strong lines in the black trace neither due to C_2H nor the precursor acetylene molecule C_2H_2. Given the reactivity of C_2H and its proclivity to form longer chain species with C_2H_2, this is not surprising. Indeed, C_2H in the jet will lead to a range of possible radicals as well as stable long chain hydrocarbon species. As an evidence of this, for example, we have obtained high resolution jet-cooled spectra of larger chain species such as diacetylene and triacetylene, which are currently under analysis. The presence of such C_4 and C_6 species provides evidence for rich bimolecular chemistry taking place, even on the 5-10 μs time scale of the slit jet expansion reaching the laser probe region.

6.4.5 4107 cm^{-1} Band

Figure 6.8 shows sample data for the final $^2\Pi$-$^2\Sigma^+$ band presented in this work. The two panels in Figure 6.8 each show two experimentally observed lines, one line corresponding to a main branch transition and one to a satellite branch transition (the upper panel shows two members of a progression). The downward going gray vertical bars represent simulations of each peak, where the predicted frequencies are determined using the excited state constants from Table 6.9 (column 4), the ground state constants from previous microwave studies,[4] and the appropriate matrix element expressions discussed in Sec. 6.5 for the $^2\Sigma^+$ and $^2\Pi$ states. Intensities are determined from rotational line strengths[6] and Boltzmann factors at T = 12 K. Observed lines are listed in Table 6.7, where assignments have been confirmed by 2-line combination differences which agree to $\leq$ 20 MHz (10 MHz rms). This band is the strongest of the four reported in this study, which permits us to observe transitions out to $J'' = 5.5$. Even at S:N $\approx$ 200:1 for the strongest lines, we still do not observe either the P_{12} or R_{21} satellite branches, which are predicted from Figure 6.2 to be the weakest.

Table 6.6: Experimental lines observed in the 4012 cm^{-1} $^2\Pi$-$^2\Sigma^+$ band (all frequencies in cm^{-1}).

J″	N″	R_1	R_{12}	Q_1	Q_{12}	P_1	R_2	Q_{21}	Q_2	P_{21}	P_2
0.5	0	4013.0237	4010.1831				4017.1221	4014.7656	4011.9363		
1.5	1	4015.9505	4010.3518	4010.1849	4004.2798		4019.6241	4017.1243	4011.5397	4011.9384	4006.0219
2.5	2	4018.7740	4010.5068	4010.3567	4001.3785	4004.2849	4022.1393	4019.6291	4011.3739	4011.5447	4002.5515
3.5	3	4021.4712		4010.5140		4001.3851			4011.3020	4011.3813	
4.5	4			4010.6225							

Table 6.7: Experimental lines observed in the 4107 cm^{-1} $^2\Pi$-$^2\Sigma^+$ band (all frequencies in cm^{-1}).

J″	N″	R_1	R_{12}	Q_1	Q_{12}	P_1	R_2	Q_{21}	Q_2	P_{21}	P_2
0.5	0	4108.1850	4105.3033				4113.0433	4110.9019	4108.0465		
1.5	1	4111.1875	4105.4674	4105.3054	4099.4415		4115.3346	4113.0453	4107.3677	4108.0484	4102.1579
2.5	2	4113.9629	4105.4490	4105.4720	4096.6149	4099.4460	4117.6418	4115.3396	4106.8849	4107.3725	4098.4727
3.5	3	4116.5719		4105.4559		4096.6220	4119.9066	4117.6488	4106.4642	4106.8924	4094.9383
4.5	4	4119.0456		4105.3186		4093.5710	4122.1030		4106.0492		
5.5	5			4105.0915							

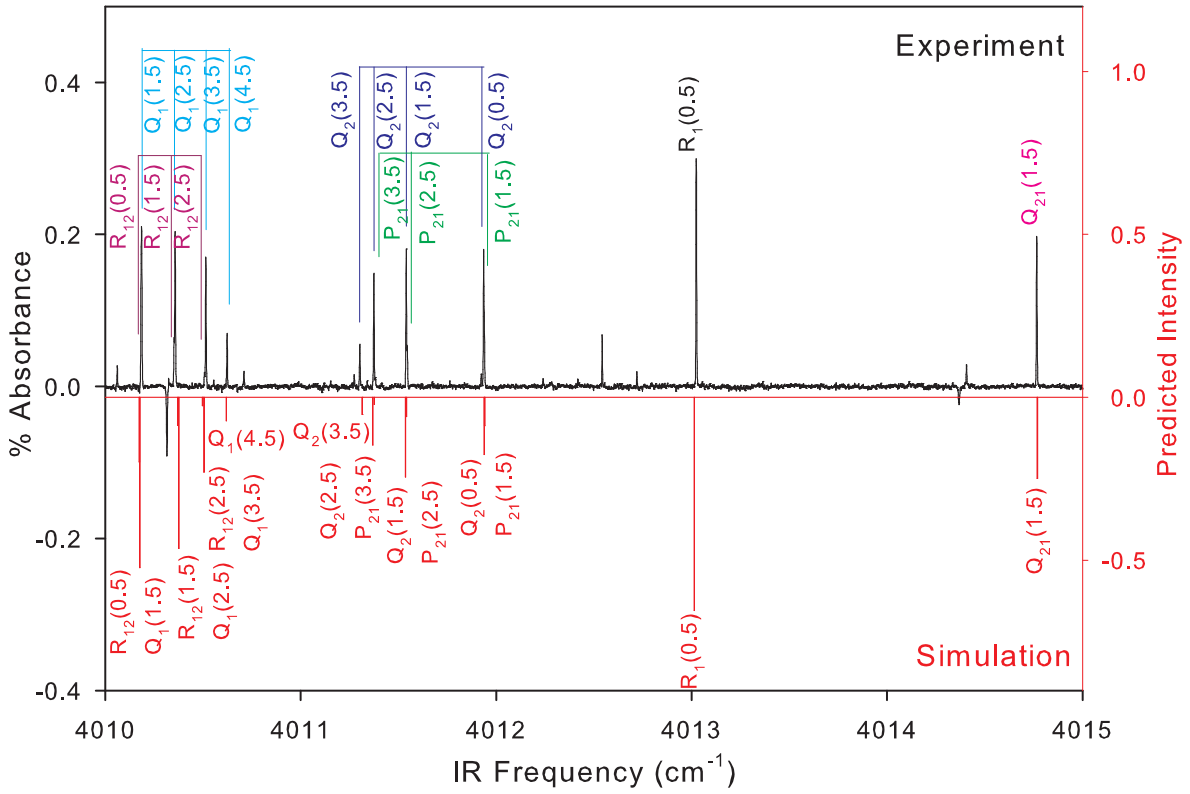

Figure 6.7: Sample experimental data for the 4012 cm^{-1} band. In this 5 cm^{-1} region, lines from the R_1, Q_1, and Q_2 main branches were observed, as well as lines from the R_{12}, P_{21}, and Q_{21} satellite branches. The downward going lines were simulated using our refined excited state constants from Table 6.8, the ground state constants determined from previous microwave studies[4], and the matrix elements for the Hamiltonian discussed in Section 6.5.1. The predicted intensities were calculated using rotational line strength factors for $^2\Pi$-$^2\Sigma^+$ bands[6] and a Boltzmann factor for a rotational temperature of 12 K.

6.5 Analysis

6.5.1 Hamiltonian

The effective Hamiltonian used for fitting the ground $^2\Sigma^+$ state is

$$H = BN^2 - DN^4 + \gamma(N \cdot S) \tag{6.4}$$

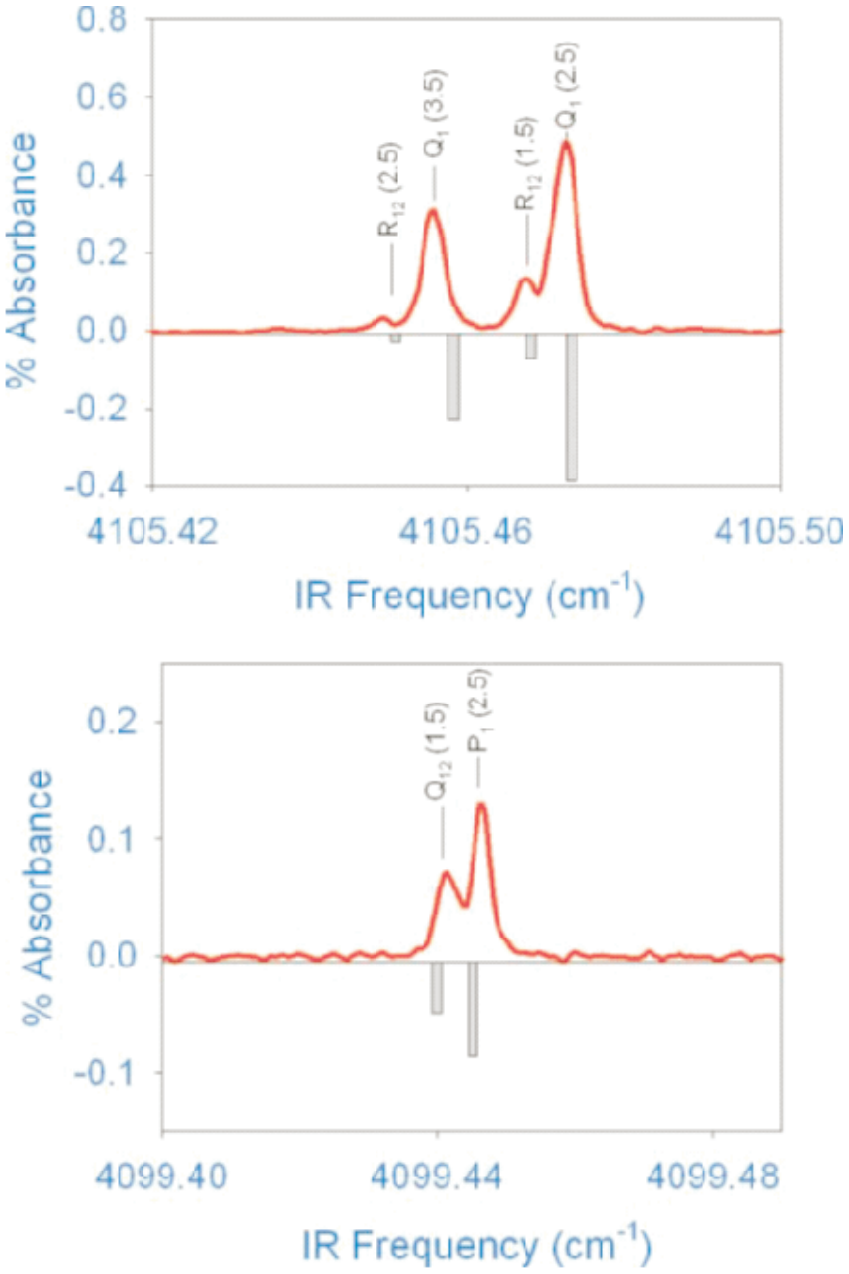

Figure 6.8: Sample data for the 4107 cm^{-1} band showing blow-ups of individual satellite transitions appearing as shoulders to individual main branch transitions. The downward going gray vertical bars represent simulations of each peak, whereby the predicted frequency positions were determined using the excited state constants from Table 6.8, the ground state constants from microwave studies[4], and the Hamiltonian expressions discussed in Section 6.5.1 for the $^2\Sigma^+$ and $^2\Pi$ states. The intensities of the vertical bars were determined from a rotational line strength factor[6] and a Boltzmann factor for T = 12 K.

which gives the following energy level expressions

$$E(F_1) = BN(N+1) - DN^2(N+1)^2 + \gamma N/2 \tag{6.5}$$

$$E(F_2) = BN(N+1) - DN^2(N+1)^2 - \gamma(N+1)/2 \tag{6.6}$$

Since the B″, D″, and γ'' rotational and spin-rotational ground state constants have been determined to high accuracy from microwave data, we simply fix these to the literature values[4] in all fits, namely, B″ = 1.456 825 10, D″ = 3.519 60 × 10^{-6}, and γ'' = -0.002 088 45 cm^{-1}.

The Hamiltonian utilized for fitting the upper $^2\Pi$ state is[199]

$$H = H_{rot} + H_{so} + H_{sr} + H_{LD} \tag{6.7}$$

$$H_{rot} = BR^2, \text{ where } R = ((J-S)-L)^2 \tag{6.8}$$

$$H_{so} = A(L \cdot S) \tag{6.9}$$

$$H_{sr} = \gamma((J-S) \cdot S) \tag{6.10}$$

$$\begin{aligned} H_{LD} = q/2(J_+ + J_-)^2 - (q/2 + p/4)[(J_+ + J_-)(S_+ + S_-) \\ +(S_+ + S_-)(J_+ + J_-)] + q/2 + p/2(S_+ + S_-)^2 \end{aligned} \tag{6.11}$$

Note that unlike previous rotational analysis,[195, 19, 197] we have adopted a case (a) basis for describing the $^2\Pi$ state, since we are safely in this limit with only low J states populated in the jet. Additionally, we have omitted higher order terms in the Hamiltonian due to centrifugal distortion of lambda doubling (i.e., p_D and q_D), since this should be a negligible effect at the low J levels we observe. Furthermore, Curl and coworkers noted the presence of significant deviations between observed and fitted line positions either for an isolated J′ level (local perturbation) or over a series of high J′ levels (global perturbation).[181, 19] It is possible that the anomalous magnitudes of such p_D and q_D terms reflect partial compensation for such perturbing effects in the $^2\Pi$ states. Therefore, these terms have been excluded to see if the low J′ data can be explained and understood by this simpler Hamiltonian model.

Evaluated in a Hund's case (a) basis, this results in a fourth order secular determinant yielding values of (i) F_1, F_2 and (ii) parity (+/-) for a given total J, the solutions of which are detailed elsewhere.[199]

6.5.2 Fitting Results

The 3692 cm^{-1} band data are least squares fit to the matrix eigenvalue expressions for the effective $^2\Pi$ Hamiltonian described above to determine revised excited state constants. Table 6.8 reports fit results for the present jet cooled data (column 5) along with the results from previous room temperature studies (column 2) of Curl et al.[19] Note that the residual standard deviation (σ = 13 MHz) of the high resolution fit to the simplified Hamiltonian is extremely good, consistent with experimental uncertainty in frequency measurement and 5 × smaller than previous studies. The results for B, D, γ, and A are also in excellent agreement with Curl's reported values but with an apparent sign reversal in the extracted lambda doubling parameters.

Table 6.8: Excited state constants for the 3692 cm^{-1} $^2\Pi$-$^2\Sigma^+$ band (all in cm^{-1}). Numbers in parentheses constitute the error in each reported value.

Excited State Constants	Curl's Fit of Curl's Data	Revised Fit of Curl's Data	Revised Fit II	This work
ν_0	3692.606(1)	3692.604(2)	3692.606(2)	3692.6084(2)
B	1.41171(2)	1.41187(7)	1.41178(8)	1.41169(4)
D (x 10^5)	-0.51(1)	-0.37(4)	-0.45(4)	-0.34(15)
γ	0.0158(1)	0.0157(5)	0.0162(5)	0.0164(1)
A	-5.405(1)	-5.406(5)	-5.407(6)	-5.4018(4)
p	0.0044(4)	-0.005(1)	-0.0033(8)	-0.0021(1)
q	0.00967(3)	-0.0094(1)	-0.00981(5)	-0.00950(2)
p_D (x 10^5)	-1.1(4)	2.6(1.3)		
q_D (x 10^5)	0.02(3)	-0.37(8)		
st dev	0.002	0.0079	0.0094	0.00042

[a] From Curl *et al.*[19].

[b] Revised fit of all Curl's reported lines[19] for the 3692 cm^{-1} band, excluding lines indicated as strongly overlapped.

[c] Revised fit of Curl's data[19] with the revised Hamiltonian in this work, discussed in Section 6.5.1, i.e., no centrifugal distortion of lamda doubling terms.

To test for possible errors in the Hamiltonian treatment, we also have performed two revised fits of data of Curl et al. for this band.[19] Revised fit I (column 3) uses Curl's original case (b) effective Hamiltonian expression, with higher order p_D and q_D distortion constants explicitly included. We also pursue a revised fit II (column 4) to Curl's data, which uses the case (a) Hamiltonian given above, but neglecting p_D and q_D distortion constants. In an attempt to minimize effects due to perturbations, Curl et al.[19] fitted only an unspecified subset (53 out of 59), whereas our work fits all unblended reported lines. Nevertheless, the reasonable zeroth order expectation would be that revised fits I and II should yield essentially identical results as the original analysis.[19]

Immediately clear from Table 6.8 is that there is a sign reversal for p and q between results of Curl *et al.* and the revised fits as well as a suggestion of an additional sign reversal in p_D and q_D between the two nominally identical fits (columns 2 versus 3) to the same case (b) Hamiltonian. By way of contrast, there is an excellent agreement between fits to the current high resolution results with jet cooled C_2H (column 5) and the two revised fits for data of Curl *et al.* (columns 3 and 4). Specifically, each treatment yields lambda doubling constants p and $q < 0$, in contrast yet consistent with a systematic parity misassignment in the previous work.[19] Interestingly, Hsu *et al.*[197] also inferred negative signs for the lambda doubling constants in this $^2\Pi$ state from dispersed fluorescence excitation spectroscopy but had ascribed this difference to use of *l*-doubling versus lambda doubling terms in the Hamiltonian.[197] The current high resolution analysis clearly confirms that this is due to an early parity misassignment in the $^2\Pi$ state, as confirmed by subsequent discussions with Curl. Indeed, sign changes in the lambda doubling Hamiltonian were later introduced by Curl and co-workers in their analysis of C_2D spectra, though without revisiting the analysis of the C_2H bands currently under consideration. Note that since parity reversal is numerically equivalent to a sign change in p, q, p_D, q_D, such an error would have had no influence on quality of fits originally reported by Curl *et al.* However, this can and does have a major impact on using high resolution data to identify the correct symmetry of dark

states perturbing the $\tilde{A}$ state spectrum, as will be demonstrated elsewhere.

In summary, the fit to high resolution data at low J states shows that the simplified Hamiltonian treatment describes the $^2\Pi$-$^2\Sigma^+$ band at 3692 cm^{-1} very well, with a standard deviation on the order of experimental precision ($\approx$ 10 MHz). Additionally, the excited state constants for this Hamiltonian (after appropriate sign reversal in p, q) are in good agreement with those found by Curl *et al.*,[19] with fivefold smaller residuals than fits to the much larger (albeit lower resolution) data sets in previous works.[19, 197] To make this more explicit, Figure 6.9 displays a plot of deviations from best fit parameter predictions as a function of J and branch. The upper panel in Figure 6.10 shows residuals (observed-predicted) for the R_1 (circles), Q_1 (squares), and R_{12} (diamonds) branches, while the lower graph shows residuals for the R_2 (circles), Q_2 (squares), and P_{21} (diamonds) branches. In all cases, the points are clustered tightly around zero, with an rms value of 0.0003 cm^{-1} (10 MHz) and the largest deviations $\leq$ 0.001 cm^{-1} (30 MHz).

Similar least squares fits have been carried out on the high resolution $^2\Pi$-$^2\Sigma^+$ bands centered around 3786, 4012, and 4107 cm^{-1}, based on the simplified Hamiltonian for the $^2\Pi$ states discussed above and with results presented in Table 6.9. Both the 3786 and 4107 cm^{-1} bands (columns 2 and 4) are very accurately described, as evidenced by standard deviations ($\approx$ 0.0003 cm^{-1}) close to experimental precision. However, this is not the case for the 4012 cm^{-1} band, which is clearly not as well fit by the effective Hamiltonian for the excited state. This is evident in the 30 $\times$ larger standard deviation (σ = 0.01 cm^{-1} (300 MHz)) of the least squares fit for the 4012 cm^{-1} band, which even though small by typical Doppler broadened infrared standards, corresponds to 30 $\times$ higher than our sub-Doppler experimental precision.

This point is clearly illustrated in Figure 6.10, which plots the residuals (observed.predicted) from the least squares fit of our data, where again the upper graph is a plot of the residuals for the R_1 (circles), Q_1 (squares), and R_{12} (diamonds) branches, and the lower graph is a plot of the residuals for the R_2 (circles), Q_2 (squares), and P_{21} (diamonds) branches. Note the tenfold increase in the scale from Figure 6.9, and that the residuals are now scattered

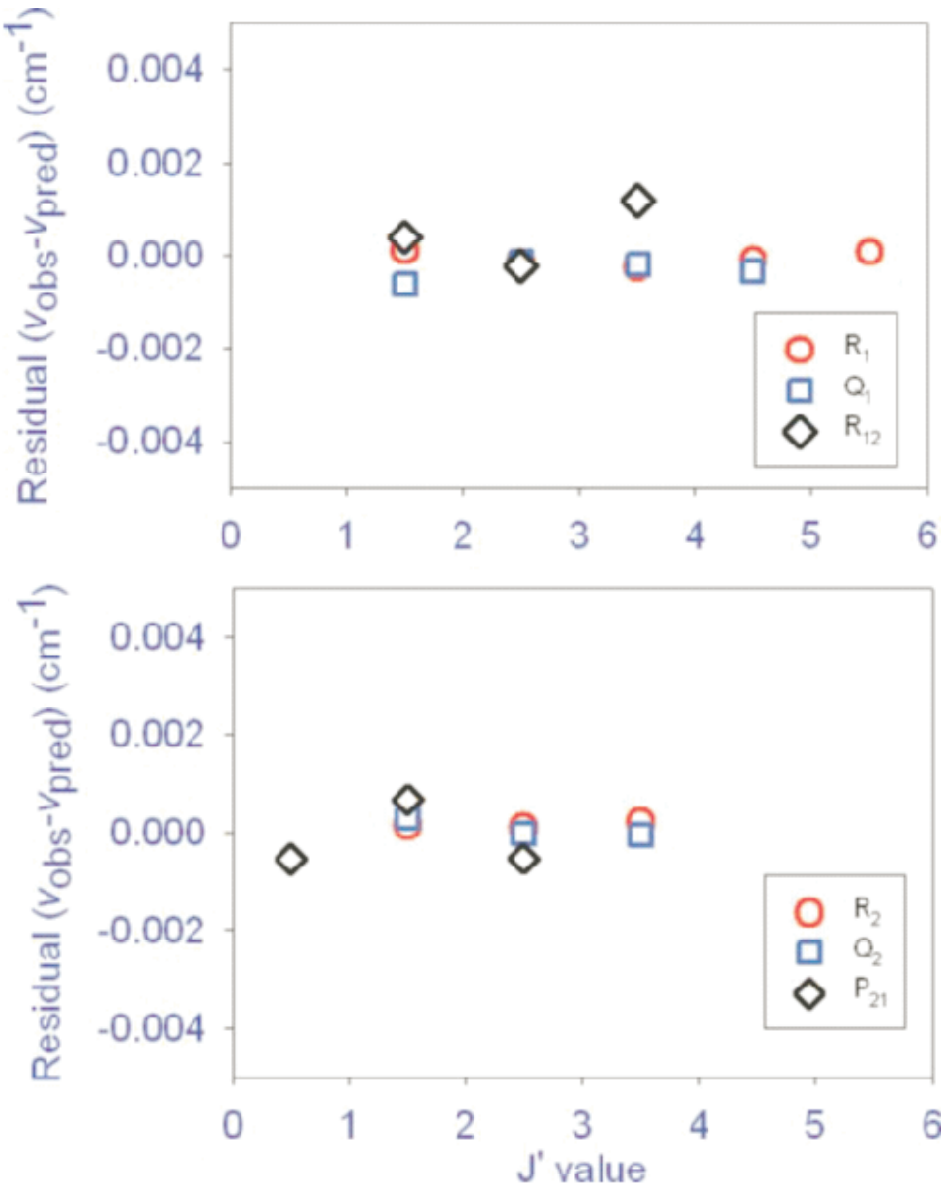

Figure 6.9: Residuals (observed-calculated) from fit, described in Section 6.5.2, for the $^2\Pi$-$^2\Sigma^+$ centered around 3692 cm^{-1}. The upper graph shows residuals for the R_1 (circle points), Q_1 (square points), and R_{12} (diamond points) branches, while the lower graph shows residuals for the R_2 (circle points), Q_2 (square points), and P_{21} (diamond points) branches.

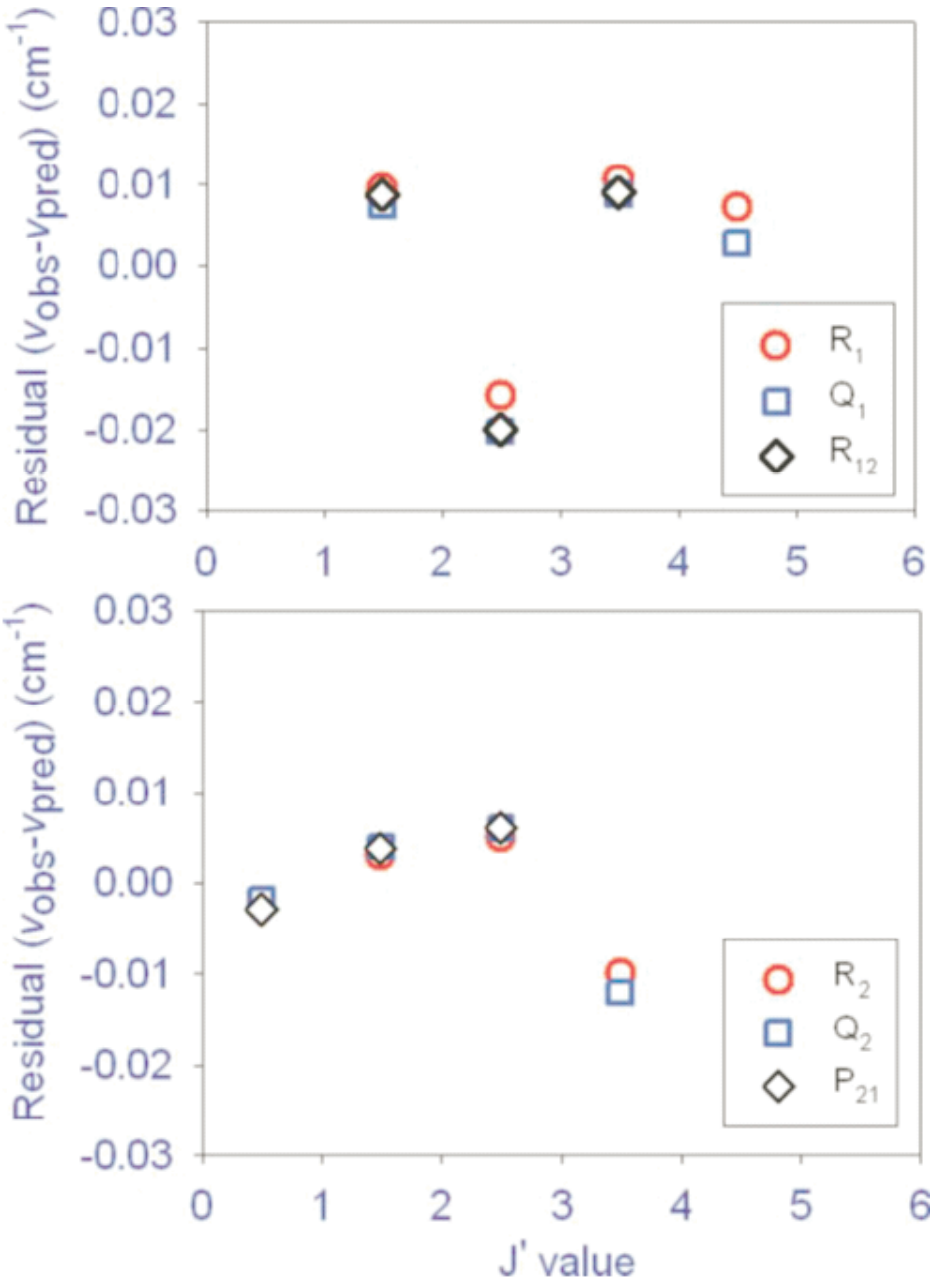

Figure 6.10: Residuals (observed-calculated) from fit, described in Section 6.5.2, for the $^2\Pi$-$^2\Sigma^+$ band centered around 4012 cm^{-1}. The upper graph shows residuals for the R_1 (circle points), Q_1 (square points), and R_{12} (diamond points) branches, while the lower graph shows residuals for the R_2 (circle points), Q_2 (square points), and P_{21} (diamond points) branches.

Table 6.9: Excited state constants for the 3786 cm^{-1}, 4012 cm^{-1}, and 4107 cm^{-1} $^2\Pi$-$^2\Sigma^+$ bands (all in cm^{-1}). Numbers in parentheses constitute the error in each reported value.

Excited State Constants	3786 cm^{-1} Band	4012 cm^{-1} Band	4107 cm^{-1} Band
ν_0	3786.0910(2)	4012.284(4)	4107.8753(5)
B	1.42266(6)	1.437(1)	1.41429(9)
D (x 10^5)	2.3(3)	-16(6)	-1.2(2)
γ	0.00254(10)	-0.011(2)	0.0006(3)
A	-2.4406(4)	-2.16(1)	-3.286(1)
p	-0.0016(1)	-0.0023(28)	-0.0171(3)
q	-0.02735(2)	-0.0411(4)	-0.02195(4)
st dev	0.00042	0.011	0.0016

around zero by on the order of 0.01-0.02 cm^{-1}. It is particularly evident in the upper panel in Figure 6.10 that there is a precipitous dip at $J' = 2.5$, indicative of a "local" perturbation in the F_1 manifold caused by a close-lying dark state of C_2H. By way of contrast, note the extremely tight clustering of residuals for each of the three transitions to the same upper J state, a point we will return to in Sec. 6.5.3. Part of this is to be expected; since Q_2 and R_{12} (as well as Q_1 and P_{21} for the lower panel) transitions reach the same final parity level, this agreement is completely consistent with 2-line combination differences for the ground state and thus experimental precision. However, the fact that we also see a similar tight clustering of the Q_1 and R_1 transitions, which necessarily access states of opposite parity, is particularly noteworthy. Specifically, this means that the local perturbation of the F_1 $J' = 2.5$ parity levels must arise from a near resonant state also with both +/- parity levels in close proximity. From Figure 6.1, this implies that the dark state cannot be $^2\Sigma$; i.e., it must be a state with $\Lambda > 0$.

To rule out that this effect at $J' = 2.5$ is caused by a global perturbation, a least squares fit has been performed on the 4012 cm^{-1} data, but with the lines terminating in $J' = 2.5$, F_1 manifold, namely, $R_1(1.5)$, $P_1(3.5)$, $Q_1(2.5)$, $R_{12}(1.5)$, and $Q_{12}(2.5)$, removed from the data set. The results for this revised fit are presented in Table 6.10 (column 3), compared with those presented earlier in Table 6.9 and summarized in column 2 of Table

6.10. Already by leaving out transitions to this more strongly perturbed upper state, the standard deviation of the fit improves fivefold from 0.01 to 0.002 cm^{-1}. Interestingly, there is an additional manifestation of this local perturbation in the F_2 manifold in the vicinity of $J' = 3.5$, as evident in the lower panel of Figure 6.10. Similar to what is seen in the F_1 manifold, the tight clustering of the Q_2/P_{21} and R_2 transitions (which by symmetry must access different parity levels) confirms the presence of local vibronic mixing from a dark state with closely spaced levels of both + and - parities, i.e., $^2\Pi$, $^2\Delta$, etc. Based on the (i) quality of high level *ab initio* vibronic calculations and (ii) sparse vibrational level density for C_2H at only 3500-4000 cm^{-1} of internal energy, this bodes well for being able to identify the actual vibrational state responsible, as discussed below.

Table 6.10: Comparing excited state constants for the 4012 cm^{-1} $^2\Pi$-$^2\Sigma^+$ band (all in cm^{-1}), with and without perturbed $^2\Pi$ F_1 levels. Numbers in parentheses constitute the error in each reported value.

Excited State Constants	4012 cm^{-1} Band	Revised Fit for 4012 cm^{-1} Band
ν_0	4012.284(4)	4012.2867(9)
B	1.437(1)	1.4393(3)
D (x 10^5)	-16(6)	-5.7(1.3)
γ	-0.011(2)	-0.0093(5)
A	-2.16(1)	-2.148(2)
p	-0.0023(28)	-0.0035(6)
q	-0.0411(4)	-0.04094(9)
st dev	0.011	0.0022

[a] Revised fit of the 4012 cm^{-1} band as discussed in Section 6.5.2, whereby the lines that terminated in F_1 $J' = 2.5$ were removed from the data input to the fit.

6.5.3 Perturbation Analysis

6.5.3.1 3600 Band

The present least squares fit to the unperturbed Hamiltonian in Table 6.11 (column 2 with $\sigma = 0.13$ cm^{-1}) fails to reproduce the 10 MHz (0.0003 cm^{-1}) experimental accuracy of

our sub-Doppler measurements. At first glance, this would appear to be an even worse fit quality than the results of Curl and coworkers ($\sigma = 0.004$ cm^{-1}). However, it is important to note that the previous analysis was for room temperature spectra with strongly perturbed low J transitions selectively removed from the analysis, thus precluding a direct comparison with the current treatment of all lines in the jet cooled spectrum.

Table 6.11: Excited state constants for the 3600 cm^{-1} $^2\Pi$-$^2\Sigma^+$ band (all in cm^{-1}). Numbers in parentheses constitute the error in each reported value.

Excited State Constants	Curl's Fit	This work I	This work II
ν_0	3600.353(1)	3600.38(5)	3600.3521(2)
B	1.40529(1)	1.40(1)	1.40499(5)
D (x 10^5)	1.710(5)	-31.4(34.4)	1.6(2)
γ	-0.0127(1)	-0.005(29)	-0.0092(1)
A	-7.219(2)	-7.2(1)	-7.2191(1)
p	-0.0016(4)	0.03(3)	0.0083(1)
q	0.00816(2)	-0.009(5)	-0.00748(2)
p_D (x 10^5)	1.7		
q_D (x 10^5)	-0.407(9)		
ν_{pert}			3611.45(2)
B_{pert}			1.450(2)
β_0			0.11765(7)
st dev	0.004	0.13	0.00051

[a] From Curl and coworkers[181].
[b] Fit of all lines given in Table 6.1 to the unperturbed model.
[c] Fit of all lines given in Table 6.1 to the perturbed model presented in Section 6.5.3, which includes the local perturbation of the $^2\Pi_{1/2}$ state.

The data in column 2 of Table 6.11 clearly indicate that the sub-Doppler high resolution spectrum is poorly fit by the unperturbed Hamiltonian model for the $^2\Pi$ state. This point is further emphasized in Figure 6.3, which compares a sample scan region of high resolution spectral data (in black) with unperturbed predictions (in red) calculated using the energy level expressions from the Hamiltonian model for the $^2\Pi$ state given above and the constants determined in column 4, along with the energy level expressions for the $^2\Sigma^+$ state (given in eqn (2) and (3)) and the ground state constants determined from previous microwave studies.16 While the experimental R_1 lines and the first two members of the Q_2 and P_{21}

progressions agree, deviation between experiment and the unperturbed simulation become much more prominent at $Q_2(2.5)/P_{21}(3.5)$ and $Q_2(3.5)/P_{21}(4.5)$. To highlight the source of discrepancy in our model, Figure 3 displays plots of the residuals for the Q_2, P_{21}, R_2, and P_2 branches for the unperturbed model fitting results versus J′. Particularly evident is that the residuals ($\nu_{obs} - \nu_{calc}$) for the R_2 and P_2 branches are scattered closely around zero ($\Delta\nu = 0.0005$ cm^{-1}), while those of Q_2 and P_{21} deviate by as much as 1000-fold more from zero, particularly in the vicinity of the doubled set of lines observed for $Q_2(3.5)$, each of which is nearly symmetrically pushed away from the residuals at lower J. This doubling of the spectral lines was also observed in the Curl data and tentatively assigned as $Q_2(3.5)$.

As an important additional piece of evidence, the jet cooled IR spectrum reveals this doubling of lines to be replicated for $P_{21}(4.5)$, which terminates in the same upper state (i.e., $^2\Pi_{1/2}$ $F_2(J_0 = 3.5)$) as $Q_2(3.5)$. This permits unambiguous confirmation of the J state assignment by 2-line ground state combination differences that agree to within experimental precision ($<$ 10 MHz). In the residuals for our data in Figure 6.11, there is a striking discontinuity from J′ = 3.5 to J′ = 4.5 in the case of the Q_2 branch (and from J′ = 2.5 to J′ = 3.5 in the case of P_{21}). This behavior is consistent with a strong local perturbation in the upper state manifold near J′ = 3.5, which therefore both (i) vibronically mixes optically bright and dark state of the same overall rovibronic symmetry and parity to yield additional mixed state lines in the spectrum, as well as (ii) introduces systematic shifts in adjacent rotational levels in the vicinity of J′ = 3.5. Each of these effects are evident and can be quantitatively analyzed in the high resolution jet cooled spectrum, as described in detail below.

The energy level diagram insets in each residual plot given in Figure 6.11 demonstrate that the noticeably perturbed bands (i.e. Q_2 and P_{21}) have transitions that only terminate in the upper parity level for a given value of J′ in the $^2\Pi_{1/2}$ state. Conversely, R_2 and P_2, which exhibit no such perturbation and are well fit with the unperturbed Hamiltonian, have transitions that terminate exclusively in the lower parity level for a given value of J′. Since J

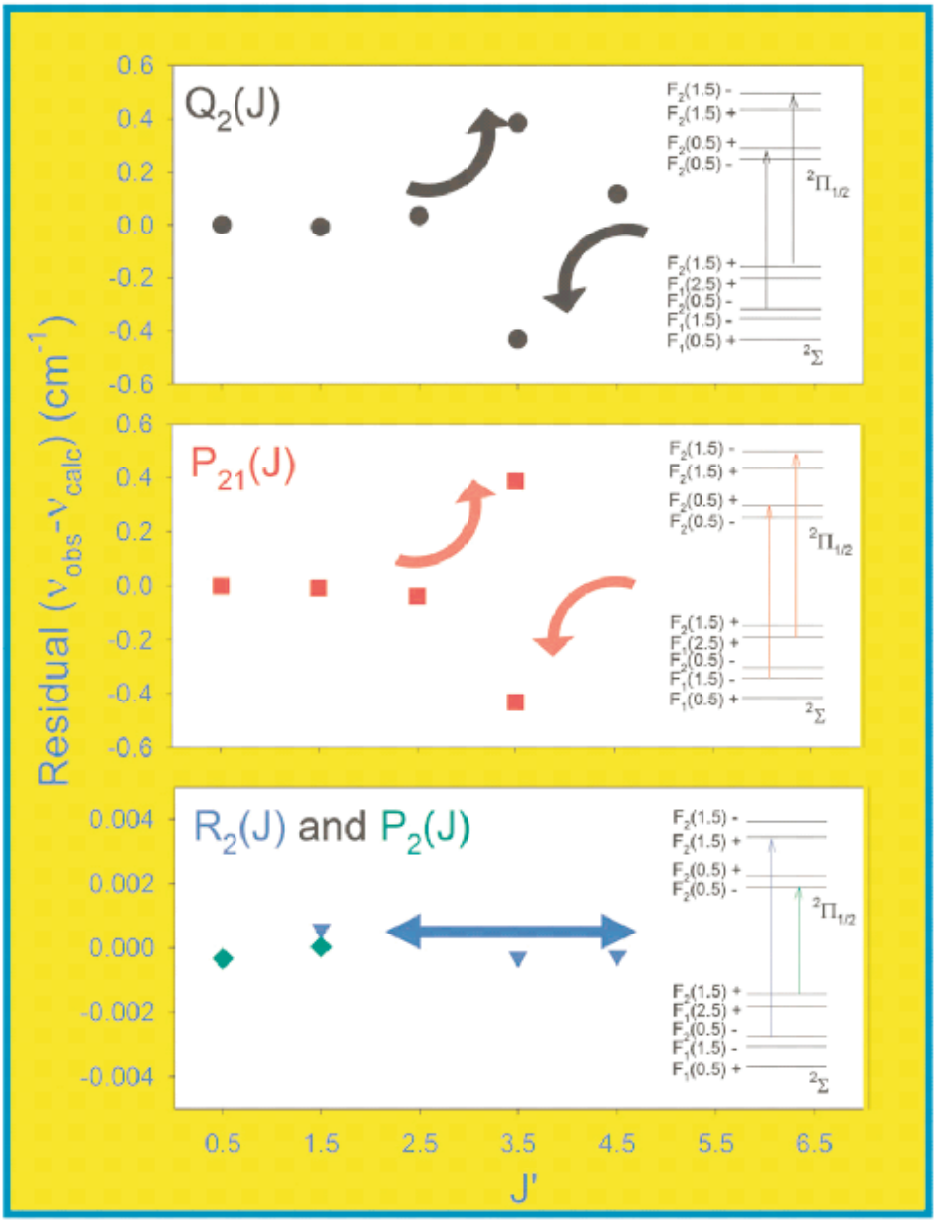

Figure 6.11: Residuals (ν_{obs}-ν_{calc}) for the 3600 cm^{-1} band for the Q_2, P_{21}, R_2, and P_2 branches plotted as a function of J′, where ν_{calc} was determined from the unperturbed Hamiltonian model discussed in Section 6.5.1. These clearly demonstrate a local perturbation in the Q_2 and P_{21} branches at J′ = 3.5, evident in not only in the discontinuity in the plot but also in that two lines are observed at J′ = 3.5 for both of these branches. The residual plots for P_2 and R_2 reflect no such local perturbation. The energy level diagram schematics to the right demonstrate the transitions being depicted in each plot. From these, it is easy to see that the Q_2 and P_{21} transitions terminate in the upper parity level in the $^2\Pi$ state, while the R_2 and P_2 transitions terminate in the lower parity level.

and parity are good quantum numbers and must be rigorously conserved in a unimolecular interaction, this permits the symmetry of the perturbing state to unambiguously identified. First of all, since only one of the two closely spaced parity levels for every J in the $^2\Pi_{1/2}$ state is perturbed, this implies that the perturbing manifold must belong to a state without parity doubling, i.e. a $^2\Sigma$ state. Secondly, since overall parity in a $^2\Pi_{1/2}$ manifold necessarily alternates with J, the fact that only the negative parity $^2\Pi_{1/2}$ level with J$'$ = 3.5 is perturbed requires that the associated ground state $^2\Sigma$ J$'$ = 0.5 level (i.e., ΔJ = odd) must be of positive parity, therefore identifying the perturbing state to be of $^2\Sigma^+$ symmetry. This non-adiabatic interaction therefore represents a heterogeneous perturbation between states with different vibronic symmetries and projection of angular momentum along the molecular axis, which can be treated isomorphically as ΔK = $\pm$ 1 $\Sigma - \Pi$ Coriolis coupling.

It is relatively straightforward to include this local perturbation into our Hamiltonian model. To do this, we form the 2 $\times$ 2 coupling matrix

$$\begin{pmatrix} E_\Pi & \beta \\ \beta & E_\Sigma \end{pmatrix} \tag{6.12}$$

where E_Π and E_Σ represent the zeroth order unperturbed energies for the optically bright $^2\Pi_{1/2}$ and dark $^2\Sigma^+$ state, and β is the associated rovibronic matrix element, which for ΔK = $\pm$1, $\Sigma - \Pi$ coupling scales as

$$\beta \;=\; \beta_0\sqrt{\mathrm{N(N+1)}} \tag{6.13}$$

As we shall see, the deperturbed $^2\Pi_{1/2}$ state energies are extremely well described by the eigenvalue solutions to the equations in section 6.5.1. Though the spectral data clearly contain less quantitative information on the dark perturbing $^2\Sigma^+$ state, the unperturbed energy levels can be adequately approximated by a simple rigid rotor (B_{pert}) built on a band origin energy (ν_{pert}):

$$E_1 \;=\; \nu_{pert} \;+\; B_{pert}(N(N+1)) \tag{6.14}$$

where only the lowest order contributions to a $^2\Sigma^+$ state have been included for simplicity.

Subsequent matrix diagonalization yields the two coupled state energies, E_+ and E_- as analytic functions of E_Π, E_Σ, and β:

$$E_\pm = \frac{E_1 + E_2}{2} \pm \frac{\sqrt{\frac{E_1 - E_2}{2} + 4\beta^2}}{2} \tag{6.15}$$

By least squares fitting the observed bright and dark state transition frequencies to this model, we thereby extract improved excited state parameters for both $^2\Pi_{1/2}$ and $^2\Pi_{3/2}$ states, as well as new information on the dark $^2\Sigma^+$ state, specifically β_O, B_{pert}, and ν_{pert}.

Results from such least squares fits to the perturbed model incorporating $\Sigma - \Pi$ Coriolis coupling are summarized in Table 6.11, column 4. First of all, the standard deviation of this fit is dramatically improved over 100-fold to $\sigma = 0.00051$ cm^{-1} (15 MHz), i.e., now comparable to the experimental precision of ± 10 MHz. The visual quality of this fit is illustrated in the simulation trace (in pink) in Figure 6.3 labeled perturbed, where the frequencies and intensities are predicted from the eigenvalues and eigenvectors of the 2 × 2 matrix. In contrast with the unperturbed simulation (in red), the perturbed trace accurately predicts all of the experimental C_2H lines, and in particular, the strongly split pair of $Q_2(3.5)/P_{21}(4.5)$ lines.

There is additional confirmation of the model in the relative intensities of the bright and dark state transitions, which can be predicted from the matrix eigenvectors. Specifically, the mixing angle θ is determined from β, E_Π, and E_Σ by

$$\theta = \frac{\arctan \frac{2\beta}{E_1 - E_2}}{2} \tag{6.16}$$

In terms of this mixing angle, the new eigenfunctions can be expressed as

$$\begin{aligned} \psi_+ &= \sin\theta\psi_u + \cos\theta\psi_p \\ \psi_- &= \cos\theta\psi_u + \sin\theta\psi_p \end{aligned} \tag{6.17}$$

where ψ_b and ψ_d represent the unperturbed bright and dark state wavefunctions, respectively.

For example, in our fit, we determined $\beta_0 = 0.11765$ cm^{-1} (see column 4 of Table 6.11). Therefore, at J = 0.5 (N = 0 in terms of the $^2\Sigma$ state), $\beta = 0$ according to Eq. 6.13, and

$\theta = 0$ according to Eq. 6.16, so the perturbed energy levels (E_+ and E_-) look exactly like the unperturbed J = 0.5 levels for the $^2\Sigma$ and $^2\Pi_{1/2}$ states, respectively. Whereas, for J = 1.5 (N = 1), $\beta = 0.1665$ cm^{-1} and $\theta = 2.275°$. Therefore, the perturbed wavefunctions are

$$\psi_+ \;=\; 0.0397\psi_{\mathrm{u}} \;+\; 0.999\psi_{\mathrm{p}}\psi_- \;=\; 0.999\psi_{\mathrm{u}} \;+\; 0.0397\psi_{\mathrm{p}} \tag{6.18}$$

for J = 1.5. Obviously then, the transitions observed in our spectrum must be to $E_\pm$ levels that have a sizeable amount of ψ_{u} or bright state character, and so the $Q_2(1.5)$ transition terminates in the E_- level.

This determines relative transition intensities to coupled pairs of upper levels observed in the spectrum,

$$\frac{\mathrm{I}(\mathrm{E}_+)}{\mathrm{I}(\mathrm{E}_-)} \;=\; \tan^2\theta \tag{6.19}$$

which in turn reflects the fractional bright state character in the E_+ vs. E_- upper state. This is represented in Figure 6.12 by red vs. blue fraction for a given J, which corresponds to the predicted intensity ratio for a pair of transitions terminating in the upper perturbed level. This expression also explains why we measure appreciable frequency shifts at high resolution over a wide series of transitions, but only with sufficiently strong local mixing to see the dark state at J = 3.5. For example, the mixing angle ($\theta \approx 43.4°$) at N = 3 from equation 6.19 predicts an intensity ratio of 0.89; this agrees well with the two, nearly equally strong $Q_2(3.5)$ lines that are observed, terminating in the E_- level or E_+ level. However, even for one J higher or lower, the intensity ratios for the corresponding dark state lines according to equation 6.19 are down by 420-fold and thus not observed above the experimental noise level.

6.5.3.2 4012 Band

Figure 6.10, which plots the residuals (observed.predicted) from the least squares fit of our data, where again the upper graph is a plot of the residuals for the R_1 (circles), Q_1 (squares), and R_{12} (diamonds) branches, and the lower graph is a plot of the residuals for

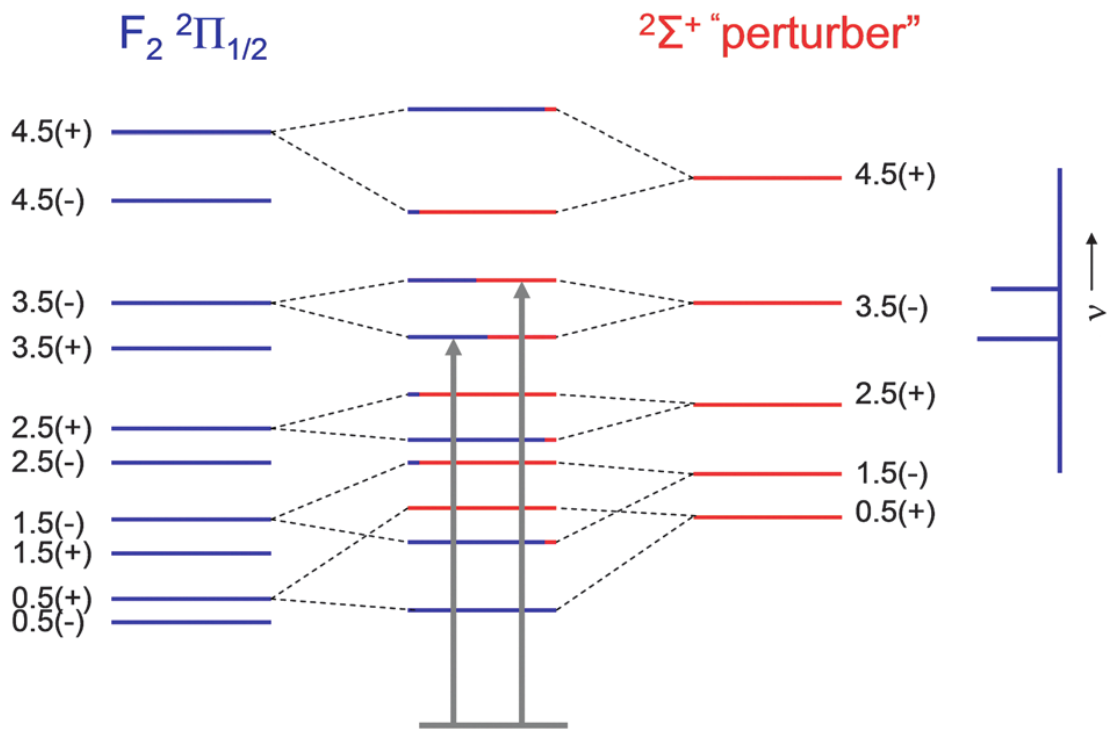

Figure 6.12: Energy level diagram illustrating perturbation of the upper parity levels in the bright $^2\Pi_{1/2}$ excited state by a close-lying dark $^2\Sigma^+$ state. The Σ-Π Coriolis perturbation breaks the degeneracy in the $^2\Pi$ upper parity energy levels for a given J and gives rise to mixed energy levels (drawn in the center of the excited state), which contain partial character of the bright and dark states. The unperturbed $^2\Pi_{1/2}$ energy levels are blue, while the unperturbed $^2\Sigma^+$ levels in the excited state are red. The mixed states in the center are then combinations of red and blue, which portrays the predicted intensity for a transition terminating in these levels, based on the percentage of blue (or bright character) depicted in each. At $J' = 3.5$, this mixing is approximately 50/50, yielding an integrated intensity ratio of 0.89, and hence, we observe transitions to both $J' = 3.5(-)$ perturbed levels. The green arrows indicate the observed transitions in the Q_2 branch.

the R_2 (circles), Q_2 (squares), and P_{21} (diamonds) branches. Note the tenfold increase in the scale from Figure 6.9, and that the residuals are now scattered around zero by on the order of 0.01-0.02 cm^{-1}. It is particularly evident in the upper panel in Figure 6.10 that there is a precipitous dip at $J' = 2.5$, indicative of a "local" perturbation in the F_1 manifold caused by

a close-lying dark state of C_2H. By way of contrast, note the extremely tight clustering of residuals for each of the three transitions to the same upper J state, a point we will return to in Sec. 6.6. Part of this is to be expected; since Q_2 and R_{12} (as well as Q_1 and P_{21} for the lower panel) transitions reach the same final parity level, this agreement is completely consistent with 2-line combination differences for the ground state and thus experimental precision. However, the fact that we also see a similar tight clustering of the Q_1 and R_1 transitions, which necessarily access states of opposite parity, is particularly noteworthy. Specifically, this means that the local perturbation of the F_1 $J' = 2.5$ parity levels must arise from a near resonant state also with both +/- parity levels in close proximity. From Figure 6.1, this implies that the dark state cannot be $^2\Sigma$; i.e., it must be a state with $\Lambda > 0$.

To rule out that this effect at $J' = 2.5$ is caused by a global perturbation, a least squares fit has been performed on the 4012 cm^{-1} data, but with the lines terminating in $J' = 2.5$, F_1 manifold, namely, $R_1(1.5)$, $P_1(3.5)$, $Q_1(2.5)$, $R_{12}(1.5)$, and $Q_{12}(2.5)$, removed from the data set. The results for this revised fit are presented in Table 6.10 (column 3), compared with those presented earlier in Table 6.9 and summarized in column 2 of Table 6.10. Already by leaving out transitions to this more strongly perturbed upper state, the standard deviation of the fit improves fivefold from 0.01 to 0.002 cm^{-1}. Interestingly, there is an additional manifestation of this local perturbation in the F_2 manifold in the vicinity of $J' = 3.5$, as evident in the lower panel of Figure 6.10. Similar to what is seen in the F_1 manifold, the tight clustering of the Q_2/P_{21} and R_2 transitions (which by symmetry must access different parity levels) confirms the presence of local vibronic mixing from a dark state with closely spaced levels of both + and - parities, i.e., $^2\Pi$, $^2\Delta$, etc. Based on the (i) quality of high level *ab initio* vibronic calculations and (ii) sparse vibrational level density for C_2H at only 3500-4000 cm^{-1} of internal energy, this bodes well for being able to identify the actual vibrational state responsible, as discussed below.

6.6 Vibronic Assignments

One important issue to address is vibronic assignment of the four C_2H $^2\Pi$-$^2\Sigma^+$ bands observed in this work. There has been excellent theoretical effort on this topic, most notably the recent predictions by Tarroni and Carter,[8, 9] which make detailed assignments for both energies and vibronic transition intensities throughout the 3000-6000 cm^{-1} region. For example, they predict a strong band at 3690.5 cm^{-1} which is in remarkably good first principles agreement with experimental observation at 3692.6084 cm^{-1}. Similar quality predictions are also made for the other three strong bands, i.e., (i) 3790.9 versus 3786.0910 cm^{-1} (obs), (ii) 4011.4 versus 4012.2840 cm^{-1} (obs), and (iii) 4093.6 versus 4107.8753 cm^{-1} (obs). In particular, they offer general assignment of the upper states for these four bands to complex admixtures of electronic and vibrational excitation. As one example, theory suggests the upper state character of the 3690.5 cm^{-1} band to be a superposition of $^\Pi$ states $\tilde{A}(0,0,0)$ and $\tilde{X}(0,1^1,2)$ and $\tilde{X}(1,1^1,0)$, where (ν_1, ν_2, ν_3), corresponds to the C-H stretching, CCH bending, and C-C stretching vibrations, respectively, and the superscript indicates quanta in vibrational angular momenta, l. Given that the $\tilde{A}$ state manifold is embedded in the $\tilde{X}$ manifold at relatively low energy, one might well anticipate strong first order vibronic mixing between (i) high lying $^2\Pi$ symmetry vibrational levels in the ground state $\tilde{X}$ manifold and (ii) low lying levels of the excited $^2\Pi$ electronic $\tilde{A}$ state.

This picture can be further tested by experimental band intensities, which also agree well with the predicted absorption cross-sections of Tarroni and Carter.[9] For a common rotational temperature, relative oscillator strengths for each band can be quantitatively obtained by comparing intercepts in Boltzmann plots such as in Figure 6.5. Normalized to the 3962 cm^{-1} band, the experimental band intensities are found to be 1.0 (3692 cm^{-1}): 1.5 (3786 cm^{-1}): 2.7 (4012 cm^{-1}): 4.9 (4107 cm^{-1}). This is in excellent qualitative agreement with the corresponding 1.0 : 1.2 : 2.8 : 3.2 band strength ratios predicted by Tarroni and Carter, lending further credence to a picture of extensive vibronic coupling between $^2\Pi$ states

in the $\tilde{A}$ and $\tilde{X}$ manifolds.

The perturbed 3600 cm^{-1} $^2\Pi$-$^2\Sigma^+$ origin band has been analyzed and the high resolution slit-jet-cooled data successfully fit using the zero-order (unperturbed) Hamiltonian for the $^2\Pi$ upper state along with Σ - Π Coriolis coupling terms. We can now incorporate the previous high J data, reported by Yan et al.,[181] into our fit and see if these high J lines are still well characterized with our perturbed model. As mentioned earlier, Curl and coworkers[182] reported evidence for (i) a strong local perturbation at $N' = 4$ as well as (ii) increasing frequency shifts away from the least squares fits with increasing rotational state ($N' > 19$) in the 3600 cm^{-1} band data. We have clearly identified this local vibronic coupling at low N′ in the supersonic jet data, but in addition this may also be responsible for what looks a more global interaction at higher N′. Specifically, second order perturbation theory predicts that the resulting frequency shifts due to bright state-dark state coupling should grow approximately as $\pm\beta/|\Delta E|$, where $\Delta E = E_\Pi - E_\Sigma$ is the difference in unperturbed energies. For Σ-Π Coriolis coupling (i.e.,$\beta = \beta_0\sqrt{N(N+1)}$) and an energy spacing dominated by differences in a rigid rotor progression (i.e., $\Delta \approx \Delta B[N(N+1])$, these level shifts will asymptotically approach a constant displacement of $\beta^2/|\Delta E| \approx \beta_0^2/\Delta B$, which therefore could explain the gradual perturbation in the residuals reported by Yan et al.[181] at high N. Indeed, the magnitude of this shift $\beta_0^2/\Delta B = 0.31$ cm^{-1} is directly predicted from our least squares fitted values in the low N regime, which is consistent with the offsets observed by Curl and coworkers in their original study. More quantitatively, a combined fit of our low J data with the previously reported high J data[182] using the perturbed Hamiltonian model discussed in detail in Section 6.5 yields residuals for the Q_2(J) branch consistent within experimental error for all J, suggesting that only one Σ-Π Coriolis interaction with a single dark state plays a role in the high resolution spectroscopic analysis. This makes much better sense, as the density of vibrational states for a simple triatomic such as C_2H in the 3600 cm^{-1} region is predicted to be ≈ 0.02 states/cm^{-1}, i.e. yielding typical energy spacings more than an order of magnitude higher than typical Coriolis coupling matrix elements at low J

values in the supersonic jet.[8, 9] One immediate corollary of this low density of background states is that the extent of vibronic state mixing and therefore perturbations in the spectra are much more isolated (and thus analyzable and assignable) than perhaps previously appreciated.

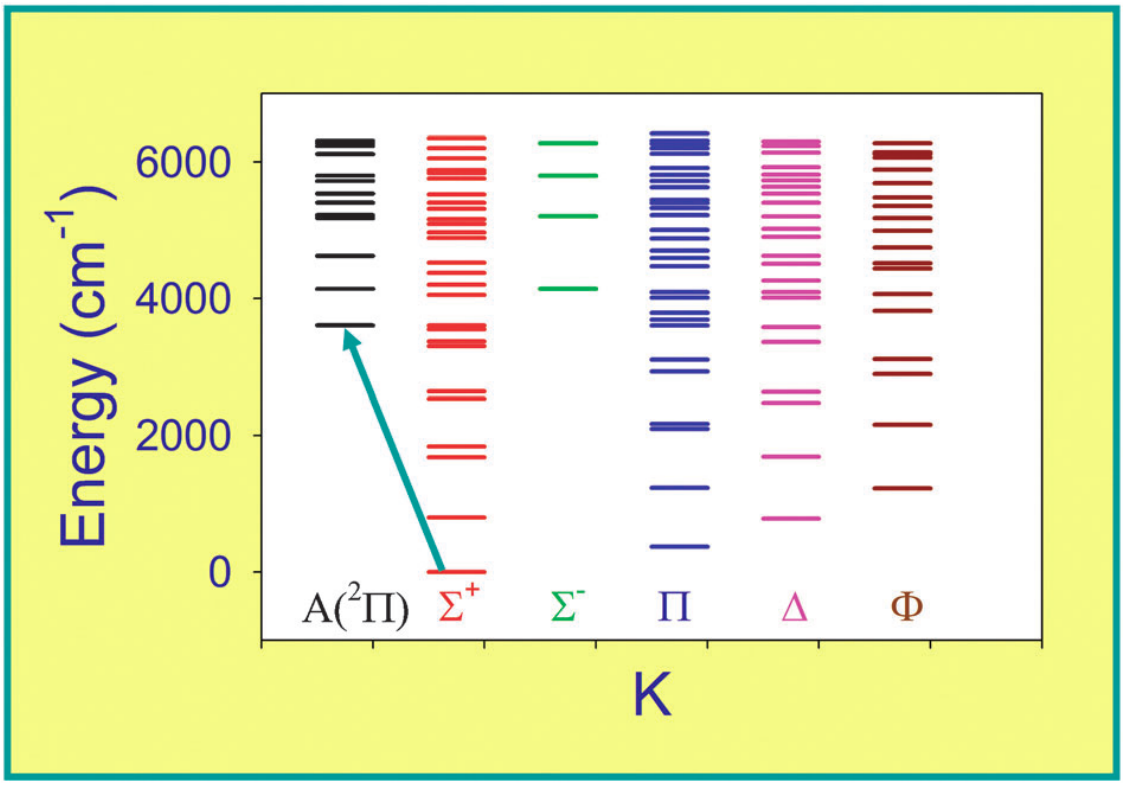

Figure 6.13: Energy level diagram for C_2H from the theoretical work of Tarroni and Carter[8, 9] revealing the predicted vibronic state densities for each angular momentum K value. Note the sparse vibronic manifold for a triatomic such as C_2H at low energies, which provides a novel opportunity to identify the explicit vibrational level(s) involved in the "bright state ($^2\Pi_{1/2}$) -"dark state ($^2\Sigma^+$) vibronic interaction

As one example, this unusual combination of (i) a high resolution jet cooled spectral data analysis and (ii) the relatively low density of states in a triatomic such as in C_2H provides a rather novel opportunity for unambiguously determining the *vibrational identity* of the vibronically perturbing dark state in a highly reactive radical species. For this purpose we take advantage of the theoretical work by Tarroni and Carter,[8, 9] which provides an

excellent first order description of the complete set of background states. The relevant results are summarized in Figure 6.13, which list the predicted energies from 06000 cm^{-1} for all vibronic states in C_2H as a function of electronic/vibrational angular momentum K along the molecular axis. Also listed in the left most column are the vibronic energy levels thought to be largely dominated by the $\tilde{A}(^2\Pi)$ electronically excited state, the lowest of which is nominally the band origin of the $\tilde{A}(^2\Pi) \leftarrow \tilde{X}(^2\Sigma^+)$ transition, as indicted by the arrow. It is worth noting that the states appear relatively discrete and well separated even on such a coarse energy scale, particularly when labeled by angular momentum symmetry. The simple patterns in the lowest Σ^+, Π, Δ, Φ states reflect a regular progression in the CCH bend, which has a $^2\Pi \leftarrow {}^2\Sigma^+$ fundamental transition at 371 cm^{-1}. The pattern becomes slightly more complex with the additional states arising from CC stretch excitation, starting around the $^2\Sigma^+ \leftarrow {}^2\Sigma^+$ fundamental band at 1840 cm^{-1}. Finally, the CH stretch excitation predicted at 3298 cm^{-1} contributes state density in the vicinity of the $\tilde{A}(^2\Pi) \leftarrow \tilde{X}(^2\Sigma^+)$ electronic transition, though the assignment of this vibration is still a matter of controversy. The CCH bending[175] and CC stretching[174] fundamentals have been definitively assigned previously, while there is still uncertainty in the CH stretching fundamental, hence the frequency for the best candidate for this fundamental[177] in Figure 6.13. The $^{\Pi}$-$^2\Sigma^+$ band reported here has previously[181, 192] been assigned as the origin of the $\tilde{A}$-$\tilde{X}$ electronic transition. However, the calculations by Tarroni and Carter[8] illustrate that the coupling between the $\tilde{A}$ and $\tilde{X}$ states is so strong that there is no pure origin transition, but rather their assignment for the level calculated to be at 3604.4 cm^{-1} is a complex admixture of $\tilde{X}$ $(0,1^1,2)$, $\tilde{X}$ $(1,1^1,0)$, $\tilde{A}$ $(0,0,0)^1$, where (ν_1, ν_2, ν_3), correspond to the CH stretching, CCH bending, and the CC stretching vibrations, respectively, and the superscript indicates quanta in vibrational angular momenta, l. Their calculations predict that while the origin of the $\tilde{A}$ state is vibronically distributed among several $^2\Pi$ levels, the largest amplitude is calculated for the level predicted at 3604.4 cm^{-1}. Hence, the $^2\Pi$-$^2\Sigma^+$ band located at 3600.3521 cm^{-1} can be reasonably assigned as the origin band of the $\tilde{A}$-$\tilde{X}$ electronic transition in C_2H.

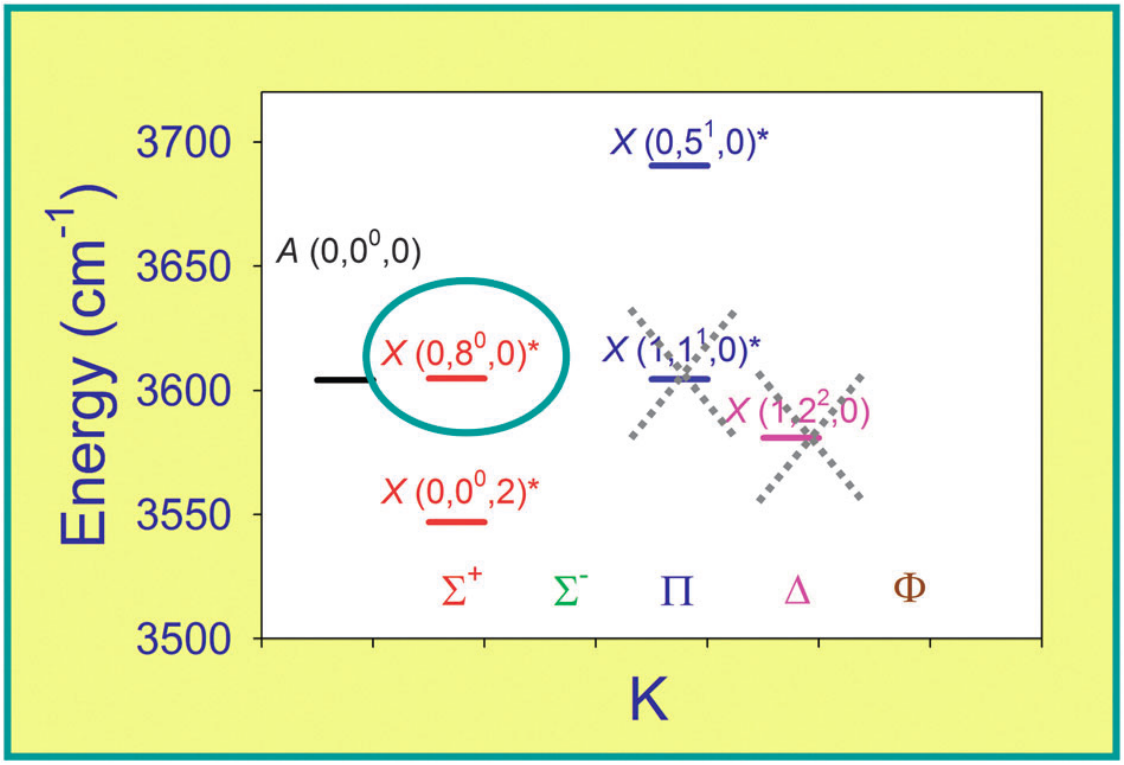

Figure 6.14: A $\approx$ 200 cm^{-1} blow up region of the Tarroni and Carter[8, 9] energy level diagram for C_2H in the $^2\Pi$-$^2\Sigma^+$ 3600 cm^{-1} origin band region, sorted by K quantum number and clearly identifying the only near-resonant vibrational states available for strong vibronic interaction via a a local curve crossing. Near-resonant coupling with the Π, Δ, Φ manifolds can be immediately ruled out (by dashed crosses) since only the upper parity level is selectively perturbed, which leaves only $\Delta K = \pm 1$ Π-Σ Coriolis coupling with only one possible resonant state (blue-green circle) in the $^2\Sigma^+$ manifold. The variational calculations by Tarroni and Carter suggest this state is predominantly $(0,8^0,0)$ with partial $(0,0^0,2)$ character. Note the low overall state density ($\approx$ 0.02 states/cm^{-1}) in this triatomic molecule, which permits unambiguous identification of the near resonant vibronic interaction.

One can take this considerably further in Figure 6.14, which shows an expanded region around the $\tilde{A}$-$\tilde{X}$ spectral band origin. At this higher spectral resolution, the calculations of Tarroni and Carter now predict only five states total in the $\pm$ 100 cm^{-1} window surrounding the band origin region between 3500 and 3700 cm^{-1}. Furthermore, of these five states, three are of Π or higher character (i.e., K $>$ 1), and therefore rigorously unable to mix with the upper $^2\Pi$ state by Δ K = $\pm$1, Σ - Π Coriolis interactions. Interestingly, there are no

states whatsoever of Σ^- symmetry within the nearby $\pm$ 500 cm^{-1} region. Indeed, based on the earlier parity assignment, this symmetry state would have been necessarily implicated in Coriolis coupling, the complete absence of which confirms the correctness of the revised parity labeling. This leaves only two Σ^+ states within a $\pm$ 100 cm^{-1} window and of the correct symmetry determined in the perturbation analysis. This immediately supports assignment of the $^2\Sigma^+$ state at 3604.6 cm^{-1} as the dark perturbing species, which is essentially resonant ($\approx$ + 0.2 cm^{-1}) with their predicted $^2\Pi$ band origin at 3604.4 cm^{-1}. From the variational calculations of Tarroni and Carter, this state is predominantly $\tilde{X}$ (0,8^0,0), i.e. the 7th overtone of the CCH bending vibration, but also with contributions from the $\tilde{X}$ (0,0^0,2) state $\approx$ 57.5 cm^{-1} *lower* in energy at 3546.9 cm^{-1}. Based on these theoretical predictions, the dark state at 3611.4(1) cm^{-1} from our spectral deperturbation can be confidently assigned to the zeroth order $\tilde{X}$ (0,8^0,0) vibrational level. Given the small error ($\approx$ 7 cm^{-1} or 0.3%) of these predictions, this speaks to the remarkable accuracy of the *ab initio* surfaces, coupling matrix elements and variational treatment of Tarroni and Carter.[8, 9]

As a final comment, there is additional confirmation from Hsu et al., who have performed extensive studies on C_2H using laser induced fluorescence (LIF) techniques.[197, 20, 180] Specifically, these studies used 193 nm excimer light to fragment HCCH into C_2H + H under both cell and supersonic jet conditions, followed by tunable UV LIF to excite the C_2H on a series of UV transitions to K = 03 levels in the upper electronic state. Rotationally resolved spectroscopic data on high lying vibrational levels in the electronic ground state were then obtained from dispersed fluorescence (DF) back down to the $\tilde{X}$ manifold. Of interest to the present work, these studies were able to probe DF down to both $\tilde{X}$ (0,0^0,2) and $\tilde{X}$ (0,8^0,0) vibrational levels, thus yielding term values of 3546.75 cm^{-1} and 3611.54 cm^{-1}, respectively, above the $\tilde{X}$ (0,0^0,0) ground electronic state. The upper term value (3611.54 cm^{-1}) of Hsu et al. is clearly in excellent agreement with the value (3611.4(1) cm^{-1}) obtained from the present high resolution deperturbation analysis.[197, 20, 180] Indeed, by way of additional confirmation, the rotational constant for the perturbing state from

our high resolution analysis is found to be B_{pert} = 1.45(1) cm^{-1}, i.e., again in quantitative agreement[197] with the reported Hsu et al. value of B = 1.441 cm^{-1}. Furthermore, the appearance of vibronic coupling facilitated by high quanta in the ν_2 and ν_3 vibrations also makes excellent physical sense in light of the potential surface crossing predicted between the electronically excited Π state and ground Σ states as a function of both CC stretching and CCH bending coordinates.[8, 9, 184, 185, 186, 187, 188, 189, 190]

In summary, high resolution infrared spectroscopy in a slit supersonic discharge has yielded evidence for outstanding first principles agreement between both theory and experiment for the identification and assignment of resonantly coupled states in the vibronic manifold of C_2H. This provides strong encouragement that the powerful combination of *ab initio* and high resolution methods will enable further spectroscopic exploration of this critically important combustion radical as well as establish a solid benchmark for understanding non-adiabatic vibronic interactions between multiple Born Oppenheimer potential surfaces.

In addition to strong global mixing between $^2\Pi$ states of the same projection ($|\Lambda| = 1$) of electronic/vibrational angular momentum, the data also show clear indications of much weaker, local mixing between isolated rotational states of same J and parity, which come accidentally into resonance, as illustrated nicely by the 4012 cm^{-1} band in Figure 6.10. This much weaker coupling almost certainly implies states of different angular momentum projection, mixing, for example, by Λ-Π Coriolis interactions with $\Delta\Lambda = \pm 1$. In conjunction with high quality *ab initio* predictions by Tarroni and Carter, the unusually low state density in the $\tilde{X}$ manifold for C_2H offers a rare opportunity to assign such local vibronic interactions as well.

Figure 6.15 illustrates this with a blow up region around 4012 cm^{-1}, where the zeroth order symmetries and energies are taken directly from Tarroni and Carter. From the above discussion, we argued that the source of local coupling at $J' = 3.5$ in F_1 and $J' = 2.5$ in F_2 manifolds, respectively, required that the "dark" state responsible for the coupling be of $^2\Pi$, $^2\Delta$, . . . (i.e., non-Σ) symmetry. This was based on the high resolution evidence

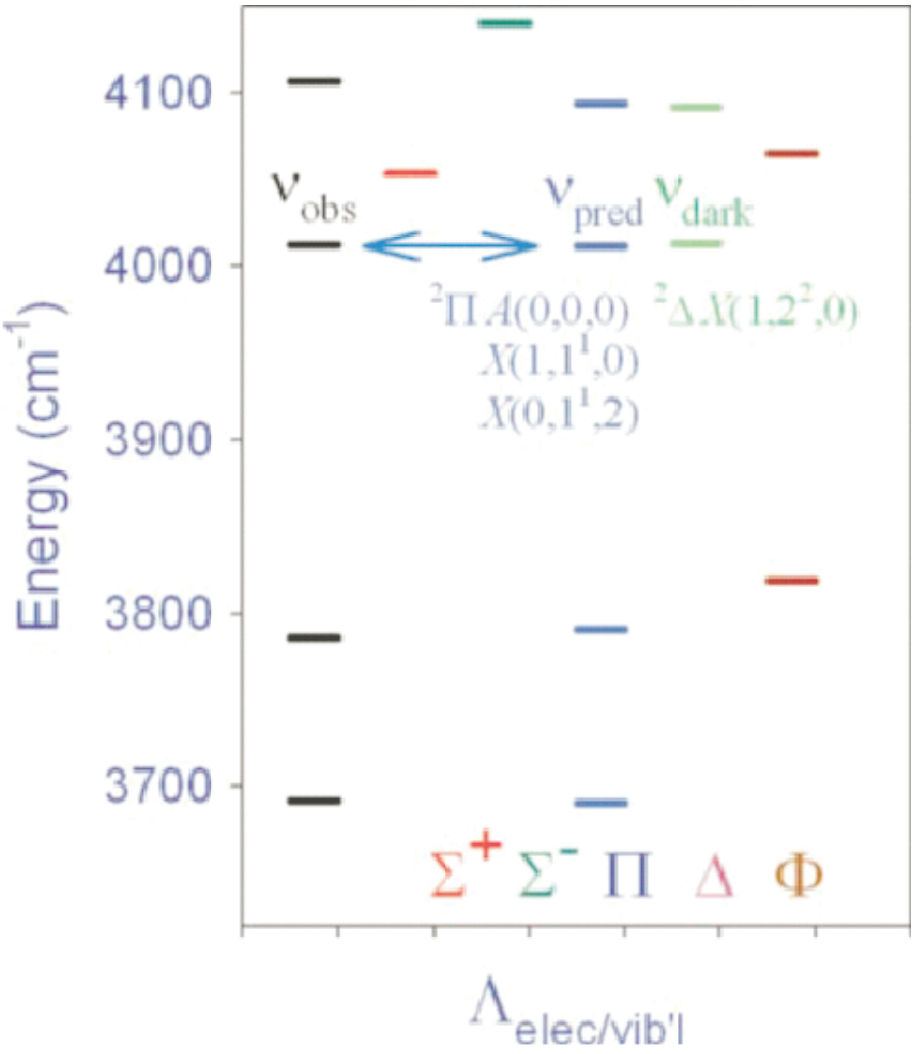

Figure 6.15: Overview of the experimentally observed (leftmost, in black) and calculated vibronic states in C_2H, where the predictions are from Tarroni and Carter and organized by angular momentum projection quantum number Λ. Note the excellent agreement between the four observed (black) and predicted (blue) $^2\Pi$ band origins. Also note the prediction of a highly vibrationally excited $^2\Delta$ $\tilde{X}$ (1,2^2,0) state in resonance with the 4012 cm^{-1} band origin, with no other state inside of a 300 cm^{-1} window. This makes for unambiguous assignment of the dark state responsible for the J dependent shifts observed in Figure 6.10 to $^2\Delta$ $\tilde{X}$ (1,2^2,0), i.e., one quantum of CH stretch and 2 quanta of CCH bend, which couples with the $\tilde{A}$ (0,0,0) state by $^2\Pi$-$^2\Delta$ Coriolis interactions.

in Figure 6.10 for perturbations involving both + and - parity levels, which implies that the dark state must also have both parity levels in close proximity. Furthermore, since $\Delta\Lambda = 0$ state mixing with the $^2\Pi$ electronic manifold is too strong to be consistent with 0.01 cm^{-1} displacements of only a single rotational level, one anticipates the perturber to be $^2\Delta$ symmetry ($\Delta\Lambda = 1$) or possibly higher. Interestingly, Tarroni and Carter[8, 9] predict two states (Π and Δ) in the 4012 cm^{-1} region, with no other states of any symmetry predicted inside of a 300 cm^{-1} window. The one state (Π) is the vibronically mixed state to which the strong $^2\Pi$ - $^2\Sigma^+$ band is already assigned. This leaves the remaining Δ state, $\tilde{X}$ (1,2^2,0), specifically one quantum of C-H stretch and two quanta of CCH bend, as the sole culprit for local vibronic interactions, coupling with the $^{\Pi}$ state via Δ-Π Coriolis interactions (i.e. $\Delta\Lambda = \pm 1$). With good signal to noise, the mixed states can acquire sufficient oscillator strength to be observed, which permits such an analysis to be taken even further. For example, we see a particularly clear example of highly localized crossing of manifolds in what is nominally the $\tilde{A} \leftarrow \tilde{X}$ band origin near 3600 cm^{-1}, which has permitted a detailed spectroscopic analysis of the dark state, as discussed elsewhere. In any event, the present high resolution data already offers a rigorous benchmark for understanding vibronic interactions in Renner-Teller systems as well as a rare glimpse into relatively high vibrational states of the $\tilde{A}$ manifold for such a fundamentally important combustion radical.

6.7 Summary and Conclusion

Infrared spectra for five $^2\Pi$ - $^2\Sigma^+$ bands of jet-cooled ethynyl radical (C_2H) in the gas phase have been reported at sub-Doppler resolution, which permits first observation of resolved main and satellite branches in each $^2\Pi$ - $^2\Sigma^+$ band. Parity state assignments have been corrected, with the observed lines nonlinearly least squares fit to a Hamiltonian model containing rotational, spin-rotational, spin-orbit, and lambda-doubling contributions for the $^2\Pi$ state. Three of the five bands can be quantitatively well-described by this simple Hamiltonian to within an experimental precision is 10 MHz rms. From these fits, we report

revised excited state constants and band origins for each of the bands. Vibronic assignments are revisited for the four observed bands and the dark perturbing state in the 4012 cm^{-1} $^2\Pi$ - $^2\Sigma^+$ band is unambiguously assigned to the $\tilde{X}^2\Delta$ ($1,2^2,0$) state, based on parity labeling and previous frequency and intensity predictions by Tarroni and Carter.[8, 9]

For the 3600 cm^{-1} band, this analysis reveals that the $^2\Pi_{1/2}$ upper parity levels are strongly and selectively perturbed by a close-lying dark state of $^2\Sigma^+$ symmetry, which limits the quality of such fits to $>$ 100-fold worse than expectations. However, incorporation of Σ-Π Coriolis coupling into the spectral model allows one to successfully fit the upper state to 15 MHz, i.e. comparable to experimental accuracy. Additionally, high resolution analysis of the spectral shifts and additional bright and dark state transitions has permitted a band origin (ν_{pert}) and rotational constant (B_{pert}) for the perturbing $^2\Sigma^+$ state to be determined, as well as the magnitude of the Coriolis coupling constant β_0. Finally, this facilitates unambiguous vibronic assignments to be made for the bright $^2\Pi$ as well as the dark $^2\Sigma^+$ state, guided by previous theoretical[8, 9] and experimental[197, 181] work. Identifying the locations of these perturbing dark states helps map out the complicated energy level structure in ethynyl radical, which represents a crucial step toward understanding and accurately modeling combustion and interstellar chemistry.

Chapter 7

High-Resolution Direct-Absorption Spectroscopy of Hydroxymethyl Radical in the CH Symmetric Stretching Region

7.1 Introduction

Hydroxymethyl radical, CH_2OH, has been the subject of over 100 experimental and theoretical papers in the last 40 years,[204] in large measure due to the important role it plays as a reactive intermediate in combustion and environmental chemistry. As one example, the combustion initiation step for oxygenated hydrocarbon fuels such as methanol is thought to be hydrogen abstraction by O_2 to produce hydroxymethyl radical, i.e., $CH_3OH + O_2 \leftarrow CH_2OH + HO_2$.[205, 206] There is also key hydroxymethyl radical in many of the subsequent chain reaction kinetics, for example, a fundamental chain propagation step in the oxidative combustion of methanol is $CH_3OH + HO_2 \leftarrow CH_2OH + H_2O_2$. Indeed, real time monitoring capabilities for CH_2OH radical in methanol combustion, as well as a detailed understanding of the underlying kinetics would be invaluable to optimizing the combustion process. Significantly complicating this task is the ubiquitous presence of methoxy radical (CH_3O) in many combustion systems, which has the same chemical composition as hydroxymethyl radical and consequently makes mass spectrometry sampling much less powerful for monitoring the underlying radical kinetics.

Roberts, M. A.; Sharp-Williams, E. N.; Nesbitt, D. J. *in preparation*

In addition to fundamental combustion processes, hydroxymethyl radical is an important intermediate for oxidative reactions occurring in the troposphere. Indeed, atmospheric scrubbing reactions of alkanes, alkenes, and alcohols all involve hydroxymethyl radical as a reactive intermediate. As one example, alkenes account for about 10 % of the non-methane organic compound concentration in many urban areas as a result of gasoline-based fuels and motor vehicle exhaust emissions. The initial oxidative scrubbing reactions of the simplest alkene (such as ethene) are initiated by hydroxyl (OH) radical attack, which features several steps involving CH_2OH as an intermediate.[207] Furthermore, methanol itself has a non-trivial concentration in the troposphere, ranging from 400-700 ppt depending upon the latitude, with about 85 % of atmospheric oxidative scrubbing reactions producing hydroxymethyl radical as a transient intermediate.[208]

The above examples provide strong motivation for development of high resolution near-IR experimental tools for spectroscopic identification of hydroxymethyl radical, as a key reactive intermediate in combustion and atmospheric reactions. Such keen levels of interest have spurred significant spectroscopic efforts. The earliest such studies on hydroxymethyl radical were based on electron spin resonance (ESR) detection, which, in conjunction with high level *ab initio* theoretical efforts, predicted a quasi-planar structure of the radical.[125] Low resolution infrared detection of CH_2OH radical was first obtained via matrix isolation spectroscopy and UV photolysis of methanol, which identified several vibrational modes in the fingerprint region.[209] These pioneering efforts stimulated a plethora of additional theoretical, kinetic, and spectroscopic studies.[210, 211, 212, 213, 214] Of particular relevance to our work is a series of resonance enhanced multiphoton ionization (REMPI) studies by Hudgens and coworkers, which identified multiple Rydberg states and Franck-Condon active vibrational progressions in these lower and upper state manifolds.[215, 216, 217]

In order to facilitate interpretation of their spectral data, Hudgens and coworkers calculated a 2-dimensional potential energy surface (MP2/6-311G(2df,2p) level) of the OH torsion (ν_8) and CH_2 (ν_9) wag coordinates, yielding detailed energy/frequency predictions for

these two coupled modes. By way of example, their potential surface calculations predict the frequency of the first excited ν_9 wag mode at 238 cm^{-1}, which is in excellent agreement with the observed value at 234 $\pm$ 5 cm^{-1}. Furthermore, these studies determined that quantum state labels for the two modes remained approximately separable, at least for vibrational energies sufficiently low with respect to the roughly 1700 cm^{-1} OH torsion barrier height. Most importantly, the presence of such a torsional barier predicts closely spaced tunneling levels, specifically with splittings between the ground and first excited torsional modes (ν_8) lower than the 1 cm^{-1} precision of the calculations.[204] Based on such an upper limit for these torsional splittings, one expects both ground and first excited tunneling levels to be populated even under jet-cooled conditions and thus the possibility for doubling of the near-IR spectra.

More recently, Reisler and coworkers did a number of studies on dissociation dynamics and the spectroscopy of hydroxymethyl radical.[218, 219, 220, 221, 222, 21, 223] In particular, these studies elucidated the spectroscopy of low lying electronic states including the 3s, $3p_x$, and $3p_z$ Rydberg levels as well as the CH symmetric stretch, CH asymmetric stretch, and OH stretch fundamental and first overtone. Specifically, Feng et al. exploited double resonant ionization detected IR spectroscopy via the $3p_z$ Rydberg state to probe both CH and OH stretches with a roughly 0.4 cm^{-1} laser linewidth and thus achieving partial rotational resolution. Least squares analysis of the rovibrational band contours yielded i) vibrational band origins and ii) A, B, and C rotational constants for the upper states, based upon *ab initio* estimates for the ground state. The CH asymmetric stretch and OH stretch spectra closely matched theoretical predictions of pure B-type, and A\B mixed type bands, respectively, as predicted by *ab initio* calculations. In contrast, the CH symmetric stretch was theoretically predicted to be predominantly A-type, but in fact required a more mixed 60% A-type \ 40% B-type character to adequately fit the data. Additionally, Feng et al. did not see any evidence of additional structure in their data due to the OH torsional mode, which also provided an upper limit of 0.1 cm^{-1} for the ground state tunneling splitting.

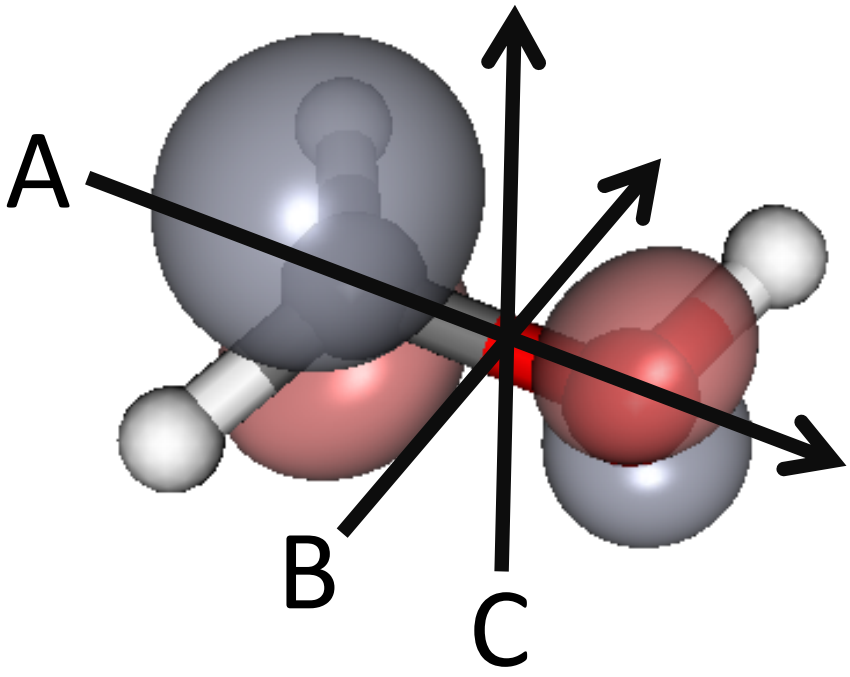

Figure 7.1: Quasiplanar structure of hydroxymethyl radical with HOMO and priciple axis orientation shown. The equilibrium geometry has a slightly bent methyl group in the out-of-plane bend coordinate, due to competition between sp^3 and sp^2 hybridization around the central C atom.

In the current study, we have built on the pioneering work of Reisler and coworkers to help guide a near-IR search for hydroxymethyl radical with sub-Doppler, fully rovibrationally resolved spectral splitting. Figure 7.1 shows the equilibrium structure and principal axes of hydroxymethyl radical and the highest occupied molecular orbital (HOMO), calculated at the B3LYP/6-311g++(3df,3pf) level[3]. Although we have very good estimates from previous studies for all three H-stretching bands, we have chosen first to focus on the symmetric CH stretch spectral region near 3043 cm^{-1}, which is predicted to have the highest integrated band intensity. Indeed, we observe a surprisingly rich spectrum in this region, partially congested by discharge-induced hot band transitions in methanol and presently under analysis.

However, as first high resolution data on this critical combustion radical, we have been able to unambiguously identify and assign the $K_a = 0 \leftarrow 0$ progression of symmetric stretch excited CH_2OH, and which serves as the primary focus of this report.

7.2 Experiment

The high-resolution infrared spectrometer used in these experiments has been described in detail elsewhere and will only be briefly summarized here.[82, 81, 1] Narrow-linewidth (< 2 MHz), high-precision infrared light is generated by difference frequency generation of a single frequency argon ion laser (Ar^+) and a tunable cw dye laser (R6G, Exciton dyes) in a temperature-tuned periodically-poled lithium niobate ($LiNbO_3$) crystal. The infrared radiation is split into reference and signal beams, with the reference beam directed onto a liquid-nitrogen cooled InSb detector. The signal beam is directed through a CaF_2 window into a 16-pass Herriot cell mounted in the slit jet discharge expansion vacuum chamber, with each pass sampling a 4 cm long path length of jet of radicals. Spectra of CH_2OH radical are recorded via transient depletion of the transmitted IR light monitored by the signal InSb detector. The signals from the two detectors are combined in a common mode noise subtractor before being sent to a lock-in detector and subsequently recorded on a computer (via a NI-6025E analogue-digital card). Relative frequency precision (10 MHz) is obtained by monitoring dye laser fringes through an actively stabilized (< 1 MHz rms) Fabry-Perot etalon, with the Ar^+ laser actively locked to the same Fabry-Perot cavity to provide single frequency operation and stability while scanning. Absolute frequency calibration is achieved by comparison with well characterized ν_3 CH stretch absorptions of jet cooled methane doped into the expansion and monitored in the same spectral region.[83]

Jet-cooled hydroxymethyl radicals are produced by supersonic expansion of trace amounts of precursor in 70% neon, 30% helium (Ne70) buffer gas mixture through a pulsed slit jet nozzle (19 Hz, 500 s duration). Radicals are generated via electron associative detachment in a square-wave modulated (50 KHz) discharge at the expansion orifice. For the many radicals

previously studied with this apparatus, the precursor has been designed to contain a weak bond cleavage point (typically C-Br or C-I) to form the desired target radical, typically by dissociative detachment. Such precursors for hydroxymethyl radical are unstable, which led us to develop two recipes based on methanol, though this requires cleavage of a strong CH bond. Our first approach, i.e., simply a Ne70 discharge with trace methanol, was successful in generating sufficient concentrations of hydroxymethyl radical but also generated spectral interferences from methane and vibrationally excited methanol. Our second approach was based on doping Cl_2 into the Ne70/methanol discharge expansion, which generates hydroxymethyl radical my selective CH bond abstraction reactions of Cl + $CH_3OH \rightarrow CH_2OH$ + HCl and, more importantly, yields fewer spectral interferences. Similar chemistry has been used before by several groups, but they used photolysis to generate Cl radicals to react with CH_3OH and generate CH_2OH.[224, 225, 226]

Figure 7.2 shows traces of three different species generated with the two different synthesis, with the black line showing the CH_3OH in Ne70 discharge and the red line showing the CH_3OH + Cl_2 + Ne70 discharge. The first panel plots the CH_2OH $4_{04} \leftarrow 3_{03}$ ($N'_{K'_aK'_c} \leftarrow N''_{K''_aK''_c}$ labeling) line, which shows an appreciable percent increase in absorbance with addition of Cl_2 (assignment will be discussed in detail in section 7.3). The second panel illustrates that methane is produced in a methanol discharge, but with the addition of the chlorine, no methane is detectable. The third panel is a methanol absorption line to illustrate the decrease in precursor absorption with the addition of molecular chlorine. The measured linewidths of the transition is 80 MHz in both syntheses. While both spectra are congested in this region, the synthesis with Cl_2 makes CH_2OH with fewer other molecules.

7.3 Results and Analysis

A sample region of the CH_2OH symmetric stretch is shown in Figure 7.3. A representative section of experimental data is plotted in panel a), with the assignment above the line, panel b) shows the predictions based upon the constants obtained in the fit, discussed below,

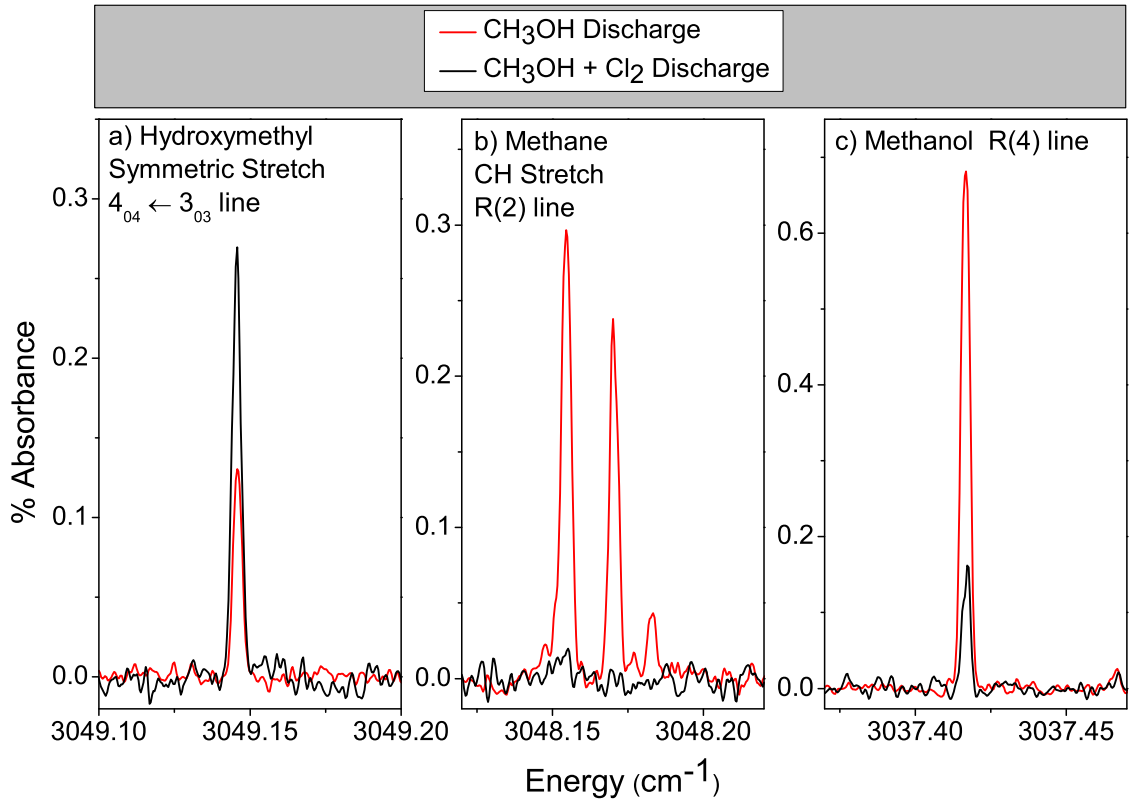

Figure 7.2: Comparison of two difference discharge chemistries for "synthesis" of jet cooled CH_2OH. The red line represents three sample spectral regions for a discharge with CH_3OH doped into Ne-70 diluent, with the corresponding black line representing comparable data scans for a $CH_3OH + Cl_2$ discharge, which generates hydroxymethyl radical by $Cl + CH_3OH \rightarrow HCl + CH_2OH$ chemistry. Panel a) illustrates how the CH_2OH number density nearly doubles for chemical formation via H atom abstraction by discharge generated Cl atoms. Interestingly, panels b) and c) also reveal how the spectral density of undesired species (such as methane and precursor methanol) can be substantially minimized under the Cl atom synthetic pathway.

and an inset highlighting the signal-to-noise is in panel c). The identified hydroxymethyl radical lines are the $K_a = 0 \leftarrow 0$ progression, which is predicted to be the highest intensity progression based upon nuclear spin statistics and will be discussed in Section 7.4. The spacing between the $K_a = 0$ lines is approximately (B+C)/2. Using *ab initio* rotational constants to guide the search, we are able to identify a clear progression of lines with this spacing. As

an additional confirmation of the assignment, we compare the spectrum with two different mechanisms of generating hydroxymethyl radical. While the progression appears with both chemistries, it is much more intense with the Cl_2 synthesis. This allows us to identify the lines that are most likely due to CH_2OH based upon an increase in intensity upon adding Cl_2 and ignore the lines from other species.

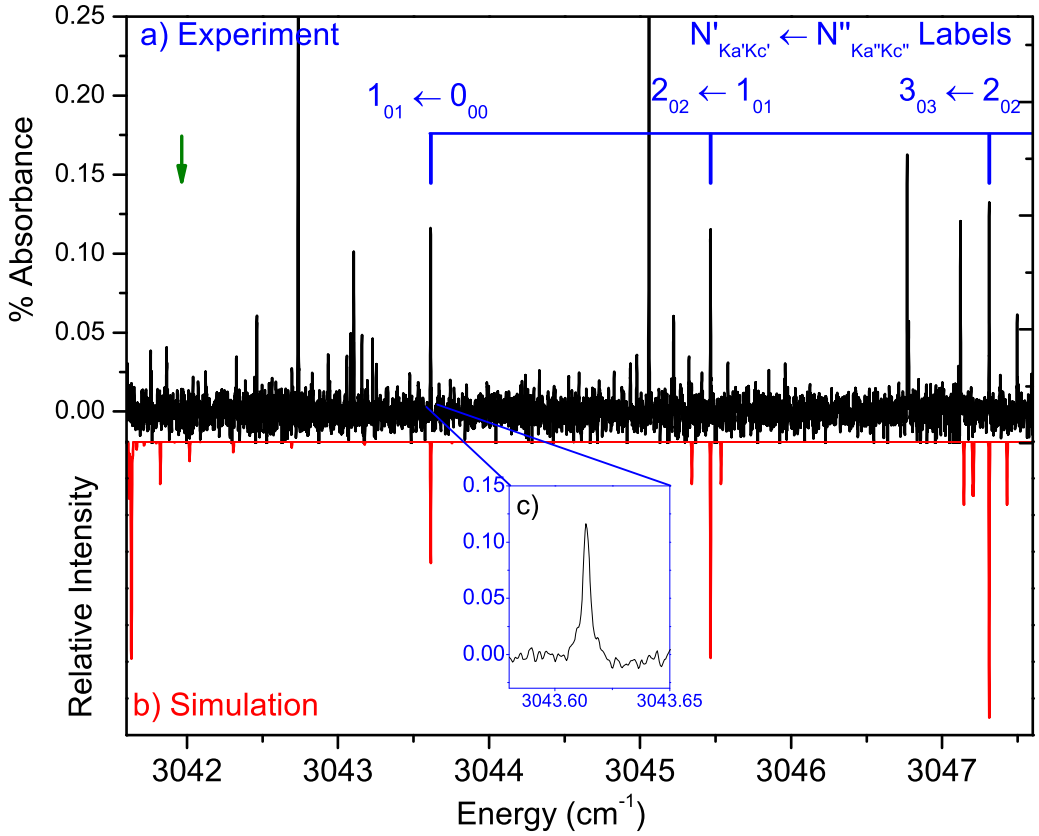

Figure 7.3: Sample data shown with simulation based upon least squares fits to a Watson asymmetric top Hamiltonian. Panel a) reveals a spectral scan region near the ν_3 symmetric CH stretch band origin, with assignment of the $K_a = 0 \leftarrow 0$ progression shown above (in blue). The green arrow indicates the missing spectral line in the progression makes the band origin assignment and J-labeling unambiguous. Panel b) provides a spectral simulation (in red) of the A type band $K_a = 0 \leftarrow 0$ progression based upon spectroscopic constants from the least-squares fit. The blow up region in panel c) illustrates a single $1_{01} \leftarrow 0_{00}$ absorption line in the ν_3 band, which serves to characterize typical signal-to-noise levels of $>$ 10:1 in the current experiment.

There will rigorously be no Q-branch for the $K_a = 0$ band, which makes the identification of the band origin straightforward. As is seen in Figure 7.3, there is a line missing in the progression unambiguously identifying the band origin. In the study by Feng et al,[21] the band origin they list is 3043.4 cm^{-1}, which differs from the band origin obtained in this study by approximately (B+C)/2. With the high-resolution of the present work, we are able to resolve the lack of a $K_a = 0$ line. Without the ability to identify a missing line it is reasonable to have an assignment shifted by J, as in the study by Feng et al. Table 7.3 shows the list of lines and assignments. The $K_a = 0 \leftarrow 0$ progression is fit to a Watson asymmetric top Hamiltonian. Because of the nature of the progression, there is not enough information to fit the A-constants, so those are fixed at *ab initio* values. Specifically, the constants varied in the fit are $\overline{B}''$, D''_J, $\overline{B}'$, and D'_J and the Hamiltonian used is ν + B J(J+1) + D_J $[J(J+1)]^2$. The fit results are summarized in Table 7.3 and the predictions based upon these constants are shown in panel b of Figure 7.3.

Table 7.1: Experimental line positions of the $K_a = 0 \leftarrow 0$ progression with assignments using the $N'_{K'_aK'_c} \leftarrow N''_{K''_aK''_c}$ notation.

Frequency (cm^{-1})	$N'_{K'_aK'_c}$	$N''_{K''_aK''_c}$
3034.31828	303	404
3036.17478	2_{02}	3_{03}
3038.03187	1_{01}	2_{02}
3039.89590	0_{00}	1_{01}
3043.61368	1_{01}	0_{00}
3045.46667	2_{02}	1_{01}
3047.31135	3_{03}	2_{02}
3049.14586	4_{04}	3_{03}
3050.96781	5_{05}	4_{04}
3052.77492	6_{06}	5_{05}
3054.56541	7_{07}	6_{06}

Table 7.2: Comparison of molecular constants, all constants in wavenumbers (cm^{-1}). Present work fit to ν + B J(J+1) + D_J $[J(J+1)]^2$ Hamiltonian

	scaled *ab initio* values	Previous Work[21]	Present Work
B′′	0.9371		0.9305(2)
$D''_J \times 10^{-4}$			0.91(2)
B′		0.93(2)	0.9291(2)
$D'_J \times 10^{-4}$			0.95(2)
ν	3022(10)	3043.3	3041.7560(5)

[a] Calculated at the B3LYP\6-311++g(3df,3pd) level[3], band origin frequency scaled by 0.9637 (scaling factor from Dong et al[1]).

7.4 Discussion

The intensity of the lines is used to characterize the rotational temperature of the molecules in the slit-jet and in this case verify that the two chemistries have the same rotational temperature. The intensity of any one rotational line is a function of the appropriate Hönl-London factor, degeneracies, and a Boltzmann factor of lower state energy and jet rotational temperature. Figure 7.4 presents a standard semilogarithmic Boltzmann plot of the experimental populations vs. rotational energy of the lower state. The red squares are from the CH_3OH + Cl_2 synthesis and the blue circles are from the CH_3OH only discharge. The difference in total quantity of CH_2OH produced in the two syntheses is reflected in the different y-intercepts. Not only do the points fit to a straight line, indicating that the rotational population distribution is well described by a temperature, but it also shows that both methods of producing CH_2OH produce it at the same rotational temperature, within the error of the fits, of about 29 K.

One thing to notice is that, based upon intensity predictions, we should be able to see clearly the $K_a = 1 \leftarrow 1$ progression. In the absence of other effects, the $K_a = 1 \leftarrow 1$ progression would be comparably intense as the $K_a = 0 \leftarrow 0$ progression. However, in hydroxymethyl radical there is the possibility of seeing the effects of nuclear spin statistics as a result of the two equivalent hydrogen atoms bonded to the carbon atom. In this

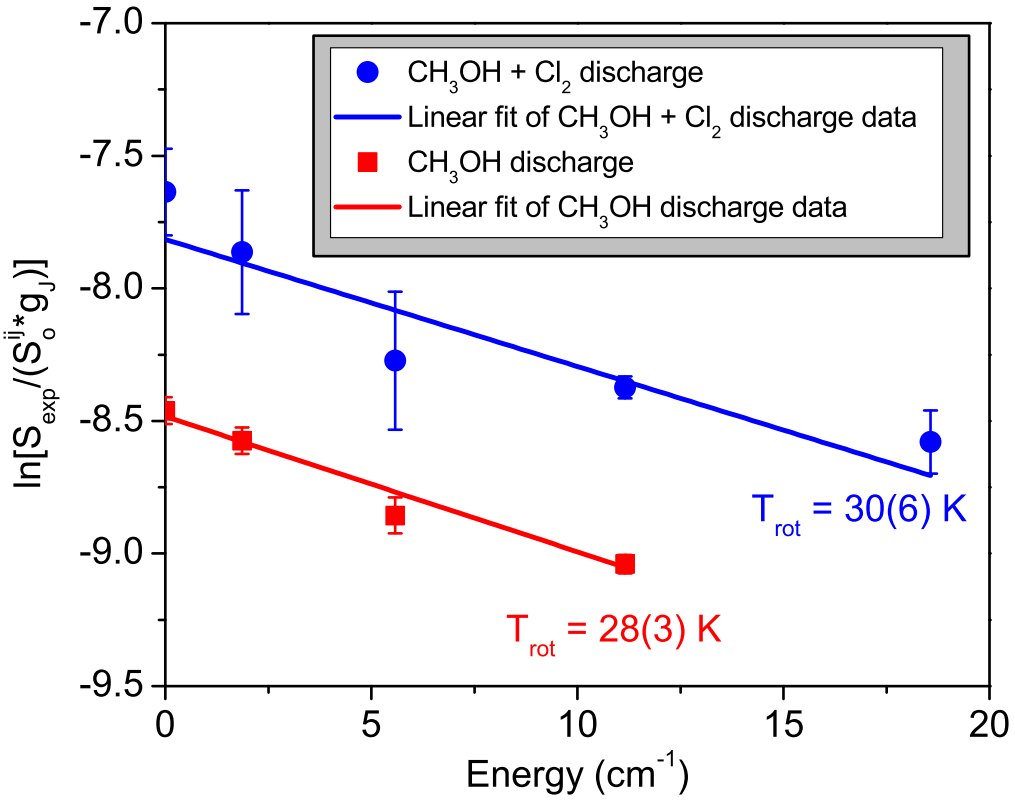

Figure 7.4: Boltzmann plot analysis of $\nu 3$ symmetric CH stretch band spectral line intensities for jet cooled CH2OH radical obtained under both i) CH_3OH doped discharge (red squares) as well as ii) Cl_2/CH_3OH discharge (blue circles) conditions. S_{exp} is the integrated line strength in units of absolute absorbance), with S_{ij} and g_J = 2J+1 representing the line strength factor and m_J degeneracy, respectively. The difference in y-intercepts reflects the roughly 60% lower density of CH_2OH radical in the CH_3OH-only discharge.

case, the two hydrogen atoms are equivalent via a 180° rotation along the CO axis and a rotation of the OH torsional motion. At the energies accessible in this experiment, it is expected that the hydrogen bonded to the oxygen is not interchangeable with the other two hydrogen atoms so it does not need to be included in the nuclear spin statistics calculation. Hydrogen atoms are Fermions with a nuclear spin of $\frac{1}{2}$ and as such, the overall wavefunction of the molecule must be antisymmetric with respect to exchange of those two hydrogen nuclei. The overall wavefunction, Ψ_{tot} , is a product of the individual components,

$\Psi_{electronic}\Psi_{torsion}\Psi_{vibrational}\Psi_{rotational}\Psi_{nuclearspin}$. The electronic component, $\Psi_{electronic}$, can be visualized as the orbital shown in figure 7.1 and is antisymmetric with respect to the 180° rotation. The vibrational wavefuntion, broken into two parts for clarity, $\Psi_{torsion}$ and $\Psi_{vibrational}$, are symmetric in the ground vibrational state and lowest tunneling state. From the *ab initio* predictions, the A-axis of the molecule is approximately along the CO bond, as shown in figure 7.1 and consequently the rotational wavefunction, $\Psi_{rotational}$, is symmetric for even K_a values and antisymmetric for odd K_a values. Therefore, the ground tunneling state has a 3:1 intensity pattern for $K_a = 0 : K_a = 1$ states. The first excited tunneling level will an antisymmetric $\Psi_{torsion}$ and will therefore have the opposite nuclear spin statistics. Furthermore, if we are able to resolve the transitions out of the different tunneling levels, not only might we see two progressions, but the two progressions will have different nuclear spin statistics.

The observed transition out of the ground vibrational state and ground torsional state is to the ground torsional level of the first excited CH symmetric stretch. The transition out of the first excited torsional level of the ground vibrational state would go to the first excited torsional level of the CH symmetric stretch. Consequently, the different in band origin between the two bands is equal to the difference in tunneling splitting between the ground vibrational state and the CH symmetric stretch state, which is likely quite small. If the splitting between the two bands is too small to be resolved, no nuclear spin statistics will be observed and the K_a = even and K_a = odd progressions will be of equal nuclear spin weight. Given the prominence of the $K_a = 0 \leftarrow 0$ progression, in the case of overlapping torsional bands, there would be a prominent $K_a = 1 \leftarrow 1$ progression. Since we do not see a $K_a = 1 \leftarrow 1$ progression, it is quite possible that we can resolve the splitting between the two torsional bands. We have looked for, but not yet identified, transitions originating from the first excited torsional level. This is quite reasonable considering the likely decrease in population between the ground and first excited torsional level in a supersonic jet. Adding to this decrease in signal is that the now 1:3 ($K_a = 0$: $K_a = 1$) nuclear spin statistics decrease

the signal of the most prominent $K_a = 0 \leftarrow 0$ band. It is not surprising then, that the band originating out of the first excited torsional level is not seen.

At this point, we are unable to see the $K_a = 1 \leftarrow 1$ progression, in spite of predictions indicating it should be visible. One possibility for this is that there is an anomalously large change in the A constant upon vibrational excitation, shifting the K_a $1 \leftarrow 1$ progression farther from the K_a $0 \leftarrow 0$ progression than initially predicted. Even in with this scenario, we might expect to fine the $K_a = 1 \leftarrow 1$ progression within several wavenumbers, which we don't see. The identification of the $K_a = 1 \leftarrow 1$ progression as well as any B-type progression and progressions out of the upper tunneling state are ongoing. Even though predictions indicate that the $K_a = 1 \leftarrow 1$ band should be detectable based upon the signal-to-noise levels and that the band should be close to the $K_a = 0 \leftarrow 0$ band, we are not able to find it even with a larger search region. This clearly indicates that the rigid rotor predictions are somewhat inadequate for describing the rotational structure of hydroxymethyl radical. The identification of B-type transitions is contingent upon obtaining 2-line combination differences that either form 4-line combination differences with other B-type transitions or match energy levels from the identified A-type band. Even with the estimate of 40% of B-type character, the p-branch transitions will have very low signal-to-noise due to unfavorable Hönl-London factors, which precludes using internal B-type 4-line combination differences. With only the A-type K_a $0 \leftarrow 0$ band identified, no inter-band 4-line combination differences have been found. This could be because the contribution of the B-type band is small than reported previously or with the congested spectra we do not yet have enough information to make a positive identification.

7.5 Conclusion and Summary

First fully rotationally resolved high resolution spectra of hydroxymethyl radical have been obtained in the $K_a = 0 \leftarrow 0$ symmetric CH stretch region, resulting in much improved experimental values for ground state rotational constants and vibrational band ori-

gin. Additional confirmation of the spectra arising from hydroxymethyl radical is achieved by synthesizing the radical in two different ways: i) via electron bombardment cleavage of methanol doped in a supersonic discharge expansion ($CH_3OH \rightarrow CH_2OH + H$) and ii) selective chemical H atom removal by $Cl + CH_3OH \rightarrow CH_2OH + HCl$ reactions in a Cl_2 and methanol doped discharge. The precision of the ground state rotational constants provide reliable frequency predictions to minimize spectral search and thereby enable further laboratory detection and characterization of this highly reactive radical in the microwave, mm wave, far-IR and near-IR spectroscopic region. The large amplitude COH torsional tunneling and out of plane CH_2 wagging motion provide important state-of-the-art challenges for benchmarking high quality potential energy surfaces as well as furthering the development of efficient computational methods for multidimensional QM dynamics calculations. It is our hope that such synergism between high resolution spectroscopic efforts, *ab initio* chemistry and rigorous dynamical theory will help elucidate the role of this important radical in diverse venues ranging from combustion chemistry to atmospheric chemistry.

Chapter 8

Conversion of Coherent 899-29 system into high-accuracy, high-precision automatically-tunable laser: application in a new mid-IR spectrometer for study of transient intermediates

8.1 Introduction

High resolution spectroscopy has proven a powerful technique for the structure and bonding of molecules.[227] For example, in vibrational spectroscopy increasing the resolution often reveals rich rotational structure that allows for direct experimental observation of the molecular structure. Sometimes even smaller effects, such as energy level shifts due to electron-spin nuclear-spin interaction can be resolved and tell even more about the electronic structure.[35] For molecular spectroscopy, knowing the frequency of a transition with a precision of 10 MHz permits unambiguous assignment of the rotational and vibrational transitions for many molecules. Another recent motivation for developing high resolution systems has stemmed from a desire to accurately measure the Boltzmann constant by measuring molecular transition line profiles, which also requires high accuracy and precision[37, 38]. A popular tool for high-resolution spectroscopy is the Coherent 899-29 Ti:Sapphire laser system. This commercial system was designed for automated scanning at high-resolution and is commonly used in the field of spectroscopy. The laser system includes a wavemeter, electronics, and computer system to automatically scan the desired frequency range. The laser has a stable

Roberts, M. A.; Sharp-Williams, E. N.; Nesbitt, D. J. *in preparation*

narrow linewidth that lends itself to high-resolution work. However the achievable resolution is only about 200 MHz, limiting the quality of the spectroscopic data that can be obtained with the system. In this paper, we provide a cost effective and straightforward solution to improve the resolution of this laser system to <10 MHz, while improving upon the automated scanning capability of the laser. To demonstrate the new capability of the laser system, we incorporate it into a new mid-IR automated scanning spectrometer with improvements over previously published spectrometers. One aspect that separates this spectrometer from its predecessors is the fast and automated scanning; there are also other improvements including an extended frequency range, different method of obtaining the frequency axis, and the use of solid state lasers providing a more stable setup.

In creating a mid-IR spectrometer, there are many experimental challenges that need to be overcome and subsequently the technology used to mid-IR spectroscopy has changed as technology improved. One of the older technologies for creating tunable infrared (IR) light is the color center laser. These lasers have a limited tuning range and are experimentally challenging and delicate; the crystals are very hygroscopic and light sensitive and therefore must be keep under high vacuum, cooled by liquid nitrogen, and away from light[41]. Lead salt Diode lasers can be used, but are limited by a relatively small tuning range of tens of wavenumbers. Quantum cascade lasers (QCL) also reach the mid-IR, however currently most QCL's have a limited continuous tuning range, usually on the order of several tens of wavenumbers. The external cavity quantum cascade lasers can have up to 250 cm^{-1} tuning range, but compared to a 1500 cm^{-1} tuning range of a dye laser, it is still quite small[42, 43, 44]. Frequency conversion is the most frequently used method for generating mid-IR radiation. Miller and coworkers have used Raman stimulation of a gas cell to create mid-infrared light, with a resolution of about 200 MHz[45]. Difference frequency generation of a single frequency argon ion laser with a tunable dye laser in a lithium niobate crystal to create mid-infrared light[26] was first reported by Pine et al. in 1974. Pine's system is very versatile and has been very successfully adapted, with modification, by many groups [53]

including our group but still requires partial manual scanning.[57] The spectrometer in our group uses a tunable ring dye laser and a single frequency argon ion laser to generate mid-IR light via difference frequency generation in a periodically poled lithium niobate crystal and has a frequency precision of better than 10 MHz. An optical parametric oscillator (OPO) configuration is a very common way to generate mid-IR radiation and there are many in the literature as well as commercial models.[228] One advantage of just DFG over an OPO is that with DFG all of the frequency diagnostics, locks, and scanning mechanisms can be applied to the visible (or near-IR) lasers and not the mid-IR, making finding optics and detectors easier, cheaper, and extendible to other frequencies with the change of a crystal or single-frequency laser.

In order to improve upon existing mid-IR spectrometers, this system needs i) a large, continuously tunable frequency range in the mid-IR, ii) frequency precision and accuracy of 10 MHz or better, iii) an improvement in speed and ease of data acquisition, iv) high detection sensitivity, and v) ability to create relatively large concentrations of radicals and ions. The technique presented in this paper combines an actively stabilized Nd:YAG laser and the tunable Ti:Sapphire laser in a periodically poled lithium niobate crystal where, via difference frequency generation, tunable mid-IR light is generated. To our knowledge, there are two other Ti:Sapph and YAG DFG systems published, both in 2008, for sensing applications[47, 48] and measuring the Boltzmann constant[49]. They utilized much more complicated methods to stabilize their YAG laser and were limited by the stability of the Ti:Sapph laser. Those systems also lack the scanning infrastructure to scan continuously for long distances and they are setup to only look at Doppler-limited neutrals. The system presented here is unique in combining the laser system, with the sub-Doppler radical and ion generation system, with the machinery for extended and automated continuous scanning.

Since the scanning functionality used is heavily based upon the Ti:Sapphire and Autoscan system, a brief introduction is useful. The Ti:Sapph laser is set up in a vertical ring configuration with a Faraday Rotator in the cavity to ensure unidirectional lasing. A bire-

fringent filter and two intracavity etalons narrow the laser linewidth to a single cavity mode. The thick intracavity etalon consists of two mirrors separated by a piezo cylinder and is locked to peak transmission output and therefore tracks with the laser cavity length change. The thin intracavity etalon, consisting of a single optic, also tracks with the laser scanning, but tracks by tilting. All of the electronics necessary to achieve locking and scanning up to 30 GHz are contained in the laser control box. For increased stability, the laser is locked to an external cavity with feedback sent to a piezo-mounted cavity mirror. Tunability of the laser is achieved by galvo-controlled rotation of a quartz plate that changes the cavity length. The laser achieves tunability by rotation of a plate in the external cavity changing that cavities length, which causes the laser to follow the scanning by changing the laser cavity length by rotation of the quartz plate in the laser cavity.

The laser system also includes an attached wavemeter and system for automated scanning of large frequency regions, called Autoscan, and consists of a separate set of electronic controls and a computer. The Autoscan computer provides an interface to read the frequency of the laser, change the laser frequency to any specified frequency, and automatically scan the laser any specified frequency range. Scanning of the laser is achieved through control over the laser elements listed above and a stepper motor attached to the birefringent filter. This allows the Autoscan system and laser move to any specified frequency at which the laser lases. Autoscan contains algorithms to check the laser frequency, move the elements in the laser (birefringent filter, etalons, etc.), check the frequency again and repeat until the desired laser frequency is reached. To scan, the system first moves to the specified starting position. It then scans by moving the reference cavity plate, forcing the laser to follow. In step-scan mode, the mode used here, the user specifies the frequency step in between each data point. The laser has a linearization procedure to determine what voltage to apply to the reference cavity plate to generate the most linear scan. This continues for 10.2 GHz and is called a segment. At the end of a segment, the laser uses the wavemeter to move to a frequency that is 10 GHz from the starting frequency of the previous segment. Once

the laser reaches the new frequency, it scans another 10.2 GHz segment. This procedure is repeated until the desired frequency region is scanned, completing what is referred to as a scan. The frequency associated with each data point is given as the starting frequency plus 10 GHz times the segment number (with zero corresponding to the first segment) plus the step-size times the data point number for the segment. The wavemeter used to measure the frequencies at the start of each segment has a stated accuracy of 200 MHz and that means there is a 200 MHz uncertainty at the start of each segment. To obtain the frequency for each data point, the step size is defined as the frequency length between data points and is added to the start frequency. This means that each data point has a 200 MHz uncertainty, plus any difference between the stated step size and the actual step size (found to be usually within a few MHz). This large uncertainty in the frequency of each 10.2 GHz segment is the crux of the problem with the Autoscan system.

There are two major improvements needed before the Autoscan system can be used for high-resolution mid-IR spectroscopy. Since the wavemeter is integral to the automated scanning system, we are motivated to keep as much of the system as possible. The first problem that needs to be address is the precision and accuracy of the frequency axis provided by the Autoscan system. The second problem is the integration of the laser system into a larger system. In this paper, we present a novel implementation to improve upon the accuracy of the Coherent 899-29 laser system such that is can be used to high-resolution spectroscopy with frequency precision of about 10 MHz. Using a set of locked cavities, we are able to take advantage of the frequency readings provided by the associated wavemeter and the frequency axis provided by the Autoscan system but correct the frequency such that the precision is improved more than 10-fold. This solution means that we are taking advantage as much of the existing machinery as possible in order to minimize the work needed improve the frequency precision. To illustrate the use of the improved system, we integrate the laser into a fully automated mid-IR scanning spectrometer that has several improvements from previously published mid-IR spectrometers.

The organization of the chapter is as follows: In section 8.2 the two major modifications of the Coherent Autoscan system are discussed. First the modifications necessary to the Autoscan system are described: the procedure for correcting the Autoscan-generated axis is in section 8.2.1 and the remote operation of the laser and Autoscan is in section 8.2.2. The mid-IR spectrometer for studying transient species is presented in section 8.3 and some sample data illustrating the success of the spectrometer are in section 8.4.

8.2 Precision Automated Scanning of Ti:Sapphire Laser

8.2.1 Frequency Determination

The frequency axis needs to be corrected in order to obtain high-precision scans. The two problems that need to be fixed are i) lack of frequency accuracy causing errors when stitching together segments and scans and ii) nonlinear scanning during a segment. To fix these problems we will use the Autoscan wavemeter, with accuracy of 200 MHz, and two stabilized optical transfer cavities, one with a 1.5 GHz FSR and another with a 250 MHz FSR. While the Ti:Sapphire laser is scanning, we record the Ti:Sapphire transmission through each cavity. At the start of each segment, the Autoscan wavemeter reading is used to assign a fringe number to the 1.5 GHz FSR cavity fringe. A Snyder peak-finder algorithm[34] is used to find the peak positions of each fringe. The fringe number on the 1.5 GHz FSR cavity is used to assign a fringe number to the 250 MHz FSR cavity. The Autoscan wavemeter is not accurate enough to unambiguously assign a fringe number to the 250 MHz cavity but is accurate enough to assign a fringe number to the 1.5 GHz FSR cavity. To correct for the nonlinearity in scanning, we define the frequency difference between each 250 MHz FSR etalon peak to be the precise value of the FSR and then linearly interpolate the data points between each peak. Using a relatively small (250 MHz) FSR cavity for this step minimizes the number of data points to be interpolated. Once a peak from the 250 MHz FSR cavity in each segment of each scan is assigned a fringe number and the scan is

linearized, it is possible to precisely stitch together scans and assign an absolute frequency using a molecular reference line. A sample scan showing fringes from the locked 250 MHz cavity before and after the correction process is is Fig. 8.1. The choice of 1.5 GHz and 250 MHz is discussed in section 8.2.1.1.

The 250 MHz optical transfer cavity consists of two curved dielectric mirrors mounted to a hollow tube. The tube has 2.5 cm of piezo material on one end, a section of pyrex glass, a section of stainless steel wrapped in a resistive heater, and finally another section of pyrex. The piezo allows for fast changes of cavity length and the heated steel responds to slow changes. The cavity is aligned in a confocal bowtie configuration. A home-built polarization-stabilized HeNe laser[54] is sent through the cavity and the peak of the transmission fringe is used to lock the frequency of the cavity mode. Once the HeNe is stabilized, it is used to provide a stable source to lock the cavities needed in the rest of the instrument[31]. The 1.5 GHz cavity is similar, but does not have the stainless steel segment, the heater is wrapped directly around the pyrex glass tube, and the piezo material is only 1.5 cm long. These changes are only necessary because of the difference in distance changes necessary to correct for errors in a physically shorter cavity are small than for a physically longer cavity. Once the two optical transfer cavities are locked to the HeNe, the free spectral range of the cavity is precisely determined. While the Ti:Sapphire laser is scanning the transmission fringes through both the 250 MHz cavity and 1.5 GHz cavity are recorded; sample data from two different scans is shown in panel a) of Fig. 8.1.

To correct for both the nonlinearity in scanning and the inaccurate and imprecise frequency readings of the Autoscan, we adopted a two cavity solution. At the start of each segment the Autoscan wavemeter sets itself to within $\pm$ 100 MHz of the desired starting frequency for that segment and starts to step-scan. As the laser scans, we record the inference fringes of the Ti:Sapphire laser output through two locked bow-tie confocal cavities, one with an approximate free spectral range of 1.5 GHz and the other with about a 250 MHz free spectral range. Since we don't have control over where each segment begins, we are not able

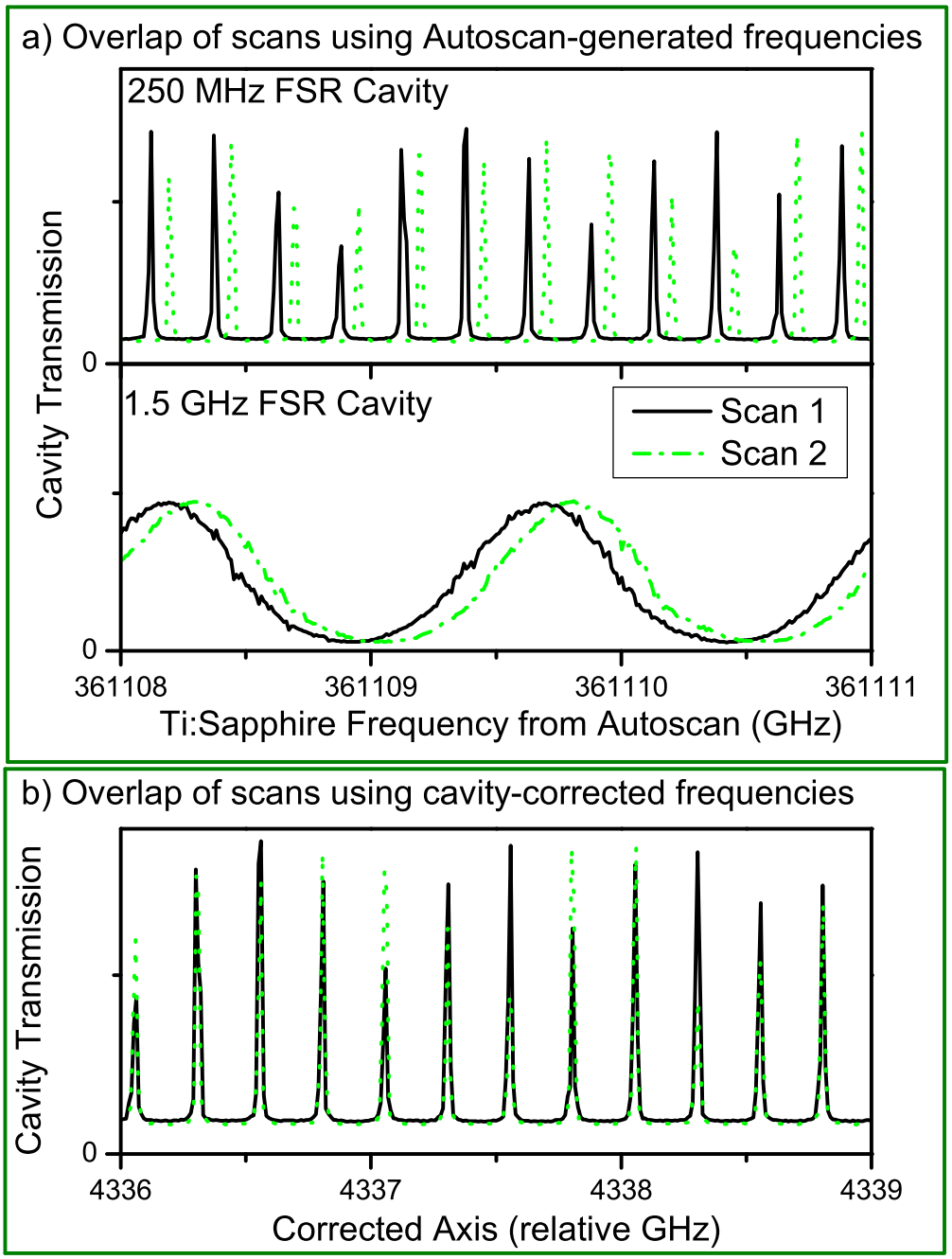

Figure 8.1: Two sample Ti:Sapphire laser transmission fringes through the two optical transfer cavities. Panel a) shows an overlap of the two scans if the frequency generated by Autoscan is used to overlap two scans. The fringes from the two scans do not overlap, but there is no ambiguity as to which 1.5 GHz cavity fringes should overlap while there is ambiguity for the 250 MHz cavity fringes. Panel b) illustrates the high quality of the overlap between scans when the corrected frequency axis is used.

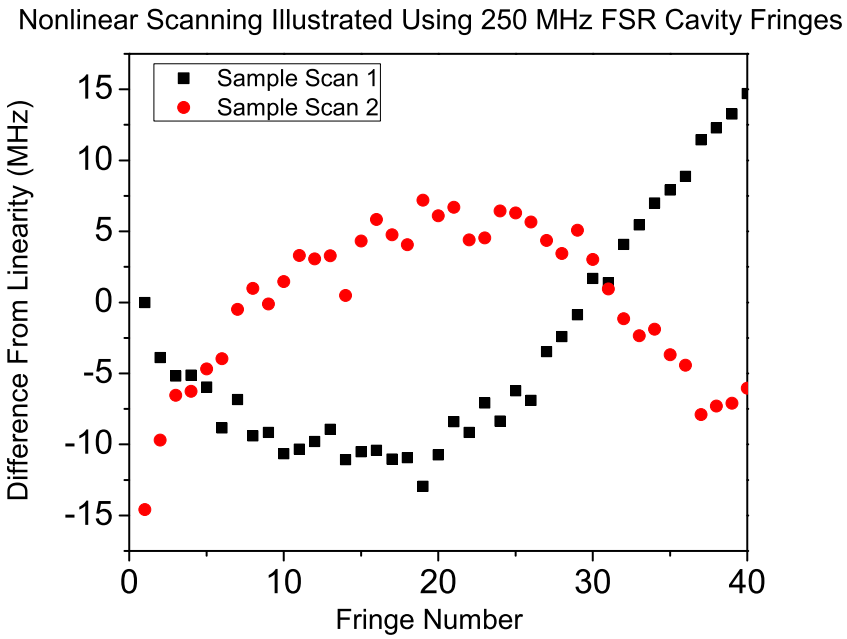

Figure 8.2: Illustration of nonlinear scanning of the Ti:Sapphire laser system. The plot is of the difference between the 250 MHz FSR cavity peak positions and simulated peak positions for a linear scan plotted as a function of the fringe count during the segment.

to always start on the peak of the fringe, which is not an issue with the two cavity method. The frequency determination can be quantified with propagation of error calculations. Each Autoscan wavemeter reading has an error, based upon the specification, of 200 MHz; this error is usually less than the specified error and can depend upon how well the wavemeter is aligned and calibrated. This means that every time Autoscan reads the frequency there is an error of 100 MHz, which is too large for high-resolution spectroscopy. Additionally, if we wanted to stich together scans the way the old spectrometer does, with a 250 MHz cavity, we would likely make fringe assignment errors every few segments; since we scan tens of segments a day, this is an unacceptable number of errors.

8.2.1.1 Choice of Cavity Size

The design of the 2-cavities is motivated by understanding the precision and accuracy of the wavemeter and propagating that error. The functionality of the optical transfer cavities is twofold, i) accurately reference the start frequency of each segment and ii) correct for the nonlinearity of the scanning. In order to linearize the scan, we interpolate between the fringes and want to minimize the number of points to be interpolated between the peak of the fringes. At the same time, we need the FSR to be large enough to unambiguously assign a mode number to the fringe. Therefore we need one cavity with a small enough FSR to minimize possible inaccuracies while interpolating and a second cavity with a large enough FSR so that if the Autoscan frequency is used to assign a fringe number there is no ambiguity to the fringe count.

The choice of the large FSR cavity is based upon the ability to assign a number to the cavity mode, with an acceptable level un uncertainty. The stated level of accuracy of the Ti:Sapph wavemeter is 200 MHz. Accuracy is the correct number here because of the method by which the Ti:Sapph starts each scan. At the start of each segment, the laser takes an absolute frequency number and uses that to set the starting point for the scan; therefore the start of every segment involves an absolute frequency reading. In order to get the relative fringe number for the experiment, we take the difference between two fringe readings. Specifically,

$$\mathrm{F_n} = \frac{\text{peak A} \; - \; \text{peak B}}{\mathrm{FSR}} \tag{8.1}$$

where F_n is the difference between the two fringes in units of fringe number. The error associated with calculating F_n is calculated by propagating the error associated with this calculation. The result of propagating the error on this process, the uncertainty in the fringe number, is

$$\Delta\mathrm{F_n} = (\frac{\mathrm{step}}{\mathrm{FSR}})\sqrt{(\frac{\sqrt{2 \times \mathrm{acc}^2}}{\mathrm{step}})^2 + (\frac{\delta\mathrm{FSR}}{\mathrm{FSR}})^2} \tag{8.2}$$

where *acc* is the accuracy in the measurement, *step* is the difference in frequency between

the two measurements (peak A - peak B), FSR is the free spectral range of the cavity, and δFSR is the uncertainly in the free spectral range. For the 1.5 GHz cavity, the term involving the error in the FSR becomes almost negligible. Fig. 8.3 illustrates these ideas for a sample cavity with a 250 MHz free spectral range and a 2 MHz uncertainly in the FSR with the uncertainly in the fringe number shown with the contours, the distance between two frequency measurements, and the accuracy of the absorbance measurements. The important thing to notice about this graph is that with an uncertainty in the accuracy of a frequency measurement of 100 MHz (a lower limit of the Autscan accuracy), there will always be an uncertainly of half a fringe in any given measurement, irrespective of the distance between the two measurements. This illustrates the need to use a cavity with a much larger FSR in order to accurately stitch scans together, especially scans from different frequency regions. This type of error propagation analysis led to the choice of a 1.5 GHZ cavity to be able to confidently assign a relative fringe number to the start of each scan.

8.2.2 Integration of Autoscan with larger program

The second problem with the Autoscan system is that it is not sophisticated enough to run the entire high resolution system and must be integrated into a program that can run all of the necessary equipment while maintaining the scanning functionality. The approach taken to control the Autoscan system, and subsequently the laser system, splits the control into two parts, i) complete remote control of Autoscan computer program and ii)coordinate step scan with pulse valve and data recording. Figure 8.4 shows a brief outline of the master scan program and the flow of information to and from the program. Using A/D output channels connected directly to the Autoscan electronics and RS232 communication to the Autoscan computer, control over the Ti:Sapphire laser and Autoscan system is entirely through the master program. In addition to controlling the laser system, this program coordinates the use of all lab equipment necessary to take data. The program triggers the pulsed nozzle and discharge, controls the gas flow and discharge, laser scanning and timing of recording data.

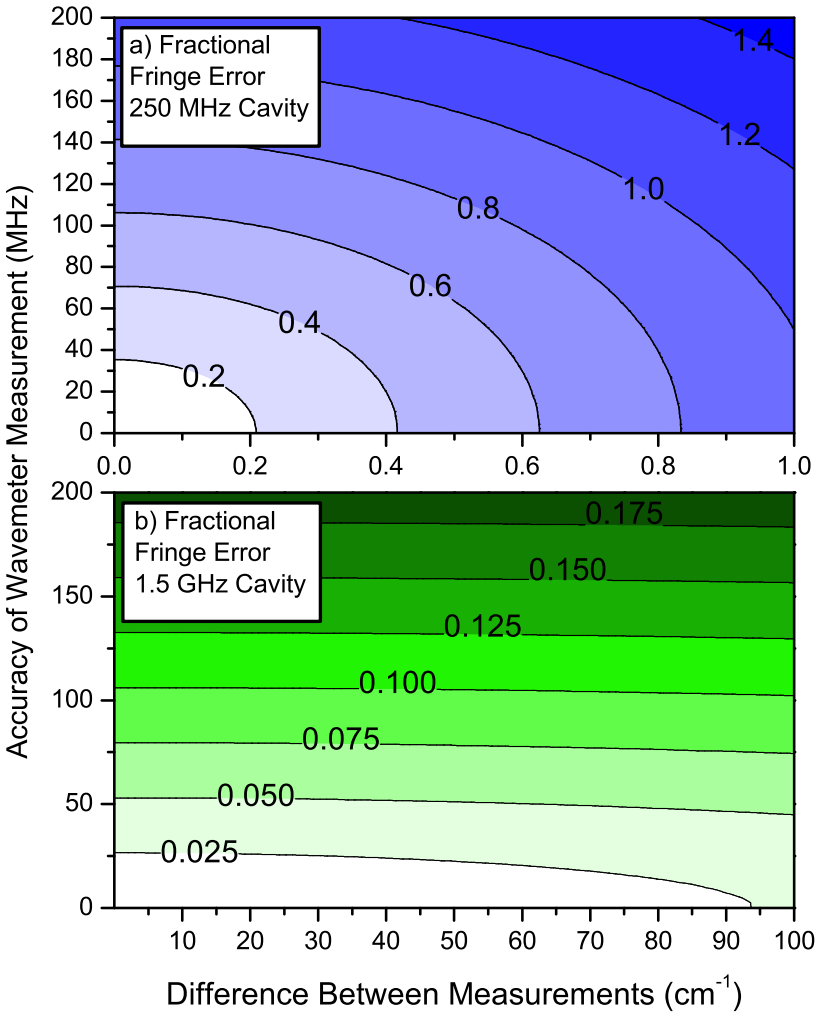

Figure 8.3: Plots of the error in counting fringes between two fringe measurements, in units of fractions of a fringe, as a function of the accuracy of the frequency measurement and the difference in frequency between the two fringes. Panel a) shows the calculation for the 250 MHz FSR cavity and panel b) plots the calculation for the 1.5 GHz FSR cavity. Note the difference in x-axis scale between the two plots.

This requires control over the laser scanning machinery, timing and triggers for the pulsed valve and discharge, and data and diagnostics recording processes. Figure 8.4 diagrams the connectivity between the computer dedicated to running the scannew program and the other lab equipment. To communicate with the lab equipment, two analogue-to-digital cards (NI-6110 and NI-6025E) are used as well as several RS232 ports.

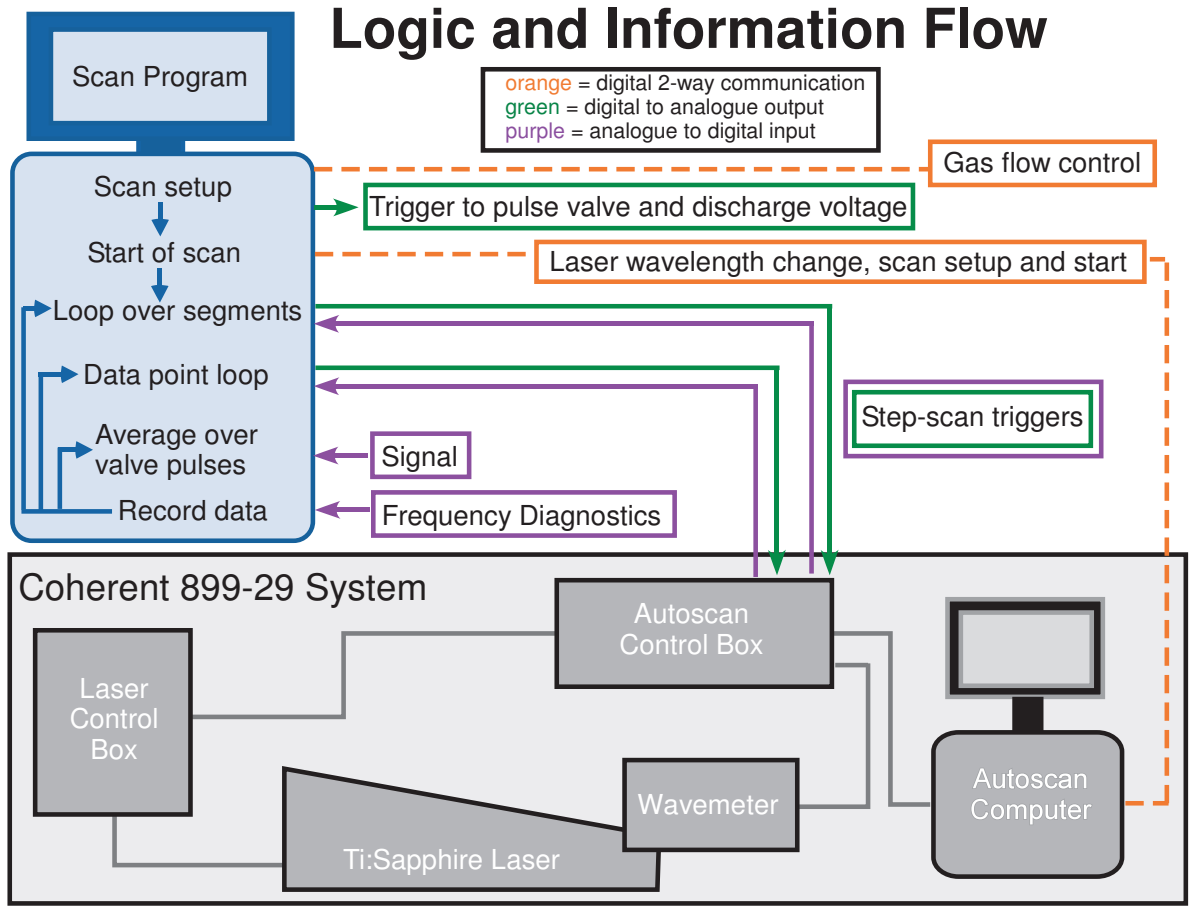

Figure 8.4: Schematic showing the logic and connectivity of the master scanning program.

The computer program piece of the Autoscan system has the ability to be controlled through a series of RS232 commands. For our purpose, these commands are used to change and read the laser frequency, start and end a scan, and specify what type of scan to execute,

such as scan length and step size. Once a scan is in progress, the computer program takes over control of the Autoscan scanning electronics through analogue connections. The laser is operated in step-scan mode, more specifically that the laser pauses at each point until told to step by the designated step size and then pauses again until told to take another step. This is repeated for 10.2 GHz, at which point the laser ends the segment and moves back 0.2 GHz while peaking the power. Once the laser has reached the new frequency, it signals to the computer and waits for the signal to begin the step-scan. To achieve this level of communication, the programs employs nested *while* loops and *dig_in_line* LabWindows command to monitor the status of the communication from the laser, and *dig_out_line* to send commands to the laser indicating the computer is done recording data and is ready step in frequency. Fig. 8.4 also shows an outline of the logic of the computer program. The combination of analogue and digital communication between the Autoscan system and main computer are all that is needed to transfer the frequency control and scanning functionality of Autoscan to a master program where it is incorporated into a larger instrument.

8.3 Mid-IR spectrometer for studying transient molecules

The advantage of putting so much effort into creating a high-resolution, high-precision frequency axis with the visible/near-IR laser is that when we use DFG to generate mid-IR light, the precision, resolution, tunability, and automation is transferred to the mid-IR light as long as the second laser is a locked, stable, single frequency source. This setup could easily be adapted to other IR frequencies of light by simply changing the single-frequency laser, nonlinear crystal, and potentially the detectors. This flexibility provides a huge advantage over systems where the frequency precision and tunability are tied to an IR laser or an IR-specific OPO.

The mid-IR light is generated via difference frequency generation (DFG) of the tunable Ti:Sapphire light with the single-frequency Nd:YAG light in a temperature-tuned, periodically-poled lithium niobate crystal. The Nd:YAG laser frequency is stabilized by

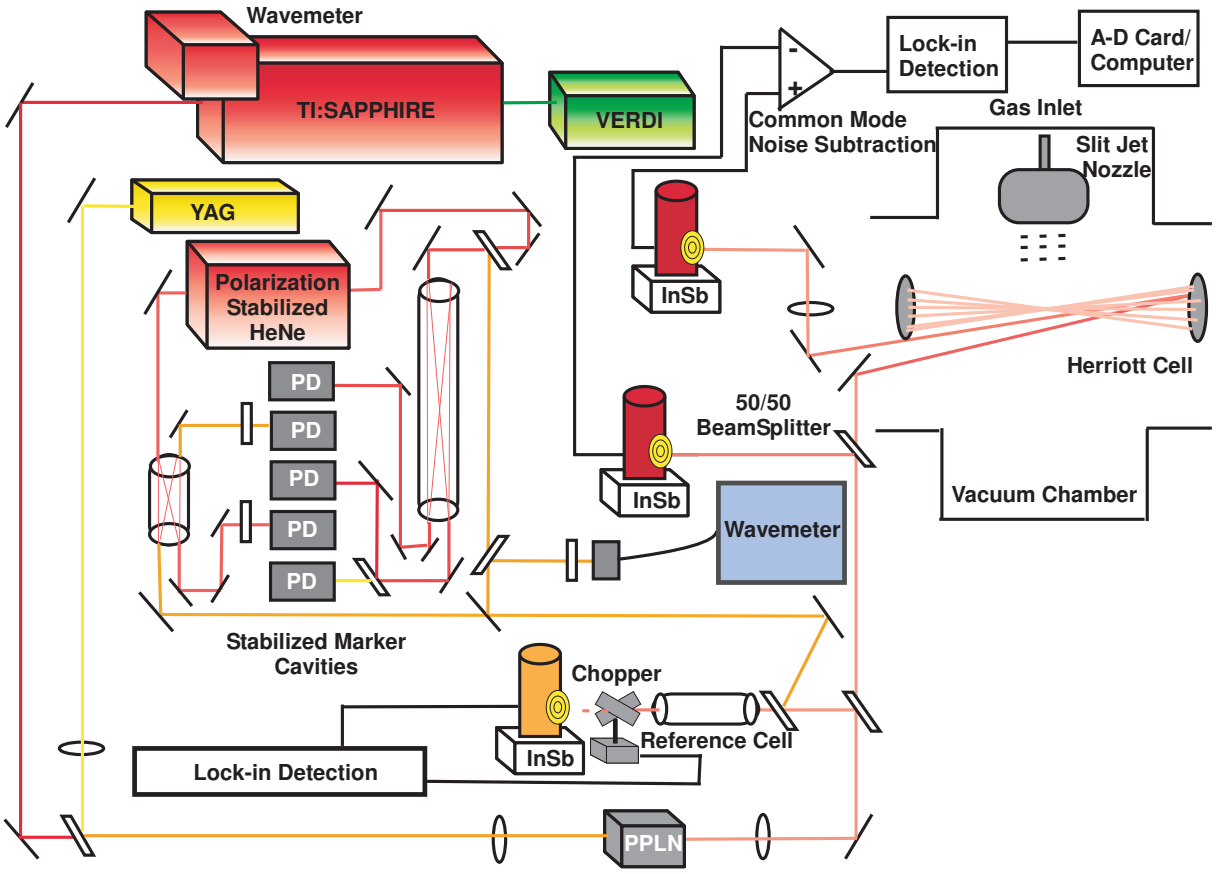

Figure 8.5: Optical layout of the high-resolution spectrometer. The radiation from a tunable Ti:Sapphire laser is overlapped with the single-frequency light of a Nd:YAG laser in a periodically poled lithium niobate crystal (PPLN) and via difference frequency generation to produce the mid-infrared light. The frequency axis is precise to 10 MHz.

active locking to the 250 MHz optical transfer cavity discussed previously. Details of the YAG locking are found in the appendix. The radiation resulting from the DFG is split into two beams of roughly equal intensity, a signal and a reference beam, and detected with matched InSb photovoltaic detectors. The signal beam is directed through a CaF2 window and into the vacuum chamber where it passes 16 times through the long axis of the slit orifice (4 cm) in a Herriot cell configuration, increasing the pathlength to 64 cm. The Herriot cell consists of two 2" gold mirrors with a 40 cm radius of curvature, mounted just under 40 cm apart in the vacuum chamber.

The transient species, in this case molecular ions such as HD_2O^+, are produced by adiabatically expanding a mixture of D_2O in H_2. The flow and mixture percentage is controlled through the use of mass flow controllers just before passing through a slit nozzle(4cm by 300 μm) pulsing at 19 Hz with an adjustable opening time of 1-2 ms. The limiting orifice of the slit is a pair of adjustable steal jaws, attached to an Ultem insulator plate that is attached to the body of the nozzle. This nozzle setup is a near-replica of the one described in detail elsewhere[33, 55] and the discharge setup is similar to the setup described in Davis et al.[56]. Absorbance signals are generated by automatic subtraction electronics and then, if a discharge is being used, sent to a homebuilt lock-in detector. The lock-in detector takes advantage of the concentration modulation with the 50 KHz discharge frequency serving as the local oscillator so that the output contains signal only from species produced in the modulating discharge. This signal is sent to the computer via a A/D card (NI6110E). The time trace of the signal is gated and integrated in coincidence with the pulse valve and discharge.

8.4 Spectrometer test results

For high resolution spectroscopy, the most important piece of information is the accuracy and precision of the frequency axis. The test the frequency axis, we repeatedly recorded molecular absorption lines and compared the peak frequency positions obtained on different days. Specifically, a $\sim$100 cm^{-1} region was scanned with D_2O in H_2 discharge. The region

was fully scanned at least 3 times and all lines appearing in each scan were used to compare how well the spectrometer reproduced the frequencies. Figure 8.6 is a plot of the frequency of each line on the frequency axis with the standard deviation of the repeated measurements on the absorbance axis. The average standard deviation of all the lines taken is 9.3 MHz, which is right in the target range. The lines looked at include known D_2O lines and H_3^+ lines, as well as many unidentified lines, many of which belong to HD_2O^+. This level of frequency reproducibility is good enough for doing high-resolution studies of radicals and ions.

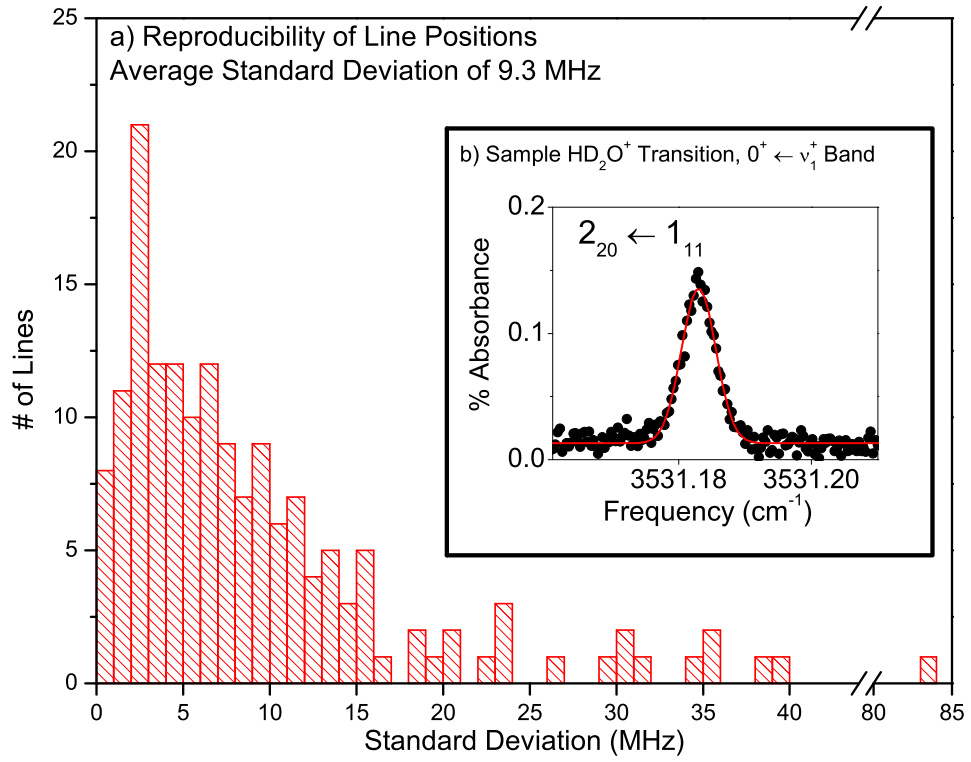

Figure 8.6: Illustration of the precision of the new instrument. This region was scanned a minimum of three time and the standard deviation of the measurements for each line in the region is plotted as a function of the frequency position of the line. The average standard deviation of the measurements is 9.3 MHz. Sample HD_2O^+ data in the OH stretching region illustrating the ability of the new instrument to produce molecular ions in appreciable quantities.

The initial project for this new spectrometer was to look at the the OD stretches of HD_2O^+ to complement the study of the OH stretch done on the older instrument in the

lab[57]. This is also a useful test for the instrument as it was already studied in the lab so we would have some nice benchmarks to assess how the new instrument compares to the existing instrument. As determined by previous spectroscopic studies[57, 58] HD_2O^+ is a near-prolate top with a low barrier to inversion along the umbrella coordinate. Even with the low temperature of the slit jet expansion, the first excited tunneling level of the ground vibrational state is populated, however transitions from the lower tunneling level of the ground state to the lower tunneling level are the most intense. To test the our ability to create ions and detect them with the new setup, we began by taking some lines from the OH stretch and checking against the published lineshapes and intensities. The OH stretch is an b-type transition and the $2_{20} \leftarrow 1_{11}$ and $1_{11} \leftarrow 0_{00}$ transitions are shown in figure 8.6. The integrated intensity for the $2_{20} \leftarrow 1_{11}$ transition is the same as that in Figure 5 of Dong et al.[57].

8.5 Appendix: YAG Lock Description

The concept and method for locking the YAG laser to a single frequency is based upon methodology successfully used for many years for locking an Ar^+ laser to a single frequency. To the best of our knowledge, the literature does not include application of these methods for locking a YAG laser. The YAG laser is use here is a Lightwave Electronics Series 126. The laser is a non-planar ring oscillator with the crystal interface acting as the cavity mirrors. There are two ways to tune the crystal: piezo-induced strain and temperature variance using a thermoelectric cooler attached to the crystal. The frequency of the laser is stable in the short term, but tends to drift over long times so it is only necessary to correct for slow fluctuations in frequency. The response of the temperature tuning of the laser results in about -3.1 GHz change per degree Celsius and continuous tuning is achievable for about 10 GHz before a laser mod hop occurs.

A small portion of the YAG light is sent through the locked 250 MHz FSR cavity and recorded on a photodiode. Fig. 8.7 is a schematic of the locking circuit. The 4 KHz dither

applied to the 250 MHz cavity is used as the local oscillator for the top-of-line locking circuit. Since only slow errors need to be corrected, the servo-loop only has integrated feedback. With the GHz/°C conversion of the laser, only mV level corrections generally need to be made. Therefore directly at the input to the laser is a voltage divider to ensure that the voltages passed through cables are large but that the voltage corrections supplied to the laser are appropriate. With this circuit, the Nd:YAG laser frequency is stabilized for an entire day of scanning.

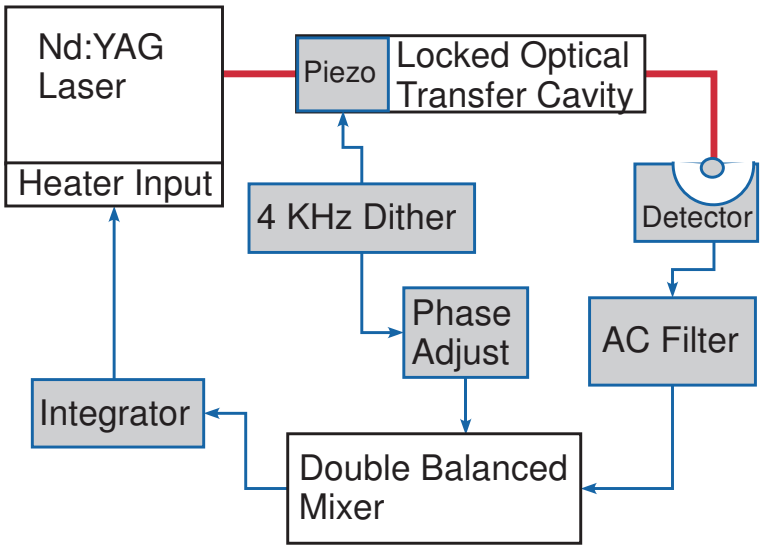

Figure 8.7: Schematic representation of the Nd:YAG locking circuit.

Bibliography

[1] Dong, F., Davis, S., and Nesbitt, D. (2006) J. Phys. Chem. A **110(9)**, 3059–3070.

[2] Kawaguchi, K. (2001) Can. J. Phys. **79**, 449–459.

[3] Frisch, M. J., Trucks, G. W., Schlegel, H. B., Scuseria, G. E., Robb, M. A., Cheeseman, J. R., Zakrzewski, V. G., J. A. Montgomery, J., Stratmann, R. E., Burant, J. C., Dapprich, S., Millam, J. M., Daniels, A. D., Kudin, K. N., Strain, M. C., Farkas, O., Tomasi, J., Barone, V., Cossi, M., Cammi, R., Mennucci, B., Pomelli, C., Adamo, C., Clifford, S., Ochterski, J., Petersson, G. A., Ayala, P. Y., Cui, Q., Morokuma, K., Malick, D. K., Rabuck, A. D., Raghavachari, K., Foresman, J. B., Cioslowski, J., Ortiz, J. V., Baboul, A. G., Stefanov, B. B., Liu, G., Liashenko, A., Piskorz, P., Komaromi, I., Gomperts, R., Martin, R. L., Fox, D. J., Keith, T., Al-Laham, M. A., Peng, C. Y., Nanayakkara, A., Gonzalez, C., Challacombe, M., Gill, P. M. W., Johnson, B., Chen, W., Wong, M. W., Andres, J. L., Gonzalez, C., Head-Gordon, M., Replogle, E. S., and Pople, J. A. Gaussian 98, revision a.7 Gaussian, Inc., Pittsburgh PA, 1998.

[4] Padovani, M., Walmsley, C. M., Tafalla, M., Galli, D., and Müller, H. S. P. (2009) Astron. and Astrophys. **505**, 1199.

[5] Zare, R. N. (1988) Angular Momentum: Understanding Spatial Aspects in Chemistry and Physics, John Wiley and Sons, New York.

[6] Zare, R. N. (1988) Angular Momentum: Understanding Spatial Aspects in Chemistry and Physics, John Wiley and Sons, New York.

[7] Gottlieb, C. A., Gottlieb, E. W., and Thaddeus, P. (1983) Ap. J. **264**, 740.

[8] Tarroni, R. and Carter, S. (2003) J. Chem. Phys. **119**, 12878.

[9] Tarroni, R. and Carter, S. (2004) Mol. Phys. **102**, 2167.

[10] Hudson, Jr., R. D. (1969) Infrared System Engineering, John Wiley and Sons, Inc., New York.

[11] Tyndall, J. (1859) P. R. Soc. London **10**, 37–39.

[12] Barr, E. S. (1960) Am. J. Phys. **28**, 42–54.

[13] Rabkin, Y. M. (1987) Isis **78(1)**, 31–54.

[14] McMahon, R. J., McCarthy, M. C., Gottlieb, C. A., Dudek, J. B., Stanton, J. F., and Thaddeus, P. (2003) Astrophys. J. **590**, L61L64.

[15] Williams, A. and Smith, D. B. (1970) Chem. Rev. **70**, 267.

[16] Tucker, K. D., Kutner, M. L., and Thaddeus, P. (1974) Ap. J. **193**, L115.

[17] Homann, K. H. (1967) Combust. Flame **11**, 265.

[18] Carrick, P. G., Merer, A. J., and R. F. Curl, J. (1983) J. Chem. Phys. **78**, 3652.

[19] R. F. Curl, J., Carrick, P. G., and Merer, A. J. (1985) J. Chem. Phys. **82**, 3479.

[20] Hsu, Y.-C., Lin, J. J.-M., Papoušsek, D., and Tsai, J.-J. (1993) J. Chem. Phys. **98**, 6690.

[21] Feng, L., Wei, J., and Reisler, H. (2004) J. Phys. Chem. A **108(39)**, 7903–7908.

[22] Lovejoy, C. M. Intramolecular Dynamics of Van Der Waals Complexes as Elucidated by Infrared Spectroscopy in Slit Supersonic Expansions PhD thesis University of Colorado, Boulder (1990).

[23] John T. Farrell, J. High Resolution Intrared Spectroscopy of Van Der Waals and Hydrogen Bonded Clusters: Pairwise and Nonpairwise Additive Intermolecular Forces in Ar_nHF/DF and $(HF)_n$ Complexes PhD thesis University of Colorado, Boulder (1995).

[24] Davis, S. High Resolution Infrared Spectroscopy of Slit-Jet Cooled Transient Molecules: From van der Waals Clusters, to Hydrogen Bound Dimers, to Small Organic Radicals PhD thesis University of Colorado, Boulder (1999).

[25] Whitney, E. S. High-resolution infrared spectroscopy: jet-cooled halogenated methyl radicals and reactive scattering dynamics in an atom + polyatom system PhD thesis University of Colorado, Boulder (2006).

[26] Pine, A. S. (1974) J. Opt. Soc. Am. **64(12)**, 1683–1690.

[27] Verdeyen, J. T. (1995) Laser Electronics, Prentice Hall, New Jersey.

[28] Guenther, R. (1990) Modern Optics, John Wily and Sons, Inc., New York.

[29] Evans, J. W. (1949) J. Opt. Soc. Am. **39**, 229–242.

[30] Zhu, S. (1990) Appl. Opt. **29**, 410–415.

[31] Riedle, E., Ashworth, S. H., J. T. Farrell, J., and Nesbitt, D. J. (1994) Rev. Sci. I. **65(1)**, 42–48.

[32] G. Scoles, (ed.) (1988) Atomic and Molecular Beam Methods, Oxford University Press, New York.

[33] Lovejoy, C. M. and Nesbitt, D. J. (1987) Rev. Sci. I. **58(5)**, 807–811.

[34] Snyder, J. J. (1980) Appl. Opt. **19(8)**, 1223–1225.

[35] Hirota, E. (1992) Chem. Rev. **92**, 141–173.

[36] Snow, T. P. and Bierbaum, V. M. (2008) Annu. Rev. Anal. Chem. **1**, 229–259.

[37] Daussy, C., Guinet, M., Amy-Klein, A., Djerroud, K., Hermier, Y., Briaudeau, S., Bordé, C. J., and Chardonnet, C. (2007) Phys. Rev. Lett. **98**, 250801.

[38] Cygan, A., Lisak, D., Wójtewicz, S., Domysławska, J., Hodges, J. T., Trawiński, R. S., and Ciuryło, R. (2012) Phys. Rev. A **85**, 022508.

[39] Grilli, R., Ciaffoni, L., Hancock, G., Peverall, R., Ritchie, G. A. D., and Orr-Ewing, A. J. (2009) Appl. Opt. **48**, 5696–5703.

[40] Galli, I., Bartalini, S., Borri, S., Cancio, P., Mazzotti, D., De Natale, P., and Giusfredi, G. (2011) Phys. Rev. Lett. **107**, 270802.

[41] Zolot, A. M. Energy Partitioning in Polyatomic Chemical Reactions: Quantum State Resolved Studies of Highly Exothermic Atom Abstraction Reactions from Molecules in the Gas Phase and at the Gas-Liquid Interface PhD thesis University of Colorado at Boulder (2009).

[42] Brumfield, B. E., Stewart, J. T., Weaver, S. L. W., Escarra, M. D., Howard, S. S., Gmachl, C. F., and McCall, B. J. (2010) Rev. Sci. I. **81(6)**, 063102.

[43] Welzel, S., Lombardi, G., Davies, P. B., Engeln, R., Schram, D. C., and Röpcke, J. (2008) J. Appl. Phys. **104(9)**, 093115.

[44] Kasyutich, V. L., Holdsworth, R. J., and Martin, P. A. (2008) Appl. Phys. B **92**, 271–279.

[45] Wu, S., Dupre, P., and Miller, T. A. (2006) Phys. Chem. Chem. Phys. **8**, 1682–1689.

[46] Chen, W., Cousin, J., Poullet, E., Burie, J., Boucher, D., Gao, X., Sigrist, M. W., and Tittel, F. K. (2007) Comp. Rend. Phys. **8(10)**, 1129 – 1150.

[47] Cao, Z., Gao, X., Deng, L., Chen, W. D., Yuan, Y., Zhang, W., and Gong, Z. (2007) Spectrochim. Acta A **68(1)**, 74 – 77.

[48] Deng, W.-P., Gao, B., Cheng, C.-F., Cheng, G.-S., Hu, S.-M., and Zhu, Q.-S. (2008) Rev. Sci. I. **79(12)**, 123101.

[49] Deng, L., Gao, X., Cao, Z., Chen, W., Yuan, Y., Zhang, W., and Gong, Z. (2008) Opt. Comm. **281(6)**, 1686 – 1692.

[50] Boyd, R. W. (2003) Nonlinear Optics, Academic Press, San Diego, CA 2nd edition edition.

[51] Jundt, D. H. (1997) Opt. Lett. **22**, 1553–1555.

[52] Deng, L. H., Gao, X. M., Cao, Z. S., Chen, W. D., Yuan, Y. Q., Zhang, W. J., and Gong, Z. B. (2006) Opt. Commun. **268**, 110–114.

[53] Canarelli, P., Benko, Z., Curl, R., and Tittel, F. K. (1992) J. Opt. Soc. Am. B **9**, 197–202.

[54] Niebauer, T. M., Faller, J. E., Godwin, H. M., Hall, J. L., and Barger, R. L. (1988) Appl. Opt. **27**, 1285–1289.

[55] Anderson, D. T., Davis, S., Zwier, T. S., and Nesbitt, D. J. (1996) Chem. Phys. Lett. **258**, 207–212.

[56] Davis, S., Anderson, D. T., Duxbury, G., and Nesbitt, D. J. (1997) J. Chem. Phys. **107(15)**, 5661–5675.

[57] Dong, F., Uy, D., Davis, S., Child, M., and Nesbitt, D. J. (2005) J. Chem. Phys. **122**, 224301.

[58] Furuya, T. and Saito, S. (2008) J. Chem. Phys. **128(3)**, 034311.

[59] Friderichsen, A. V., Radziszewski, J. G., Nimlos, M. R., Winter, P. R., Dayton, D. C., David, D. E., and Ellison, G. B. (2001) J. Am. Chem. Soc. **123**, 19771988.

[60] Radziszewski, J. G., Nimlos, M. R., Winter, P. R., and Ellison, G. B. (1996) Journal of the American Chemical Society **118(31)**, 7400–7401.

[61] Niu, J. Y. and Hu, J. Y. (1999) Marine Petroleum Geol. **16**, 8595.

[62] Strausz, O., Mojelsky, T., Payzant, J., Olah, G., and Prakash, G. (1999) Energy & Fuels **13(3)**, 558–569.

[63] Agafonov, G. L., Naydenova, I., Vlasov, P. A., and Warnatz, J. (2007) Proc. Combust. Inst. **31(Part 1)**, 575–583.

[64] Miller, J. A. and Melius, C. F. (1992) Combust. Flame **91(1)**, 21–39.

[65] Marinov, N. M., Pitz, W. J., Westbrook, C. K., Castaldi, M. J., and Senkan, S. M. (1996) Combust. Sci. Technol. **116(1-6)**, 211–287.

[66] Wang, H. and Frenklach, M. (1994) J. Phys. Chem. **98(44)**, 11465–11489.

[67] Kaiser, R., Asvany, O., Lee, Y., Bettinger, H., Schleyer, P., and Schaefer, H. (2000) J. Chem. Phys. **112(11)**, 4994–5001.

[68] Herbst, E. (1995) Annu. Rev. Phys. Chem. **46**, 27–53.

[69] Bennett, J. E., Mile, B., and Thomas, A. (1966) Proc. Royal Soc. London Series A-Math. Phys. Sci. **293(1433)**, 246–248.

[70] Bennett, J. E., Mile, B., and Thomas, A. (1965) Chem. Commun **12**, 265–267.

[71] Kasai, P. H., Hedaya, E., and Whipple, E. B. (1969) J. Am. Chem. Soc. **91(16)**, 4364.

[72] Pacansky, J. and Bargon, J. (1975) J. Am. Chem. Soc. **97(23)**, 6896–6897.

[73] Radziszewski, J. G. (1999) Chem. Phys. Lett. **301(5-6)**, 565–570.

[74] Wallington, T., Egsgaard, H., Nielsen, O., Platz, J., Sehested, J., and Stein, T. (1998) Chem. Phys. Lett. **290(4-6)**, 363–370.

[75] Engert, J. and Dick, B. (1996) Appl. Phys. B: Lasers Opt. **63(5)**, 531–535.

[76] Lin, M. C. and Yu, T. (1993) Int. J. Chem. Kinet. **25(10)**, 875–880.

[77] Yu, T. and Lin, M. C. (1993) J. Am. Chem. Soc. **115(10)**, 4371–4372.

[78] Yu, T. and Lin, M. C. (1994) J. Am. Chem. Soc. **116(21)**, 9571–9576.

[79] Yu, T. and Lin, M. C. (1995) J. Phys. Chem. **99(21)**, 8599–8603.

[80] Gunion, R. F., Gilles, M. K., Polak, M. L., and Lineberger, W. C. (1992) Int. J. Mass Spectrom. Ion Processes **117(1-3)**, 601–620.

[81] Davis, S., Uy, D., and Nesbitt, D. J. (2000) J. Chem. Phys. **112(4)**, 1823–1834.

[82] Davis, S., Farnik, M., Uy, D., and Nesbitt, D. (2001) Chem. Phys. Lett. **344(1-2)**, 23–30.

[83] Pine, A. S. (1976) J. Opt. Soc. Am. **66**, 97–108.

[84] Peterson, K. A., Kendall, R. A., and Dunning, T. H. (1993) J. Chem. Phys. **99(3)**, 1930–1944.

[85] Woon, D. E. and Dunning, T. H. (1993) J. Chem. Phys. **98(2)**, 1358–1371.

[86] Herzberg, G. (1950) Molecular Spectra and Molecular Structure, II. Infrared and Raman Spectra of Polyatomic Molecules, Krieger Publishing Company, Florida reprint edition edition.

[87] Jacox, M. E. (1994) Chem. Phys **189(2)**, 149–170.

[88] Nesbitt, D. J. and Field, R. W. (1996) J. Phys. Chem. **100(31)**, 12735–12756.

[89] Lehmann, K. K., Scoles, G., and Pate, B. H. (1994) Annu. Rev. Phys. Chem. **45**, 241–274.

[90] Elles, C. G. and Crim, F. F. (2006) Annu. Rev. Phys. Chem. **57**, 273–302.

[91] Yoo, H., McWhorter, D., and Pate, B. (2004) J. Phys. Chem. A **108(8)**, 1380–1387.

[92] Bethardy, G. A., Wang, X. L., and Perry, D. S. (1994) Can. J. Chem.-Rev. Can. Chim. **72(3)**, 652–659.

[93] McIlroy, A., Nesbitt, D. J., Kerstel, E. R. T., Pate, B. H., Lehmann, K. K., and Scoles, G. (1994) J. Chem. Phys. **100(4)**, 2596–2611.

[94] Pate, B. H., Lehmann, K. K., and Scoles, G. (1991) J. Chem. Phys. **95(6)**, 3891–3916.

[95] Kemper, M. J. H., Vandijk, J. M. F., and Buck, H. M. (1978) Chem. Phys. Lett. **53(1)**, 121–124.

[96] Miller, J. A., Kee, R. J., and Westbrook, C. K. (1990) Annu. Rev. Phys. Chem. **41**, 345–387.

[97] Scherer, J. J., Aniolek, K. W., Cernansky, N. P., and Rakestraw, D. J. (1997) J. Chem. Phys. **107**, 6196–6203.

[98] Griffiths, J. F. and Barnard, J. A. (1995) Flame and Combustion, Blackie Academic and Professional, New York third edition.

[99] Ravishankara, A. R. (1988) Annu. Rev. Phys. Chem. **39**, 643.

[100] Heicklen, J. (1976) Atmospheric Chemistry, Academic Press, New York.

[101] Blanksby, S. and Ellison, G. (2003) Acc. of Chem. Res. **36(4)**, 255–263.

[102] Conny, J. and Currie, L. (1996) Atmos. Environ. **30(4)**, 621–638.

[103] Watson, W. D. (1976) Rev. Mod. Phys. **48**, 513–552.

[104] Suzuki, H. (1979) Prog. Theor. Phys. **62**, 936.

[105] Cassam-Chenai, P., Pauzat, F., and Ellinger, Y. (1995) J. Mol. Struct. (Theochem) **330**, 167–175.

[106] Hollenstein, H., Marquardt, R. R., Quack, M., and Suhm, M. (1994) J. Chem. Phys. **101**, 3588–3602.

[107] Herzberg, G. and Shoosmith, J. (1956) Can. J. Phys. **34**, 523–525.

[108] Herzberg, G. (1961) Proc. R. Soc. Lond. A **262**, 291–317.

[109] Andrews, L. and Pimentel, G. C. (1967) J. Chem. Phys. **47**, 3637–3644.

[110] Milligan, D. E. and Jacox, M. E. (1967) J. Chem. Phys. **47**, 5146–5156.

[111] Snelson, A. (1970) J. Phys. Chem. **74**, 537–544.

[112] Andrews, W. L. S. and Pimentel, G. C. (1966) J. Chem. Phys. **44**, 2527–2528.

[113] Jacox, M. E. (1977) J. Mol. Spec. **66**, 272–287.

[114] Tan, L. Y., Winer, A. M., and Pimentel, G. C. (1972) J. Chem. Phys. **57**, 4028–4037.

[115] Yamada, C., Hirota, E., and Kawaguchi, K. (1981) J. Chem. Phys. **75**, 5256–5264.

[116] Amano, T., Bernath, P. F., Yamada, C., Endo, Y., and Hirota, E. (1982) J. Chem. Phys. **77**, 5284–5287.

[117] Triggs, N. E., Zahedi, M., Nibler, J. W., DeBarber, P., and Valentini, J. J. (1991) J. Chem. Phys. **96**, 1822–1831.

[118] Seakins, P. W., Robertson, S. H., Pilling, M. J., Wardlaw, D. M., Nesbitt, F. L., Thorn, R. P., Payne, W. A., and Stief, L. J. (1997) J. Phys. Chem. A **101**, 9974–9987.

[119] Holiday, R. J., Kwon, C. H., Annesley, C. J., and Crim, F. F. (2006) J. Chem. Phys. **125**, 133101.

[120] Yamada, T., Komaguchi, K., Shiotani, M., Benetis, N. P., and Sornes, A. R. (1999) J. Phys. Chem. A **103**, 4823–4829.

[121] Dmitriev, Y. A. and Zhitnikov, R. A. (2003) Low Temp. Phys. **29**, 519–521.

[122] Dmitriev, Y. A. (2005) Low Temp. Phys. **31**, 423–428.

[123] Brum, J. L., III, R. D. J., and Hudgens, J. W. (1993) J. Chem. Phys **98**, 3732–3736.

[124] Schulenburg, A. M., Alcaraz, C., Grassi, G., and Merkt, F. (2006) J. Chem. Phys. **125**, 104310.

[125] Fessenden, R. W. (1967) J. Phys. Chem. **71**, 74–83.

[126] deMiranda, B. K. C., Alcaraz, C., Elhanine, M., Noller, B., Hemberger, P., Fischer, I., Garcia, G. A., Soldi-Lose, H., Gans, B., Mendes, L. A. V., Boye-Peronne, S., Douin, S., Zabka, J., and Botschwina, P. (2010) J. Phys. Chem. A **114**, 4818–4830.

[127] Nesbitt, D. J., Whitney, E. S., Roberts, M., and Savage, C. (2007) Mol. Phys. **105**, 467–475.

[128] Davis, S., Farnik, M., Uy, D., and Nesbitt, D. J. (2001) Chem. Phys. Lett. **344**, 23.

[129] Riedle, E., Ashworth, S. H., J. T. Farrell, J., and Nesbitt, D. J. (1993) Rev. Sci. Instrum. **65**, 42–48.

[130] Pine, A. S. (1976) J. Opt. Soc. Am. **66**, 97–108.

[131] Frisch, M. J., Trucks, G. W., Schlegel, H. B., Scuseria, G. E., Robb, M. A., Cheeseman, J. R., Scalmani, G., Barone, V., Mennucci, B., Petersson, G. A., Nakatsuji, H., Caricato, M., Li, X., Hratchian, H. P., Izmaylov, A. F., Bloino, J., Zheng, G., Sonnenberg, J. L., Hada, M., Ehara, M., Toyota, K., Fukuda, R., Hasegawa, J., Ishida, M., Nakajima, T., Honda, Y., Kitao, O., Nakai, H., Vreven, T., J. A. Montgomery, J., Peralta, J. E., Ogliaro, F., Bearpark, M., Heyd, J. J., Brothers, E., Kudin, K. N., Staroverov,

V. N., Keith, T., Kobayashi, R., Normand, J., Raghavachari, K., Rendell, A., Burant, J. C., Iyengar, S. S., Tomasi, J., Cossi, M., Rega, N., Millam, J. M., Klene, M., Knox, J. E., Cross, J. B., Bakken, V., Adamo, C., Jaramillo, J., Gomperts, R., Stratmann, R. E., Yazyev, O., Austin, A. J., Cammi, R., Pomelli, C., Ochterski, J. W., Martin, R. L., Morokuma, K., Zakrzewski, V. G., Voth, G. A., Salvador, P., Dannenberg, J. J., Dapprich, S., Daniels, A. D., Farkas, O., Foresman, J. B., Ortiz, J. V., Cioslowski, J., and Fox, D. J. Gaussian 09, Revision B.01 Gaussian, Inc., Wallingford CT, 2010.

[132] Dong, F., Davis, S., and Nesbitt, D. J. (2006) J. Phys. Chem. A **110**, 3059.

[133] Watson, J. K. G. Vibrational Spectra and Structure. A Series of Advances volume **6**, Elsevier Amsterdam (1977).

[134] Hirota, E. (1985) High-Resolution Spectroscopy of Transient Molecules, Springer-Verlag, Berlin.

[135] Davis, S., Anderson, D. T., Duxbury, G., and Nesbitt, D. J. (1997) J. Chem. Phys. **107**, 5661–5675.

[136] Brown, J. and Carrington, A. (2003) Rotational Spectroscopy of Diatomic Molecules, Cambridge University Press, United Kingdom.

[137] Wu, S., Sedo, G., Grumstrup, E. M., and Leopold, K. R. (2007) J. Chem. Phys. **127**, 204315.

[138] McKenzie, I., Brodovitch, J.-C., Ghandi, K., McCollum, B. M., and Percival, P. W. (2007) J. Phys. Chem. A **111**, 10625–10634.

[139] Bizzocchi, L., Esposti, C. D., and Dore, L. (2008) Phys. Chem. Chem. Phys. **10**, 658–665.

[140] Kukolich, S. G. (1975) Mol. Phys. **29**, 249–255.

[141] Mokarram, M. and Ragle, J. L. (1973) J. Chem. Phys. **59**, 2770–2771.

[142] Whitney, E. S., Haeber, T., Schuder, M. D., Blair, A. C., and Nesbitt, D. J. (2006) J. Chem. Phys. **125**, 054303.

[143] Whitney, E. S., Dong, F., and Nesbitt, D. J. (2006) J. Chem. Phys. **125**, 054304.

[144] Hirota, E. and Yamada, C. (1982) J. Mol. Spectrosc. **96(1)**, 175–182.

[145] E.B. Wilson, J., Decius, J. C., and Cross, P. C. (1955) Molecular Vibrations: The Theory of Infrared and Raman Vibrational Spectra, Dover Publications, Inc., New York, NY 1980 dover edition.

[146] Papousek, D., Stone, J. M. R., and Spirko, V. (1973) J. Mol. Spectrosc. **48(1)**, 17–37.

[147] Danielis, V., Papousek, D., Spirko, V., and Horak, M. (1975) J. Mol. Spectrosc. **54(3)**, 339–349.

[148] Spirko, V., Stone, J. M. R., and Papousek, D. (1976) J. Mol. Spectrosc. **60(1-3)**, 159–178.

[149] Spirko, V. and Bunker, P. R. (1982) J. Mol. Spectrosc. **95(1)**, 226–235.

[150] Spirko, V. (1983) J. Mol. Spectrosc. **99(1)**, 243.

[151] Spirko, V. (1983) J. Mol. Spectrosc. **101(1)**, 30–47.

[152] Spirko, V. and Bunker, P. R. (1982) J. Mol. Spectrosc. **95(2)**, 381–390.

[153] Sears, T. J., Frye, J. M., Spirko, V., and Kraemer, W. P. FEB 15 1989 J. Chem. Phys. **90(4)**, 2125–2133.

[154] Spirko, V. and Kraemer, W. P. (1991) J. Mol. Spectrosc. **147(2)**, 541–542.

[155] Child, M. S. and Lawton, R. T. (1981) Farad. Discuss. **71**, 273–285.

[156] Mills, I. M. and Robiette, A. G. (1985) Mol. Phys. **56(4)**, 743–765.

[157] Mills, I. M. and Mompean, F. J. (1986) Chem. Phys. Lett. **124(5)**, 425–431.

[158] Westre, S. G., Liu, X., Getty, J. D., and Kelly, P. B. (1991) J. Chem. Phys. **95(12)**, 8793–8802.

[159] Halonen, L. and Child, M. S. (1982) Mol. Phys. **46(2)**, 239–255.

[160] Abramowitz, M. and Stegun, I. (1964) Handbook of mathematical functions with formulas, graphs, and mathematical tables, Number v. 55, no. 1972 in Applied mathematics seriesU.S. Govt. Print. Off., .

[161] Miller, S. A. (1965) Acetylene: Its Properties, Manufacture and Uses, Academic Press, London.

[162] Laufer, A. H. and Fahr, A. (2004) Chem. Rev. **104**, 2813.

[163] Frenklach, M., Clary, D. W., Gardiner, W. C., and Stein, S. E. (1985) Symp. Combust., [Proc.] **20**, 887.

[164] Bettens, R. P. A. and Herbst, E. (1997) Ap. J. **478**, 585.

[165] Vuitton, V., Scemama, A., Gazeau, M.-C., Chaquin, P., and Bénilan, Y. (2001) Adv. Space Res. **27**, 283.

[166] Stephens, J. W., Hall, J. L., Solka, H., Yan, W.-B., R. F. Curl, J., and Glass, G. P. (1987) J. Phys. Chem. **91**, 5740.

[167] Lander, D. R., Unfried, K. G., Glass, G. P., and R. F. Curl, J. (1990) J. Phys. Chem. **94**, 7759.

[168] Opansky, B. J., Seakins, P. W., Pedersen, J. O. P., and Leone, S. R. (1993) J. Phys. Chem. **97**, 8583.

[169] Look, H. V. and Peeters, J. (1995) J. Phys. Chem. **99**, 16284.

[170] Lee, S., Samuels, D. A., Hoobler, R. J., and Leone, S. R. (2000) J. Geophys. Research **105**, 15085.

[171] Nizamov, B. and Leone, S. R. (2004) J. Phys. Chem. A **108**, 1746.

[172] Saykally, R. J. and Veseth, L. (1983) J. Chem. Phys. **80**, 2247.

[173] Killian, T. C., Gottlieb, C. A., and Thaddeus, P. (2007) J. Chem. Phys. **127**, 114320.

[174] Kanamori, H., Seki, K., and Hirota, E. (1987) J. Chem. Phys. **87**, 73.

[175] Kanamori, H. and Hirota, E. (1988) J. Chem. Phys. **89**, 3962.

[176] Kawaguchi, K., Amano, T., and Hirota, E. (1988) J. Mol. Spectrosc. **131**, 58.

[177] Stephens, J. W., Yan, W.-B., Richenow, M., Solka, H., and Curl, R. F. (1988) J. Mol. Struc. **190**, 41.

[178] Ervin, K. M. and Lineberger, W. C. (1991) J. Phys. Chem. **95**, 1167.

[179] Yan, W.-B. and Amano, T. (1993) J. Chem. Phys. **99**, 4312.

[180] Chiang, W.-Y. and Hsu, Y.-C. (1999) J. Chem. Phys. **111**, 1454.

[181] Yan, W.-B., Hall, J. L., Stephens, J. W., Richenow, M. L., and R. F. Curl, J. (1987) J. Chem. Phys. **86**, 1657.

[182] Yan, W.-B., Dane, C. B., Zeitz, D., Hall, J. L., and R. F. Curl, J. (1987) J. Mol. Spectrosc. **123**, 486.

[183] Pfelzer, C., Havenith, M., Perić, M., Mürtz, P., and Urban, W. (1996) J. Mol. Spectrosc. **176**, 28.

[184] Shih, S., Peyerimhoff, S. D., and Buenker, R. J. (1977) J. Mol. Spectrosc. **64**, 167.

[185] Perić, M., Buenker, R. J., and Peyerimhoff, S. D. (1990) Mol. Phys. **71**, 673.

[186] Perić, M., Peyerimhoff, S. D., and Buenker, R. J. (1990) Mol. Phys. **71**, 693.

[187] Perić, M., Engels, B., and Peyerimhoff, S. D. (1991) J. Mol. Spectrosc. **150**, 56.

[188] Perić, M., Engels, B., and Peyerimhoff, S. D. (1991) J. Mol. Spectrosc. **150**, 70.

[189] Perić, M., Peyerimhoff, S. D., and Buenker, R. J. (1991) J. Mol. Spectrosc. **148**, 180.

[190] Perić, M., Reuter, W., and Peyerimhoff, S. D. (1991) J. Mol. Spectrosc. **148**, 201.

[191] Carter, S., Handy, N. C., Puzzarini, C., and Tarroni, R. (2000) Mol. Phys. **98**, 1967.

[192] Jacox, M. E. and Olsen, W. B. (1986) J. Chem. Phys. **86**, 3134.

[193] Shepherd, R. A. and Graham, W. R. M. (1986) J. Chem. Phys. **86**, 2600.

[194] Forney, D., Jacox, M. E., and Thompson, W. E. (1995) J. Mol. Spectrosc. **170**, 178.

[195] Carrick, P. G., Pfeiffer, J., R. F. Curl, J., Koester, E., Tittel, F. K., and Kasper, J. V. V. (1982) J. Chem. Phys. **76**, 3336.

[196] Vervloet, M. and Herman, M. (1988) Chem. Phys. Lett. **144**, 48.

[197] Hsu, Y.-C., Shiu, Y.-J., and Lin, C.-M. (1995) J. Chem. Phys. **103**, 5919.

[198] Zhou, J., Garand, E., and Neumark, D. M. (2007) J. Chem. Phys. **127**, 114313.

[199] Brown, J. and Carrington, A. (2003) Rotational Spectroscopy of Diatomic Molecules, Cambridge University Press, United Kingdom.

[200] Herzberg, G. (1950) Molecular Spectra and Molecular Structure, I. Spectra of Diatomic Molecules, Krieger Publishing Company, Florida reprint edition edition.

[201] Davis, S., Uy, D., and Nesbitt, D. J. (2000) J. Chem. Phys. **112**, 1823.

[202] Camy-Peyret, C., Flaud, J., Guelachvili, G., and Amiot, C. (1973) Molecular Physics **26(4)**, 825–855.

[203] Guelachvili, G. (1976) Optics Communications **19(1)**, 150 – 154.

[204] Johnson, R. D. and Hudgens, J. W. (1996) J. Phys. Chem. **100(51)**, 19874–19890.

[205] Westbrook, C. K. and Dryer, F. L. (1979) Combustion Science and Technology **20**, 125–140.

[206] Li, J., Zhao, Z., Kazakov, A., Chaos, M., Dryer, F. L., and Jr., J. J. S. (2006) Int. J. Chem. Kinet. **39**, 109–136.

[207] Heicklen, J. (1976) Atmospheric Chemistry, Academic Press, New York.

[208] Seinfeld, J. H. and Pandis, S. N. (2006) Atmospheric chemistry and physics - from air pollution to climate change, John Wiley and Sons, 2nd edition.

[209] Jacox, M. E. and Milligan, D. E. (1973) J. Mol. Spectrosc. **47(1)**, 148 – 162.

[210] Bernardi, F., Epiotis, N. D., Cherry, W., Schlegel, H. B., Whangbo, M.-H., and Wolfe, S. (1976) J. Am. Chem. Soc. **98(2)**, 469–478.

[211] Ha, T.-K. (1975) Chem. Phys. Lett. **30**, 379–382.

[212] Niki, H., Maker, P. D., Savage, C. M., and Breitenbach, L. P. (1978) J. Phys. Chem. **82(2)**, 135–137.

[213] Radford, H. E. (1980) Chem. Phys. Lett. **71**, 195–197.

[214] Radford, H. E., Evenson, K. M., and Jennings, D. A. (1981) Chem. Phys. Lett. **78**, 589–591.

[215] Dulcey, C. S. and Hudgens, J. W. (1983) Bull. Soc. Chim. Belg. **92**, 583.

[216] Dulcey, C. S. and Hudgens, J. W. (1983) J. Phys. Chem. **87(13)**, 2296–2298.

[217] Dulcey, C. S. and Hudgens, J. W. (1986) J. Chem. Phys. **84(10)**, 5262–5270.

[218] Aristov, V., Conroy, D., and Reisler, H. (2000) Chem. Phys. Lett. **318(4-5)**, 393–401.

[219] Feng, L., Huang, X., and Reisler, H. (2002) J. Chem. Phys. **117(10)**, 4820–4824.

[220] Feng, L., Demyanenko, A. V., and Reisler, H. (2003) J. Chem. Phys. **118(21)**, 9623–9628.

[221] Feng, L., Demyanenko, A. V., and Reisler, H. (2004) J. Chem. Phys. **120(14)**, 6524–6530.

[222] Feng, L. and Reisler, H. (2004) J. Phys. Chem. A **108(45)**, 9847–9852.

[223] Wei, J., Karpichev, B., and Reisler, H. (2006) J. Chem. Phys. **125(3)**, 034303.

[224] Smith, J. D., Desain, J. D., and Taatjes, C. A. (2002) Chem. Phys. Lett. **366**, 417–425.

[225] Ahmed, M., Peterka, D. S., and Suits, A. G. (2000) Phys. Chem. Chem. Phys. **2**, 861–868.

[226] Dobe, S., Berces, T., Turanyi, T., Marta, F., Grussdorf, J., Temps, F., and Wagner, H. G. (1996) J. Phys. Chem. **100(51)**, 19864–19873.

[227] Pratt, D. W. (1998) Annu. Rev. Phys. Chem. **49**, 481–530.

[228] Krieg, J., Klemann, A., Gottbehüt, I., Thorwirth, S., Giesen, T. F., and Schlemmer, S. (2011) Rev. Sci. I. **82(6)**, 063105.

Appendix A

Harmonically Coupled Morse Oscillator (HCMO) fitting routine

This is the full fitting program, with sample input file, for the Harmonically Coupled Morse Oscillator model presented in chapter 5.

Sample Input File:

```
3004.436        1       1
3160.82118      1       0
3160.82118      1       1

2283.3          2       1
3065.63346      2       1
3158.33273      2       1

2221.5          3       1
2381            3       0
3114.577        3       1

2156.5          4       1
2381.08860      4       0
2381.08860      4       1

-999    0       0

1.007825,2.014102,12.0000,120.,1.0818
7,7,7
1
4
7.8794175d-12
1.903033d8
2580.1732d0
0.72

0
0
0
0
```

Main Program:

```
      PROGRAM wgtLSQ
      IMPLICIT double precision(A-H,O-Z)
      CHARACTER*16 DATAFILE
      DIMENSION XM(25,2),wt(250),RES(250),SCRAT(5000),
     x COEF(10),SPLST(10),STAT(10),PV(250,2),SDPV(250),SDRES(250),
     x VCV(10,10),STEP(10),DSTAK(20000),SCALE(10),STP(10),IFIXED(10),
     . spec(100),coefp(5),F(12),y(25),ctemp(10),ytmp(25),fcm(12)
      COMMON/CSTAK/DSTAK
      common/flag/iflag,ieflag
```

```
      common/constants/hconstant(10),ihconstant(10),gmat(3,3,4)
      EXTERNAL MODEL

c **********************************************************************c

c this version will also fit overtone bands and print out the
c eigenfunctions.

      LDSTAK = 20000
      IXM=250
C     THE FOLLOWING WERE ADDED TO ACCESS THE NLSWS VERSION OF NLSQ
C     THIS VERSION USES WEIGHTED LEAST SQUARES FITTING OF <= 10 PARAMS
      DELTA = -1.0
      IVAPRX=1
      MIT = 100
      IVCV = 25
      NPRT = 22222
do i=1,10
c      SCALE(i)=-1.0d-5
STP(i)=1.0d-5
enddo
SCALE(1)=-1.
c SCALE(3)=1.d-5
c      STP(1)=-1.0d0
      STOPP = 1.d-7
      STOPSS = 1.d-7
      m=3

iflag=0
c  this routine will fit the predicted frequencies from a harmonically
c coupled morse oscillator model to experimental frequencies of all
c the methyl radical isotopes.
c I will make it general so that I can change the hamiltonian and basis
c set if that is needed.

c first set up some of the constants that will be needed in the model
c some idiot first programmed this shit in cgs units, evidently it should be
c in atomic units if one wants to have reasonable numbers.

c hbar = 1.054571628d-27
c cms = 2.99792458d10

hbar=1.
cms=137.036

C
      DATAFILE='mfrinput.dat'
      OPEN(UNIT=7,FILE=DATAFILE,IOSTAT=IOS,STATUS='OLD')
      REWIND 7
      N=0
   10 READ (7,*) y(N+1),spec(N+1), WT(N+1)
      IF(y(N+1).EQ.-999.) GO TO 15
      N=N+1
      GO TO 10
   15 continue

c read in the hydrogen mass, deuterium mass, carbon mass, the
c bond angle, and the bond length

read (7,*) hmass,dmass,cmass,ba,bl

c read in the basis set parameters you want to use for the fit
c specifically, the max quanta you want in each stretch
c and store the values in hconstant

      read(7,*) nq1, nq2, nq3

c read in the ifit, which is 1 if you want to fit or 0 if you just
c want to predict the spectra based on the input force constants

      read(7,*) ifit

c read in the stuff about the variables that you will have starpact fit
      READ(7,*) NPAR

C the parameters are (in this order):
c       De, aa, Frr,wni
c where De is the dissociation energy, aa is the morse parameter
c and Frr is the force constant coupling the different stretches


      READ(7,*) (coef(J), J=1,NPAR)
      READ(7,*) (IFIXED(J), J=1,NPAR)

      close(unit=7)

c turn the parameters into atomic units from cgs units
c de in energy, a in 1/length, frr in cm-1/ang^2

c enau=4.35974394d-18
```

```
c ajscgs=1.0d-7
c alenau=0.52917720859d0
c erghar=4.35974820000e-11
c cmhar=219474.6313705
c coef(1)=ctemp(1)*ajscgs/enau
c coef(2)=ctemp(2)*alenau*1.0d-8
c coef(3)=ctemp(3)*alenau*alenau/(cmhar)

c print *,ctemp(1),ctemp(2),ctemp(3)
c print *,coef(1),coef(2),coef(3)


c write the info that will be passed on to model via common blocks

ihconstant(1) = nq1
ihconstant(2) = nq2
ihconstant(3) = nq3
hconstant(4) = hbar
hconstant(5) = cms

c now calculate the g-matrix and write that to gmat so it can get
c passed on to model

amug=1.66053886d-24
emassg=9.10938215d-28
acm=1.0d8
hmcgs=hmass*amug/emassg
dmcgs=dmass*amug/emassg
cmcgs=cmass*amug/emassg
c print *,hmcgs,dmcgs,cmcgs
blcgs=bl/acm
call gmiso(hmcgs,dmcgs,cmcgs,blcgs,ba)

c this is the output file for the eigenvalues and vectors

        open(unit=8,file='output.dat',status='unknown')

ieflag=0
c now split between the fitting and the modeling part of program

      if (ifit.eq.1) then

       CALL NLSWS(Y,WT,XM,N,M,IXM,MODEL,COEF,NPAR,RES,LDSTAK,
     X IFIXED,STP,MIT,STOPSS,STOPP,SCALE,DELTA,IVAPRX,NPRT,
     X NNZW,NPARE,RSD,PV,SDPV,SDRES,VCV,IVCV)

ieflag=1
        call model(coef,npar,XM,N,M,IXM,F)
        print *,f


C
      else

c this is to correct the the dimensions of coef
        do i=1,npar
        coefp(i) = coef(i)
        enddo

ieflag=1
        call model(coefp,npar,XM,N,M,IXM,F)
print *,'F list'

print *,f

      endif

close(8)

      call exit
      end


c ***********************************************************************
c ***********************************************************************

      SUBROUTINE MODEL(P,NPAR,XM,N,M,IXM,F)
      IMPLICIT double precision (A-H,O-Z)
      DIMENSION P(NPAR),XM(IXM,M),F(N),pcoef(npar),
     .          gmatiso(3,3),freq(1000),temp(3,4),
     . unpert(10),dkpert(10),pertu(10),pertl(10),ftmp(N)
      COMMON/constants/hconstant(10),ihconstant(10),gmat(3,3,4)
      common/flag/iflag


        HBAR = hconstant(4)
        cms = hconstant(5)
        pi=4.d0*atan(1.d0)
        hh=hbar*2.d0*pi
```

```
c        enau=4.35974394d-18
c        ajscgs=1.0d-7
        alenau=0.52917720859d-8
        erghar=4.35974394e-11
        cmhar=219474.6313705
c        pcoef(1)=p(1)*ajscgs/enau
pcoef(1)=p(1)/erghar
        pcoef(2)=p(2)*alenau
        pcoef(3)=p(3)*alenau*alenau/(erghar)

c        print *,p(1),p(2),p(3)
c        print *,pcoef(1),pcoef(2),pcoef(3)


C I will have to loop over this calculation for each isotope

do i=1,4

c for each isotope, I will put the gmatrix into gmatiso and send to
c the matrix elements routine

 do j=1,3
  do k=1,3
    gmatiso(j,k)=gmat(j,k,i)
  enddo
 enddo

c now calculate the eigenvalues for that isotope

call trans(pcoef,gmatiso,freq)

c store the frequencies in a temporary place

do j=1,3
 temp(j,i)=freq(j)
enddo

c end loop over isotopes
enddo

c now add the correction for the fermi interaction
c first pull out the relevant perturbed frequencies
c ch2d,chd2,cd3

c unpert(1)=temp(1,2)
c unpert(2)=temp(1,3)
c unpert(3)=temp(1,4)

c then make the matrix containing the perturbing frequencies

c dkpert(1)=2338d0/cmhar
c dkpert(2)=2054d0/cmhar
c dkpert(3)=2056d0/cmhar

c then send each to have the energies corrected for the pertebation
c the wni term is the off diagonal matrix element that we will be fitting

c wni=p(4)

c do i=1,3
c  en=unpert(i)
c  ei=dkpert(i)
c  call fermi(en,ei,wni,outu,outl)
c  pertu(i)=outu
c  pertl(i)=outl
c enddo

c put all of the frequency data into the F-matrix
c and turn them form hartrees to wavenumbers

        cmhar=219474.6313705
scale=p(4)

do i=1,4
 do j=1,3
   k=(i-1)*3+j
   Ftmp(k)=temp(j,i)*cmhar
 enddo
enddo

c call the new fermi routine that takes all the stretches and calculates
c the Fermi interaction

call fermi2(Ftmp,F,scale)

c now replace the perturbed frequencies

c F(4)=pertl(1)*cmhar
c F(7)=pertu(2)*cmhar
c F(10)=pertu(3)*cmhar
```

```
c print *, 'perturbed states'
c do i=1,3
c  print *,pertl(i)*cmhar,pertu(i)*cmhar
c enddo

END


c ***********************************************************************
c ***********************************************************************
      subroutine trans(p,gmatiso,freq)
      IMPLICIT double precision (A-H,O-Z)
      DIMENSION freq(1000),p(10),eigval(1000),gmatiso(3,3),
     . eigvecmat(1000,1000),ibasis(1000,4),hmat(1000,1000)
      COMMON/constants/hconstant(10),ihconstant(10),gmat(3,3,4)
      common/flag/iflag

c this is the maximum number of basis sets that can be used

nmax=1000

C THIS SUBROUTINE CALCULATES ENERGY LEVELS FOR A HAMILTONIAN USING MORSE
C OSCILLATOR BASIS SET USING THE EXACT EXPRESSIONS FOR A MORSE OSC.

C GENERATE BASIS SET LABELLING SCHEME

CALL MAKEBASIS(iBASIS,NMAX,nbasis)
c print *,'basis made'

C CALCULATE THE HAMILTONIAN MATRIX ELEMENTS
C AND RETURN THEM IN THE HERMITIAN MATRIX HMAT(NTOT,NTOT)

CALL MATRIXEL(iBASIS,HMAT,nbasis,nmax,p,gmatiso)
c  print *,'matrixel done'
C NOW CALL THE DIAGONALIZATION ROUTINES

CALL hmatdiag(nbasis,hmat,nmax,EIGVECMAT,EIGVAL)
c print *,'hmatdiag done'
C THIS RETURNS...
C THE NTOT ASCENDING EIGENVALUES IN EIGVAL(J=1,NTOT)
C THE CORRESPONDING MATRIX OF EIGENVECTORS IN EVECMAT(I=1,NTOT,J)
C WHERE EIGENVAL(J) CORRESPONDS TO THE JTH COLUMN VECTOR


C sort and store the values for further analysis
call store(ibasis,EIGVECMAT,EIGVAL,nbasis,NMAX,freq)

c do i=1,3
c print *,freq(i)
c enddo

return
END


c ***********************************************************************
c ***********************************************************************

SUBROUTINE MAKEBASIS(iBASIS,nmax,nbasis)
IMPLICIT double precision (A-H,O-Z)
DIMENSION iBASIS(NMAX,4)
COMMON/constants/HCONSTANT(10),ihconstant(10),gmat(3,3,4)
common/flag/iflag

C      THIS SUBROUTINE GENERATES THE BOOKKEEPING FOR HOW BASIS
C      FUNCTIONS ARE LABELLED

C READ IN BASIS SET PARAMETERS, STORED IN ICONSTANT

C the basis is labeled by the bond number and the number of quanta
C in each bond. basis(n,1) holds the quantum numbers for bond 1, etc.

nq1 = ihconstant(1)
nq2 = ihconstant(2)
nq3 = ihconstant(3)

NBASIS = 0
ni=nq1+1
nj=nq2+1
nk=nq3+1
do i = 1,ni
 do j = 1,nj
  do k = 1,nk
  nbasis = nbasis + 1
  ibasis(nbasis,1) = nbasis
  ibasis(nbasis,2) = i-1
  ibasis(nbasis,3) = j-1
  ibasis(nbasis,4) = k-1
  enddo
```

```
 enddo
enddo

c PRINT OUT THE BASIS SET LIST IF IFLAG = 1
if (iflag.eq.1) then
DO I = 1,nbasis
PRINT *, iBASIS(I,1),iBASIS(I,2),iBASIS(I,3),iBASIS(I,4)
ENDDO
ENDIF

RETURN
END
C *********************************************************************
C *****************************************************************

SUBROUTINE MATRIXEL(iBASIS,HMAT,nbasis,NMAX,p,gmatiso)
IMPLICIT double precision (A-H,O-Z)
DIMENSION HMAT(NMAX,NMAX),iBASIS(NMAX,4),p(10),gmatiso(3,3),
     .  delta(10),energyr(10),energyp(10),emorse(10)
COMMON/constants/HCONSTANT(10),ihconstant(10),gmat(3,3,4)

c print *,'entered matrixel'

C THIS SUBROUTINE HAS THE RESPONSIBILITY TO CALCULATE THE
C MATRIX ELEMENTS OF HMAT(NTOT,NTOT)
c the matrix elements are explicit matrix elements of a morse oscillator

C SET UP HAMILTONIAN CONSTANTS
hbar = hconstant(4)
cms = hconstant(5)
pi=4.*atan(1.)
hh=hbar*2.*pi


c read in the parameters for the hamiltonian that are being fit by starpac

De = p(1)
aa = p(2)
frr = p(3)

c now for the actual expressions for the matrix elements
c loop through the list of basis fcns

do n=1, nbasis
do nn=1,nbasis

c first make the necessary matrix elements

 do m=1,3
        gmu=1./gmatiso(m,m)
        ak=fcnk(gmu,de,aa,hbar)
   nl=ibasis(n,m+1)
   nu=ibasis(nn,m+1)
c print *,nu,nl
   energyr(m)=rcoupling(gmu,nu,nl,aa,de,ak)
   energyp(m)=pcoupling(gmu,nu,nl,aa,de,ak,hbar)
   delta(m)=deltakron(nu,nl)
   emorse(m)=dmorse(hbar,de,gmu,cms,aa,nl)
c print *,nu,nl,delta(m),energyr(m),energyp(m),emorse(m)
 enddo

c then combine them to make the hmat entry

fm=emorse(1)*delta(1)*delta(2)*delta(3)
sm=delta(1)*emorse(2)*delta(2)*delta(3)
tm=delta(1)*delta(2)*emorse(3)*delta(3)
totmorse=(fm+sm+tm)
c print *,fm,sm,tm,totmorse

first=energyr(1)*energyr(2)*delta(3)
second=energyr(1)*energyr(3)*delta(2)
third=delta(1)*energyr(2)*energyr(3)
potential=frr*(first+second+third)
c print *,frr,first,second,third,potential

c the -1 here is for the i^2 term
fk=-1.d0*energyp(1)*energyp(2)*delta(3)
fkp=gmatiso(1,2)
sk=-1.d0*energyp(1)*delta(2)*energyp(3)
skp=gmatiso(1,3)
tk=-1.d0*delta(1)*energyp(2)*energyp(3)
tkp=gmatiso(2,3)
ekinetic=(fk*fkp+sk*skp+tk*tkp)
c print *,fk,sk,tk

c sum up each piece of the matrix element and store in the proper place
c in the hmat matrix

tot=totmorse+potential+ekinetic
hmat(n,nn)=tot
```

```
c end the loop over the basis functions

enddo
enddo


c print *,'end loop in matrixel'

c print out hamiltonian matrix for debugging
c        IF(IFLAG.EQ.1) THEN
c        DO N1=1,nbasis
c        DO N2=1,nbasis
c if (abs(hmat(n1,n2)).gt.(1.0d-10)) then
c        PRINT *, iBASIS(N1,2),ibasis(n1,3),iBASIS(N1,4),
c     .  iBASIS(N2,2),ibasis(n2,3),iBASIS(N2,4),HMAT(N1,N2)
c endif
c        ENDDO
c        ENDDO
c        ENDIF

        END

C *****************************************************************
C *****************************************************************
        SUBROUTINE hmatdiag(nmat,AMAT,nmax,EVEC,EIG)
        IMPLICIT double precision (A-H,O-Z)
        DIMENSION AMAT(nmax,nmax),EVEC(nmax,nmax),
     .  Work(2*nmat**2+6*nmat+1),
     .  IWORK(5*nmat+3),EIG(nmax)
        CHARACTER job,uplo
        EXTERNAL sSYEVD


c     THIS SUBROUTINE DIAGONALIZES THE HAMILTONIAN WITH
C     DSYEVD ROUTINE FROM MKL LIBRARY
c       Integer IA,N,IV,IFAIL
c       Real AMAT(IA,NMAT),EIG(NMAT),EVEC(IV,NMAT),WORK(3*NMAT)
c       Parameters
c            AMAT   a real array of dimension at least NMAT X NMAT
c
c            IA  initial dimension of A, at least N
c            NMAT   order of matrix
c            EIG   real array, dim'n at least NMAT    on exit, contains
c                     eigenvalues in ASCENDING order
c            EVEC   real array, at least NMAT X NMAT.     on exit, contains
c                     eigenvectors in ascending order, such that
c                     EVEC(I,J), I=1,2,...,N correspond to EIG(J)
c            WORK   real array, used as scratch
c            IFAIL  must be set=0 before entry; if IFAIL<>0 on exit,
c                     an error has occurred

        ia=Nmax
        lwork=2*nmat**2+6*nmat+1
        liwork=5*nmat+3
        IFAIL=0
        job = 'V'
        uplo = 'L'



c       first need to write AMAT into EVEC, since the input matrix
c       is replaced with the eigenvector matrix anyway
        do i=1,nmat
        do j=1,nmat
        evec(i,j) = amat(i,j)
        enddo
        enddo


        CALL DSYEVD(JOB,UPLO,nmat,evec,ia,eig,work,lwork,
     .    IWORK,liwork,IFAIL)
        IF(IFAIL.NE.0) THEN
        PRINT *, 'PROBLEMS IN MATRIX DIAGONALIZATION ROUTINE'
        PRINT *, 'IFAIL =  ',IFAIL
        ENDIF


c print *, 'nmat=',nmat
c do i=1,nmat
c print *,eig(i)
c enddo

      RETURN
      END

c *****************************************************************
c *****************************************************************
subroutine store(iBASIS,EIGVECMAT,EIGVAL,nbasis,NMAX,Fiso)
implicit double precision (a-h,o-z)
```

```
dimension ibasis(nmax,4),eigvecmat(nmax,nmax),eigval(nmax),
     .  fiso(nmax)
common/flag/iflag,ieflag

c this takes the list of eigenvalues and puts them in the f-matrix
c so that it can be least-squares fit

c the eigenvalues come out sorted in ascending order
c the first number is the zpe and will be subtracted off
c the complete list of values and eigenfunctions will be
c written in another file. the 3 ch stretch data will be put
c in the f-matrix


do i=1,3
j=i+1
 temp=eigval(j)-eigval(1)
Fiso(i)=temp
enddo

c print out to a new file the list of eigenvalues and corresponding eigenvector

if (ieflag.eq.1) then

c        DO I = 1,nbasis
c        write(8, *) iBASIS(I,1),iBASIS(I,2),iBASIS(I,3),iBASIS(I,4)
c        ENDDO

do i=1,20
temp2=(eigval(i)-eigval(1))*219474.6313705
write(8,*) eigval(i),temp2

do j=1,nbasis
        aa=ibasis(j,2)
        bb=ibasis(j,3)
        cc=ibasis(j,4)
        tot=aa+bb+cc

        if (abs(eigvecmat(j,i)).ge.1.e-2) then
 write(8,*) eigvecmat(j,i),ibasis(j,2),ibasis(j,3),ibasis(j,4)
endif
enddo
enddo

endif

c    10 format('',D10.8)

return
end

c ****************************************************************
c ****************************************************************

subroutine gmiso(hmass,dmass,cmass,bl,ba)
implicit double precision (a-h,o-z)
dimension ch3m(10),ch2dm(10),chd2m(10),
     . chd3m(10),cd3m(10),ch3c(10),ch2dc(10),chd2c(10),cd3c(10),
     . ch3gm(10,10),ch2dgm(10,10),chd2gm(10,10),cd3gm(10,10)
        COMMON/constants/HCONSTANT(10),ihconstant(10),gmat(3,3,4)
        common/flag/iflag


c this is the bookkeeping routine for the calculating all of the
c g-matrices for each of the isotopes

c this is the number of coordinates in the g-matrix


ncoord=3

c separate the data by species and create masses and coordinates for each

c      masses in amu for CH3
       ch3m(1)=hmass
       ch3m(2)=hmass
       ch3m(3)=hmass
       ch3m(4)=cmass

c     enter coords (ang and degrees)
c     r12, r13, r14, phi142, phi143
       ch3c(1) = bl
       ch3c(2) = bl
       ch3c(3) = bl
       ch3c(4) = ba
       ch3c(5) = ba

c calculate the g-matrix elements for this isotope

       call gmatrix(ch3m,ncoord,ch3c,ch3gm)
```

```
c now repeat for the second species, CH2D

c      masses for CH2D
       ch2dm(1)=hmass
       ch2dm(2)=hmass
       ch2dm(3)=dmass
       ch2dm(4)=cmass

c      enter coords (ang and degrees)
c      r12, r13, r14, phi142, phi143
       ch2dc(1) = bl
       ch2dc(2) = bl
       ch2dc(3) = bl
       ch2dc(4) = ba
       ch2dc(5) = ba

c calculate the g-matrix elements for this isotope

       call gmatrix(ch2dm,ncoord,ch2dc,ch2dgm)

c now for the third species, CHD2

c      masses in amu for CHD2
       chd2m(1)=hmass
       chd2m(2)=dmass
       chd2m(3)=dmass
       chd2m(4)=cmass

c      enter coords (ang and degrees)
c      r12, r13, r14, phi142, phi143
       chd2c(1) = bl
       chd2c(2) = bl
       chd2c(3) = bl
       chd2c(4) = ba
       chd2c(5) = ba

c calculate the g-matrix elements for this isotope

       call gmatrix(chd2m,ncoord,chd2c,chd2gm)

c repeat for the fourth species, CD3

c      masses in amu for CD3
       cd3m(1)=dmass
       cd3m(2)=dmass
       cd3m(3)=dmass
       cd3m(4)=cmass

c      enter coords (ang and degrees)
c      r12, r13, r14, phi142, phi143
       cd3c(1) = bl
       cd3c(2) = bl
       cd3c(3) = bl
       cd3c(4) = ba
       cd3c(5) = ba
c calculate the g-matrix elements for this isotope

       call gmatrix(cd3m,ncoord,cd3c,cd3gm)

c compile all the gmat data into the gmat matrix


do i=1,3
do j=1,3
 gmat(i,j,1)=ch3gm(i,j)
enddo
enddo

do i=1,3
do j=1,3
 gmat(i,j,2)=ch2dgm(i,j)
enddo
enddo

do i=1,3
do j=1,3
 gmat(i,j,3)=chd2gm(i,j)
enddo
enddo

do i=1,3
do j=1,3
 gmat(i,j,4)=cd3gm(i,j)
enddo
enddo

return
end
```

```
c ****************************************************************
c ****************************************************************
      subroutine gmatrix(amass,ncoord,coord,gmat)
      implicit double precision(a-h,o-z)
      dimension gmat(10,10), amass(10), coord(10)

c  this subroutine calculates the Wilson G matrix as per
c  the elements listed in WDC appendix VI

c  we assume a planar 4-atom molecule with atom 4 as the central atom
c  the coordinates are 3 bond lengths and 2 angles
c  the unique atom is number one, and the two angles surround
c  that atom. this g-matrix is only for the 3 stretches

c first, define all the parameters

      am1=amass(1)
      am2=amass(2)
      am3=amass(3)
      am4=amass(4)
rmu1 = 1./am1
rmu2 = 1./am2
rmu3 = 1./am3
rmu4 = 1./am4

      pi = 4.*atan(1.)
      r14 = coord(1)
      r24 = coord(2)
      r34 = coord(3)
ro14 = 1./r14
ro24 = 1./r24
ro34 = 1./r34
      phi142rad = coord(4)*pi/180.
      phi143rad = coord(5)*pi/180.
      phi243rad = 2.*pi-phi142rad-phi143rad


c      cospsi321 = cospsi123

c print *,'cos coords'
c print *,cospsi132,cospsi312,cospsi321

c     now calculate the Gij matrix elements

      gmat(1,1) = rmu1+rmu4
      gmat(1,2) = rmu4*cos(phi142rad)
      gmat(1,3) = rmu4*cos(phi143rad)
      gmat(2,2) = rmu2 + rmu4
      gmat(2,3) = rmu4*cos(phi243rad)
      gmat(3,3) = rmu3 + rmu4

c complete the matrix

      do i=1,ncoord
      do j=1,i
      gmat(i,j)=gmat(j,i)
      enddo
      enddo

      return
      end

C ****************************************************************
c ****************************************************************

function dmorse(hbar,de,gmu,cms,aa,nn)
implicit double precision (a-h,o-z)

c this calculates the morse oscillator energy levels, the Ho part
c of the Hamiltonian

pi=4.*atan(1.)
hh=hbar*2.*pi
rnn=nn

ww=2.*aa*hbar*sqrt(de/(2.*gmu))
wa=2*log(aa)
wh=2*log(hbar)
wb=log(2.)
wc=log(gmu)
wx=exp(wa+wh-wb-wc)

temp=(rnn+0.5)*ww-wx*(rnn+0.5)**2.
dmorse=temp

return
end

c ****************************************************************
c****************************************************************
```

```
function deltakron(nu,nl)
implicit double precision (a-h,o-z)

c kronicker delta function
c this function returns 0.0 if nu is not equal to nl and 1.0 if nu=nl

if (nu.eq.nl) then
temp=1.0d0
else
temp=0.0d0
endif

deltakron=temp

return
end

c *************************************************************************
c *************************************************************************

FUNCTION digamma(dgx)
IMPLICIT double precision (A-H,O-Z)
DATA cs,d1/100.d0,-0.5772156649d0/

c this calculates the digamma function for values greater than -1 to an
c accuracy of better that 1 part in 10^8 (this can be changed by changing
c where you start using the stirling approximation - ie change cs)
c This uses the stirling approximation at large values (eq 6.3.18 of
c Abromowitz and Stegun) and then uses the recurrence formula (6.3.5) to
c get the smaller values of the function.
c This algorithm was inspired by Appl. Statistics (1976) vol. 25 no. 3
c algorithm AS 103 by JM Bernado

y = dgx
s3 = 1.d0/12.d0
s4 = 1.d0/120.d0
s5 = 1.d0/252.d0

if (y.le.0.0) then
 temp = 0.0
endif

temp = 0.0

   10 if (y.ge.cs) go to 20
temp = temp -1.0d0/y
y = y + 1.0d0
go to 10

   20  rr = 1/y
temp = temp+dlog(y)-0.5d0*rr
rr = rr*rr
temp = temp-rr*(s3-rr*(s4-rr*s5))

digamma = temp

return
END

c *************************************************************************
c *************************************************************************


FUNCTION fcnk(fmu,dd,aa,hbar)
IMPLICIT double precision (A-H,O-Z)

p1 = 2.d0/(aa*hbar)
p2 = dsqrt(2.d0*fmu*dd)
tmp = p1 * p2

fcnk = tmp


RETURN
END

c *************************************************************************
c *************************************************************************

FUNCTION pcoupling(rmu,nu,nl,aa,de,ak,hbar)
IMPLICIT double precision (A-H,O-Z)

c this function returns the matrix element for the momentum operator when
c the upper state is not equal to the lower state, as per Halonene and Child
c print *,nu,nl

rnu = nu
rnl = nl
inu = nu
inl = nl
```

```
cc=1.0d0

c taking advantage of the Hermitian operators

        if (inu.lt.inl) then
         tp = rnu
         rnu = rnl
         rnl = tp
         inn = inu
         inu = inl
         inl = inn
 cc = -1.0d0
        endif

        rj = rnu-rnl
jj = inu-inl

if (inu.eq.inl) then
 temp=0.0

else
 p1 = hbar* (-1.d0)**(rj+1.)*aa/2.d0
 p2= dsqrt((ak-2.d0*rnl-1.d0)*(ak-2.d0*(rnl+rj)-1.d0))
 prod=1.d0
 do m=1,jj
  rm=float(m)
  prod= prod*(rnl+rm)/(ak-rnl-rm)
 enddo
 temp=p1*p2*dsqrt(prod)
endif

pcoupling = temp*cc
c print *,nu,nl,pcoupling

RETURN
END


c *************************************************************************
c *************************************************************************

FUNCTION rcoupling(fmu,nu,nl,aa,de,ak)
IMPLICIT double precision (A-H,O-Z)

c this function calculates the off diagonal matrix elements for non-zero
c changes in n for the potential energy cross term

c print *,'entered rcoupling'

        rnu = nu
        rnl = nl
knu = nu
knl = nl

c taking advantage of the Hermitian operators

if (nu.lt.nl) then
 tp = rnu
 rnu = rnl
 rnl = tp
 knn = knu
 knu = knl
 knl = knn
endif

rj = rnu-rnl
jj = knu-knl

        if (knu.eq.knl) then
temp=0.0d0
 if (knl.eq.0) then
           p1 = dlog(ak)
           arg2 = ak-1.d0-2.d0*rnl
          p2 = digamma(arg2)
    temp= (p1-p2)/aa

 else
  p1 = dlog(ak)
  arg2 = ak-1.d0-2.d0*rnl
  p2 = digamma(arg2)
  sum = 0.0d0
  do i=1,nl
   ri = float(i)
   sum = sum+1.d0/(ak-rnl-ri)
  enddo
  p3 = sum
  temp = (p1-p2+p3)/aa
 endif

        elseif (knu.gt.knl) then
```

```
 p1=(-1.d0)**(rj+1)/aa
         p2= dsqrt((ak-2.d0*rnl-1.d0)*(ak-2.d0*(rnl+rj)-1.d0))
         prod=1.d0
         do m=1,jj
          rm=float(m)
          prod= prod*(rnl+rm)/(ak-rnl-rm)
         enddo
 p3=rj*(ak-2.d0*rnl-rj-1.d0)
         temp = p1*p2*dsqrt(prod)/p3

        elseif (knu.lt.knl) then
print *,error
temp = 0.0
        endif

        rcoupling = temp

RETURN
END

c *******************************************************************
c *******************************************************************

subroutine fermi(en,ei,wni,outu,outl)
implicit double precision (a-h,o-z)


eniave=(en+ei)*0.5d0
del=en-ei
outu=eniave+0.5d0*dsqrt(4.d0*wni*wni+del*del)
        outl=eniave-0.5d0*dsqrt(4.d0*wni*wni+del*del)
c print *,en,ei,eniave,del,wni

return
end

c *****************************************************************
c *****************************************************************

subroutine fermi2(ftmp,f,scale)
implicit double precision (a-h,o-z)
dimension ftmp(12),f(12),ach2d(4,4),achd2(4,4),
     .  eigchd2(4),eigch2d(4),evch2d(4,4),evchd2(4,4),
     .  ach3(4,4),eigch3(4),evch3(4,4),
     .  acd3(4,4),eigcd3(4),evcd3(4,4)

c this subroutine calculates the effect of all coupling with
c 2 quanta states for all isotopomers
c print *,'before coupling'
c print *,ftmp
c print *,'after coupling'
c first CH3


        ach3(1,1)=ftmp(2)
        ach3(1,2)=185.593*0.5d0*scale/2.d0
        ach3(1,3)=-185.556*0.5d0*scale/2.d0
ach3(1,4)=0.d0
        ach3(2,2)=2795.
        ach3(2,3)=0.d0
ach3(2,4)=191.746*0.5d0*scale/2.d0
ach3(3,3)=2795.d0
ach3(3,4)=191.746*0.5d0*scale/2.d0
        ach3(4,4)=ftmp(1)

c make it symmetrical
        do i=1,4
         do j=i,4
          ach3(j,i)=ach3(i,j)
         enddo
        enddo

        nmch3=4
        call hmatdiag(nmch3,ach3,nmch3,evch3,eigch3)

c now pull out the stretches and put them in the f matrix

        f(1)=eigch3(3)
        f(2)=eigch3(4)
f(3)=f(2)

c end alternate way to get ch3 coupling


c then ch2d, start with symmetric stretches

ach2d(1,1)=ftmp(4)
ach2d(1,2)=-104.598*0.5d0*scale/2.d0
ach2d(1,3)=10.315*0.5d0*scale/2.d0
```

```
ach2d(1,4)=0.0
ach2d(2,2)=2338.
ach2d(2,3)=0.
ach2d(2,4)=159.268*0.5d0*scale/2.d0
ach2d(3,3)=2774.
ach2d(3,4)=262.485*0.5d0*scale/2.d0
ach2d(4,4)=ftmp(5)

c make it symmetrical
do i=1,4
 do j=i,4
  ach2d(j,i)=ach2d(i,j)
 enddo
enddo

nmch2d=4
call hmatdiag(nmch2d,ach2d,nmch2d,evch2d,eigch2d)

c now pull out the stretches and put them in the f matrix

f(4)=eigch2d(1)
f(5)=eigch2d(4)

c ch2d asymmetric stretch

en=ftmp(6)
ei=2556
wni=-264.846*(1.d0/dsqrt(8.d0))*scale
        eniave=(en+ei)*0.5d0
        del=en-ei
        outu=eniave+0.5d0*dsqrt(4.d0*wni*wni+del*del)
        outl=eniave-0.5d0*dsqrt(4.d0*wni*wni+del*del)
f(6)=outu


c next: chd2 the symmetric stretches

        achd2(1,1)=ftmp(7)
        achd2(1,2)=163.879*0.5d0*scale/2.d0
        achd2(1,3)=10.267*0.5d0*scale/2.d0
        achd2(1,4)=0.0
        achd2(2,2)=2054
        achd2(2,3)=0
        achd2(2,4)=-47.064*0.5d0*scale/2.d0
        achd2(3,3)=2554
        achd2(3,4)=383.853*0.5d0*scale/2.d0
        achd2(4,4)=ftmp(9)

c make it symmetrical
        do i=1,4
         do j=i,4
          achd2(j,i)=achd2(i,j)
         enddo
        enddo

        nmchd2=4
        call hmatdiag(nmchd2,achd2,nmchd2,evchd2,eigchd2)

c now pull out the stretches and put them in the f matrix

        f(7)=eigchd2(2)
        f(9)=eigchd2(4)

c chd2 asymmetric stretch
c just print out the uncoupled values so we can couple it later

f(8)=ftmp(8)

c        en=ftmp(8)
c        ei=2304
c        wni=72.942*scale
c        eniave=(en+ei)*0.5d0
c        del=en-ei
c        outu=eniave+0.5d0*dsqrt(4.d0*wni*wni+del*del)
c        outl=eniave-0.5d0*dsqrt(4.d0*wni*wni+del*del)
c        f(8)=outu


c finally, cd3
c the 2v4 state perturbes both the stretches, separtely
c first the symmetric stretch

c        en=ftmp(10)
c        ei=2056
c        wni=-127.945*0.5d0*scale
c        eniave=(en+ei)*0.5d0
c        del=en-ei
c        outu=eniave+0.5d0*dsqrt(4.d0*wni*wni+del*del)
c        outl=eniave-0.5d0*dsqrt(4.d0*wni*wni+del*del)
c        f(10)=outu
```

```
c cd3 asymmetric stretch

c        en=ftmp(11)
c        ei=2056
c        wni=131.35*0.5d0*scale
c        eniave=(en+ei)*0.5d0
c        del=en-ei
c        outu=eniave+0.5d0*dsqrt(4.d0*wni*wni+del*del)
c        outl=eniave-0.5d0*dsqrt(4.d0*wni*wni+del*del)
c        f(11)=outu
c        f(12)=f(11)

c alternate frequency method cds

        acd3(1,1)=ftmp(11)
        acd3(1,2)=120.069*0.5d0*scale/2.d0
        acd3(1,3)=-120.041*0.5d0*scale/2.d0
acd3(1,4)=0.d0
        acd3(2,2)=2056.d0
        acd3(2,3)=0.d0
acd3(2,4)=117.625*0.5*scale/2.d0
        acd3(3,3)=2056.d0
acd3(3,4)=117.625*0.5*scale/2.d0
acd3(4,4)=ftmp(10)

c make it symmetrical
        do i=1,4
         do j=i,4
          acd3(j,i)=acd3(i,j)
         enddo
        enddo

        nmcd3=4
        call hmatdiag(nmcd3,acd3,nmcd3,evcd3,eigcd3)

c now pull out the stretches and put them in the f matrix

        f(10)=eigcd3(3)
        f(11)=eigcd3(4)
        f(12)=f(11)

c end alternate method

return
end

c ****************************************************************
c ****************************************************************
```

Appendix B

LabWindows Code for the New Spectrometer

Included here is the LabWindows code used to run the new spectrometer presented in chapter 3.

```
/* ************************************************************************
************************************************************************

SCAN.C



*NB See Quicknotes for updates and Settings

This is the first working version of the data acquisition program written
in C language that interfaces to NI 6110 and 6025 cards in a pentium-based PC

The main subroutines in this program are as follow:

MAIN is the first subroutine accessed.  It defines global variables (static)
and set up the user interface panels

Main_Done is the subroutine for quitting out of the program

Measure is the subroutine that acquires the data (IR absorbance, etalon, ref cell,
and IR power) and displays them to the screen

The Wave_Form subroutine captures and displays the time dependent waveform of the
signal.  It is used to set gates and maximize signals.

Save_Data subroutine saves the data as a binary file to be passed to the array of
fortran programs developed to plot and analyze data.

New_Scan resets the counter variables for a new data scan.


This version of the program generates pulses on the 6110 card.  The rising edge
of the pulse is used to trigger the pulse valve and the falling edge, which comes
after some delay, is used to start the data acquisition of the signal wave form
on the 6110 card which usesthe internal 20 MHz counter to set the rate.  2000 data
points are acquired at 1 MHz covering 2 ms of signal.  The waveform is integrated
with a signal and two baseline gates.  This integral is averaged for the number of
averages specified.

Multiple other channels are read on the 6025 card and plotted and stored.  */

#include "ScanUI.h"
#include <cvirte.h>
#include <userint.h>
#include <analysis.h>
#include <formatio.h>
#include <ansi_c.h>
#include <utility.h>
#include <easyio.h>
#include <Dataacq.h>
#include <stdlib.h>
#include <NIDAQEX.h>
#include <string.h>
```

```
#include <rs232.h>
#include <math.h>
#include <time.h>

#define MaxScanSize 4100
#define TACres 64
#define NTraces 5

struct traces
{
double *ACSig;  /* AC Coupled Signal (Gated)  */
double *DCSig;  /* DC Voltage from Signal Detector  */
double *DCRef; /* DC Voltage from Reference Detector  */
double *TAC1; /* TAC for syncing with AutoScan */
double *Fr1500;
double *Fr250;
};

char *Newdir(char *currdir,char *append_this ,int *Ierror); // Creates a directory and updates string
char *strrchr(const char *save_file, int c);

/* AutoScan I/O */
static int iDIOSegOut  = 1;  // Blue
static int iDIODataOut = 2;  // Red
static int iDIOSegIn   = 3;  // Yellow
static int iDIODataIn  = 4;  // Orange

const int iPCI6110 = 1;  // PCI-6110
const int iPCI6025 = 2;  // PCI-6025E
const int iAutoscan = 1;  //RS232 port, COM1 connected to Autoscan
const int iMFC = 3;   //RS232 port, COM3, connected to CCR Mass Flow Controler box

static int isPulsing=0; // Status of Pulse Valve
static int iChangeWFGates=0;   // Triggers update of the gates in the waveform
static int iChangeWFGain =0; // Triggers update of the A2D gain for the waveform
static int iSaveWaveform =0;  // Triggers the saving of the waveform

double *adScan; // Array for storing the data (now dynamic)
// Data is stored in sequential blocks
unsigned long ulDataPoints; // # X Data Points Expected

// static double adData[4*MaxScanSize];    // Old array for storing data - deprecated

static double dOffsetDCSig, dOffsetDCRef, dOffsetVSaw, dOffsetFr250, dOffsetFr1500;


const char sINITfile[10]="b212.ini";
char sdate[88]="MM-DD-YYYY";
char sDirDefDate[MAX_PATHNAME_LEN];
char sDirDef[MAX_PATHNAME_LEN];
char DirDef[MAX_PATHNAME_LEN];

static int isigamp=2, ietamp=2, iTACamp=1, iIRamp=1;
static int iADamp=2; /* Gain changed from 20 to 2 on 06/25/06 by FD */
static int isigoffset=200, ietoffset=1600, iTACoffset=500, iIRoffset=1000;
static long lB1Start, lB1Length, lB2Start, lB2Length;
static long lSigStart, lSigLength, ulPulseRate;
static int panel0, panel1, panel2, panel3, panel4, panel5, panel6;
static int istopflag=0, iControl, iautocount, iexit=0;
static int imenubar, iloopcount;

static double LSB0=2.44; /* Least Significant Bit in mV. */
static double FreqStepSize=12.5; /* in MHz */

/*          Variables that can be changed to alter the waveform acquisition and length of scan  */
const unsigned int uMaxPoints=4096; /*max. number of data points acquired in full scan  */
const static int ArraySize=4100; /* dimension must be greater than uMaxPoints */
static short uladata[16400]; /* dimension must be greater than 4*uMaxPoints  */
static double dlpdata[10000];
static double dlpdatan[10000];

const int iPoints_Per_Screen=1024; /* 683 => 6-screen scan, 1024 => 4-screen,1365 => 3-screen */

const double dSampleRate=1000000.0;  /*frequency at which sample waveform points are taken*/
const unsigned long ulCount=2000; /*number of points in sample waveform  */
static double pdVoltBuffer[2001]; /* dimension must be greater than ulCount  */
static short piBuffer[2001]; /* dimension must be greater than ulCount  */

static long icounter=0, ibreakflag=0;
static int iOldPlot, iOldV1, iOldV2, iOldV3;
static long  uPulseAve;
static short sboard2, sboard1; /* 1: PCI-6110 2: PCI-6025E */
static short LamReadStep=10;
static double dLam[4][20], dTemp[5], dLamMeas[4][410];
static char save_file[MAX_PATHNAME_LEN], asave_file[MAX_PATHNAME_LEN], asave[MAX_PATHNAME_LEN];
static char Default_Directory[12]="C:Scan_Data";

int SendAutoscan(char command[50],char reading[50], int iType);
int ReadAutoscan(char reading[50]);
```

```
char ScanFileName[20];
int iStepSize, ulNumSeg;
char allocbuf[85];



/* MAIN */

int main (int argc, char *argv[])
{
int i;
int iStatus, iRetVal, iexclaim, iIgnoreWarning;

char sError[6];
char message[MAX_PATHNAME_LEN];

double dPulseDelay, dVmin, dVmax, dRefOffset, dSigOffset;
float  fPulseDelay, fVmin, fVmax, fRefOffset, fSigOffset;

int iScanStep;
int iPulseRate, iPulseAve;
int iB1start, iB2start, iSstart;
int iB1length, iB2length, iSlength;
int iWFgain;
int iASgain;
int iTrashAS, iTrashMFC;


const char sINITfile[10]="b212.ini";
FILE *fINITfile;

if (InitCVIRTE (0, argv, 0) == 0)
return -1; /* out of memory */
if ((panel0 = LoadPanel (0, "ScanUI.uir", PANEL_0)) < 0)
return -1;
if ((panel1 = LoadPanel (0, "ScanUI.uir", PANEL_1)) < 0)
return -1;
if ((panel2 = LoadPanel (0, "ScanUI.uir", PANEL_2)) < 0)
return -1;


/* Initialize DAQ and set default values; read calibration data */

if (Init_DA_Brds (2, &sboard2))
{
iexclaim = MessagePopup ("Fatal Error",
"Fatal Error: DAQ Boards not operating");
return -1;
}
if (Init_DA_Brds (1, &sboard1))
{
iexclaim = MessagePopup ("Fatal Error",
"Fatal Error: DAQ Boards not operating");
return -1;
}


/* Initialize the RS232 communication with Autoscan and the Mass Flow Controllers  */
// Must open the rs323 port connection and configure it to match params.as

iTrashAS = OpenComConfig (iAutoscan, "COM1", 9600, 0, 8, 1, 512, 512);
if (iTrashAS < 0)
{
MessagePopup ("Fatal Error",
"Fatal Error: Autoscan RS232 not working");
};

 iTrashMFC = OpenComConfig (iMFC, "COM3", 9600, 0, 8, 1, 512, 512);
 if (iTrashMFC < 0)
 {
 MessagePopup ("Fatal Error",
"Fatal Error: MFC RS232 not working");
 };


/* Setup Digital I/O lines for communication with AutoScan */
DIG_Line_Config (iPCI6025, 0, iDIOSegOut,  0);
DIG_Line_Config (iPCI6025, 0, iDIODataOut, 0);
DIG_Line_Config (iPCI6025, 0, iDIOSegIn,   1);
DIG_Line_Config (iPCI6025, 0, iDIODataIn,  1);

/* Set initial values to LOW */
DIG_Out_Line (iPCI6025, 0, iDIOSegIn,  0);
DIG_Out_Line (iPCI6025, 0, iDIODataIn, 0);


SetPanelAttribute (panel0, ATTR_VISIBLE, 1);   /*  the startup panel  */
SetPanelAttribute (panel1, ATTR_VISIBLE, 0);   /*  the difference freq signal panel - data  */
SetPanelAttribute (panel2, ATTR_VISIBLE, 0);   /*  the panel to display the waveform in real time  */
// SetPanelAttribute (panel3, ATTR_VISIBLE, 0);   /*  the panel with end of scan options  */
```

```
/* Load the Initialization File with the saved values */
if ( (fINITfile = fopen(sINITfile,"r+")) == NULL)
{
iexclaim = MessagePopup ("File Error","Intialization file b212.ini missing \n Execution Aborted");
return -1;
}
else
{
fscanf(fINITfile,"%d\n",&iScanStep);
fscanf(fINITfile,"%d\n",&iPulseRate);
fscanf(fINITfile,"%f\n",&fPulseDelay);
fscanf(fINITfile,"%d\n",&iPulseAve);
fscanf(fINITfile,"%d\n",&iB1start);
fscanf(fINITfile,"%d\n",&iB1length);
fscanf(fINITfile,"%d\n",&iSstart);
fscanf(fINITfile,"%d\n",&iSlength);
fscanf(fINITfile,"%d\n",&iB2start);
fscanf(fINITfile,"%d\n",&iB2length);
fscanf(fINITfile,"%f\n",&fVmin);
fscanf(fINITfile,"%f\n",&fVmax);
fscanf(fINITfile,"%f\n",&fSigOffset);
fscanf(fINITfile,"%f\n",&fRefOffset);
fscanf(fINITfile,"%d\n",&iWFgain);
fscanf(fINITfile,"%d\n",&iASgain);
fgets(sDirDef, 256, fINITfile);

fclose(fINITfile);

i = 0;
while (isprint(sDirDef[i]) != 0)
{
DirDef[i] = sDirDef[i];
i++;
}

// iStatus = MakeDir(DirDef);
if ( (iStatus = 0) || (iStatus = -9) )
{ // Success
memcpy(sdate, DateStr(),88);
strcpy(sDirDefDate,Newdir(DirDef,sdate,&iStatus));
}
else
{   // Failure
strcat(message,"Directory Issues \n MakeDir error = ");
Fmt(sError,"%s<%i[w5p0]",iStatus);
strcat(message, sError);
strcat(message,"\n Execution Aborted");
iexclaim = MessagePopup ("Directory Error",message);
return -1;
}

SetCtrlVal (panel0, PANEL_0_STRING_directory,sDirDefDate);

// SetCtrlVal (panel0, PANEL_0_RING_StepSize, iScanStep);
SetCtrlVal (panel0, PANEL_0_NUMERIC_pulse_rate, iPulseRate);
SetCtrlVal (panel0, PANEL_0_NUMERIC_time_delay, (double) fPulseDelay);
SetCtrlVal (panel0, PANEL_0_NUMERIC_Average, iPulseAve);
SetCtrlVal (panel0, PANEL_0_NUMERIC_B1_GATE, iB1start);
SetCtrlVal (panel0, PANEL_0_NUMERIC_B1_LENGTH, iB1length);
SetCtrlVal (panel0, PANEL_0_NUMERIC_S_GATE, iSstart);
SetCtrlVal (panel0, PANEL_0_NUMERIC_S_LENGTH, iSlength);
SetCtrlVal (panel0, PANEL_0_NUMERIC_B2_GATE, iB2start);
SetCtrlVal (panel0, PANEL_0_NUMERIC_B2_LENGTH, iB2length);
SetCtrlVal (panel1, PANEL_1_NUMERIC_Vmin, (double) fVmin);
SetCtrlVal (panel1, PANEL_1_NUMERIC_Vmax, (double) fVmax);
SetCtrlVal (panel1, PANEL_1_NUMERIC_offsetDCSig, (double) fSigOffset);
SetCtrlVal (panel1, PANEL_1_NUMERIC_offsetDCRef, (double) fRefOffset);
SetCtrlVal (panel2, PANEL_2_RINGSLIDE_Gain, iWFgain);
SetCtrlVal (panel0, PANEL_0_RING_ADgain, iWFgain);
SetCtrlVal (panel0, PANEL_0_RING_ASGain, iASgain);
}

RunUserInterface ();

/* Update the ini file when closing . . .*/
if ( (fINITfile = fopen(sINITfile,"r+")) == NULL)
{
iexclaim = MessagePopup ("File Error","Intialization file b212.ini missing \n Execution Aborted");
return -1;
}
else
{
// GetCtrlVal (panel0, PANEL_0_RING_StepSize, &iScanStep);
GetCtrlVal (panel0, PANEL_0_NUMERIC_pulse_rate, &iPulseRate);
GetCtrlVal (panel0, PANEL_0_NUMERIC_time_delay, &dPulseDelay);
GetCtrlVal (panel0, PANEL_0_NUMERIC_Average, &iPulseAve);
GetCtrlVal (panel0, PANEL_0_NUMERIC_B1_GATE, &iB1start);
GetCtrlVal (panel0, PANEL_0_NUMERIC_B1_LENGTH, &iB1length);
GetCtrlVal (panel0, PANEL_0_NUMERIC_S_GATE, &iSstart);
```

```
GetCtrlVal (panel0, PANEL_0_NUMERIC_S_LENGTH, &iSlength);
GetCtrlVal (panel0, PANEL_0_NUMERIC_B2_GATE, &iB2start);
GetCtrlVal (panel0, PANEL_0_NUMERIC_B2_LENGTH, &iB2length);
GetCtrlVal (panel1, PANEL_1_NUMERIC_Vmin, &dVmin);
GetCtrlVal (panel1, PANEL_1_NUMERIC_Vmax, &dVmax);
GetCtrlVal (panel1, PANEL_1_NUMERIC_offsetDCSig, &dSigOffset);
GetCtrlVal (panel1, PANEL_1_NUMERIC_offsetDCRef, &dRefOffset);
GetCtrlVal (panel0, PANEL_0_RING_ADgain, &iWFgain);
GetCtrlVal (panel0, PANEL_0_RING_ASGain, &iASgain);


fprintf(fINITfile,"%d\n",iScanStep);
fprintf(fINITfile,"%d\n",iPulseRate);
fprintf(fINITfile,"%10.3f\n",dPulseDelay);
fprintf(fINITfile,"%d\n",iPulseAve);
fprintf(fINITfile,"%d\n",iB1start);
fprintf(fINITfile,"%d\n",iB1length);
fprintf(fINITfile,"%d\n",iSstart);
fprintf(fINITfile,"%d\n",iSlength);
fprintf(fINITfile,"%d\n",iB2start);
fprintf(fINITfile,"%d\n",iB2length);
fprintf(fINITfile,"%10.3f\n",dVmin);
fprintf(fINITfile,"%10.3f\n",dVmax);
fprintf(fINITfile,"%10.3f\n",dSigOffset);
fprintf(fINITfile,"%10.3f\n",dRefOffset);
fprintf(fINITfile,"%d\n",iWFgain);
fprintf(fINITfile,"%d\n",iASgain);
fputs(DirDef,fINITfile);
fclose(fINITfile);
}

if (adScan) free(adScan);

DiscardPanel (panel0);
DiscardPanel (panel1);
DiscardPanel (panel2);

return 0;
}


/*  ********************************************************* */

int CVICALLBACK Main_Done (int panel, int control, int event,
void *callbackData, int eventData1, int eventData2)
{
int query=0;
int iStatus;
    unsigned int ulGpctr0 = ND_COUNTER_0;
char command[10],reading[10];

switch (event)
{
case EVENT_COMMIT:
query = ConfirmPopup ("Quit", "                   Are you sure?");
if (query)
{
iStatus=AO_VWrite (1, 0, 0);
iStatus=AO_VWrite (2, 0, 0);

ibreakflag = 1;
istopflag = 1;

    /* Reset GPCTR. */
iStatus = GPCTR_Control(iPCI6110, ulGpctr0, ND_RESET);

/* Close COM1 RS232 communication */

strcpy(command,"END");
SendAutoscan(command, reading, 4);
// CloseCom(iAutoscan);

QuitUserInterface (0);
}
}
return 0;
}



/* ************************************************************** */
// This subroutine will use the RS232 to communicate with the
// Autoscan computer
/* ************************************************************** */

int CVICALLBACK ChangeWavelength (int panel, int control, int event,
void *callbackData, int eventData1, int eventData2)


{
```

```
int iTrash;
double dwavelength;
char send_data[50],wavelength_data[20],send_data2[50];
char *read_data = allocbuf;
char *read_data2=allocbuf;
// char read_error[100];


 switch (event)
 {
 case EVENT_COMMIT:




iTrash = GetCtrlVal (panel0, PANEL_0_NUMERIC_Wavelength, &dwavelength);
if (dwavelength < 1.0)
{
MessagePopup ("Error", "Must Input Initial Wavelength");
return 0;
}

SetXMode(iAutoscan,0);
SetCTSMode (iAutoscan, 0);
SetComTime (iAutoscan, 5.0);

//this moves the laser to specified wavelength

strcpy(send_data,"GOK ");
Fmt(wavelength_data, "%s<%f[p4]",dwavelength);
strcat(send_data,wavelength_data);

SendAutoscan(send_data,read_data,0);



// now to read the wavelength

strcpy(send_data2,"READK");
SendAutoscan(send_data2,read_data2,1);
// SetCtrlVal(PANEL_0,PANEL_0_CONSTANT_kvalue,read_data2);


break;
 }

return 0;
}

/* ************************************************************ */
/* The ReadAutoscan subroutine reads the output of RS232 */

int ReadAutoscan(char reading[50])
{

int bytes_read;

bytes_read = ComRd(iAutoscan,reading,50);
return 0;
}




/*    ************************************************************  */
/* The SendAutoscan Subroutine actually sends the Macro
/* commands to the Autoscan computer. I set it up this way because
/* it gets around the fact that the subroutine must end in order for
/* the command to get sent across the RS232 cable
/* ************************************************************  */

int SendAutoscan (char command[50],char reading[50], int iType)
{

// int iAutoscan, bytes_sent;
// char command[500];
int bytes_sent,bytes_read;
char *string;
char *pch;
// double Num;
char *ans = allocbuf;
char *strNum;



strcat(command,"\r");
bytes_sent = ComWrt(iAutoscan,command, StringLength(command));
bytes_read = ComRd(iAutoscan,ans,85);
```

```
SetCtrlVal(PANEL_0,PANEL_0_STRING_output,ans);



switch (iType)
{
// case 0:   /* GOK */
/* bytes_read = ComRd(iAutoscan,reading,50);
// this checks to make sure the laser moved successfully

if (bytes_read!=25)
{
MessagePopup ("Warning","Wavelength Change Failed.");
return -1;
}
break;   */


case 1:    /* READK */

// bytes_read = ComRd(iAutoscan,ans,50);
pch = strtok (ans," ");
pch = strtok (NULL," ");
strNum = strtok (NULL," ");
// Num = atof(strNum);
SetCtrlVal(PANEL_0,PANEL_0_CONSTANT_kvalue,strNum);
break;

// case 2: /* SCAN filename */
/* bytes_read = ComRd(iAutoscan,ans,50);
// FlushInQ(iAutoscan);
break;

case 3:  /* EXECUTE */
/* break;

case 4: /* END */
// FlushInQ(iAutoscan);
// break;
}
return 0;
}


/* ************************************************************** */
/* this routine reads what type of scan you want to do, accesses    */
/*  scan filename , and makes the step size and number of segments   */
/* global variables. If you make a new scanfile, just add the info  */
/*  here and on the actual button on the GUI  */
/* ************************************************************** */

int CVICALLBACK ScanSpecs (int panel, int control, int event,
void *callbackData, int eventData1, int eventData2)
{

int iScanType;

 switch(event)
 {
 case EVENT_COMMIT:
GetCtrlVal(panel0,PANEL_0_RING_ScanType, &iScanType);



switch(iScanType)
{
case 1:
   strcpy(ScanFileName, "SCANA");
   iStepSize = 2;
   ulNumSeg = 1;
   break;
case 2:
strcpy(ScanFileName,"SCANB");
iStepSize = 10;
ulNumSeg = 3;
break;
case 3:
strcpy(ScanFileName,"SCANC");
iStepSize = 10;
ulNumSeg = 1;
break;
case 4:
strcpy(ScanFileName,"SCAND");
iStepSize = 10;
ulNumSeg = 15;
break;
}
break;
 }
```

```
 return 0;
}


/* ************************************************************ */
/*  ** This sets up the flow controller ************************* */
/*  ************************************************************ */

int CVICALLBACK MFCStart (int panel, int control, int event,
void *callbackData, int eventData1, int eventData2)
{

int iTrash;
char mfcsetting[20], setpoint[12], mfcreply[100];
int bytes_sent, bytes_read;



switch (event)
{
case EVENT_COMMIT:

switch (control)
{
case PANEL_0_COMMANDBUTTON_omfc1:
GetCtrlVal(panel0,PANEL_0_STRING_ch1,setpoint);
strcpy(mfcsetting, "SP1");
strcat(mfcsetting,setpoint);
break;

case PANEL_0_COMMANDBUTTON_omfc2:
GetCtrlVal(panel0,PANEL_0_STRING_ch2,setpoint);
strcpy(mfcsetting, "SP2");
strcat(mfcsetting,setpoint);
break;

case PANEL_0_COMMANDBUTTON_omfc3:
GetCtrlVal(panel0,PANEL_0_STRING_ch3,setpoint);
strcpy(mfcsetting, "SP3");
strcat(mfcsetting,setpoint);
break;

case PANEL_0_COMMANDBUTTON_omfc4:
GetCtrlVal(panel0,PANEL_0_STRING_ch4,setpoint);
strcpy(mfcsetting, "SP4");
strcat(mfcsetting,setpoint);
break;
}



if (StringLength(mfcsetting)!= 9)
{
MessagePopup("Error","Incorrect number of digits for flow meter");
return -1;
};



strcat(mfcsetting,"\r");
bytes_sent = ComWrt(iMFC,mfcsetting, StringLength(mfcsetting));
bytes_read = ComRd(iMFC,mfcreply,100);
SetCtrlVal(PANEL_0,PANEL_0_STRING_mfcoutput,mfcreply);




break;
}
return 0;
}



/* ************************************************************ */
/* *****This stops the flow of gas to the flow controller****** */
/* ************************************************************ */

int CVICALLBACK MFCClose (int panel, int control, int event,
void *callbackData, int eventData1, int eventData2)
{

int bytes_read, bytes_sent;
char mfcsettingc[20], mfcreplyc[100];

switch (event)
{
case EVENT_COMMIT:
```

```
switch (control)
{
case PANEL_0_COMMANDBUTTON_cmfc1:
strcpy(mfcsettingc, "SP1");
break;

case PANEL_0_COMMANDBUTTON_cmfc2:
strcpy(mfcsettingc, "SP2");
break;

case PANEL_0_COMMANDBUTTON_cmfc3:
strcpy(mfcsettingc, "SP3");
break;

case PANEL_0_COMMANDBUTTON_cmfc4:
strcpy(mfcsettingc, "SP4");
break;
}


strcat(mfcsettingc, "0.0000");

strcat(mfcsettingc,"\r");
bytes_sent = ComWrt(iMFC,mfcsettingc, StringLength(mfcsettingc));
bytes_read = ComRd(iMFC,mfcreplyc,85);
SetCtrlVal(PANEL_0,PANEL_0_STRING_mfcoutput,mfcreplyc);


break;
}
return 0;
}



/* ************************************************************ */
/*  ********* This function allows you to send any command ********* */
/*  ********* to the mass flow controller box that you want ******** */
/*  ************************************************************ */

int CVICALLBACK MFCMessage (int panel, int control, int event,
void *callbackData, int eventData1, int eventData2)
{

char fcmessage[50], mfcreplyc[85];
int bytes_sent,bytes_read;

switch (event)
{
case EVENT_COMMIT:

GetCtrlVal(PANEL_0,PANEL_0_STRING_message,fcmessage);
strcat(fcmessage,"\r");
bytes_sent = ComWrt(iMFC, fcmessage,StringLength(fcmessage));
bytes_read = ComRd(iMFC,mfcreplyc,85);
SetCtrlVal(PANEL_0,PANEL_0_STRING_mfcoutput,mfcreplyc);


break;
}
return 0;
}



/*    ************************************************************  */
/*    **  The Measure subroutine sets up a counter, A/D and D/A   **  */
/*    **  conversions.  The signal waveform is acquired and       **  */
/*    **  integrated with signal and baseline gates.  Supporting  **  */
/*    **  other data such as etalons are also acquired.           **  */
/*    ************************************************************  */

int CVICALLBACK Measure (int panel, int control, int event,
void *callbackData, int eventData1, int eventData2)
{

int iStatus=0, iRetVal, iIgnoreWarning, iEventLoc=-1, ipanelloc;
short sTimeBase=1;
    short iDAQstopped=0;
unsigned int ulGpctr0 = ND_COUNTER_0;
    unsigned int ulGpctr1 = ND_COUNTER_1;
  unsigned int ulLOWcnt1, ulHIGHcnt1;
    unsigned int ulLOWcnt2, ulHIGHcnt2;
    unsigned int ulRun1, ulRun2;
    unsigned short uSampInt=0;
    unsigned long ulRetrieved;
double dTimeDelay;

int iADgain;
```

```
int iASgain;

double dwavelength;

short iSegOut=0, iDataOut=0;

int iLPulse, iLSeg;   // LCV
int iLBase1, iLBase2, iLSig;   // LCV

double dBase1Length, dBase2Length, dSignalLength;
    long   lBase1Sum=0,  lBase2Sum=0,  lSigSum=0, lSumInt=0;
double dBase1Sum,    dBase2Sum,    dSigSum,   dSumInt,   dIntPlot;
double dBase1VSum,   dBase2VSum,   dSigVSum,  dSumVInt,  dIntVPlot;

double dcheck, dfraction, dtrash;

unsigned long ulPointsPerSeg;
int iCountSeg,iAnswer;


double dVmin, dVmax;
double dLastPlot, dLastVPlot, dLastDCSig, dLastDCRef, dLastFr250, dLastFr1500;

int iMax, iADmax;
int iScanType;

double dDCSig, dDCRef,dFr1500, dFr250;
double dVTACstep;
double dASVout;

char execute[50], reading[50], FileSend[50];
char sCount[7];
char message[MAX_PATHNAME_LEN]="";

dVTACstep = 10.0 / TACres;

istopflag=0;
ibreakflag=0;
iADmax = -2048;

switch (event)
{
case EVENT_COMMIT:
/* DiscardPanel (panel0);      */

if (!isPulsing)
{
MessagePopup ("Smooth Move Exlax", "Pulse Valve Not Running");
return 0;
}

GetCtrlVal (panel0, PANEL_0_NUMERIC_Wavelength, &dwavelength);
if (dwavelength < 1.0)
{
MessagePopup ("Error","Must Input Initial Wavelength");
return 0;
}
SetCtrlVal (panel1, PANEL_1_NUMERIC_Wavelength, dwavelength);

GetCtrlVal (panel0, PANEL_0_RING_ADgain, &iADgain);
GetCtrlVal (panel0, PANEL_0_RING_ASGain, &iASgain);



ulDataPoints = ulNumSeg * (1 + 10200 / iStepSize);

// ulPointsPerSeg = 10200 / iStepSize;
// Missing data points on the overlap.  This should get the count right now. (4/23/08 - TAB)
ulPointsPerSeg = 1 + 10200 / iStepSize;


if (adScan) free(adScan);

adScan = malloc ((ulDataPoints*(NTraces+1))*sizeof(double));
if (!adScan)
{
MessagePopup ("Memory Allocation Failure", "Insufficient Memory for adScan.\nScan Aborted!");
return 0;
}

SetCtrlVal (panel1, PANEL_1_NUMERIC_ADmax, iADmax);
SetCtrlVal (panel1, PANEL_1_LED_A2D, 0);
SetCtrlVal (panel1, PANEL_1_NUMERIC_LSB, 2. * 10. / iADgain / uMaxPoints * 1000.);
SetCtrlVal (panel1, PANEL_1_RING_ADgain, iADgain);

SetCtrlAttribute (panel1, PANEL_1_COMMANDBUTTON_Return, ATTR_DIMMED, 1);
SetCtrlAttribute (panel1, PANEL_1_COMMANDBUTTON_Save,   ATTR_DIMMED, 1);
SetCtrlAttribute (panel1, PANEL_1_COMMANDBUTTON_Stop,   ATTR_DIMMED, 0);
SetCtrlAttribute (panel1, PANEL_1_COMMANDBUTTON_GetXY,  ATTR_DIMMED, 1);
```

```
SetPanelAttribute (panel0, ATTR_VISIBLE, 0);
SetPanelAttribute (panel1, ATTR_VISIBLE, 1);
SetPanelAttribute (panel2, ATTR_VISIBLE, 0);

icounter=0;


/* Read Values off the Setup Control Panel  */
GetCtrlVal (panel0, PANEL_0_NUMERIC_Average, &uPulseAve);

/*   Read the Baseline1 start and length   */
GetCtrlVal (panel0, PANEL_0_NUMERIC_B1_GATE, &lB1Start);
GetCtrlVal (panel0, PANEL_0_NUMERIC_B1_LENGTH, &lB1Length);
dBase1Length = (double) lB1Length;

/*   Read the Baseline2 start and length   */
GetCtrlVal (panel0, PANEL_0_NUMERIC_B2_GATE, &lB2Start);
GetCtrlVal (panel0, PANEL_0_NUMERIC_B2_LENGTH, &lB2Length);
dBase2Length = (double) lB2Length;

/*   Read the Signal start and length   */
GetCtrlVal (panel0, PANEL_0_NUMERIC_S_GATE, &lSigStart);
GetCtrlVal (panel0, PANEL_0_NUMERIC_S_LENGTH, &lSigLength);
dSignalLength = (double) lSigLength;

   SetCtrlVal (panel1, PANEL_1_NUMERIC_AR_Display, dLam[1][11]);
   SetCtrlVal (panel1, PANEL_1_NUMERIC_Dye_Display, dLam[2][11]);
   SetCtrlVal (panel1, PANEL_1_NUMERIC_IR_Display, dLam[3][11]);

   SetCtrlVal (panel1, PANEL_1_NUMERIC_Sig_Amp, isigamp);
   SetCtrlVal (panel1, PANEL_1_NUMERIC_Et_Amp, ietamp);
SetCtrlVal (panel1, PANEL_1_NUMERIC_Sig_Offset, isigoffset);
SetCtrlVal (panel1, PANEL_1_NUMERIC_Et_Offset, ietoffset);

/*      Set up the graph on which to show data  */
SetCtrlAttribute (panel1, PANEL_1_GRAPH_signal, ATTR_DATA_MODE,
  VAL_DISCARD);

/* The following call is needed to clear the plot before the next begins  */
GetCtrlVal (panel1, PANEL_1_NUMERIC_Vmin, &dVmin);
GetCtrlVal (panel1, PANEL_1_NUMERIC_Vmax, &dVmax);
GetCtrlVal (panel1, PANEL_1_NUMERIC_offsetDCSig, &dOffsetDCSig);
GetCtrlVal (panel1, PANEL_1_NUMERIC_offsetDCRef, &dOffsetDCRef);

DeleteGraphPlot (panel1, PANEL_1_GRAPH_signal, -1, VAL_IMMEDIATE_DRAW);

SetAxisScalingMode (panel1, PANEL_1_GRAPH_signal, VAL_XAXIS,
VAL_MANUAL, 0.0, ulPointsPerSeg);

SetAxisScalingMode (panel1, PANEL_1_GRAPH_signal, VAL_LEFT_YAXIS,
VAL_MANUAL, dVmin, dVmax);

SetCtrlAttribute (panel1, PANEL_1_GRAPH_signal, ATTR_REFRESH_GRAPH, 1);
SetCtrlAttribute (panel1, PANEL_1_GRAPH_signal, ATTR_XGRID_VISIBLE, 0);
SetCtrlAttribute (panel1, PANEL_1_GRAPH_signal, ATTR_YGRID_VISIBLE, 0);
SetCtrlAttribute (panel1, PANEL_1_GRAPH_signal, ATTR_PLOT_BGCOLOR,VAL_WHITE);

/*     Set up fast data acquisition for external start and use of internal clock for
cycle of other conversions   */
        iIgnoreWarning = 0;
iStatus = DAQ_Config (iPCI6110, 1, 0);
iRetVal = NIDAQErrorHandler(iStatus, "DAQ_Config", iIgnoreWarning);

/*    Set trigger source for AI initiation - Triggers on falling edge on PFI6 */
iStatus = Select_Signal (iPCI6110, ND_IN_START_TRIGGER, ND_PFI_6,ND_HIGH_TO_LOW);

iStatus = DAQ_Rate (dSampleRate, 0, &sTimeBase, &uSampInt);

/* To time the speed of the program, call the clock() routine at two times  */
ulRun1=clock();

SetCtrlAttribute (panel1, PANEL_1_LED_SegOut, ATTR_CTRL_VAL, 0);


/* Now that everything is set up, we can start scanning. The scanning is started by
/* A macro sent over the RS232 cable that tells the laser what file to load in order
/* to start scanning. */



strcpy(FileSend,"SCAN ");
strcat(FileSend,ScanFileName);
SendAutoscan(FileSend, reading, 2);

strcpy(execute,"EXECUTE");
SendAutoscan(execute,reading,3);
```

```
/*  This for loop, loops over each segment that autoscan puts together  */
/* Each segment is 10.2 GHz as defined by Autoscan     */

for (iLSeg = 1; (iLSeg <= ulNumSeg && !istopflag); iLSeg++)
{

SetCtrlVal(panel1, PANEL_1_NUMERIC_SegNum,iLSeg);

/* Display Active Segment Scanning */
DeleteGraphPlot (panel1, PANEL_1_GRAPH_signal, -1, VAL_IMMEDIATE_DRAW);
SetAxisScalingMode (panel1, PANEL_1_GRAPH_signal, VAL_XAXIS, VAL_MANUAL,
ulPointsPerSeg*(iLSeg-1), ulPointsPerSeg*iLSeg);

/* Need to keep icounter in sync with segments */
icounter = (iLSeg-1)*ulPointsPerSeg;
iCountSeg = 0;

DIG_Out_Line(iPCI6025,0,iDIOSegIn,0); // Reset SegIn
SetCtrlAttribute (panel1, PANEL_1_LED_SegOut, ATTR_CTRL_VAL, 0);
iSegOut = 0;




while (!iSegOut && ! istopflag)
{
DIG_In_Line(iPCI6025,0,iDIOSegOut,&iSegOut);
ProcessSystemEvents();
}


SetCtrlAttribute (panel1, PANEL_1_LED_SegOut, ATTR_CTRL_VAL, 1);
/* AutoScan Ready for a Segment */

DIG_Out_Line(iPCI6025,0,iDIOSegIn,1); // Tell AutoScan, we too are ready
//  May need to delay a call to set iDIOSegIn to 0 to pause between segments



while (iSegOut && !istopflag)
{
iDataOut = 0;
while (!iDataOut)
{
DIG_In_Line(iPCI6025,0,iDIODataOut,&iDataOut);
}
/* AutoScan Ready for a data point */

// if (ibreakflag==1) /*  gets out of measure loop is "quit program" button is pressed  */
//    break;

if (istopflag!=1) /*  continue to scan until "stop scan" button is pressed  */
   {
/*  Read system event once every 10 points - it takes time to do this   */
dcheck = (double) icounter/10.;
dfraction = modf (dcheck, &dtrash);
if ((icounter!=0)&&(dfraction)<0.05)
{
GetUserEvent (0, &ipanelloc, &iEventLoc);
if (iEventLoc!=-1)
ProcessSystemEvents ();
}



/* Loop over the number of pulses to signal average  */
dSumVInt = 0.0;
dSumInt  = 0.0;

for (iLPulse=1; iLPulse <=uPulseAve; iLPulse++)
{
/*  Obtain ulCount data points on  CH0 of 6110 board */
/* The gain is set at 2 for a -5V - +5V range. */
iStatus = DAQ_Start (iPCI6110, 0, iADgain, piBuffer, ulCount, sTimeBase, uSampInt);
        iStatus = DAQ_Check (iPCI6110, &iDAQstopped, &ulRetrieved);
     while ((iDAQstopped != 1) || (iStatus != 0))
     {
/*  Loop until acquisition is complete.  */
         iStatus = DAQ_Check(iPCI6110, &iDAQstopped, &ulRetrieved);
  }

/* Convert the Digital Number to its Analog Voltage ch0 or 6110 board*/
iStatus = DAQ_VScale (iPCI6110, 0, iADgain, 1, 0, 2000, piBuffer, pdVoltBuffer);

/*  Calculate the average of baselines and signal and subtract   */
dBase1VSum= 0;
dBase1Sum = 0;
lBase1Sum = 0;
```

```
if (lB1Length > 0)
{
for (iLBase1=lB1Start; iLBase1<=(lB1Start+lB1Length); iLBase1++)
{
dBase1VSum += pdVoltBuffer[iLBase1];
lBase1Sum += piBuffer[iLBase1];
}
dBase1Sum = (double) lBase1Sum / dBase1Length;
dBase1VSum = dBase1VSum/dBase1Length;
}

dSigVSum=0;
lSigSum =0;
iMax = -2048;
for (iLSig=lSigStart; iLSig<=(lSigStart+lSigLength); iLSig++)
{
dSigVSum += pdVoltBuffer[iLSig];
lSigSum += piBuffer[iLSig];
if (piBuffer[iLSig] > iMax)
{
iMax = piBuffer[iLSig];
}
}
dSigSum  = (double) lSigSum / dSignalLength;
dSigVSum = dSigVSum/dSignalLength;

dBase2VSum= 0;
dBase2Sum = 0;
lBase2Sum = 0;
if (lB2Length > 0)
{
for (iLBase2=lB2Start; iLBase2<=(lB2Start+lB2Length); iLBase2++)
{
dBase2VSum += pdVoltBuffer[iLBase2];
lBase2Sum += piBuffer[iLBase2];
}
dBase2Sum  = (double) lBase2Sum / dBase2Length;
dBase2VSum = dBase2VSum/dBase2Length;
}

  dSumVInt = dSumVInt + dSigVSum - (dBase1VSum+dBase2VSum)/2; // Value in Volts
dSumInt  = dSumInt + dSigSum - (dBase1Sum+dBase2Sum)/2; // Value in ADU


// MaxMin1D (piBuffer, 2000, &dmax, &imax, &dmin, &imin);
SetCtrlVal (panel1, PANEL_1_NUMERICTHERM_A2D, iMax);
if (iMax > iADmax)
{
iADmax = iMax;
SetCtrlVal (panel1, PANEL_1_NUMERIC_ADmax, iADmax);
if (iMax > 2040)  SetCtrlVal (panel1, PANEL_1_LED_A2D, 1);
}

/* Read inputs on 6025 board (Etalon and IR power) */
  /* We read each board four times to eliminate cross-talk between channels  */

//     iStatus = AI_Read (iPCI6025, 0, 1, &sEtalon); /*  Etalon - CH 0  */
//     iStatus = AI_Read (2, 0, 1, &sVoltTrash); /*  Etalon - CH 0  */
//     iStatus = AI_Read (2, 0, 1, &sVoltTrash); /*  Etalon - CH 0  */
//     iStatus = AI_Read (2, 0, 1, &sTempVoltIn1); /*  Etalon - CH 0  */

//     dSumVoltIn1 = dSumVoltIn1 + sTempVoltIn1;

//     iStatus = AI_Read (iPCI6025, 2, 1, &sTempVoltIn3); /*  IR Power - CH 2 */
//     iStatus = AI_Read (2, 2, 1, &sVoltTrash); /*  IR Power - CH 2 */
//     iStatus = AI_Read (2, 2, 1, &sVoltTrash); /*  IR Power - CH 2 */
//     iStatus = AI_Read (2, 2, 1, &sTempVoltIn3); /*  IR Power - CH 2 */

//     dSumVoltIn3 = dSumVoltIn3 + sTempVoltIn3;

/* Read the Signal Detector DC Voltage */
// iStatus = AI_VRead (iPCI6110, 0, 1, &dDCSig);

}  // Close Loop for Pulse Averaging

/* Pulse Average and Invert */
dIntVPlot=dSumVInt/uPulseAve;  // Value in Volts
dIntPlot=dSumInt/uPulseAve;    // Value in ADU

/* Output the Value of the datapoint to the Analog Out - to AutoScan */

/* For debugging purposes . . .
if (dVolt == 1.0)
{
dVolt = 2.0;
}
else
{
dVolt = 1.0;
}
```

```
iStatus = AO_VWrite (2, 0, dVolt);  */

// Currently scaled and offset.  Need to think about what this really is . . .
// Autoscan is 0-10V with 12bit resolution
// dASVout = 2.5 + iASgain * dIntVPlot;
// if (dASVout > 10.0 ) dASVout = 10.0;
// if (dASVout <  0.0 ) dASVout =  0.0;
// iStatus = AO_VWrite (iPCI6025, 0, dASVout);

/* Output Voltage Saw */
// dVSaw = (double) (icounter % TACres) * dVTACstep;
// iStatus = AO_VWrite (iPCI6025, 1, dVSaw);

/*   Read inputs on 6025 board - using 6110 Board b/c 6025 is broken   */
/* We read each board four times to eliminate cross-talk between channels  */
/* The gain is set at 1 for a range of -10V - +10V  */

/* Read the Ti:Sapph Fringes from the 250 MHz Marker Cavity */
iStatus = AI_VRead (iPCI6025, 2, -1, &dFr250);


/* Read the Signal Detector DC Voltage */
iStatus = AI_VRead (iPCI6025, 0, 1, &dDCSig);
// dDCSig = 0;

/* Read the Reference Cell Detector DC Voltage */
iStatus = AI_VRead (iPCI6025, 1, 10, &dDCRef);


/* Read the Ti:Sapph Fringes from the 1500 MHz Marker Cavity */
iStatus = AI_VRead (iPCI6025, 3, -1, &dFr1500);

/* Plot all points except the first point  */
if (icounter!=0)
{
   SetCtrlVal (panel1, PANEL_1_NUMBER_OF_POINTS, icounter);

ulRun2=clock();
SetCtrlVal (panel1, PANEL_1_SCAN_TIME, (double)(ulRun2-ulRun1)/CLOCKS_PER_SEC);

/*  Plot the Signal  */
// Changed to voltage instead of ADU - TAB
PlotLine (panel1, PANEL_1_GRAPH_signal, icounter-1, dLastVPlot,
   icounter,dIntVPlot, VAL_BLACK);
dLastVPlot = dIntVPlot;

PlotLine (panel1, PANEL_1_GRAPH_signal, icounter-1, dLastDCSig+dOffsetDCSig,
   icounter,dDCSig+dOffsetDCSig, VAL_GREEN);
dLastDCSig = dDCSig;

PlotLine (panel1, PANEL_1_GRAPH_signal, icounter-1, dLastDCRef+dOffsetDCRef,
   icounter,dDCRef+dOffsetDCRef, VAL_RED);
dLastDCRef = dDCRef;

PlotLine (panel1, PANEL_1_GRAPH_signal, icounter-1, dLastFr250+dOffsetFr250,
   icounter,dFr250+dOffsetFr250, VAL_BLUE);
dLastFr250 = dFr250;

PlotLine (panel1, PANEL_1_GRAPH_signal, icounter-1, dLastFr1500+dOffsetFr1500,
   icounter,dFr1500+dOffsetFr1500, VAL_MAGENTA);
dLastFr1500 = dFr1500;
}


dLastVPlot = dIntVPlot;
dLastDCSig = dDCSig;
dLastDCRef = dDCRef;
dLastFr250  = dFr250;
dLastFr1500 = dFr1500;

/* Tell AutoScan it can read the data point */
DIG_Out_Line(iPCI6025,0,iDIODataIn,1);
Delay(0.001);
DIG_Out_Line(iPCI6025,0,iDIODataIn,0);

/* Save data in adScan */
adScan[icounter+ulDataPoints]    = dIntVPlot;
adScan[icounter+2*ulDataPoints] = dFr250;
adScan[icounter+3*ulDataPoints] = dDCRef;
adScan[icounter+4*ulDataPoints] = dDCSig;
adScan[icounter+5*ulDataPoints] = dFr1500;


  } /*    End of istopflag != 1   */
  else
  {
  /* istopflag = 1 --> Scan was interupted */
GetUserEvent (0, &ipanelloc, &iEventLoc);
if (iEventLoc!=-1)
  ProcessSystemEvents ();
```

```
ulRun2=clock();
SetCtrlVal (panel1, PANEL_1_SCAN_TIME, (double)(ulRun2-ulRun1)/CLOCKS_PER_SEC);

/* Reset DIGital outs */
DIG_Out_Line(iPCI6025,0,iDIOSegIn,0);
DIG_Out_Line(iPCI6025,0,iDIODataIn,0);

SetCtrlVal (panel1, PANEL_1_LED_A2D, 0);
SetCtrlAttribute (panel1, PANEL_1_COMMANDBUTTON_Return, ATTR_DIMMED, 0);
SetCtrlAttribute (panel1, PANEL_1_COMMANDBUTTON_Save,   ATTR_DIMMED, 0);
SetCtrlAttribute (panel1, PANEL_1_COMMANDBUTTON_Stop,   ATTR_DIMMED, 1);

return 0;
}
DIG_In_Line(iPCI6025,0,iDIOSegOut,&iSegOut);
icounter = icounter + 1;
iCountSeg++;
  }
/*  End of While (iSegOut == 1) loop  */

if (iCountSeg != ulPointsPerSeg)
{
strcpy(message,"");
strcat(message,"Missed or Extra Datapoints\n Found :");
Fmt(sCount,"%s<%i[w5p0]",iCountSeg);
strcat(message, sCount);
strcat(message,"   Expected : ");
Fmt(sCount,"%s<%i[w5p0]",ulPointsPerSeg);
strcat(message,sCount);
strcat(message,"\n Do you wish to continue scan?");
iAnswer = ConfirmPopup ("Segment Datapoint Error", message);
if (iAnswer == 0) // Stop Scan
{
break; // Break out of For over segments Loop
}
}
ProcessSystemEvents ();

} /* Close For over segments Loop  */

if (istopflag)  // Need to reset user interface in case of crash
{ /* Reset DIGital outs */
DIG_Out_Line(iPCI6025,0,iDIOSegIn,0);
DIG_Out_Line(iPCI6025,0,iDIODataIn,0);

SetCtrlVal (panel1, PANEL_1_LED_A2D, 0);
SetCtrlAttribute (panel1, PANEL_1_COMMANDBUTTON_Return, ATTR_DIMMED, 0);
SetCtrlAttribute (panel1, PANEL_1_COMMANDBUTTON_Save,   ATTR_DIMMED, 0);
SetCtrlAttribute (panel1, PANEL_1_COMMANDBUTTON_Stop,   ATTR_DIMMED, 1);
}


SetCtrlAttribute (panel1, PANEL_1_LED_SegOut, ATTR_CTRL_VAL, 0);

/* Replot Full Scanned Data */
DeleteGraphPlot (panel1, PANEL_1_GRAPH_signal, -1, VAL_IMMEDIATE_DRAW);
SetAxisScalingMode (panel1, PANEL_1_GRAPH_signal, VAL_XAXIS, VAL_MANUAL,
0.0, icounter);

PlotWaveform (panel1, PANEL_1_GRAPH_signal, adScan, icounter, VAL_DOUBLE,
1., 0., 0., 1.0, VAL_THIN_LINE, VAL_NO_POINT, VAL_SOLID, 1, VAL_BLACK);

PlotWaveform (panel1, PANEL_1_GRAPH_signal, adScan+ulDataPoints, icounter, VAL_DOUBLE,
1.0, dOffsetDCSig, 0, 1, VAL_THIN_LINE, VAL_NO_POINT, VAL_SOLID, 1, VAL_GREEN);

PlotWaveform (panel1, PANEL_1_GRAPH_signal, adScan+2*ulDataPoints, icounter, VAL_DOUBLE,
1.0, dOffsetDCRef, 0, 1, VAL_THIN_LINE, VAL_NO_POINT, VAL_SOLID, 1, VAL_RED);

PlotWaveform (panel1, PANEL_1_GRAPH_signal, adScan+3*ulDataPoints, icounter, VAL_DOUBLE,
1.0, dOffsetVSaw, 0, 1, VAL_THIN_LINE, VAL_NO_POINT, VAL_SOLID, 1, VAL_BLUE);

ulRun2=clock();
SetCtrlVal (panel1, PANEL_1_SCAN_TIME, (double)(ulRun2-ulRun1)/CLOCKS_PER_SEC);

DIG_Out_Line(iPCI6025,0,iDIOSegIn,0);
DIG_Out_Line(iPCI6025,0,iDIODataIn,0);

SetCtrlVal (panel1, PANEL_1_LED_A2D, 0);
SetCtrlAttribute (panel1, PANEL_1_COMMANDBUTTON_Return, ATTR_DIMMED, 0);
SetCtrlAttribute (panel1, PANEL_1_COMMANDBUTTON_Save,   ATTR_DIMMED, 0);
SetCtrlAttribute (panel1, PANEL_1_COMMANDBUTTON_Stop,   ATTR_DIMMED, 1);
SetCtrlAttribute (panel1, PANEL_1_COMMANDBUTTON_GetXY,  ATTR_DIMMED, 0);

  break;
}

 return 0;
}
```

```
/*   ********************************************************************  */
/*  **  This subroutine displays the signal waveform and shows where    **  */
/*   **  three integration gates are located.  **  */
/*   ********************************************************************  */
int CVICALLBACK Wave_Form (int panel, int control, int event,
void *callbackData, int eventData1, int eventData2)
{
int iStatus=0, iRetVal, iIgnoreWarning=0, iYieldON;
    const int iDevice = 1;        /*   This is the PCI-6110    */
short sTimeBase=1, iDAQstopped=0;
    unsigned int ulGpctr0 = ND_COUNTER_0;
    unsigned int ulGpctr1 = ND_COUNTER_1;
unsigned int ulLOWcnt1, ulHIGHcnt1;
    unsigned int ulLOWcnt2, ulHIGHcnt2;
    unsigned int ulRun1, ulRun2, ulPulseRate;
    unsigned short uSampInt=0;
    unsigned long ulRetrieved;
    const unsigned long ulCount=2000; /*  This is the number of data points in waveform  */
double dVoltage, dVoltout, dcounter, dTimeDelay;
const double dSampleRate=1000000.0; /*  This is the sample rate in Hz  */

int iBase1, iBase2, iSig;
    long lBase1Sum=0, lBase2Sum=0, lSigSum=0;
double dBase1Sum, dBase2Sum, dSigSum, dSig;

double dVolt = 1.0;
double dtmin, dtmax, dYmin, dYmax;
int iADgain;

// double dTimeDelay;
time_t now;
struct tm *tp;
long StoreDate;
int ic;
long fheader[11];

istopflag=0;
ibreakflag=0;
iexit = 0;
switch (event)
{
case EVENT_COMMIT:

if (!isPulsing)
{
MessagePopup ("Smooth Move Exlax", "Pulse Valve Not Running");
return 0;
}

/* Read the Delay between pulse valve trigger and trigger to DAQ   */
GetCtrlVal (panel0, PANEL_0_NUMERIC_time_delay, &dTimeDelay);

SetPanelAttribute (panel2, ATTR_VISIBLE, 1);

/* Read the Baseline1 start and length AND transfer to waveform panel */
GetCtrlVal (panel0, PANEL_0_NUMERIC_B1_GATE, &lB1Start);
GetCtrlVal (panel0, PANEL_0_NUMERIC_B1_LENGTH, &lB1Length);

SetCtrlVal (panel2, PANEL_2_NUMERIC_B1_GATE, lB1Start);
SetCtrlVal (panel2, PANEL_2_NUMERIC_B1_LENGTH, lB1Length);

/* Read the Baseline2 start and length AND transfer to waveform panel */
GetCtrlVal (panel0, PANEL_0_NUMERIC_B2_GATE, &lB2Start);
GetCtrlVal (panel0, PANEL_0_NUMERIC_B2_LENGTH, &lB2Length);

SetCtrlVal (panel2, PANEL_2_NUMERIC_B2_GATE, lB2Start);
SetCtrlVal (panel2, PANEL_2_NUMERIC_B2_LENGTH, lB2Length);

/* Read the Signal start and length AND transfer to waveform panel */
GetCtrlVal (panel0, PANEL_0_NUMERIC_S_GATE, &lSigStart);
GetCtrlVal (panel0, PANEL_0_NUMERIC_S_LENGTH, &lSigLength);

SetCtrlVal (panel2, PANEL_2_NUMERIC_S_GATE, lSigStart);
SetCtrlVal (panel2, PANEL_2_NUMERIC_S_LENGTH, lSigLength);

/* Read the Gain AND transfer to waveform panel */
GetCtrlVal (panel0, PANEL_0_RING_ADgain, &iADgain);
SetCtrlVal (panel2, PANEL_2_RINGSLIDE_Gain, iADgain);

dYmax =  10. / (double) iADgain;
dYmin = -10. / (double) iADgain;

/* Set up fast data acquisition for external start
and use of internal clock for cycle of other conversions   */
iStatus = DAQ_Config (iDevice, 1, 0);
iRetVal = NIDAQErrorHandler(iStatus, "DAQ_Config", iIgnoreWarning);

/* Set trigger source for AI initiation - Triggers on falling edge on PFI6 */
iStatus = Select_Signal (iDevice, ND_IN_START_TRIGGER, ND_PFI_6, ND_HIGH_TO_LOW);
```

```
iStatus = DAQ_Rate (dSampleRate, 0, &sTimeBase, &uSampInt);

/* Setup Plots */
SetAxisScalingMode (panel2, PANEL_2_GRAPH_WF, VAL_LEFT_YAXIS, VAL_MANUAL,-10./ (double) iADgain, 10./ (double)iADgain);
SetCtrlAttribute (panel2, PANEL_2_GRAPH_WF, ATTR_PLOT_BGCOLOR, VAL_WHITE);

/*  Loops until the button at bottom of screen is clicked   */
while (ibreakflag!=1)
{
  ProcessSystemEvents ();

if (iChangeWFGates)
{
/* Read the Baseline1 start and length  AND transfer to original panel */
GetCtrlVal (panel2, PANEL_2_NUMERIC_B1_GATE, &lB1Start);
GetCtrlVal (panel2, PANEL_2_NUMERIC_B1_LENGTH, &lB1Length);

SetCtrlVal (panel0, PANEL_0_NUMERIC_B1_GATE, lB1Start);
SetCtrlVal (panel0, PANEL_0_NUMERIC_B1_LENGTH, lB1Length);

/* Read the Baseline2 start and length  AND transfer to original panel */
GetCtrlVal (panel2, PANEL_2_NUMERIC_B2_GATE, &lB2Start);
GetCtrlVal (panel2, PANEL_2_NUMERIC_B2_LENGTH, &lB2Length);

SetCtrlVal (panel0, PANEL_0_NUMERIC_B2_GATE, lB2Start);
SetCtrlVal (panel0, PANEL_0_NUMERIC_B2_LENGTH, lB2Length);

/* Read the Signal start and length     AND transfer to original panel */
GetCtrlVal (panel2, PANEL_2_NUMERIC_S_GATE, &lSigStart);
GetCtrlVal (panel2, PANEL_2_NUMERIC_S_LENGTH, &lSigLength);

SetCtrlVal (panel0, PANEL_0_NUMERIC_S_GATE, lSigStart);
SetCtrlVal (panel0, PANEL_0_NUMERIC_S_LENGTH, lSigLength);

/* Read the times to display */
GetCtrlVal (panel2, PANEL_2_NUMERIC_tmin,&dtmin);
GetCtrlVal (panel2, PANEL_2_NUMERIC_tmax,&dtmax);

SetAxisScalingMode (panel2, PANEL_2_GRAPH_WF, VAL_BOTTOM_XAXIS, VAL_MANUAL,
dtmin, dtmax);

iChangeWFGates = 0;
}

if (iChangeWFGain)
{
GetCtrlVal (panel2, PANEL_2_RINGSLIDE_Gain, &iADgain);

dYmax =  10. / (double) iADgain;
dYmin = -10. / (double) iADgain;

SetAxisScalingMode (panel2, PANEL_2_GRAPH_WF, VAL_LEFT_YAXIS, VAL_MANUAL,
dYmin, dYmax);
SetCtrlAttribute (panel2, PANEL_2_GRAPH_WF, ATTR_PLOT_BGCOLOR, VAL_WHITE);

SetCtrlVal(panel0, PANEL_0_RING_ADgain,iADgain);

iChangeWFGain = 0;
}

/*  Obtain ulCount data points on  CH0 of fast card */
iStatus = DAQ_Start (iDevice, 0, iADgain, piBuffer, ulCount, sTimeBase, uSampInt);
   iStatus = DAQ_Check(iDevice, &iDAQstopped, &ulRetrieved);

     while ( (iDAQstopped != 1) || (iStatus != 0))
     {
/* Loop until all acquisition is complete.  HINT: You can be
        doing other foreground tasks during this time. */
       iStatus = DAQ_Check(1, &iDAQstopped, &ulRetrieved);
}

iStatus = DAQ_VScale (iDevice, 0, iADgain, 1, 0, 2000, piBuffer, pdVoltBuffer);

DeleteGraphPlot (panel2, PANEL_2_GRAPH_WF, -1,VAL_IMMEDIATE_DRAW);

PlotY (panel2, PANEL_2_GRAPH_WF, pdVoltBuffer, ulCount,
VAL_DOUBLE, VAL_THIN_LINE, VAL_NO_POINT, VAL_SOLID,1, VAL_BLUE);

/* Plot a line for the first baseline gate  */
PlotLine (panel2, PANEL_2_GRAPH_WF, lB1Start, 0,
lB1Start+lB1Length,0, VAL_BLACK);

PlotLine (panel2, PANEL_2_GRAPH_WF, lB1Start+lB1Length, dYmin,
lB1Start+lB1Length,dYmax, VAL_BLACK);

PlotLine (panel2, PANEL_2_GRAPH_WF, lB1Start, dYmin,
lB1Start,dYmax, VAL_BLACK);

PlotText (panel2, PANEL_2_GRAPH_WF, lB1Start+lB1Length/2-60, dYmin, "Base1",
   VAL_APP_META_FONT, VAL_BLACK, VAL_WHITE);
```

```
/* Plot a line for the second baseline gate  */
PlotLine (panel2, PANEL_2_GRAPH_WF, lB2Start, 0,
lB2Start+lB2Length,0, VAL_GREEN);

PlotLine (panel2, PANEL_2_GRAPH_WF, lB2Start+lB2Length, dYmin,
lB2Start+lB2Length,dYmax, VAL_GREEN);

PlotLine (panel2, PANEL_2_GRAPH_WF, lB2Start, dYmin,
lB2Start,dYmax, VAL_GREEN);

PlotText (panel2, PANEL_2_GRAPH_WF, lB2Start+lB2Length/2-60, dYmin, "Base2",
VAL_APP_META_FONT, VAL_GREEN, VAL_WHITE);


/* plot a line for the signal gate   */
PlotLine (panel2, PANEL_2_GRAPH_WF, lSigStart, 0,
lSigStart+lSigLength, 0, VAL_DK_RED);

PlotLine (panel2, PANEL_2_GRAPH_WF, lSigStart+lSigLength, dYmin,
lSigStart+lSigLength, dYmax, VAL_DK_RED);

PlotLine (panel2, PANEL_2_GRAPH_WF, lSigStart, dYmin,
lSigStart, dYmax, VAL_DK_RED);

PlotText (panel2, PANEL_2_GRAPH_WF, lSigStart+lSigLength/2-60, dYmin, "Signal",
VAL_APP_META_FONT, VAL_DK_RED, VAL_WHITE);

/*   Calculate the integral of baselines and signal and subtract   */
dBase1Sum=0;
if (lB1Length > 0)
{
for (iBase1=lB1Start; iBase1<=(lB1Start+lB1Length); iBase1++)
dBase1Sum += pdVoltBuffer[iBase1];
dBase1Sum = dBase1Sum / (double) lB1Length;
}

dSigSum=0;
for (iSig=lSigStart; iSig<=(lSigStart+lSigLength); iSig++)
dSigSum += pdVoltBuffer[iSig];
dSigSum= dSigSum / (double) lSigLength;

dBase2Sum=0;
if (lB2Length > 0)
{
for (iBase2=lB2Start; iBase2<=(lB2Start+lB2Length); iBase2++)
dBase2Sum += pdVoltBuffer[iBase2];
dBase2Sum= dBase2Sum / (double) lB2Length;
}

  dSig=dSigSum-(dBase1Sum+dBase2Sum)/2;

SetCtrlVal(panel2, PANEL_2_NUMERIC_Signal,dSig);

if (iSaveWaveform)
{
now=time(NULL);
tp=localtime(&now);
StoreDate=(tp->tm_year+1900)*10000+(tp->tm_mon+1)*100+tp->tm_mday;

for (ic=0; ic <= 10; ic++) {fheader[ic] = 0;};
fheader[0]=StoreDate; /* The date of the acquisition  */
fheader[1]=iADgain+1; /* ADgain setting (+1 to deal with 20V) */
fheader[2]=(int) dTimeDelay * 1000;  /* Time Delay for Acquisition */
fheader[3]=lB1Start;    /*  start of first baseline gate   */
fheader[4]=lB1Length;    /*  length of first baseline gate   */
fheader[5]=lSigStart;    /*  start of signal gate   */
fheader[6]=lSigLength;    /*  length of signal gate   */
fheader[7]=lB2Start;     /*  start of second baseline gate   */
fheader[8]=lB2Length;  /*  length of second baseline gate   */
// fheader[9]=ulPulseRate;  /*  repetition rate for pulsed valve */

/* Popup window for saving data  */
// iStatus = FileSelectPopup ("c:\\Documents and Settings\\richard\\Desktop", "*.wfm", "*.wfm", "Waveform File Save",
//    VAL_SAVE_BUTTON, 0, 1, 1, 1, save_file);
iStatus = FileSelectPopup (sDirDefDate, "*.wfm", "*.wfm",
"Waveform File Save", VAL_SAVE_BUTTON, 0, 1, 1, 1, save_file);

if (iStatus > 0)
{
/* Saves header material as defined above as integers.    */
iStatus = ArrayToFile (save_file, fheader, VAL_INTEGER, 10, 1, VAL_GROUPS_TOGETHER,
VAL_GROUPS_AS_ROWS, VAL_SEP_BY_TAB, 10, VAL_ASCII, VAL_TRUNCATE);

/* Saves the data traces/waves     */
iStatus = ArrayToFile (save_file, pdVoltBuffer, VAL_DOUBLE, 2000, 1, VAL_GROUPS_TOGETHER,
   VAL_GROUPS_AS_COLUMNS, VAL_CONST_WIDTH, 12, VAL_ASCII, VAL_APPEND);
     } /* if iStatus */
```

```
iSaveWaveform = 0;
} // Close Save Waveform
} // ibreakflag != 1

SetPanelAttribute (panel2, ATTR_VISIBLE, 0);
SetPanelAttribute (panel0, ATTR_VISIBLE, 1);

break;
}
return 0;
}



/*   ************************************************************  */
/*   **  This subroutine saves the data in binary format  **  */
/*   **  It also saves header material that is used in some of the   **  */
/*   **  array of fortran programs used to plot and analyze data     **  */
/*   ************************************************************  */
int CVICALLBACK Save_Data (int panel, int control, int event,
void *callbackData, int eventData1, int eventData2)
{

int iStatus, isave, itrace, iStatus2;
double dfraction, dtrash, dLamAr, dLamDye, dLamIR, dStdIR;
double dwavelength;
char dwavelengthr[40];
double dReadWavelength;
long fheader[39], now, StoreDate;
float fstepsize;
const short spacer[0]={3};
char ch, ndate, c;
int ic, addloc;
struct tm *tp;
int iADgain;
char AutoscanFileName[20];
char  datafile[20], datafileout[20];


switch (event)
{
case EVENT_COMMIT:

now=time(NULL);
tp=localtime(&now);

StoreDate=(tp->tm_year+1900)*10000+(tp->tm_mon+1)*100+tp->tm_mday;

GetCtrlVal (panel0, PANEL_0_NUMERIC_Wavelength, &dwavelength);
GetCtrlVal (panel0, PANEL_0_CONSTANT_kvalue, &dwavelengthr[0]);

dReadWavelength = atof(dwavelengthr);

GetCtrlVal (panel0, PANEL_0_RING_ADgain, &iADgain);


for (ic=0; ic <= 38; ic++) {fheader[ic] = 0;};
adScan[0]=(long) floor(dwavelength*10000);
adScan[1]=NTraces; /* Number of types of data stored for plotting (abs, ET, TAC, IR power)  */
adScan[2]=(long) uPulseAve;
adScan[3]=lB1Start;    /*  start of first baseline gate   */
adScan[4]=lB1Length;    /*  length of first baseline gate   */
adScan[5]=lSigStart;    /*  start of signal gate   */
adScan[6]=lSigLength;    /*  length of signal gate   */
adScan[7]=lB2Start;     /*  start of second baseline gate   */
adScan[8]=lB2Length;  /*  length of second baseline gate   */
adScan[9]=ulPulseRate;  /*  repetition rate for pulsed valve */
adScan[10]=icounter;  /*  Number of data points taken   */
adScan[11]=dReadWavelength;
adScan[15]=StoreDate; /*  The date of data acquisition */

adScan[25]=ulNumSeg; /* # of Segments  */
adScan[26]=10200 / iStepSize; /* # Points per Segment */
adScan[27]=ulDataPoints; /* Total Number of Points */

adScan[30]=iADgain+1; /* ADgain setting (+1 to deal with 20V */
adScan[31]=iStepSize; /* AS Step Size in MHz */

adScan[38]=7; /* Version Info */

// GetCtrlVal (panel0, PANEL_0_RING_Step_Size, &FreqStepSize);
// fheader[36] = (long) FreqStepSize*icounter;    /*  approximate length of scan in MHz  */

/* Popup window for saving data  */
iStatus=FileSelectPopup (sDirDefDate, "*.scn", "*.scn", "File Save",
VAL_SAVE_BUTTON, 0, 0, 1, 1,save_file);

if (iStatus > 0)
{
/* In the data saving routine below, we only save the data acquired so file size
```

```
will be dependent on the number of data points.  */

/* Saves header material as defined above as integers.    */
// iStatus = ArrayToFile (save_file, fheader, VAL_INTEGER, 39, 1, VAL_GROUPS_TOGETHER,
// VAL_GROUPS_AS_ROWS, VAL_SEP_BY_TAB, 10, VAL_ASCII, VAL_TRUNCATE);

/* Saves the data traces/waves     */
/* itrace = 0: Gated Signal Detector
itrace = 1: DC Signal Detector
itrace = 2: DC Reference Detector
itrace = 3: Unused */
iStatus = ArrayToFile (save_file, adScan, VAL_DOUBLE, (NTraces+1)*ulDataPoints, (NTraces+1),
VAL_GROUPS_TOGETHER, VAL_GROUPS_AS_COLUMNS, VAL_CONST_WIDTH, 15, VAL_ASCII, VAL_APPEND);

/* Dim Button because Data is Saved */
     SetCtrlAttribute (panel1, PANEL_1_COMMANDBUTTON_Save,   ATTR_DIMMED, 1);
    }; /* if iStatus */


/* Now tell Autoscan to save the x-axis data */

// iStatus2 = PromptPopup("Save Autoscan Data","Enter name of file to save Autoscan data (8 digit max)",
// AutoscanFileName,8);

// strcpy(datafile,"WRITE ");
// strcat(datafile,AutoscanFileName);
// SendAutoscan(datafile,datafileout ,4);


}
return 0;
}

/*  ********************************************************  */
/*  ********************************************************  */
int CVICALLBACK Signal_Up (int panel, int control, int event,
void *callbackData, int eventData1, int eventData2)
{
switch (event)
{
case EVENT_COMMIT:

isigoffset=isigoffset+100;
SetCtrlVal (panel1, PANEL_1_NUMERIC_Sig_Offset, isigoffset);
break;
}
return 0;
}

/*  ********************************************************  */
/*  ********************************************************  */
int CVICALLBACK Signal_Down (int panel, int control, int event,
void *callbackData, int eventData1, int eventData2)
{
switch (event)
{
case EVENT_COMMIT:

isigoffset=isigoffset-100;
SetCtrlVal (panel1, PANEL_1_NUMERIC_Sig_Offset, isigoffset);
break;
}
return 0;
}

/*  ********************************************************  */
/*  ********************************************************  */
int CVICALLBACK Etalon_Up (int panel, int control, int event,
void *callbackData, int eventData1, int eventData2)
{
switch (event)
{
case EVENT_COMMIT:

ietoffset=ietoffset+100;
SetCtrlVal (panel1, PANEL_1_NUMERIC_Et_Offset, ietoffset);
break;
}
return 0;
}

/*  ********************************************************  */
/*  ********************************************************  */
int CVICALLBACK Etalon_Down (int panel, int control, int event,
void *callbackData, int eventData1, int eventData2)
{
switch (event)
{
case EVENT_COMMIT:
```

```
ietoffset=ietoffset-100;
SetCtrlVal (panel1, PANEL_1_NUMERIC_Et_Offset, ietoffset);
break;
}
return 0;
}

/*  ********************************************************  */
/*  ********************************************************  */
int CVICALLBACK Signal_Amplify (int panel, int control, int event,
void *callbackData, int eventData1, int eventData2)
{
switch (event)
{
case EVENT_COMMIT:

isigamp=isigamp*2;
   SetCtrlVal (panel1, PANEL_1_NUMERIC_Sig_Amp, isigamp);
break;
}
return 0;
}

/*  ********************************************************  */
/*  ********************************************************  */
int CVICALLBACK Signal_Attenuate (int panel, int control, int event,
void *callbackData, int eventData1, int eventData2)
{
switch (event)
{
case EVENT_COMMIT:

isigamp=isigamp/2;
if (isigamp<1)
isigamp=1;
SetCtrlVal (panel1, PANEL_1_NUMERIC_Sig_Amp, isigamp);
break;
}
return 0;
}

/*  ********************************************************  */
/*  ********************************************************  */
int CVICALLBACK Etalon_Amplify (int panel, int control, int event,
void *callbackData, int eventData1, int eventData2)
{
switch (event)
{
case EVENT_COMMIT:

ietamp=ietamp*2;
   SetCtrlVal (panel1, PANEL_1_NUMERIC_Et_Amp, ietamp);
break;
}
return 0;
}

/*  ********************************************************  */
/*  ********************************************************  */
int CVICALLBACK Etalon_Attenuate (int panel, int control, int event,
void *callbackData, int eventData1, int eventData2)
{
switch (event)
{
case EVENT_COMMIT:


ietamp=ietamp/2;
if (ietamp<1)
ietamp=1;
   SetCtrlVal (panel1, PANEL_1_NUMERIC_Et_Amp, ietamp);
break;
}
return 0;
}

/*  ********************************************************  */
/*  **  Starts a new scan, resets control variables        **  */
/*  ********************************************************  */
int CVICALLBACK New_Scan (int panel, int control, int event,
void *callbackData, int eventData1, int eventData2)
{
int iStatus;

switch (event)
{
case EVENT_COMMIT:

// icounter=0;
// iautocount=15;
```

```
// iloopcount=15;
iStatus=AO_VWrite (1, 0, 0);
iStatus=AO_VWrite (2, 0, 0);
/*  If sending out a ramp of 10V --> 0V, replace the previous statement with:  */
/* iStatus = AO_VWrite (1, 0, 10.); */

SetPanelAttribute (panel0, ATTR_VISIBLE, 1);
SetPanelAttribute (panel1, ATTR_VISIBLE, 0);
SetPanelAttribute (panel2, ATTR_VISIBLE, 0);
SetPanelAttribute (panel3, ATTR_VISIBLE, 0);
SetPanelAttribute (panel4, ATTR_VISIBLE, 0);
SetPanelAttribute (panel5, ATTR_VISIBLE, 0);
SetPanelAttribute (panel6, ATTR_VISIBLE, 0);

ibreakflag = 1;

break;
}
return 0;
}

/*  ********************************************************  */
/*  **  sets istopflag=1 which is used to quit current scan **  */
/*  ********************************************************  */
int CVICALLBACK Scan_Stop (int panel, int control, int event,
void *callbackData, int eventData1, int eventData2)
{
switch (event)
{
case EVENT_COMMIT:

istopflag=1;
SetCtrlAttribute(panel1, PANEL_1_COMMANDBUTTON_Save, ATTR_DIMMED, 0);
SetCtrlAttribute(panel1, PANEL_1_COMMANDBUTTON_Return, ATTR_DIMMED, 0);
SetCtrlAttribute(panel1, PANEL_1_COMMANDBUTTON_Stop, ATTR_DIMMED, 1);
SetCtrlVal(panel1, PANEL_1_LED_Scanning, 0);

break;
}
return 0;
}


/*  ********************************************************  */
/*  **   Returns to current scan                 **  */
/*  ********************************************************  */
int CVICALLBACK Return_Scan (int panel, int control, int event,
void *callbackData, int eventData1, int eventData2)
{
switch (event)
{
case EVENT_COMMIT:

istopflag=0;
iexit=1;
  SetPanelAttribute (panel0, ATTR_VISIBLE, 0);
  SetPanelAttribute (panel2, ATTR_VISIBLE, 0);
  SetPanelAttribute (panel1, ATTR_VISIBLE, 1);

break;
}
return 0;
}

int CVICALLBACK Scan_Jump (int panel, int control, int event,
void *callbackData, int eventData1, int eventData2)
{
switch (event)
{
case EVENT_COMMIT:

   iexit=1;
  SetPanelAttribute (panel3, ATTR_VISIBLE, 0);
  SetPanelAttribute (panel2, ATTR_VISIBLE, 0);


break;
}
return 0;
}

int CVICALLBACK SetLPMax (int panel, int control, int event,
void *callbackData, int eventData1, int eventData2)
{
double dMin, dMax;
switch (event)
{
case EVENT_COMMIT:
    GetCtrlVal (panel6, PANEL_6_N_LP_MIN, &dMin);
    GetCtrlVal (panel6, PANEL_6_N_LP_MAX, &dMax);
```

```
    if (dMax <= dMin)
     {
     dMax=dMin+0.1;
     SetCtrlVal (panel6, PANEL_6_N_LP_MAX, dMax);
     }
SetAxisScalingMode (panel6, PANEL_6_GRAPH_LP, VAL_LEFT_YAXIS,
VAL_MANUAL, dMin, dMax);
break;
}
return 0;
}

int CVICALLBACK SetLPMin (int panel, int control, int event,
void *callbackData, int eventData1, int eventData2)
{
double dMin, dMax;
switch (event)
{
case EVENT_COMMIT:
    GetCtrlVal (panel6, PANEL_6_N_LP_MIN, &dMin);
    GetCtrlVal (panel6, PANEL_6_N_LP_MAX, &dMax);
    if (dMin >= dMax)
      {
      dMin=dMax-0.1;
      SetCtrlVal (panel6, PANEL_6_N_LP_MIN, dMin);
      }
SetAxisScalingMode (panel6, PANEL_6_GRAPH_LP, VAL_LEFT_YAXIS,
VAL_MANUAL, dMin, dMax);
break;
}
return 0;
}

int CVICALLBACK SetLPPMax (int panel, int control, int event,
void *callbackData, int eventData1, int eventData2)
{
double dMin, dMax;
switch (event)
{
case EVENT_COMMIT:
    GetCtrlVal (panel6, PANEL_6_N_LPPULSE_MIN, &dMin);
    GetCtrlVal (panel6, PANEL_6_N_LPPULSE_MAX, &dMax);
    if (dMax <= dMin)
      {
      dMax=dMin+0.1;
      SetCtrlVal (panel6, PANEL_6_N_LPPULSE_MAX, dMax);
      }
SetAxisScalingMode (panel6, PANEL_6_GRAPH_LPPULSE, VAL_LEFT_YAXIS,
VAL_MANUAL, dMin, dMax);
break;
}
return 0;
}

int CVICALLBACK SetLPPMin (int panel, int control, int event,
void *callbackData, int eventData1, int eventData2)
{
double dMin, dMax;
switch (event)
{
case EVENT_COMMIT:
    GetCtrlVal (panel6, PANEL_6_N_LPPULSE_MIN, &dMin);
    GetCtrlVal (panel6, PANEL_6_N_LPPULSE_MAX, &dMax);
    if (dMin >= dMax)
      {
      dMin=dMax-0.1;
      SetCtrlVal (panel6, PANEL_6_N_LPPULSE_MIN, dMin);
      }
SetAxisScalingMode (panel6, PANEL_6_GRAPH_LPPULSE, VAL_LEFT_YAXIS,
VAL_MANUAL, dMin, dMax);
break;
}
return 0;
}



int CVICALLBACK RefreshGraphLP (int panel, int control, int event,
void *callbackData, int eventData1, int eventData2)
{
switch (event)
{
case EVENT_COMMIT:
DeleteGraphPlot (panel6, PANEL_6_GRAPH_LP, -1, VAL_IMMEDIATE_DRAW);
break;
}
return 0;
}

int CVICALLBACK AD_Amplify (int panel, int control, int event,
```

```
void *callbackData, int eventData1, int eventData2)
{
switch (event)
{
case EVENT_COMMIT:

if (iADamp>=20)   /* DEFAULT Gain changed from 20 to 2 on 06/25/06 by FD */
    iADamp=50;
if (iADamp==10)
    iADamp=20;
if (iADamp==5)
    iADamp=10;
if (iADamp==2)
    iADamp=5;
if (iADamp==1)
    iADamp=2;
LSB0=(double) (2.*10./iADamp/uMaxPoints*1000);
   SetCtrlVal (panel1, PANEL_1_NUMERIC_AD_Amp, iADamp);
   SetCtrlVal (panel1, PANEL_1_NUMERIC_LSB, LSB0);
   break;
}
return 0;
}

int CVICALLBACK AD_Attenuate (int panel, int control, int event,
void *callbackData, int eventData1, int eventData2)
{
switch (event)
{
case EVENT_COMMIT:

iADamp=iADamp;
if (iADamp<=2)   /* DEFAULT Gain changed from 20 to 2 on 06/25/06 by FD */
    iADamp=1;
if (iADamp==5)
    iADamp=2;
if (iADamp==10)
    iADamp=5;
if (iADamp==20)
    iADamp=10;
if (iADamp>=50)
    iADamp=20;
LSB0=(double) (2.*10./iADamp/uMaxPoints*1000);
   SetCtrlVal (panel1, PANEL_1_NUMERIC_AD_Amp, iADamp);
   SetCtrlVal (panel1, PANEL_1_NUMERIC_LSB, LSB0);
break;
}
return 0;
}

/* Remove the pulse valve setup to its own section */

int CVICALLBACK SetupPV (int panel, int control, int event,
void *callbackData, int eventData1, int eventData2)
{
int iIgnoreWarning = 0, iStatus, iRetVal;
int iPulseRate, iPulseAve;
double dTimeDelay;

unsigned int ulGpctr0 = ND_COUNTER_0;
unsigned int ulHIGHcnt1, ulLOWcnt1;

switch (event)
{
case EVENT_COMMIT:

/*  Read Values off the Setup Control Panel  */

/* Read the Pulse Valve Trigger Rate   */
GetCtrlVal (panel0, PANEL_0_NUMERIC_pulse_rate, &iPulseRate);

/* Read the Number of points to average   */
GetCtrlVal (panel0, PANEL_0_NUMERIC_Average, &iPulseAve);

/* Read the Delay between pulse valve trigger and trigger to DAQ   */
GetCtrlVal (panel0, PANEL_0_NUMERIC_time_delay, &dTimeDelay);

/* Set up the counter, at the frequency read above to drive the pulse valve.  */
iStatus = GPCTR_Control(iPCI6110, ulGpctr0, ND_RESET);
     iRetVal = NIDAQErrorHandler(iStatus, "GPCTR_Control/RESET",iIgnoreWarning);

      iStatus = GPCTR_Set_Application(iPCI6110, ulGpctr0,ND_PULSE_TRAIN_GNR);
     iRetVal = NIDAQErrorHandler(iStatus, "GPCTR_Set_Application",iIgnoreWarning);

     iStatus = GPCTR_Change_Parameter(iPCI6110, ulGpctr0, ND_SOURCE,ND_INTERNAL_100_KHZ);
     iRetVal = NIDAQErrorHandler(iStatus,"GPCTR_Change_Parameter/SOURCE", iIgnoreWarning);

      ulHIGHcnt1 = 100*dTimeDelay;
      ulLOWcnt1 = 100000/iPulseRate-ulHIGHcnt1;
```

```
     iStatus = GPCTR_Change_Parameter(iPCI6110, ulGpctr0, ND_COUNT_1,ulLOWcnt1);
     iRetVal = NIDAQErrorHandler(iStatus,"GPCTR_Change_Parameter/COUNT1", iIgnoreWarning);

     iStatus = GPCTR_Change_Parameter(iPCI6110, ulGpctr0, ND_COUNT_2,ulHIGHcnt1);
     iRetVal = NIDAQErrorHandler(iStatus,"GPCTR_Change_Parameter/COUNT2", iIgnoreWarning);

/* To output a counter pulse, you must call Select_Signal. */
     iStatus = Select_Signal(iPCI6110, ND_GPCTR0_OUTPUT,ND_GPCTR0_OUTPUT, ND_LOW_TO_HIGH);
     iRetVal = NIDAQErrorHandler(iStatus,"Select_Signal/GPCTR0_OUTPUT-Enable", iIgnoreWarning);

     iStatus = GPCTR_Control(iPCI6110, ulGpctr0, ND_PROGRAM);
     iRetVal = NIDAQErrorHandler(iStatus, "GPCTR_Control/PROGRAM",iIgnoreWarning);

SetCtrlVal (panel0, PANEL_0_LED_PulseValve, 1);
isPulsing = 1;

break;
}
return 0;
}

int CVICALLBACK RescaleY (int panel, int control, int event,
void *callbackData, int eventData1, int eventData2)
{
double dVmin, dVmax;

switch (event)
{
case EVENT_COMMIT:
GetCtrlVal (panel1, PANEL_1_NUMERIC_Vmin, &dVmin);
GetCtrlVal (panel1, PANEL_1_NUMERIC_Vmax, &dVmax);
SetAxisScalingMode (panel1, PANEL_1_GRAPH_signal, VAL_LEFT_YAXIS,
VAL_MANUAL, dVmin, dVmax);

GetCtrlVal (panel1, PANEL_1_NUMERIC_offsetDCSig, &dOffsetDCSig);
GetCtrlVal (panel1, PANEL_1_NUMERIC_offsetDCRef, &dOffsetDCRef);
GetCtrlVal (panel1, PANEL_1_NUMERIC_offsetVSaw,  &dOffsetVSaw);

PlotWaveform (panel1, PANEL_1_GRAPH_signal, adScan, icounter, VAL_DOUBLE,
1., 0., 0., 1.0, VAL_THIN_LINE, VAL_NO_POINT, VAL_SOLID, 1, VAL_BLACK);

PlotWaveform (panel1, PANEL_1_GRAPH_signal, adScan+ulDataPoints, icounter, VAL_DOUBLE,
1.0, dOffsetDCSig, 0, 1, VAL_THIN_LINE, VAL_NO_POINT, VAL_SOLID, 1, VAL_GREEN);

PlotWaveform (panel1, PANEL_1_GRAPH_signal, adScan+2*ulDataPoints, icounter, VAL_DOUBLE,
1.0, dOffsetDCRef, 0, 1, VAL_THIN_LINE, VAL_NO_POINT, VAL_SOLID, 1, VAL_RED);

PlotWaveform (panel1, PANEL_1_GRAPH_signal, adScan+3*ulDataPoints, icounter, VAL_DOUBLE,
1.0, dOffsetVSaw, 0, 1, VAL_THIN_LINE, VAL_NO_POINT, VAL_SOLID, 1, VAL_BLUE);


break;
}
return 0;
}

int CVICALLBACK Scan_Return_Setup (int panel, int control, int event,
void *callbackData, int eventData1, int eventData2)
{
int isSaved, iContinue;

switch (event)
{
case EVENT_COMMIT:

GetCtrlAttribute (panel1, PANEL_1_COMMANDBUTTON_Save, ATTR_DIMMED, &isSaved);
if (! isSaved)  // File Not Saved
{
iContinue = ConfirmPopup ("Warning!", "File Not Saved.\n   Do you wish to discard scan?");
if (iContinue)    // Discarding Scan
{
  SetPanelAttribute (panel0, ATTR_VISIBLE, 1);
// SetCtrlVal(panel0,PANEL_0_NUMERIC_Wavelength,0.0);
return 0;
}
}
else
{
SetPanelAttribute (panel0, ATTR_VISIBLE, 1);
// SetCtrlVal(panel0,PANEL_0_NUMERIC_Wavelength,0.0);
}

break;
}
return 0;
}

int CVICALLBACK Wform_Return_Setup (int panel, int control, int event,
void *callbackData, int eventData1, int eventData2)
{
```

```
switch (event)
{
case EVENT_COMMIT:

ibreakflag = 1;

break;
}
return 0;
}

int CVICALLBACK Change_Gates (int panel, int control, int event,
void *callbackData, int eventData1, int eventData2)
{
switch (event)
{
case EVENT_COMMIT:

iChangeWFGates = 1;

break;
}
return 0;
}

int CVICALLBACK Save_Waveform (int panel, int control, int event,
void *callbackData, int eventData1, int eventData2)
{
switch (event)
{
case EVENT_COMMIT:

iSaveWaveform = 1;
break;
}
return 0;
}



int CVICALLBACK Waveform_Gain (int panel, int control, int event,
void *callbackData, int eventData1, int eventData2)
{
switch (event)
{
case EVENT_COMMIT:

iChangeWFGain = 1;
break;
}
return 0;
}

char *Newdir(char *currdir,char *append_this ,int *Ierror)
{
/*CREATES a new directory, and returns a pointer to an array of
characters containing the new directory. Use that name to construct
the path for saving or openning files. Use inside of strcpy to pass
the name of the new directory.
For error checking:
0  : No error
-8 : DIsk is full
-9 : DIrectory already exists
*/
int oldBreakState;
int error;
char dir[MAX_PATHNAME_LEN]="";
strcpy (dir,currdir);
    strcat(dir,"\\");
    strcat(dir,append_this);
oldBreakState = SetBreakOnLibraryErrors (0);
*Ierror=MakeDir (dir);
SetBreakOnLibraryErrors (oldBreakState);
error=*Ierror;
currdir=dir;
return currdir;
}

int CVICALLBACK GetXY (int panel, int control, int event,
void *callbackData, int eventData1, int eventData2)
{
double dX, dY;
int iIndex;

switch (event)
{
case EVENT_COMMIT:
GetGraphCursor (panel1, PANEL_1_GRAPH_signal, 1, &dX, &dY);
iIndex = floor (dX);
if (iIndex > 0 && iIndex < ulDataPoints)
```

```
{
SetCtrlVal(panel1,PANEL_1_NUMERIC_Xval,iIndex);
SetCtrlVal(panel1,PANEL_1_NUMERIC_ACSig,adScan[iIndex]);
SetCtrlVal(panel1,PANEL_1_NUMERIC_DCSig,adScan[iIndex+ulDataPoints]);
SetCtrlVal(panel1,PANEL_1_NUMERIC_DCRef,adScan[iIndex+2*ulDataPoints]);

SetGraphCursor (panel1, PANEL_1_GRAPH_signal, 1, dX, adScan[iIndex]);
}
break;
}
return 0;
}

int CVICALLBACK stopPV (int panel, int control, int event,
void *callbackData, int eventData1, int eventData2)
{

int iIgnoreWarning = 0, iStatus, iRetVal;
unsigned int ulGpctr0 = ND_COUNTER_0;


switch (event)
{
case EVENT_COMMIT:

iStatus = GPCTR_Control(iPCI6110, ulGpctr0, ND_DISARM);
     iRetVal = NIDAQErrorHandler(iStatus, "GPCTR_Control/PROGRAM",iIgnoreWarning);

SetCtrlVal (panel0, PANEL_0_LED_PulseValve, 0);
isPulsing = 0;

break;
}
return 0;
}
```

Appendix C

Data Processing Scripts and Procedures

C.1 General Description

The raw data comes in the form of a block of voltages as recorded from each input onto the A/D card. It is a bit of work to turn that into a spectra with an absolute, accurate, and precise x-axis and % Absorbance on the y-axis. To do this, I wrote a series of scripts in LabTalk (and some in C) to do this process automatically with places to check the process along the way. The first step is to open the main program in Origin's script window. The main program is set up to have an easy way to set up the file parameters, like file name and location, specifying frequency ranges for peak finding, etc. The main program then calls each subroutine, passing along the pertinent information.

C.2 Origin Code

```
////////////////////// MAIN_ET.OGS (help.txt)////////////////////;
//// INITIALIZATION FOR THE DATA ANALYSIS - PATH AND FILENAME PREFIX (from .001 to .999)////;
 %k=nov2111; %t=J:\4marobert\hd2op\nov2111;  %n=C:\Users\Melanie\Documents\NewTable\Scripts_new;
 if (exist(scanlist)!=2) {run.file(%n\EastScanList.ogs);};

//// IMPORT RAW ASCII DATA////
  for (FN=11;FN<=12;FN++){
// FN=03; ;
  gain=316; autoscan=0; segover=0; run.file(%n\EastOpenFile2.ogs);

//// Ti:Sapph Laser Etalon Fringes Smoothing and Counting ////
// FN=06;
 smooth=0; FWHM=20;  NWindow=10; FWHMPOS=3; Err=5.0; MinY=.2;
 run.file(%n\EastLEtalon.ogs);
};

//enter missed/extra number of Large Etalon Fringes////;
//then create interpolated large etalon axis and find Small etalon peaks///;

  for (FN=11;FN<=12;FN++){
//FN=01;
LFSR=1.50462922013;
run.file(%n\RelFreqL.ogs);
```

```
//FN=01;
NWindow=2; sreffile=08; offset=100000.0; MinY=0.8;
run.file(%n\EastSEtalon.ogs);
};

/////create small etalon axis/////////////;
 for (FN=11;FN<=11;FN++){
//FN=01;
sreffile=08; SFSR=0.24984691172; soffset=100000;
run.file(%n\RelFreqS.ogs);
};


///use peakfinder on the small etalon axis get freq reference peak///;
FN=02;
NWindow=4; NIni=2663; NFinal=2665; MinY=0.2;
run.file(%n\refpeak.ogs);


//// Stitch together segments////;
//enter name for spreadsheet containing concatenated data//;
//for now, list files in order of increasing freq//
 %t=%ktot2;
 files={09,10,11};
  pkGHz=24987.471865;  //relative GHz of reference peak//;
  refpk=2651.3865; //D2O v3 000 111 line//;
 run.file(%n\EastConcatenate.ogs);


////// Peak Finding on concatenated data///;
 %t=%ktot;
 Nwindow=7;  Amin=.02;
FreqIni=2605;  FreqFinal=2627; run.file(%n\EastSnyderPeakFinder.ogs);

//// Peak finding on the reference line//////;
 %t=%k001N;
 Nwindow=7;  Amin=.02;
FreqIni=24984;  FreqFinal=24992; run.file(%n\EastSnyderRefCell.ogs);

//////////////////////////////END//////////////////////////;


////////////////////////// OPENFILE.OGS////////////////////////////////////;
////////////////////////////////////////////////////////////////////////////;
/// ASCII DATA IMPORTED, AND TRANSFORMED TO THE FOUR COLUMN DATASHEET.  //;
/// PUT DATA INTO % ABSORBANCE FORM         //;
////////////////////////////////////////////////////////////////////////////;
%q=scanlist;

%p=%k$(FN); if (FN<100) %p=%k0$(FN); if (FN<10) %p=%k00$(FN);
if (exist(temp)==2)        {win -cd temp;};
if (exist(%pN)==2)          {win -cd %pN;};
win -t data data1 temp;    open -w %t\%p.scn; @WD=1;
win -t data data1 %pN;

////////////////////////////////////////////////////////////////////////////;
//// Creating worksheet ////;


   win -a %pN;
   work -a 12;

   work -n 1 Points;       work -t 1 2;
   work -n 2 GHz;          work -t 2 4;
   work -n 3 relFr;    work -t 3 1;
   work -n 4 relGHz;    work -t 4 1;
   work -n 5 Signal;       work -t 5 1;
   work -n 6 LEtalon;      work -t 6 1;
   work -n 7 SEtalon;     work -t 7 1;
   work -n 8 RefCell;      work -t 8 1;
   work -n 9 IRpower;      work -t 9 1;
   work -n 10 LEtnew;    work -t 10 1;
   work -n 11 SEtnew;    work -t 11 1;
   work -n 12 Abs;    work -t 12 1;

   %pN!wks.col1.digitmode=1;   %pN!wks.col1.digits=0;
   %pN!wks.col2.digitmode=1;   %pN!wks.col2.digits=4;
   %pN!wks.col3.digitmode=1;   %pN!wks.col3.digits=4;
   %pN!wks.col4.digitmode=1;   %pN!wks.col4.digits=4;
   %pN!wks.col5.digitmode=1;   %pN!wks.col5.digits=4;
   %pN!wks.col6.digitmode=1;   %pN!wks.col6.digits=4;
   %pN!wks.col7.digitmode=1;   %pN!wks.col7.digits=4;
   %pN!wks.col8.digitmode=1;   %pN!wks.col8.digits=4;

////////////////////////////////////////////////////////////////////////////;
///////////Entering data into worksheet/////////////////////////////////////;

  win -a temp;
  limit temp_d;
  LN = limit.size; minv=limit.ymax;
```

```
  win -a %pN;
for (i=1;i<=LN;i++)
{
%pN_Points[i]=i;
%pN_Signal[i]=temp_b[i];
%pN_SEtalon[i]=temp_c[i];
%pN_Refcell[i]=temp_d[i];
%pN_IRpower[i]=temp_e[i];
%pN_LEtalon[i]=temp_f[i];
// %pN_VET1[i]=-temp_d[i]+minv;
};

////////////////////////////////////////////////////////////////////////;
/////////making % Absorbance column//////////////////////////////////////;

  win -a %pN;
  %pN_Abs=100*(%pN_signal/$(gain))/(-1*%pN_IRpower);

////////////////////////////////////////////////////////////////////////;
////////// putting scan info into scanlist worksheet ////////////////////;

   win -a %q;

   wcol(1)[FN]$=%p;
   wcol(2)[FN]=$(FN);

if(temp_a[1]==0.0){
     wcol(17)[FN]=temp_a[12];}
else
 {wcol(17)[FN]=temp_a[1]/10000;}

   if (segover==0){
     wcol(5)[FN]=temp_a[26];
   wcol(6)[FN]=temp_a[28];
   wcol(8)[FN]=wcol(6)[FN]/wcol(5)[FN];
}
    else
    {wcol(5)[FN]=segover;
     wcol(8)[FN]=1021;
     wcol(6)[FN]=wcol(8)[FN]*wcol(5)[fn];
}

   wcol(7)[FN]=temp_a[32];
   wcol(9)[FN]=$(gain);



////////////////////////////////////////////////////////////////////////;
/////// generate x-axis if there is no autoscan file ////////////////////;


   startfreq=%q_TSStart[FN];
   startghz=startfreq*29.9792458;
   stepsize=%q_iStepSize[FN];
   seglength=%q_SegPts[FN];
   numseg=%q_ulNumSeg[FN];

   icount=1;

   for (i=0;i<numseg;i++)
      {
      for(j=0;j<(seglength);j++)
         {
 %pN_GHz[icount]=startghz+j*(stepsize/1000)+i*10;
     icount=icount+1;
 };
      };

////////////////////////////////////////////////////////////////////////;
////////////////entering VET data from autoscan if desired  //////////////;

if (autoscan==1){

win -t data data1 temp2;    open -w %t\%m0$(FN).sca;

win -a %pN;

for (i=1;i<=LN;i++)
   {
    wcol(9)[i]=temp2_b[i];
    wcol(10)[i]=temp2_b[i+1+LN];
   };

work -t 1 2;
work -t 2 4;

  };
```

```
////////////////// Draw the experiental plots (vs channels) ///////////////;

if (exist(%pfig1)==3) {win -c %pfig1;};
win -t graph %n\RawSignal %p.fig1;
   layer -i %pN_RefCell; layer -i %pN_SEtalon; layer -i %pN_Signal;
    set %pN_SEtalon -c 2;
rescale;
 layer -i %pN_VET1; layer -i %pN_LEtalon;
    set %pN_VET1 -c 5;
    set %pN_VET2 -c 17;

label -xb GHz;   label -yl VOLTS;


//////////////////////////////////////////////////////////////////////;

win -a %pN; win -h 1;
delete -v TN; delete -v %q; delete -v Nexist; win -cd temp; win -cd temp2;
////////////////////////////////// End. ////////////////////////////////;


//////////////////////////////////////////////////////////////////////;
// Subroutine for etalon fringes counting //
//////////////////////////////////////////////////////////////////////;

cm2GHz=29.97924580;

//FWHM=5;       // Gauss smoothing of the etalon signal;
//FWHMPOS=1;    // Gauss smoothing of the FPI position;
//NWindow=3;    // Snyder algorithm for finding etalon peak position (in fractional data points.
//MmiY=0.1;     // Minimum intensity (in percentage of the maximum intensity) when determining a fringe.

/* Finding scanfile name (%p) relating to filenumber FN, if the data has been analyzed before.*/

%p=%k$(FN); if (FN<100) %p=%k0$(FN); if (FN<10) %p=%k00$(FN);

win -a %pN;


//////////////////////////////////////////////////////////////////////;
////// Optional Gauss filter of the etalon signal ////////////////////;

//FWHM=5;       // Gauss smoothing of the etalon signal;

if (smooth!=0)
{
if (exist(et)==2) {win -cd et; };
win -t data data1 et;
et_A=%pN_Letalon;
et_B=et_A;
limit et_B;
NIni  =1;
NFinal=limit.size;

if(run.LoadOC("%n/Gaussfilter.c",1) != 0)
    {
     type -b "Error trying to load and compile Origin C file '%n\Gaussfilter.c";
      break 1;
     };

Gaussfilter(NIni,NFinal,FWHM,"et_A","et_B");

// limit et_B;
%pN_LETnew=et_B;
%pN_LEtnew = -%pN_LEtnew;
limit %pN_Letnew;
%pN_LEtnew = %pN_Letnew-limit.ymin;

delete -v FWHM;
win -cd et;
};

else
{
win -a %pN;
   limit %pN_Points;
   LN = limit.size;

for (i=1;i<=LN;i++)
{
%pN_LEtnew[i]=-%pN_LEtalon[i];
};
};



//////////////////////////////////////////////////////////////////;
//// create the worksheets needed to store the data ///////////////;

// data point number is the x-axis here.
//Nwindow=3;    // Snyder algorithm for finding etalon peak position (in fractional data points).
```

```
//MmiY=0.1;     // Minimum intensity (in percentage of the maximum intensity) when determining a fringe.

nseg=%q_ulNumSeg[FN];
npts=%q_SegPts[FN];

if (exist(%pP)==2)
  {
win -cd %pP;
  };

 newbook n:=%pP o:=1;
 for(j=1;j<=nseg;j++)
{
newsheet b:=%pP n:=segment_$(j) c:=6;
work -n 1 Points;     work -t 1 4;
    work -n 2 LFringes;    work -t 2 1;
    work -n 3 LEtalon;    work -t 3 1;
work -n 4 AsGHz;    work -t 4 1;
    work -n 5 LAxis;    work -t 5 4;
work -n 6 SEtalon;   work -t 6 1;
work -n 7 SFringes; work -t 7 1;
};

range ww=[%pP]Sheet1!;
ww.name$="summary";
ww.ncols=7;
ww.col1.name$=segment;
ww.col2.name$=SndLFr;
ww.col3.name$=SndSFr;
ww.col4.name$=LMissed;
ww.col5.name$=SMissed;
ww.col6.name$=LRelNo;
ww.col7.name$=SRelNo;

for(j=1;j<=nseg;j++)
{
%pP_segment[j]=j;
};

////////////////////////////////////////////////////////////////////////////;
///////////use the Snyder Peak Finder Algorithm to get the etalon peaks ///////;
////the peaks in each segment go in a different worksheet in the P workbook////;


if(run.LoadOC("%n\snyder.c",1) != 0)
{
type -b "Error trying to load and compile Origin C file '%n\snyder.c";
     break 1;
     };

//win -a %pP;
 for(k=1;k<=nseg;k++)
{
NIni=(k-1)*npts+1;
NFinal=k*npts-1;
range ne=[%pP]segment_$(k)!LEtalon;
range np=[%pP]segment_$(k)!Points;
range nf=[%pP]segment_$(k)!LFringes;
range no=[%pP]segment_$(k)!AsGHz;
snyder(NWindow,NIni,NFinal,MinY,%pN_Points,%pN_LEtnew,ne,np,nf);

// now change from points to autoscan x-axis//////////////////////;
range nf=[%pP]segment_$(k)!LFringes;
limit nf;
frnum=limit.ymax;
for(i=1;i<=frnum;i++)
      {
       strt=int(np[i]);
       diffp=np[i]-strt;
       slen=%pN_GHz[strt+1]-%pN_GHz[strt];
       interp=slen*diffp;
       no[i]=%pN_GHz[strt]+interp;
       };
};

  range ni=[%pP]summary!SndLFr;
  for(k=1;k<=nseg;k++)
{
   range no=[%pP]segment_$(k)!AsGHz;
ni[k]=no[2];
};



////////////////// Cleanup ////////////////////////////////////////////;

delete -v MinY;
delete -v %q;
delete -v Nini; delete -v NFinal; delete -v NMax;
delete -v %s;
```

```
////////////////////plot////////////////////////////////////////////////;

if (exist(%p_fig)==3) {win -cd %p_fig; };

//Create 2 panels
newpanel 2 1 name:=%p_fig optn:=1 result:=%p_fig;

//add a new layer
layadd;
layadd;

//plot the data
k=1;
plotxy iy:=[%pN]Sheet1!Signal plot:=0 legend:=0 ogl:=[%p_fig]1;


plotxy iy:=[%pN]sheet1!RefCell plot:=0 legend:=0 ogl:=[%p_fig]2;



//Set the properties of X axis in Layer3 and layer4
laysetscale igp:=[%p_fig] layer:=3 axis:=x from:=0 to:=900;
laysetscale igp:=[%p_fig] layer:=4 axis:=x from:=0 to:=900;
layer3.y.from=-20;
layer3.y.to=20;

//copy the scale from layer3 to layer4
laycopyscale igl:=3 dest:=4 axis:=2;

plotxy iy:=[%pN]sheet1!SEtalon plot:=0 legend:=0 ogl:=[%p_fig]3;
set %pN_SEtalon -c 3;
plotxy iy:=[%pN]sheet1!LEtalon plot:=0 legend:=0 ogl:=[%p_fig]4;

//Set the Width and height of each layer
layer1.width=90;
layer1.height=60;
layer2.width=90;
layer2.height=25;
layer3.width=90;
layer3.height=25;
layer4.width=90;
layer4.height=25;

//Set the layer's position
laysetpos igp:=[%p_fig] layer:=1 top:=35 unit:=page;
laysetpos igp:=[%p_fig] layer:=1 left:=5 unit:=page;
laysetpos igp:=[%p_fig] layer:=2 left:=5 unit:=page;
laysetpos igp:=[%p_fig] layer:=2 top:=35 unit:=page;
laysetpos igp:=[%p_fig] layer:=3 left:=5 unit:=page;
laysetpos igp:=[%p_fig] layer:=3 top:=10 unit:=page;
laysetpos igp:=[%p_fig] layer:=4 left:=5 unit:=page;
laysetpos igp:=[%p_fig] layer:=4 top:=10 unit:=page;


//Link layers
laylink igp:=[%p_fig] igl:=1 destlayers:=2:4 XAxis:=1;



/////////////// END. ////////////////////////////////////////////////////;



////////////////////////////////// RelFreqL.ogs ////////////////////////////////////////
//// Calculating relative frequencies based on marker cavity peak number and the FSR    /////
////////////////////////////////////////////////////////////////////////////////////////////

//// set constants and defaults. ////

cm2GHz=29.979245800;
%q=scanlist;
%p=%q_scanfile[FN]$;
nseg=%q_ulNumSeg[FN];
npts=%q_segPts[FN];

if (exist(%pS)==2) {win -cd %pS;};
@wd=1;  win -t data data1 %pS;
work -a 5*nseg+1;
work -n (5*nseg+1) datapt;
work -t (5*nseg+1) 4;


////////////////////////////////////////////////////////////////////////////////;
//// for each segment, adjust the large fringe spacing to be the large FSR   ////;
////////////////////////////////////////////////////////////////////////////////;

for(i=1;i<=nseg;i++)
{
```

```
sa=(i-1)*5+1;
work -n sa Linterp_$(i); work -t sa 1;
work -n (sa+1) Lrel_$(i);
work -n (sa+2) SEt_$(i);
work -n (sa+3) Sinterp_$(i);
work -n (sa+4) Srel_$(i);

start=(i-1)*npts+1;
end=i*npts;
count=0;
for(j=start;j<=end;j++)
 {
 count=count+1;
 %pS_datapt[count]=j
 };

range aa=[%pP]segment_$(i)!LFringes;
range bb=[%pS]Sheet1!datapt;

    %pS_Linterp$(i)=aa(bb);

};

////////////////////////////////////////////////////////////////////////;


//////////////////////////////////EastSEtalon.ogs ///////////////////////////////////////
//// Calculating relative frequencies based on marker cavity peak number and the FSR    /////
////////////////////////////////////////////////////////////////////////////////////////////////

//// set constants and defaults. ////

%q=scanlist;
cm2GHz=29.979245800;
%p=%q_scanfile[FN]$;
nseg=%q_ulNumSeg[FN];
npts=%q_segPts[FN];


%r=%q_scanfile[sreffile]$;

// calculate the relative fringe number for each segment based upon //////;
// the first segment of the reference scan.////////////////////////////////;

  range na=[%rP]summary!SndLFr;
  range nb=[%pP]summary!LRelNo;
range nd=[%pP]summary!SndLFr;
reffreq=na[1];

for(j=1;j<=nseg;j++)
{
nb[j]=(nd[j]-reffreq)/LFSR+offset;
};

//now create the large etalon relative axis//////////////////////////////;

for(k=1;k<=nseg;k++)
{
str=round(nb[k],0);
range nc=[%pS]sheet1!Linterp$(k);

for(i=1;i<=npts;i++)
 {
%pS_Lrel$(k)[i]=(nc[i]+str)*LFSR;
 };

};

////////////////////////////////////////////////////////////////////////////////;
//// use the interpolated large x-axis to find                              ////;
////  the peak positions of the small etalon                               ////;
////////////////////////////////////////////////////////////////////////////////;

//first bring in the small etalon data//;

for(j=1;j<=nseg;j++)
{
strtseg=(j-1)*npts+1;
for(i=1;i<=npts;i++)
 {
 %pS_SEt$(j)[i]=-%pN_SEtalon[strtseg+i];
 };
};

//use peak finder to find the small etalon peak wrt the large etalon rel axis//;

if(run.LoadOC("%n\snyder.c",1) != 0)
{
type -b "Error trying to load and compile Origin C file '%n\snyder.c";
     break 1;
     };
```

```
 for(k=1;k<=nseg;k++)
{
NIni=1;
NFinal=npts-1;
range ne=[%pP]segment_$(k)!SEtalon;
range np=[%pP]segment_$(k)!LAxis;
range nf=[%pP]segment_$(k)!SFringes;
snyder(NWindow,NIni,NFinal,MinY,%pS_LRel$(k),%pS_SEt$(k),ne,np,nf);
};

////take the 10th fringe and use that as the small etalon fringe///////;

  range ni=[%pP]summary!SndSFr;
  for(k=1;k<=nseg;k++)
{
   range no=[%pP]segment_$(k)!LAxis;
ni[k]=no[10];
};

////////////////cleanup/////////////////////////////////////////////////;


////////////////////////////////// RelFreqS.ogs ////////////////////////////////////
//// Calculating relative frequencies based on marker cavity peak number and the FSR    /////
////////////////////////////////////////////////////////////////////////////////////////////

//// set constants and defaults. ////

%q=scanlist;
cm2GHz=29.979245800;
%p=%q_scanfile[FN]$;
nseg=%q_ulNumSeg[FN];
npts=%q_segPts[FN];

////////////use the 10th fringe of each scan to create relative axis////;


       range ni=[%pP]summary!SndSFr;


%r=%q_scanfile[sreffile]$;

  range na=[%rP]summary!SndSFr;
  range nb=[%pP]summary!SRelNo;

sreffreq=na[1];

for(j=1;j<=nseg;j++)
{
nb[j]=(ni[j]-sreffreq)/SFSR+soffset;
};

////fill relative fringe of first segment into scanlist worksheet////////;

%q_TSFringe[FN]=nb[1];

////////////////////////////////////////////////////////////////////////////////;
//// for each segment, adjust the small fringe spacing to be the small FSR   ////;
////////////////////////////////////////////////////////////////////////////////;

work -a %pS;

for(i=1;i<=nseg;i++)
{
// sa=(i-1)*4+1;

// start=(i-1)*npts+1;
// end=i*npts;
// count=0;
// for(j=start;j<=end;j++)
//  {
//  count=count+1;
//  %pS_datapt[count]=j
//  };

range aa=[%pP]segment_$(i)!SFringes;
range bb=[%pS]Sheet1!Lrel$(i);
range cc=[%pS]Sheet1!Sinterp$(i);

    cc=aa(bb);

};


////////////////////////////////////////////////////////////////////////;

////turn the small etalon interpolated axis into a relative frequency axis///;
// and copy it into the N spreadsheet//////////////////////////////////////;

icount=0;
```

```
for(k=1;k<=nseg;k++)
{
str=round(nb[k],0);

range nc=[%pS]sheet1!Sinterp$(k);

for(i=1;i<=npts;i++)
 {
%pS_Srel$(k)[i]=(nc[i]+str)*SFSR;
 icount=(k-1)*npts+i;
        %pN_relGHz[icount]=%pS_Srel$(k)[i];
 };

};



////////////////////////////////////END////////////////////////////////////;




////////////////////////////////////////////////////////////////////////;
////subroutine for finding the peak to be used as the reference frequence//;
////////////////////////////////////////////////////////////////////////;

%q=scanlist;
%p=%q_scanfile[FN]$;
nseg=%q_ulNumSeg[FN];
npts=%q_segPts[FN];

if (exist(%prP)==2) {win -cd %prP;};
@wd=1;  win -t data data1 %prP;
work -a 1;
work -n 1 relGhz;   work -t 1 4;
work -n 2 Peak;
work -n 3 Peaknum;


////////////////////////////////////////////////////////////////////////////;
///////////use the Snyder Peak Finder Algorithm to get the etalon peaks ///////;


if(run.LoadOC("%n\snyder.c",1) != 0)
{
type -b "Error trying to load and compile Origin C file '%n\snyder.c";
     break 1;
     };

//the frequency range (Nini and Nfinal), nwindow, and minimun y-value should be//;
// entered when calling the subroutine. The relative frequency axis from the   //;
// small (250 MHz etalon)                                                      //;

range ne=[%prP]sheet1!Peak;
range np=[%prP]sheet1!relGHz;
range nf=[%prP]sheet1!Peaknum;

// snyder(NWindow,NIni,NFinal,MinY,%pN_relGHz,%pN_Abs,ne,np,nf);



//////////////////END//////////////////////////////;

delete -v MinY;
delete -v %p;
delete -v Nini; delete -v NFinal;
delete -v NWindow;


////////////////////////East Concatenate/////////////////////////////////;
////////////////////////////////////////////////////////////////////////////;

%q=scanlist;
cm2GHz=29.9792458;

if (exist(%t)==2) {win -cd %t;};
@wd=1;  win -t data data1 %t;
work -a 4;
work -n 1 frequency;   work -t 1 4;
work -n 2 percentAbs;
work -n 3 RefCell;
work -n 4 IRpower;
work -n 5 Letalon;
work -n 6 Setalon;

limit files;
num=limit.size;

icount=0;
```

```
for (k=1;k<=num;k++)
{
FN=files[k];
%p=%q_scanfile[FN]$;
nseg=%q_ulNumSeg[FN];
npts=%q_segPts[FN];
ntot=nseg*npts;
icount=;
ntot=;
 for (i=1;i<=ntot;i++)
 {
   icount=icount+1;

   %t_frequency[icount]=((%pN_relGHz[i]-pkGHz)/cm2GHz)+refpk;
   %t_percentAbs[icount]=%pN_Abs[i];
   %t_RefCell[icount]=%pN_RefCell[i];
   %t_IRpower[icount]=%pN_IRpower[i];
   %t_Letalon[icount]=%pN_LEtalon[i];
   %t_Setalon[icount]=%pN_SEtalon[i];

 };


};


// Snyder peak finder subroutine //


//Nwindow=1;
//Amin=0.005;
//FreqIni=-0.1;
//FreqFinal=47;

%r=%tP;
if (exist(%r)!=2){win -t data data1 %r; work -a 1;
                  work -n 1 X; work -n 2 Y; work -n 3 Label; work -t 3 5;};
else {win -a %r; clearworksheet %r;
      work -n 1 X; work -n 2 Y; work -n 3 Label; work -t 3 5;};

%s=snyder;
if (exist(%s)!=2){win -t data data1 %s;};
else {win -a %s; clearworksheet %s;};
//if (IFGHz==1) {%s_a=%t_GHz;}; else {%s_a=%t_CM;};
//if (IFGSSM==0) {%s_b=%t_Absorbance;}; else {%s_b=%t_GSSM;};
%s_a=%t_frequency;
%s_b=%t_percentAbs;
limit %s_b;
if (abs(FreqIni-FreqFinal)<0.0001)
   {FreqIni=Limit.xmin;
    FreqFinal=Limit.xmax;};
if (FreqIni<limit.xmin)
   {FreqIni=Limit.xmin;};
if (FreqFinal>limit.xmax)
   {FreqFinal=Limit.xmax;};
//FreqIni=; FreqFinal=;
Nini  =xindex(FreqIni,%s_b);
NFinal=xindex(FreqFinal,%s_b);

//Nini=;NFinal=;
Dif0=1.0;
Nmax=0;

for (NI=Nwindow+Nini; NI<=NFinal-Nwindow;NI++){
SumU=0.0;
SumL=0.0;
for (NJ=NI-Nwindow; NJ<=NI-1; NJ++){
SumL=SumL+%s_b[NJ];};
    for (NK=NI+1; NK<=NI+Nwindow; NK++){
SumU=SumU+%s_b[NK];};
Dif1=SumL-SumU;

Dif01=Dif0*Dif1;
If ((Dif01<=0.0)&&(%s_b[NI]>Amin)&&(dif0<0.0)){
NMax=NMax+1;
ymax0=Max(%s_b[NI-2],%s_b[NI-1],%s_b[NI],%s_b[NI+1],%s_b[NI+2]);
%r_Y[NMax]=ymax0;
DifX=%s_a[NI]-%s_a[NI-1];
%r_X[NMax]=%s_a[NI]-DifX*Dif1/(Dif1-Dif0);};
Dif0=Dif1;};

%r_Label=int(%r_X*100000)/100000;
win -a %r;  win -ch 1;

delete -v A*;
delete -v N*;
delete -v D*;
delete -v Freq*;

win -cd %s;
```

```
delete -v %s;
delete -v %r;


/* End */


/*--------------------------------------------------------------------------*
 * File Name:   *
 * Creation:  *
 * Purpose: OriginC Source C file *
 * Copyright (c) ABCD Corp. 2003, 2004, 2005, 2006, 2007, 2008, 2009, 2010 *
 * All Rights Reserved *
 *  *
 * Modification Log: made by Melanie 1/2010 *
 *--------------------------------------------------------------------------*/

////////////////////////////////////////////////////////////////////////////////
// Including the system header file Origin.h should be sufficient for most Origin
// applications and is recommended. Origin.h includes many of the most common system
// header files and is automatically pre-compiled when Origin runs the first time.
// Programs including Origin.h subsequently compile much more quickly as long as
// the size and number of other included header files is minimized. All NAG header
// files are now included in Origin.h and no longer need be separately included.
//
// Right-click on the line below and select 'Open "Origin.h"' to open the Origin.h
// system header file.
#include <Origin.h>
#include <math.h>
#include <data.h>
////////////////////////////////////////////////////////////////////////////////

//#pragma labtalk(0) // to disable OC functions for LT calling.

////////////////////////////////////////////////////////////////////////////////
// Include your own header files here.


////////////////////////////////////////////////////////////////////////////////
// Start your functions here.
// datax - x-axis of dataset
// datay - y-axis of dataset
// peaks - peak position y-axis
// points - peak position x-axis

void snyder(int Nwindow, double Nini, double NFinal,
double MinY, string datax, string datay, string peaks, string points, string frnum){

int NMax, NI, NJ, NK;
double Dif0, Dif01, Dif1, DifX, Dstep, Dstep0, SumU, SumL, ymax0, xmax0;
vector<double> test(6);

Dataset dsdX(datax);
Dataset dsdY(datay);
Dataset dspX(points);
Dataset dspY(peaks);
Dataset dspN(frnum);

vector vdX, vdY, vpX, vpY, vpN;
vdX=dsdX;
vdY=dsdY;



Dif0=1.0;
NMax=0;

for (NI=Nwindow+Nini; NI<=NFinal-Nwindow;NI++)
{

SumU=0.0;
SumL=0.0;
for (NJ=NI-Nwindow; NJ<=NI-1; NJ++){
SumL=SumL+vdY[NJ];}
    for (NK=NI+1; NK<=NI+Nwindow; NK++){
SumU=SumU+vdY[NK];}
Dif1=SumL-SumU;

Dif01=Dif0*Dif1;
if ( (Dif01<=0.0) && (vdY[NI]>MinY) && (Dif0<0.0) ){
NMax=NMax+1;
test[1]=vdY[NI-2];
test[2]=vdY[NI-1];
test[3]=vdY[NI];
test[4]=vdY[NI+1];
test[5]=vdY[NI+2];
ymax0=max(test);
DifX=vdX[NI]-vdX[NI-1];
xmax0=vdX[NI]-DifX*Dif1/(Dif1-Dif0);
```

```
vpX.Add(xmax0);
vpY.Add(ymax0);
vpN.Add(NMax);


}
Dif0=Dif1;
}

dspX=vpX;
dspY=vpY;
dspN=vpN;

}


/*--------------------------------------------------------------------------*
 * File Name:   *
 * Creation:  *
 * Purpose: OriginC Source C file *
 * Copyright (c) ABCD Corp. 2003, 2004, 2005, 2006, 2007, 2008, 2009, 2010 *
 * All Rights Reserved *
 *  *
 * Modification Log: *
 *--------------------------------------------------------------------------*/

////////////////////////////////////////////////////////////////////////////////
// Including the system header file Origin.h should be sufficient for most Origin
// applications and is recommended. Origin.h includes many of the most common system
// header files and is automatically pre-compiled when Origin runs the first time.
// Programs including Origin.h subsequently compile much more quickly as long as
// the size and number of other included header files is minimized. All NAG header
// files are now included in Origin.h and no longer need be separately included.
//
// Right-click on the line below and select 'Open "Origin.h"' to open the Origin.h
// system header file.
#include <Origin.h>
////////////////////////////////////////////////////////////////////////////////


////////////////////////////////////////////////////////////////////////////////
// Include your own header files here.


////////////////////////////////////////////////////////////////////////////////
// Start your functions here.
/* Raw - raw dataset needed to be gauss smoothed;
   gauss - New dataset after gauss smoothing
   NMin, NMax - start and End point, datapoints in-between will be gauss-smoothed*/

void Gaussfilter(int NMin, int NMax, int FWHM, string raw, string gauss){

int i, j, j0, IMax, NPoints, MinMax;
double Cutoff, sumtotal, FWHMnorm, IMax0, ssum, ff, temp;
double vFA[1000];

if (FWHM>0)
{
Cutoff=0.0001;
Dataset dsA(raw);
Dataset dsB(gauss);
vector vA, vB;
vA=dsA;
vB=dsB;
NPoints=dsA.GetSize();

/* rationalize start point NMin and End Point NMax*/
    if (NMin>NMax) {MinMax=NMin; NMin=NMax; NMax=NMin;};
    if (NMin==NMax) {NMin=1; NMax=NPoints;};
    if (NMin<1) NMin=1;
    if (NMax>=NPoints) NMax=NPoints;

    FWHMnorm=2.772588722/(FWHM*FWHM);

    IMax0=-ln(Cutoff)/FWHMnorm;
    IMax=sqrt(IMax0);
    sumtotal=0;
//    printf ("IMax=  %d\n", IMax);

    for (i=0;i<=IMax;i++){
     vFA[i]=0.0;}


    for (i=0;i<=IMax;i++){
     vFA[i]=exp(-i*i*FWHMnorm);
     sumtotal=sumtotal+vFA[i];};

    sumtotal=2*sumtotal-vFA[0];

    for (i=0;i<=IMax;i++){
        vFA[i]=vFA[i]/sumtotal;};
```

```
/*    for (i=1;i<=Nmin-1;i++){%r_B[i]=%r_A[i];}; */

    for (i=NMin;i<=NMin+IMax-1;i++){
        ssum=0;
        ff=0;
        for (j=-IMax;j<=IMax;j++){
            if ((i+j)>=1) {
                j0=abs(j);
          ssum=ssum+vFA[j0];
          ff=ff+vA[i+j]*vFA[j0];};  };
        vB[i]=ff/ssum;  };

    for (i=NMin+IMax; i<=NMax-IMax-1;i++){
        ff=vA[i]*vFA[0];
        for (j=1;j<=IMax;j++){
          ff=ff+(vA[i+j]+vA[i-j])*vFA[j];};
    vB[i]=ff;};

    for (i=NMax-IMax;i<=NMax-1;i++){
        ssum=0;
        ff=0;
        for (j=-IMax;j<=IMax;j++){
             if ((i+j)<NPoints) {
          j0=abs(j);
          ssum=ssum+vFA[j0];
          ff=ff+vA[i+j]*vFA[j0];};
          };
        vB[i]=ff/ssum;  };

        dsB=vB;
}

}

/* End */
```